University of Alberta

Cost-Effective and Scalable Solutions to Materials Science Problems--Novel Thin Film Semiconductors for Photovoltaic Applications and Template Directed Synthesis of Copper Nanowires

By

Nathan J. Gerein ©

A thesis submitted to the Faculty of Graduate Studies and Research

In partial fulfillment of the requirements for the degree of

Doctor of Philosophy

Department of Chemistry

Edmonton, Alberta
Spring 2007

Library and
Archives Canada

Published Heritage
Branch

395 Wellington Street
Ottawa ON K1A 0N4
Canada

Bibliothèque et
Archives Canada

Direction du
Patrimoine de l'édition

395, rue Wellington
Ottawa ON K1A 0N4
Canada

Your file Votre référence
ISBN: 978-0-494-29678-3
Our file Notre référence
ISBN: 978-0-494-29678-3

NOTICE:
The author has granted a non-exclusive license allowing Library and Archives Canada to reproduce, publish, archive, preserve, conserve, communicate to the public by telecommunication or on the Internet, loan, distribute and sell theses worldwide, for commercial or non-commercial purposes, in microform, paper, electronic and/or any other formats.

The author retains copyright ownership and moral rights in this thesis. Neither the thesis nor substantial extracts from it may be printed or otherwise reproduced without the author's permission.

AVIS:
L'auteur a accordé une licence non exclusive permettant à la Bibliothèque et Archives Canada de reproduire, publier, archiver, sauvegarder, conserver, transmettre au public par télécommunication ou par l'Internet, prêter, distribuer et vendre des thèses partout dans le monde, à des fins commerciales ou autres, sur support microforme, papier, électronique et/ou autres formats.

L'auteur conserve la propriété du droit d'auteur et des droits moraux qui protège cette thèse. Ni la thèse ni des extraits substantiels de celle-ci ne doivent être imprimés ou autrement reproduits sans son autorisation.

In compliance with the Canadian Privacy Act some supporting forms may have been removed from this thesis.

While these forms may be included in the document page count, their removal does not represent any loss of content from the thesis.

Conformément à la loi canadienne sur la protection de la vie privée, quelques formulaires secondaires ont été enlevés de cette thèse.

Bien que ces formulaires aient inclus dans la pagination, il n'y aura aucun contenu manquant.

Canada

For Carla and Zoë

Abstract

In Part 1 of this thesis minerals from the Cu-Bi-S and Cu-Sb-S phase systems are identified as candidates for use as the solar absorber in thin film PV devices. Thin films of the mineral wittichenite, Cu_3BiS_3, were synthesized on fused silica substrates by heating Cu-Bi metal precursor films and Cu-S-Bi metal sulfide precursor films under H_2S. The effect of precursor composition and structure, heating temperature, heating profile, and gas composition and pressure were systematically investigated. Phase-pure Cu_3BiS_3 films 250-1000 nm thick were synthesized, with the morphology of the films being dependent on the composition, structure, and heating profile of the precursor films. Regardless of processing conditions, Cu_3BiS_3 thin films produced in this two-step process are either discontinuous or contain hollow pockets between the film and substrate. The electrical resistivity of these Cu_3BiS_3 films ranged from 3-200 $\Omega\cdot$cm.

Cu_3BiS_3 thin films were also synthesized in a one-step process by reactive sputter deposition of Cu-S and Bi on heated fused silica substrates. Films produced by this process are crystalline, phase-pure, dense, smooth, and continuous. As-deposited films, 300-600 nm thick, have a direct forbidden band gap of 1.4 eV, an optical absorption coefficient of 1×10^5 cm^{-1} at 1.9 eV, p-type conductivity, and an electrical resistivity of 84 $\Omega\cdot$cm. The crystallite sizes of the films may be increased, and the electrical resistivity of the films decreased to 9.6 $\Omega\cdot$cm, by post-deposition annealing under H_2S. Cu_3BiS_3 thin films of similar quality, 1.2 μm thick, were deposited on TCO coated soda-lime and borosilicate glass substrates by the same method. Material and method compatibilities

were also investigated as a preliminary step in the application of combinatorial methods to the development of thin film PV devices based on Cu_3BiS_3.

In Part 2 of this thesis the effect of AC electrodeposition conditions on copper deposition into porous aluminum oxide templates are systematically investigated. A FFDOE was utilized to study the effect of five variables: frequency, voltage, pulsed or continuous deposition, electrolyte concentration, and barrier layer thinning voltage, on the quality of copper deposition into oxalic acid-anodized templates. Continuous AC sine wave deposition conditions yielded excellent uniformity of pore-filling, but damaged the PAO template when deposition was continued until bulk copper was deposited on the surface of the electrode. Pulsed electrodeposition yielded comparable uniformity of pore-filling and no damage to the PAO template.

Further optimization of pulsed deposition conditions was accomplished by examining the effect of square and sine waveforms, and pulse polarity, on the quality of copper deposition into sulfuric and oxalic acid-anodized templates. Pulsed square waveforms produced better pore-filling than pulsed sine waveforms. For sine wave depositions, the oxidative/reductive pulse polarity was more efficient than the commonly used reductive/oxidative pulse polarity. For square wave depositions into sulfuric acid grown pores, the reductive/oxidative pulse polarity produces more uniform pore-filling, likely as a result of enhanced resonant tunneling through the barrier layer and re-oxidation of copper in faster filling pores.

Acknowledgements

I have been fortunate to receive the support of many people during my graduate studies, without whom, the quality of this thesis would have undoubtedly suffered. First and foremost, is my supervisor Dr. Joel Haber. His honesty and integrity in the pursuit of science is exemplary, and the lessons I have learned by observing his conduct will serve me well, regardless of where my career takes me. He was always available, open to discussion, and encouraging. I consider myself fortunate to have had him as my supervisor. I would also like to acknowledge my co-supervisor, Dr Jillian Buriak. Her assistance in finding post-doctoral employment is appreciated, and her enthusiasm and passion for science continues to be an inspiration.

Others who played a role include George Braybrook, who collected the majority of the SEM data presented in this thesis. During the many hours spent in the SEM lab his interest in matters scientific, and otherwise, always kept things interesting. Additional SEM data, EDX data, and all XRD data was collected on instruments housed at the National Institute for Nanotechnology (NINT). Training and operational assistance for these instruments was provided by Daniel Salamon (SEM) and Steve Launspach (XRD). Their assistance, and the occasional distraction they provided, is appreciated. WDX and auger data presented in this thesis was collected by Segi Matveev and Shihong Xu, respectively. I would also like to thank the staff of the NanoFab for their assistance, in particular Dr. Ken Westra for his many helpful discussions. Staff of the Chemistry Machine Shop, Electronics Shop, and Glass Shop, were also of immeasurable assistance. Their creativity and skill resulted in elegant solutions to many of the problems I approached them with, and they were often responsible for getting things back on track after an equipment failure, of which there were many. On the rare occasion when they couldn't build it or fix it, the staff of the Purchasing Office was always ready to help buy it. As a student, the assistance of the staff of General Office was also appreciated, not least of all for making sure I received a regular pay check. The financial support of the Natural Sciences and Engineering Research Council of Canada and Alberta Ingenuity, in the form of graduate studentships, is also gratefully acknowledged.

On a personal level I would like to thank my wife, Carla, who put up with the long hours, and my grouchy demeanor when things weren't going according to plan. My parents, Austin and Cathy, have always encouraged me, and my sister, Jennifer, has a way of asking questions that make me feel smarter than I am--thank you. Finally, I would like to make mention of my daughter, Zoë, who has provided me with a new source of inspiration.

Table of Contents

Introduction 1

Chapter 1. Cost-Effective and Scalable Solutions to Materials Science Problems 2

Part 1–Novel Thin Film Semiconductors for Photovoltaic Applications 6

Chapter 2. Novel Semiconductors for Thin Film Photovoltaics and Device Discovery Using Combinatorial Methods 7

Introduction 7

Meeting the Terawatt Challenge with Solar Energy 9

Novel Semiconductors for Thin Film PV Devices 19

Combinatorial Device Discovery 27

References 39

Chapter 3. Synthesis of Cu_3BiS_3 Thin Films by Heating Metal and Metal Sulfide Precursor Films under Hydrogen Sulfide 46

Introduction 46

Experimental Details 47

Results 49

Discussion 75

Conclusions 80

References 81

Chapter 4. One-Step Synthesis and Optical and Electrical Properties of Thin Film Cu_3BiS_3 for Use as a Solar Absorber in Photovoltaic Devices 84

Introduction 84

Experimental Details 85

Results 87

Discussion 97

Conclusions 101

References 101

Chapter 5. One-Step Deposition of Cu_3BiS_3 on TCO and TCO/ZnSe Coated Substrates with Al, Ni, and Mo Back Contacts—Testing Method and Material Compatibilities 103

Introduction 103

Experimental Details 105

Results 108

Discussion 133

Conclusions 138

References 139

Part 2–Template Directed Synthesis of Copper Nanowires 141

Chapter 6. Synthesis of Nanomaterials by Electrodeposition into Porous Aluminum Oxide Templates 142

Introduction 142

Fabrication of Porous Aluminum Oxide Templates 144

Electrodeposition into Porous Aluminum Oxide Templates 148

References 153

Chapter 7. Effect of AC Electrodeposition Conditions on the Growth of High Aspect-Ratio Copper Nanowires in Porous Aluminum Oxide Templates 159

Introduction 159

Experimental Details 161

Results 168

Discussion 193

Conclusions 216

References 217

Conclusions and Future Work 220

Chapter 8. General Conclusions and Future Work 221

Novel Thin Film Semiconductors for Photovoltaic Applications 221

Template Directed Synthesis of Copper Nanowires 232

References 235

Appendices 238

Appendix A. Synthesis of $Cu_{12}Sb_4S_{13}$ Thin Films by Heating Metal Precursor Films under Hydrogen Sulfide 239

Introduction 239

Experimental Details 239

Results and Discussion 240

Conclusions 243

References 244

Appendix B. One-Step Synthesis of $Cu_{12}Sb_4S_{13}$ Thin Films 245

Introduction 245

Experimental Details 245

Results and Discussion 246

Conclusions 249

References 250

Appendix C. Current Density and Charge Density Data for Electrodeposition of Copper into Porous Aluminum Oxide Templates 251

List of Tables

Table 2.1. Abundance of constituent elements of Cu-Bi-S and Cu-Sb-S phase systems, indium, and tellurium. 20

Table 2.2. Cu-Bi-S and Cu-Sb-S minerals and their suitability for use as the solar absorber layer in thin film PV devices. 21

Table 2.3. Transparent conducting oxides for use in combinatorial PV device discovery strategies. 35

Table 2.4. Heterojunction couples for use in combinatorial PV device discovery strategies. 35

Table 7.1. Summary of deposition variables employed for FFDOE. 164

Table 7.2. Summary of runs and responses for ¼ fraction resolution III experimental design for identification of deposition conditions enabling filling of 4 μm deep oxalic acid-anodized pores. 170

Table 7.3. Summary of percentage of pores completely filled using pulsed electrodeposition. 182

List of Figures

Figure 2.1. Chart of progress in conversion efficiencies of various PV technologies over time. 10

Figure 2.2. Schematic of the multiple layers in a CIGS thin film device, and a band diagram of the device. 28

Figure 2.3. Photo of the Haber group multi-chamber UHV thin film combinatorial deposition system. 30

Figure 2.4. Photograph of UHV deposition chamber, and a schematic of the primary components. 31

Figure 2.5. A generic combinatorial strategy employing quaternary masks for production of 64 distinct PV combinations. 33

Figure 2.6. Continuous composition gradient of two compounds in orthogonal directions produced using a wedge-tool. 37

Figure 2.7. Continuous composition gradient of two compounds in opposite directions produced using system geometry. 38

Figure 3.1. Cu-Bi-S phase diagram at 200 °C and 300 °C. 51

Figure 3.2. Bi_2S_3-Cu_2S pseudo binary phase diagram from 270-1200 °C. 52

Figure 3.3. XRD powder patterns collected from multi-layer and co-sputtered Cu-Bi metal precursor films, and standard powder patterns for Bi and Cu. 53

Figure 3.4. Cu-Bi binary phase diagram from 200–1200 °C. 54

Figure 3.5. SEM images of a Cu_3BiS_3 film synthesized by heating a 2 µm thick co-sputtered metal precursor film on a soda-lime glass substrate under H_2S. 56

Figure 3.6. SEM images of a Cu_3BiS_3 film synthesized by heating a co-sputtered metal precursor under H_2S, XRD powder pattern, and standard powder pattern for Cu_3BiS_3. 57

Figure 3.7. SEM images of a Cu_3BiS_3 film formed by heating a multi-layer metal precursor film under H_2S. 59

Figure 3.8. SEM images of a Cu_3BiS_3 film, synthesized by heating a multi-layer metal precursor film under H_2S at 400 °C, XRD powder pattern, and standard powder pattern for Cu_3BiS_3. 60

Figure 3.9. SEM images of a film synthesized by heating a Cu_3BiS_3 film (Figure 3.4) at 600 °C under vacuum, XRD powder pattern, and standard powder pattern for Cu_2S. 61

Figure 3.10. Plots of Bi and S vapor pressure as a function of temperature. 63

Figure 3.11. Bi-S binary phase diagram from 0–900 °C. 64

Figure 3.12. Cu-S binary phase diagram from 0–1600 °C. 65

Figure 3.13. Backscattered SEM image of a film formed by heating a co-sputtered metal precursor at 300 °C for 2 hr under H_2S, XRD powder pattern, and standard powder patterns for Bi and $Cu_{1.8}S$. 67

Figure 3.14. Backscattered SEM image of a metal sulfide precursor as-deposited, XRD powder pattern, and standard powder pattern for Bi_2S_3, CuS, and S. 69

Figure 3.15. SEM images of a Cu_3BiS_3 film synthesized by heating a metal sulfide precursor under H_2S, XRD powder pattern, and standard powder pattern for Cu_3BiS_3. 71

Figure 3.16. SEM image of a $Cu_{1.8}S$ film synthesized by heating a Cu film under H_2S, XRD powder pattern, and $Cu_{1.8}S$ standard powder pattern. 72

Figure 3.17. SEM image of a Bi_2S_3 film synthesized by heating a Bi film under H_2S, XRD powder pattern, and standard powder pattern for Bi_2S_3. 74

Figure 4.1. SEM images of a Cu_3BiS_3 film synthesized by reactive deposition with a substrate temperature of 300 °C, XRD powder pattern, and standard powder pattern for Cu_3BiS_3. 88

Figure 4.2. SEM images of a Cu_3BiS_3 film synthesized by reactive deposition with a substrate temperature of 250 °C, XRD powder pattern, and standard powder pattern for Cu_3BiS_3. 89

Figure 4.3. SEM images of a Cu_3BiS_3 film synthesized by reactive deposition with a substrate temperature of 250 °C (see Figure 4.2), followed by annealing at 300 °C under H_2S, XRD powder pattern, and standard powder pattern for Cu_3BiS_3. 92

Figure 4.4. SEM images of a Cu_3BiS_3 film synthesized by reactive deposition with a substrate temperature of 300 °C (see Figure 4.1), followed by annealing at 300 °C under H_2S, XRD powder pattern, and standard powder pattern for Cu_3BiS_3. 93

Figure 4.5. Transmission and reflection data collected from a 300 nm thick Cu_3BiS_3 film, and α as a function of energy. 95

Figure 4.6. Plots of $(\alpha h\nu)^{1/n}$ against energy with $1/n = 2, 2/3, 1/2, 1/3$ for a 300 nm thick Cu_3BiS_3 thin film. 96

Figure 5.1. SEM images and optical transmission of an ITO film on soda-lime glass manufactured by Precision Glass and Optics. 110

Figure 5.2. SEM images and optical transmission of an FTO film on borosilicate glass manufactured by Solaronix. 111

Figure 5.3. SEM image of an as-deposited ZnSe film on soda-lime glass, XRD powder pattern of as-deposited film, XRD powder pattern of annealed film, and standard powder pattern for ZnSe. 113

Figure 5.4. SEM image of an as-deposited ZnSe film on ITO coated soda-lime glass, XRD powder pattern of as-deposited film, XRD powder pattern of annealed film, XRD powder pattern of ITO coated substrate, and standard powder pattern for ZnSe. 114

Figure 5.5. Transmission and reflection data for a 250 nm thick ZnSe film on soda-lime glass, plot of α against energy, and plot of $(\alpha h\nu)^2$ against energy. 116

Figure 5.6. SEM images of a Cu_3BiS_3 thin film deposited by the one-step method on an ITO coated soda-lime glass substrate, XRD powder pattern, and standard powder pattern for Cu_3BiS_3 . 118

Figure 5.7. SEM images of 3-layer samples deposited on ITO coated glass with Al, Ni, and Mo back contacts. 120

Figure 5.8. SEM images of 3-layer samples deposited on FTO coated glass with Al, Ni, and Mo back contacts. 121

Figure 5.9. SEM image of Al/Cu_3BiS_3/ITO on soda-lime glass and scanning auger intensity data. 122

Figure 5.10. SEM image of Al/Cu_3BiS_3/FTO on borosilicate glass and scanning auger intensity data. 123

Figure 5.11. SEM images of Al/Cu_3BiS_3/ZnSe (100nm)/FTO on borosilicate glass and scanning auger intensity data. 126

Figure 5.12. I-V data collected from a Mo/Cu_3BiS_3/ITO sample with colloidal silver contact, a Mo/Cu_3BiS_3/FTO sample with pressure contact, and commercial multi-crystalline Si solar cell. 128

Figure 5.13. SEM image of cross-section through a Ni/Cu_3BiS_3/ITO sample and silver print contact. 131

Figure 5.14. Ag_2S-Bi_2S_3, Bi_2S_3-Cu_2S and Cu_2S-Ag_2S pseudo binary phase diagrams from 0-900 °C. 132

Figure 6.1. Schematic of a porous aluminum oxide template. 143

Figure 6.2. SEM images PAO templates anodized in sulfuric acid, oxalic acid, and phosphoric acid. 145

Figure 6.3. SEM images of pore-bottoms separated from aluminum substrate, underside of PAO, and patterned surface of the aluminum substrate. 149

Figure 6.4. Schematics of AC electrodeposition and DC electrodeposition processes. 150

Figure 7.1. Normal probability plots for the standardized effect of variables and interactions on the following responses: yield, wire length dispersity, and electrode pitting. 172

Figure 7.2. SEM images of oxalic acid-anodized templates filled using: continuous sine wave deposition with bulk growth, pulsed sine wave deposition with bulk growth, continuous sine wave deposition without bulk growth. SEM images of sulfuric acid-anodized templates filled using continuous sine wave deposition with bulk growth. 174

Figure 7.3. Schematics of two of the wave shapes employed in this work. 177

Figure 7.4. SEM images of 24 μm deep sulfuric acid-anodized and oxalic acid-anodized pores with copper deposited using sine waves with red/ox and ox/red pulse polarity. 178

Figure 7.5. SEM images of 24 μm deep sulfuric acid-anodized and oxalic acid-anodized pores with copper deposited using square waves with red/ox and ox/red pulse polarity. 179

Figure 7.6. Percentage pore-filling as a function of depth below original surface of the template for 24 μm deep pores. 180

Figure 7.7. Current density traces, and component charge density per pulse obtained from integration of current traces, collected during sine wave pulsed electrodepositions into 24 μm deep oxalic acid-anodized pores. 183

Figure 7.8. Current density traces, and component charge density per pulse obtained from integration of current traces, collected during sine wave pulsed electrodepositions into 24 μm deep sulfuric acid-anodized pores. 185

Figure 7.9. Current density traces collected during square wave pulsed electrodepositions into 24 μm deep sulfuric acid-anodized pores collected at deposition mid-point and deposition end-point. 186

Figure 7.10. Current density traces collected during square wave pulsed electrodepositions into 24 μm deep oxalic acid-anodized pores collected at deposition mid-point and deposition end-point. 188

Figure 7.11. TEM images of wires liberated from sulfuric acid-anodized pores and oxalic acid-anodized pores and SAED pattern. 190

Figure 7.12. In-situ XRD powder patterns from wires deposited in sulfuric acid-anodized pores with ion milled surface and copper peaks indexed, wires deposited in oxalic acid-anodized pores with ion milled surface, and standard powder patterns for Cu and Cu_2O. 191

Figure 7.13. In-situ XRD powder patterns from wires as-deposited in sulfuric acid-anodized pores with Cu_2O peaks indexed, wires as-deposited in oxalic acid-anodized pores, and standard powder patterns for Cu and Cu_2O. 192

Figure 7.14. Schematic of PAO pore bottoms showing compositional variation as a function of anodizing electrolyte, and structural change that results from thinning of the barrier layer to facilitate AC electrodeposition. 195

Figure 7.15. SEM images showing disordered layer that forms during barrier layer thinning. 197

Figure 7.16. Current density trace collected at the end of a deposition into sulfuric acid-anodized pores showing the presence of a lower potential shoulder peak resulting from bulk deposition. 200

Figure 7.17. Deposition sequences used by Gösele and coworkers, Metzger and coworkers, and in this work. 202

Figure 7.18. Schematic representation of the trapezoidal potential barrier at an Al/Al_2O_3/Cu junction, and the difference in effective barrier height when biased in anodic and cathodic directions, which results in current rectification. 210

Figure 7.19. Schematic representation of the two possible defect migration scenarios that would result in reduction or elimination of current rectification in an Al/Al_2O_3/Cu junction. Formation of a multiple quantum well structure and location of a positive defect adjacent to the copper filled pore. 212

Figure 7.20. SEM images of as deposited sulfuric acid-anodized templates. Images show a nearly solid copper electrode forms regardless of pulse polarity. 215

Figure 8.1. Superstrate and substrate configurations for thin film PV devices. 225

Figure 8.2. Schematic of a pseudopotentiostat for collection of sequential I-V curves from a library chip. 227

Figure 8.3. Superstrate configuration combinatorial strategy using a TCO substrate patterned with an alumina grid. 229

Figure 8.4. Substrate configuration combinatorial strategy using a TCO substrate patterned with an alumina grid. 230

Figure A1. SEM images collected from a $Cu_{12}Sb_4S_{13}$ thin film synthesized by heating a metal precursor film under H_2S. 241

Figure A2. XRD powder pattern collected from a $Cu_{12}Sb_4S_{13}$ thin film synthesized by heating a metal precursor film under H_2S, and standard powder pattern for $Cu_{12}Sb_4S_{13}$. 242

Figure B1. SEM images collected from a $Cu_{12}Sb_4S_{13}$ film deposited with a substrate temperature of 250 °C, powder pattern collected from the film, and standard powder pattern for $Cu_{12}Sb_4S_{13}$. 247

Figure B2. SEM images collected from a $Cu_{12}Sb_4S_{13}$ film deposited with a substrate temperature of 250 °C and then annealed at 250 °C under H_2S, powder pattern collected from the film, and standard powder pattern for $Cu_{12}Sb_4S_{13}$. 248

Figure C1. Current density traces for deposition into 24 μm deep pores recorded at the midpoint of the deposition. 252

Figure C2. Charge density data for depositions into 24 μm deep sulfuric acid-anodized templates and oxalic acid-anodized templates. 253

List of Abbreviations and Symbols

AC	Alternating Current
BIPV	Building Integrated PV
CBD	Chemical Bath Deposition
CCD	Charge-coupled Device
CIGS	$Cu(In,Ga)(S,Se)_2$
CIS	$CuIn(S,Se)_2$
DC	Direct Current
DMM	Digital Multi-meter
DOE	Department of Energy
EDX	Energy Dispersive X-ray Spectroscopy
FFDOE	Fractional Factorial Design of Experiment
FTO	Fluorine Tin Oxide ($F:SnO_2$)
HIT	Heterojunction with Intrinsic Thin Layer
ITO	Indium Tin Oxide ($Sn:In_2O_3$)
OBIC	Optical Beam Induced Current
PAO	Porous Aluminum Oxide
PV	Photovoltaic
PVD	Physical Vapor Deposition
RF	Radio Frequency
RPM	Revolutions per Minute
SEM	Scanning Electron Microscopy
TCO	Transparent Conducting Oxide
TEM	Transmission Electron Microscopy
UHV	Ultra High Vacuum
WDX	Wavelength Dispersive X-ray Spectroscopy
XRD	X-ray Diffraction

Introduction

Chapter 1. Cost-Effective and Scalable Solutions to Materials Science Problems

Materials science is diverse and highly interdisciplinary, with researchers pushing the boundaries of the theory, scale, synthesis, fabrication, characterization, and application of materials. Advances in science have been implicit in many of society's steps forward, and current topics in materials research are likely to support further progress in key areas including: energy production and storage, medical diagnostics and treatment, and the development of advanced optical and electronic devices. While performance will continue to be the primary criteria for evaluating new materials and technologies, other factors may ultimately determine their success. For example, emerging technologies for energy production must be clean and efficient, but to ensure widespread deployment they must also be reliable, cost competitive with existing technologies, and able to meet ever growing demand.

If target applications of new materials require high-volume, low-cost production, synthetic strategies for these materials should be scalable, and the starting materials readily available. In this thesis, two materials science problems arising from the need for scalable and cost-effective syntheses of functional materials are addressed. In Part 1, a novel semiconductor is synthesized for possible use as the solar absorber in thin film photovoltaic devices, in an effort to increase the energy production capacity of this technology beyond that of the current, resource limited device configurations. In Part 2, the effect of AC electrodeposition conditions on the growth of copper nanowires in PAO templates are studied, in an effort to take full advantage of the scalable and cost-effective nature of the as-formed PAO templates, and develop a low-cost, high-throughput route to metal nanowires. Within the general objective of finding solutions to these two problems, the specific objectives of this thesis follow.

Part 1:

i. To introduce PV devices as a group of technologies that have the potential to provide large amounts of clean energy, but which face challenges that must be overcome before widespread deployment can be realized. For thin film PV devices the long-term challenge will be materials availability, which will require the development of novel semiconductors based on abundant, readily available elements, and the subsequent integration of these new materials into efficient devices. (Chapter 2)

ii. To introduce sulfide minerals in general, and the Cu-Bi-S and Cu-Sb-S phase systems in particular, as a promising source of novel semiconductors for thin film PV devices. Combinatorial experimental methods are identified as a promising approach to integrating any suitable compounds from these phase systems into efficient PV devices. (Chapter 2)

iii. To present details on the synthesis of thin film wittichenite (Cu_3BiS_3) by two different routes; (1) by heating metal and metal sulfide precursor films under H_2S, and (2) by a one-step reactive deposition on heated substrates. The one-step method is identified as producing superior films--with morphology, and optical and electrical properties suitable for use in thin film PV devices. (Chapters 3 and 4)

iv. To determine the compatibility of the one-step deposition process for Cu_3BiS_3 with other layers required for fabrication of a multi-layer device and to identify methods of electrically contacting devices. These are regarded as preliminary steps, necessary for the successful implementation of combinatorial device development strategies. (Chapter 5)

Part 2:

i. To introduce PAO templates as a versatile template material, with flexible pore diameter and depth, ordered pore distribution, and compatibility with a wide variety of pore-filling methods. (Chapter 6)

ii. To identify electrodeposition as a promising method for metal deposition in the pores of PAO templates, but which has not yet been effectively utilized to take full advantage of the scalable nature of PAO templates. DC electrodeposition is most commonly employed, but requires the laborious removal of the aluminum substrate, and is limited to use on relatively small areas due to the fragility of the PAO layer. AC electrodeposition is compatible with the scalable nature of as-fabricated PAO, but the quality of pore-filling is generally poor. (Chapter 6)

iii. To study the effect of AC electrodeposition conditions on the quality of pore-filling with copper, and identify improved conditions capable of uniformly filling deeper pores. A partially optimized set of conditions is identified using a fractional factorial design of experiment, and these conditions are further improved by rational examination of the wave shape, and the order in which oxidative and reductive components of pulsed wave-forms are applied. As a result, a further optimized set of conditions is identified, as well as the dynamic nature of the aluminum oxide barrier layer, and the role it plays in AC electrodeposition. (Chapter 7)

While significant progress has been made in finding solutions to these material science problems, each still requires considerable effort, if complete success is to be realized. Candidate materials for thin film PV devices must be successfully integrated into devices, and deployed. Further optimization of AC electrodeposition of metal into the pores of PAO templates may be possible, and applications must be developed that are able to take full advantage of the low-cost, high-throughput synthesis of metal nanowires. A more detailed discussion of the work still required, and promising approaches to overcoming the remaining challenges, is provided in the concluding chapter of the thesis. (Chapter 8)

Part 1–Novel Thin Film Semiconductors for Photovoltaic Applications

Chapter 2. Novel Semiconductors for Thin Film Photovoltaics and Device Discovery Using Combinatorial Methods

Introduction

Increasing energy demand and concerns over climate change caused by fossil fuel consumption are stimulating intensified interest in new energy sources in the R&D community, governments, and the general population. Primary power demand is predicted to increase from ~10 TW in 1990 to ~30 TW in 2050 and ~50 TW in 2100; under a "business-as-usual" approach the bulk of this future demand would be met by coal.[1] Anthropogenic sources have already resulted in atmospheric CO_2 rising from ~275 ppm to ~370 ppm, and unchecked, the concentration will pass 550 ppm this century.[2] It is predicted that this rapid rise in CO_2 will be accompanied by a global-mean warming in the range of 1.7-4.9 °C from 1990 to 2100.[3] In order to avoid the catastrophic consequences that would be associated with this, including coral reef bleaching, thermohaline circulation shutdown, disintegration of the West Antarctic Ice Sheet, and loss of land to rising sea levels, a stabilized atmospheric CO_2 concentration at or below 450 ppm may be required.[2] Stabilizing CO_2 at the 1990 level of 350 ppm would require 10 TW of carbon free power production by 2018, to stabilize CO_2 at 450 ppm would require this much carbon free power by 2025.[1] By mid-century this would increase to 30 TW and 20 TW respectively, by which time even CO_2 stabilization at 550 ppm would require 15 TW of carbon free power.[1] Considering that global power production in 1990 was 10 TW, and that 85% of global demand is currently derived from fossil fuels, generating 10 TW of carbon free power within the next 10-20 years will be a significant challenge.

Several methods have been proposed for low carbon or carbon free primary power generation, including terrestrial solar, wind energy, solar power satellites, biomass, nuclear fission, nuclear fusion, fission-fusion hybrids, and fossil fuels from which carbon dioxide has been sequestered; however, all of these currently have significant deficiencies which must be overcome if they are to generate power on the terawatt scale.[2] While it is likely a mix of energy sources will be used in the short term; in the long term solar energy may hold the greatest promise for large scale deployment,[4] with more solar energy incident on the earth in 1 hour than is consumed globally in 1 year.[5] Photovoltaic manufacturing, based almost entirely on silicon solar cells, has been growing at or above 30% per year, with annual sales now at the 1 GW mark and worth U.S. $10 billion.[6] However, this impressive growth still falls far short of what is required for PV to become a primary power producer in the next 10-20 years. In addition to the massive production increases required for primary power production, efficient and cost-effective chemical and/or electrical energy storage methods are needed to overcome the intermittent nature of solar insolation. Cost reductions are also required to make solar energy competitive at the consumer, and utility levels with conventional energy generation techniques, such as natural gas, coal, or nuclear.[6] The following section provides a brief review of the state-of-the-art for existing and emerging solar energy technologies, as well as the challenges associated with scaling these technologies up to the terawatt level.

Meeting the Terawatt Challenge with Solar Energy

The first silicon solar cell was reported by Bell labs in 1954.[6] In 1961 Shockley and Queisser determined the detailed balance limit of conversion efficiency to be 41% for an ideal solar cell with a single cut-off frequency.[7] When geometric factors are taken into account, and a planar solar cell irradiated by a spherical sun subtending a solid angel is considered, the maximum conversion efficiency is reduced to 31%.[7] Since that time new PV technologies have been introduced, and significant improvements have been made in the solar-to-electrical energy conversion efficiencies of these devices. Progress in record solar cell conversion efficiencies for various PV technologies is charted in Figure 2.1.

Several technological gaps continue to limit the overall efficiencies of these devices. One, the gap between theoretical and record conversion efficiencies, two, the gap between conversion efficiency of record cells and mass produced cells, and three, the gap between the conversion efficiency of cells and modules.[6] As a consequence of the last two differences, the performance of PV devices is considerably lower in application than the record cell efficiencies indicated in Figure 2.1, providing room for improvement even in a mature technology like crystalline silicon, where record cell efficiencies are only a few percentage points below theoretical values. A brief snap-shot of the current state-of-the-art, for both current and emerging technologies, as well as an indication of the potential for terawatt deployment follows.

Crystalline Silicon. Crystalline silicon devices continue to be the industry leader, with over 94 % of solar cell production based on single-crystal or multi-crystalline silicon.[6] The ubiquitous nature of silicon in opto-electronic applications has resulted in well understood material properties, which the silicon PV industry has been able to use to

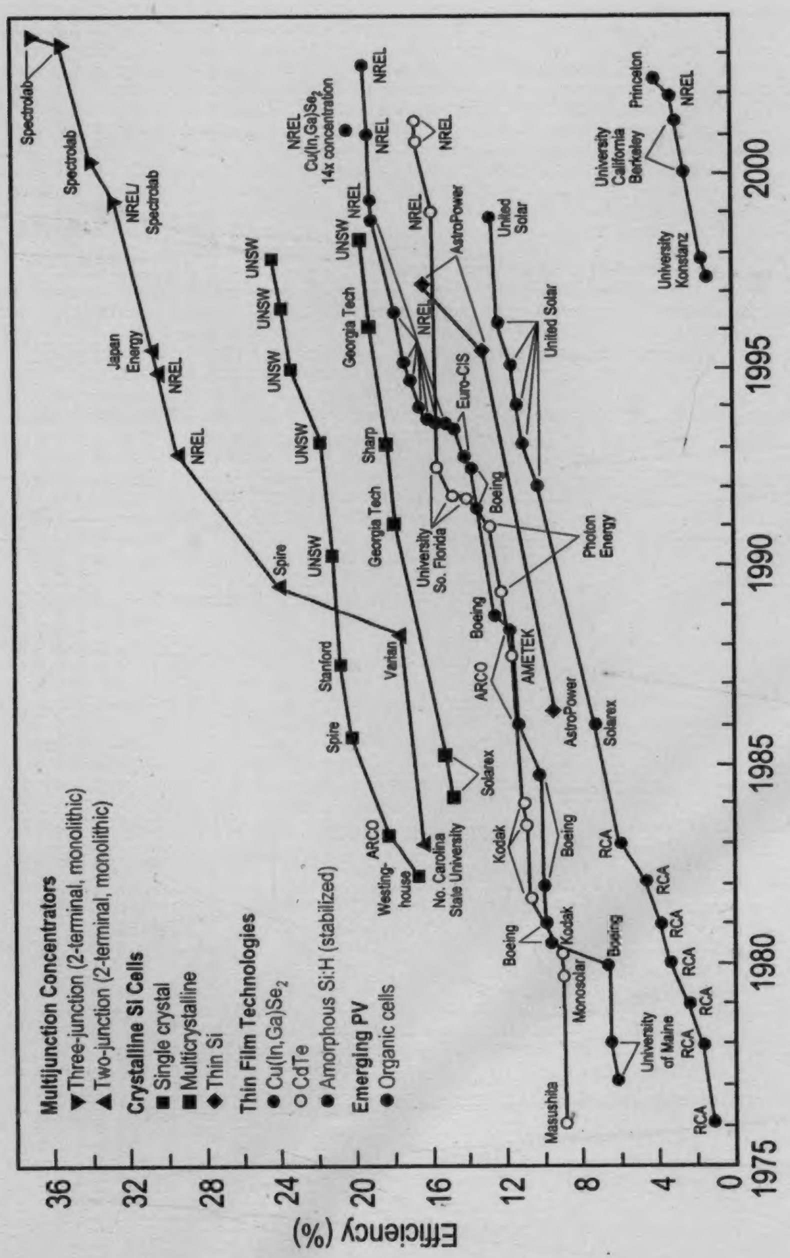

Figure 2.1. Chart of progress in conversion efficiencies of various PV technologies over time. Obtained from NREL at http://www.nrel.gov/ncpv/thin_film/.

their advantage. Record cell efficiencies of single-crystal devices are close to 25%, and the gap between record cells and commercial cells is narrowing. For example, Sanyo's commercially produced HIT cell has achieved cell and module efficiencies of over 21% and 18%, respectively.[8,9] In addition to high efficiencies, an important metric for rooftop area-limited applications, silicon cells also have market-leading warranties of 25 years. However, due to the indirect band gap of Si, a relatively thick film is required to absorb all incident radiation, which dictates the use of a high-quality material. Production of Si single-crystal ingots is energy intensive, and even with the advent of reduced kerf wire saws, roughly 35% of the material is lost during wafer production.[10] As a result, wafer production contributes 50% to the final module cost,[6,10] and also dramatically increases the energy payback time. Despite the high cost of production, single crystal silicon cells continue to account for ~30% of worldwide PV sales.[11]

One way to reduce the cost of Si cells is to use multi-crystalline silicon, an approach which has been employed for over thirty years, and is now the dominant technology with ~60% of the global PV market.[11] These cells cost about 20% less to produce than single-crystal cells, have a lower energy pay-back time, and cell efficiencies only a few percentage points less. When compared at the module level, a difference of a few percentage points in conversion efficiency remains between the best single-crystal and multi-crystalline modules, but average commercial modules have almost identical efficiencies of 12.8% (single-crystal) and 12.6% (multi-crystalline).[8]

Despite the obvious success of crystalline silicon, scale-up to the terawatt level faces significant challenges. In the short term the largest barrier is a silicon feedstock shortage. The PV industry currently consumes 1/3 of global polysilicon feedstock production, and continuing growth in the PV industry has left feedstock in short supply. The capital cost of new feedstock production facilities, along with competition from the microelectronics industry, is expected to result in substantial price increases.[6,11] Modified feedstock plants producing solar-grade silicon could offset some of this cost increase, but in the short term this will limit industry growth and increase costs.[11]

In the long term, the cost associated with utilizing high purity Si will likely prevent crystalline-silicon solar cells from realizing the lower production costs regarded as the domain of thin film PV devices, and emerging technologies such as organic solar cells. It is predicted that within the next ten years the costs for Si wafer solar cells will level off at U.S. \$1.00/W - \$1.50/W (down from the current cost of ~\$4.00/W); this is still well above the U.S. DOE target of U.S. \$0.33/W.[12] However, silicon solar cells remain an active area of research. Devices based on the growth of multi-crystalline sheets and ribbons have been commercialized, and continue to be improved. These approaches offer greatly enhanced material utilization, higher throughput, and efficiencies only slightly lower than devices produced from multi-crystalline ingots.[6] Other active areas of research include the production of Si cells from thin (< 100 μm thick) wafers,[13] or from thin polycrystalline layers deposited directly on glass substrates.[14] This continuing innovation, combined with demonstrated success, is likely to ensure the dominance of Si-based devices in the near term. What role they might play beyond that remains to be seen.

Thin Films. Thin film photovoltaic devices can be divided into three types, amorphous silicon, $Cu(In,Ga)Se_2$ (CIGS), and CdTe. Common to all three materials is strong optical absorption, enabling efficient collection of solar radiation with ~100 times less material than would be required with crystalline Si. Arguments in favor of thin film solar cells are based on lower material utilization, compatibility with high-throughput roll-to-roll manufacturing, and reduced energy costs for production. Cells based on all three of these thin film materials are in commercial production, and while the current price per watt is comparable to silicon cells, it is predicted that thin film solar cells will drop below U.S. $1.00/W in the next decade, and approach the U.S. DOE target cost of U.S. $0.33/W in the following years.[11,12,15]

Amorphous silicon solar cells were introduced 30 years ago as a promising new technology.[16] To utilize amorphous silicon as a PV material it must be hydrogenated, forming a-Si:H, to passivate dangling bonds and minimize band-gap states. The band-gap may be tuned during the hydrogenation process, by varying hydrogen content in the material from 5-20 atomic %.[8] Amorphous Si:H is 100 times more effective at absorbing solar radiation than crystalline Si, enabling efficient light absorption with a much thinner semiconductor layer.[17] These properties were thought to make it an ideal candidate for PV; however, a-Si:H cells continue to be hindered by a light-induced material degradation,[18] known as the Staebler-Wronski effect. Upon exposure to sunlight, metastable inter-band defects are formed, reducing the performance of the device, with stabilized efficiencies 10-50% below initial efficencies.[6,17] The magnitude of this performance degradation is related to the degree of disorder in the a-Si:H, with films just below the crystalline threshold having the greatest stability.[17] The best amorphous silicon cells currently have stabilized efficiencies of 12-13%.[17] Research on these devices continues, with interest focused on the material and device properties at the boundary between the amorphous and the nano-crystalline regimes. Despite this challenge, amorphous silicon cells benefit from low material and manufacturing costs, and currently account for 5% of global PV sales.[11] Devices may be produced in a roll-to-roll process on stainless steel foils, and these products have found a market in BIPV, with module efficiencies in the range of 8%.[6,11,17] However, with relatively low efficiencies and on-going problems with device stability, it may be difficult for amorphous silicon to compete with other technologies in the long term.

Thin film solar cells based on the polycrystalline materials $Cu(In,Ga)(S,Se)_2$, (CIGS) and CdTe continue to advance, and while these devices account for only 1% of global sales,[11] they have been realizing significant market growth, stimulated, in part, by the silicon feedstock shortage. CIGS and CdTe devices have many inherent advantages for application in PV devices. Like amorphous silicon, they are amenable to high throughput roll-to-roll deposition processes. With some methods they may be deposited without the use of high vacuum equipment, reducing capital and operating costs for manufacturing facilities. They have direct band gaps that reduce material utilization and increase tolerance for defects, device fabrication often requires fewer processing steps, and the use of monolithic interconnects simplifies manufacturing of large area modules.[11] In both CdTe and CIGS devices it has also been found that the grain boundaries act to enhance charge separation and transport in the device, making the polycrystalline material superior to the single-crystal material for PV applications.[19,20]

The record cell efficiency for a CIGS cell is 19.5%, and the best commercial modules have efficiencies of 13%, with average module efficiencies, including ones manufactured in a roll-to-roll process, in the range of 10-12%.[6,21] As mentioned earlier, closing the gaps between theoretical efficiencies and module efficiencies is important to maximize performance of deployed products, and even with limited manufacturing history CIGS devices are doing well in this regard. Novel approaches to manufacturing should further improve throughput and materials utilization, and reduce costs. Examples include the SUNRISE cell, where CIS and a buffer layer are deposited on 200 μm diameter glass beads, the coated beads are applied to a metal film, and the device completed by application of front and back contacts.[22] Advantages include the use of small volume, high throughput reactors for CIS deposition, minimal use of vacuum equipment, and compatibility with roll-to-roll processing. In another novel approach Nanosolar Inc. (www.nanosolar.com) is developing a roll-to-roll process where the CIGS layer is printed onto a metal foil. In addition to high-throughput deposition and elimination of vacuum equipment, this method also offers essentially 100% material utilization. To date, no efficiencies have been reported, but corporate press releases state that devices are in pilot scale production.

Efficiencies of CdTe devices are slightly lower than those of CIGS devices, with a record cell efficiency of 16.5%, and average module efficiencies in the range of 7-9%.[5] However, despite lower efficiencies, CdTe cells have been adopted for commercialization, in part due to the robust nature of CdTe and its amenability to high throughput deposition.[6,23] When considering scale-up to hundreds of megawatts of production, the rapid rate at which CdTe can be deposited makes it one of the most promising solar technologies.[6] Some material challenges associated with the use of CdTe include the fact that p-type doping is difficult, and that the high work function of CdTe (5.8 eV) makes fabrication of a stable back contact a challenge, since there is no suitable metal with a work function higher than that of CdTe (a property required for formation of an ohmic contact).[24] A final concern with CdTe is the toxicity of the material, which presents some environmental and safety issues; however, extensive studies indicate that the risk is minimal, and that any concerns can be mitigated by the use of appropriate packaging and recycling programs.[6]

The inherent advantages of CIGS and CdTe based devices would seem to make them ideal candidates for rapid scale-up and significant power production; however, a barrier to the widespread deployment of these devices is material availability. It has been reported that availability of tellurium and indium will ultimately limit the electricity generating capacity of these devices to 4% of current global demand for CdTe, and 1% for CIGS.[25] Consequently, if thin film PV devices are to realize their full potential, new materials must be identified that are not limited by the availability of constituent elements. Ideally, these new materials should also be amenable to cost-effective methods of production, and be of limited toxicity to eliminate additional costs associated with implementation of stringent packaging and tracking protocols.

High-efficiency Concentrators and Emerging Technologies. In order for PV devices to reach an even lower price/watt, either significantly higher conversion efficiencies or significantly lower production costs must realized.[15] It is predicted that devices making significant advances in either regard may eventually reach production costs as low as U.S. $0.10/Watt.

One approach to higher efficiencies is to incorporate multiple junctions into a single device, with each junction tuned to a different portion of the solar spectrum. With the addition of a second junction the theoretical efficiency jumps from 31% to 42%, and with an infinite stack the theoretical conversion efficiency is 87%.[10,15] In recent years, significant advances have been made in multi-junction cells, and efficient triple-junction cells based on GaInP/GaAs/Ge and GaInP/GaAs/GaInAs have been realized. These advances have been stimulated in large part by the need for high W/kg devices for space applications. For flat plate terrestrial applications these cells would be prohibitively expensive; however, when combined with solar concentrator and tracking systems, the economics of these devices can be enhanced considerably.

Lenses or mirrors are used to achieve solar concentration of up to 1000 times, and tracking systems enable the device to follow the sun, maintaining direct solar irradiation. These additional system components enable power production to remain relatively constant during daylight hours, and also allow the area of the solar cell to be reduced by a factor equivalent to the solar concentration, dramatically lowering the cost per watt of the system. The best conversion efficiency achieved with a device of this type is 39% for a triple-junction GaInP/GaAs/Ge cell under 360 times concentration, the highest efficiency achieved for any PV technology.[6] These systems are not well suited to residential installations, but are being considered for centralized utility installations. For centralized utility applications, cost targets are considerably lower than for installations at the consumer level. However, with continuing advances in both cells and balance of system components, these multi-junction concentrator systems would seem to be well positioned for deployment at the utility scale.

There also exists numerous emerging technologies, some demonstrated, some theoretical, that may ultimately offer significantly lower costs and/or significantly higher conversion efficiencies than current technologies. Technologies targeting reduced costs include dye-sensitized solar cells and organic solar cells. Dye-sensitized solar cells have achieved efficiencies of 11%,[6] and have the potential for very low fabrication costs; however, there are ongoing concerns about the durability of these devices. Organic solar cells, which exist in a variety of configurations,[12] have gained prominence in the last few years, and offer the possibility of very low costs combined with simple manufacturing methods. In the lab, devices of this type commonly achieve efficiencies of 3-5%.[6] However, organic solar cells are still in their infancy, and if they are to form part of the PV portfolio in the future they will have to demonstrate improved performance as well as long term stability and durability.

At the other end of the spectrum are device concepts with the potential to achieve very high conversion efficiencies. These devices are in very early stages of development, in some cases existing only in theory, and are based on several different advanced concepts. These include: thermophotovoltaic and thermophotonic devices (85% theoretical efficiency), impact ionization devices (86% theoretical efficiency), hot carrier cells (87% theoretical efficiency), and multiband cells (87% conversion efficinecy).[6,15] While these emerging technologies offer the possibility of very high conversion efficiencies, it may be the case that devices delivering the full potential of these concepts are never realized.

PV is still a young industry, and while it is growing rapidly, the net contribution to global energy production is small. Significant growth potential exists for a variety of PV technologies; however, all of these technologies face challenges. At this time it is not possible to predict what PV technology, or technologies, will become dominant in the future. Consequently, it is necessary to maintain diverse and well funded R&D programs at all levels of PV, from basic science, to large scale grid and utility integration, as well as related areas of research, such as finding efficient means of electrical or chemical storage of solar energy. One of the challenges facing thin film PV devices is material availability. The remainder of this chapter (and Chapters 3, 4, and 5) provides details on one particular effort to overcome this challenge.

Novel Semiconductors for Thin Film PV Devices

In the previous section thin film polycrystalline PV devices were identified as having immediate and growing potential for harnessing solar energy. They have successfully entered commercial production, and they are amenable to the low-cost, high-throughput fabrication methods critical for production of cost-effective devices and rapid scale-up. However, it was also identified that the long term growth of these technologies will be curtailed by the limited availability of In and Te. For large-scale deployment of thin film PV devices, the development of novel semiconductors will be required. In addition to having suitable optical and electrical properties, these new materials must also be composed of elements that are abundant and readily available, and should ideally be non-toxic as well.

One probable starting point for the identification of novel semiconductors is the hundreds of known chalcogenide minerals. A survey of 180 sulfide mineral phases identified 53 compounds as being photoactive, with band-gaps within the range of 0.9-1.8 eV required for efficient application in a single-junction PV device.[26] Amongst the minerals identified as promising were several from the Cu-Bi-S and Cu-Sb-S phase systems.[26] For both of these phase systems the abundance of the constituent elements is considerably greater than that of Te or In. Global reserves data from the U.S.G.S. 2006

Mineral Commodity Summaries is presented in Table 2.1.[27] Clearly, the use of semiconducting compounds from either the Cu-Bi-S or Cu-Sb-S phase system would significantly increase the energy production ceiling of thin film PV devices. Additionally, both Sb and Bi may be obtained directly from an antimony or bismuth ore, making them readily available, and limiting the environmental footprint that would be associated with increased recovery. Currently, due to the low demand for both Bi and Sb, production is primarily as a by-product from the refining of other metals. Antimony and many of its compounds are toxic, which would necessitate safety controls similar to those put in place for CdTe devices. Bismuth is non-toxic, and is currently used in pharmaceuticals and as a replacement for lead in ammunition, solders, and other materials where toxicity is a concern.

Table 2.1. Abundance of constituent elements of Cu-Bi-S and Cu-Sb-S phase systems, indium, and tellurium.

element	global reserve base (metric tons)[27]
Cu	940,000,000
Sb	3,900,000
Bi	680,000
Te	47,000
In	6,000

In Table 2.2 is a list of Cu-Bi-S and Cu-Sb-S phases, some of which may be suitable for use as the solar absorber layer in thin film PV devices. Where available, the band gap and other data relevant to PV applications have been included in Table 2.2. The literature associated with these compounds is limited, and most studies of these compounds have been from a mineralogical perspective. Only a handful of papers have been published investigating the material properties or technological applicability of these minerals. Consequently, assessment of the suitability of these compounds for PV applications can not be based solely on the literature, and each compound should be assessed on a case-by-case basis. A general discussion of these compounds and a review of the relevant literature follow.

Table 2.2. Cu-Bi-S and Cu-Sb-S minerals and their suitability for use as the solar absorber layer in thin film PV devices.

mineral	formula	band-gap	notes
wittichenite	Cu_3BiS_3	1.4 eV[28,29]	Synthesized as thin film, α=1x10^5 cm^{-1} at 1.9 eV, p-type, ρ=10-80 Ω·cm.[28,29]
skinnerite	Cu_3SbS_3	NA	No material properties reported, expected to have similar properties to Cu_3BiS_3.
tetrahedrite	$Cu_{12-14}Sb_4S_{13}$	1.2-1.7 eV[30,31]	Ionic conductor, metallic/semiconductor behavior depending on composition.[30-32] Not suitable for PV.
famatinite	Cu_3SbS_4	0.7 eV[33]	Little studied compound, method/quality of band-gap determination unknown.
emplecite	$CuBiS_2$	1.6-1.8 eV[34]	Synthesized as thin film, little studied compound, expected to have similar properties to $CuSbS_2$.
chalcostibite	$CuSbS_2$	1.5 eV[35]	Synthesized as thin film, p-type, ρ=35 Ω·cm, employed in a thin film PV device.[35,36]

Wittichenite (Cu_3BiS_3) is a naturally occurring mineral, whose crystal structure was first reported in 1973.[37] Wittichenite crystallizes in the orthorhombic $P2_12_12_1$ space group, has unit cell dimensions of a=7.7 Å, b=10.4 Å, and c=6.7 Å, and is stable under ambient conditions.[37,38] An unusual feature of the crystal structure is that all copper atoms are in nearly trigonal planar coordination with sulfur.[37] This has been observed in other copper sulfosalt minerals including: skinnerite (Cu_3SbS_3), tetrahedrite ($Cu_{12}Sb_4S_{13}$), and low-chalcocite (Cu_2S); however, in the vast majority of copper sulfosalt minerals copper is tetrahedrally coordinated to sulfur.[37,39] Previously reported syntheses have been by solid state methods (bulk sample),[37,38,40] and heating of chemical bath deposited precursors (thin film sample).[28,41,42] We have recently reported PVD synthesis of thin film samples by heating metal and metal sulfide precursor under H_2S, and by reactive deposition on heated substrates.[29,43] (Chapters 3 and 4 in this thesis, respectively.) Semiconductor properties reported for Cu_3BiS_3 (direct forbidden band gap of 1.4 eV, an optical absorption coefficient of 1×10^5 cm^{-1} at 1.9 eV, p-type conductivity, resistivity of 10-80 $\Omega \cdot cm$) indicate that this material may be suitable for application as a solar absorber layer in thin film PV devices.[28,29]

Skinnerite (Cu_3SbS_3) has been identified as a mineral phase, but its occurrence in nature is rare.[44] The structure of skinnerite is similar to that of wittichenite. At ambient conditions (below 122 °C) skinnerite crystallizes in the monoclinic $P2_1/c$ space group, with a=7.8 Å, b=10.2 Å, and c=13.3 Å, with β=90.3°.[39] Below -10 °C, transformation to a low temperature orthorhombic $P2_12_12_1$ polymorph occurs, with a=7.8 Å, b=10.2 Å, and c=6.6 Å.[44] This low temperature polymorph is isostructural with wittichenite at ambient conditions, and has similar cell parameters (see above). When synthesized by solid state methods skinnerite is only formed at temperatures above 359 °C, and is stable to its melting point of 607 °C.[39,44,45] If cooled slowly below 359 °C it will decompose to an assemblage of tetrahedrite, chalcostibite, and antimony. If cooled rapidly below 359 °C an orthorhombic *Pnma* Cu_3SbS_3 phase may be quenched, which persists indefinitely.[39,44,45] Further cooling results in transformations to the Cu_3SbS_3 phases identified above. Skinnerite obtained through this quenching process is often contaminated by small amounts of tetrahedrite in intimate intergrowths.[39] No studies of the material properties of Cu_3SbS_3 have been reported; however, the structural similarity between wittichenite and skinnerite leads to the reasonable inference of Cu_3SbS_3 having semiconducting properties similar to those of Cu_3BiS_3.

One potential problem with utilization of Cu_3BiS_3 or Cu_3SbS_3 in thin film PV devices could be long term stability. For both phases there exists a high temperature *Pnma* polymorph. For Cu_3SbS_3 the conversion from $P2_1/c$ to *Pnma* takes place at 122 °C,[39] for Cu_3BiS_3 the conversion from $P2_12_12_1$ to *Pnma* occurs at 191 °C.[40] It has also been reported these high temperature polymorphs may be ionic conductors.[39,40] This is based on XRD studies indicating that the transition to the high temperature polymorph is accompanied by the formation of disordered (mobile) copper ions. Below the phase transition temperature these copper ions are reported to be immobilized. Ionic conductivity was not measured in either material, and most of the XRD data referred to is unpublished.[39,40] Without further study this should only be regarded as a cautionary note; however, there is precedent for this type of behavior having catastrophic consequences for the performance of a thin film PV device.

In the 1970s and 1980s $Cu_{2-\alpha}S$/CdS thin film solar cells were developed, and eventually abandoned due to performance degradation resulting from copper ion migration and the formation of shunts in the device.[46-48] Ionic conductivity due to the presence of a highly mobile (disordered) copper species was known for high chalcocite, which forms above 105 °C.[46,47,49] The ionic conductivity of $Cu_{2-\alpha}S$ at room temperature is lower by a factor of 10^4,[46] but the existence of an ionic phase of even limited mobility proved to be an insurmountable challenge for PV device development. There is no evidence that such a problem would arise for cells based on Cu_3BiS_3 or Cu_3SbS_3; there are significant structural differences between the compounds; the temperature at which ionic conductivity is thought to occur is higher for Cu_3BiS_3 and Cu_3SbS_3, and below the transition temperature the Cu ions are thought to be frozen; for $Cu_{2-\alpha}S$ composition, as well as temperature, was found to affect Cu ion mobility,[46] and Cu_3BiS_3 and Cu_3SbS_3 are known to exist only at a fixed composition. None-the-less, if devices are produced, and are found to lack long term stability, the lessons learned from $Cu_{2-\alpha}S$/CdS solar cells may prove useful.

Tetrahedrite is the most common sulfosalt in the earth's crust, and is present in most sulfide ore deposits. The formula for natural tetrahedrite is commonly $Cu_{10}(Fe,Zn)_2Sb_4S_{13}$, although additional metals, including Hg, Zn, and Cu, are known to replace Fe or Zn; Cu can be substituted by Ag; and Sb can be substituted by As.[32,50] Synthetic tetrahedrite can be synthesized as a pure ternary compound, and the commonly accepted formula for synthetic tetrahedrite is $Cu_{12}Sb_4S_{13}$.[30,45] It also exists in a copper rich form, with a generally accepted formula of $Cu_{14}Sb_4S_{13}$.[31] However, the exact stoichiometry of these two forms is debated in the literature.[30-32,45,51-53] Regardless of the composition, tetrahedrite crystallizes in the cubic *I-43m* space group, with a=10.3-10.4 Å depending on composition.[32] Tetrahedrite is commonly synthesized by solid-state or hydrothermal methods.[32,51,54] Copper-poor tetrahedrite has also been synthesized in thin film form by PVD methods, reported in Appendices A and B of this thesis.

The composition range observed for synthetic tetrahedrite also has implications for material properties relevant to application in PV devices. In copper-poor tetrahedrite the calculated band gap is 1.2 eV.[31] However, 2 valence electron states per formula unit are unoccupied, and as a result copper-poor tetrahedrite is observed to be metallic.[30] In copper-rich tetrahedrite the valence band is filled, and consequently copper-rich tetrahedrite is observed to be a semiconductor, with a band gap of 1.7 eV.[30,31] The situation is further complicated by the fact that tetrahedrite has also been observed to be a room temperature ionic conductor.[32,53] In copper-poor tetrahedrite ionic conductivity is low. In copper rich tetrahedrite the additional copper is incorporated as mobile copper ions, and room temperature ionic conductivity is considerably higher.[32,53] Considering the compositional complexity of tetrahedrite, the metallic or semiconducting behavior depending on composition, and the room temperature ionic conductivity, it would appear that synthetic tetrahedrite may not be suitable for PV applications.

The mineral famatinite (Cu_3SbS_4) crystallizes in the tetragonal *I-42m* space group with a=5.4 Å and c=10.8 Å.[45] The structure may be derived from the sphalerite structure (cubic ZnS), with copper and antimony in tetrahedral coordination with sulfur.[45,55] It has been suggested that diamond-like semiconductors of this type are most likely to be successfully integrated into PV devices, due to their similarity to more conventional semiconductors such as Si or GaAs.[56] Bulk samples of Cu_3SbS_4 have been prepared by hydrothermal,[57] solvothermal,[58] and solid-state methods.[45,59] Cu_3SbS_4 has also been synthesized in thin film form by heating chemical bath deposited Sb_2S_3 and CuS precursor films.[60] The thin film samples produced in this way were poorly crystalline and of unknown purity, and no detailed characterization was performed.[60] A minimum band gap of 0.74 eV has been reported;[33] however, the nature of the gap and method of determination are not known. While this is below the value of 0.9 eV generally considered to be the lowest acceptable band gap for a single-junction cell, the uncertainty surrounding the data may warrant further investigation. Little is known about the material properties of famatinite, and it is possible that synthesis of a high quality sample may reveal a material suitable for PV applications.

Emplecite ($CuBiS_2$) and chalcostibite ($CuSbS_2$) are naturally occurring isostructural minerals that crystallize in the orthorhombic *Pnma* space group. Unit cell dimensions are almost identical; for emplecite a=6.1 Å, b=3.9 Å, c=14.5 Å, for chalcostibite a=6.0 Å, b=3.8 Å, and c=14.5 Å. The compounds are also known to form a complete solid solution.[61,62] In these compounds Cu is found with tetrahedral coordination to S, while Sb is found to have square pyramidal coordination to S.[61,62] In general, these compounds have received little attention. Both compounds have been synthesized in bulk form by solid-state methods[61-65] and in thin film form by annealing of chemical bath deposited precursor films.[34,35] Significantly, a rudimentary PV device utilizing $CuSbS_2$ has been recently reported.[36] The performance of the device was poor, but it is none-the-less an encouraging result for researchers interested in integrating new materials into thin film PV devices. It is noted by Nair and co-workers that the device they report has not been optimized, and they hope to significantly enhance its performance.[36]

Combinatorial Device Discovery

While the first step in developing new thin film PV devices is the synthesis of a suitable absorber material, a no less formidable task is integration of the new absorber into a device exhibiting a reasonable conversion efficiency. A schematic of the multiple layers in a CIGS thin film device is shown in Figure 2.2 (a), along with a band diagram of the device in Figure 2.2 (b). When considering the development of a new and similarly complex thin film PV device, it is reasonable to divide the task into two parts: (1) identification of a device that has conversion efficiency on the order of 5%, and (2) optimization of the device to increase conversion efficiency to 10-20%. If a new device with efficiency on the order of 5% is identified, it is likely that other researchers in the field will work on the device, accelerating optimization. It is also likely that the use of combinatorial methods will facilitate rapid progress in both phases of device development. Combinatorial strategies for device discovery based on the Cu_3BiS_3 films synthesized in Chapter 4 have not been implemented; however, some preliminary experiments have been performed, and these are detailed in Chapter 5. A general introduction to combinatorial methods, and the applicability of these methods to PV device discovery and development, follows.

The forerunner of combinatorial materials science was the multiple sample concept, developed by Hanak at RCA over 30 years ago.[66,67] At the time, the approach did not gain widespread acceptance, in part due to the lack of associated equipment necessary for high speed characterization and data handling.[66] For successful application of a combinatorial method it is necessary to have a characterization technique that is able to screen high-throughput libraries as rapidly as they are produced. In more recent years

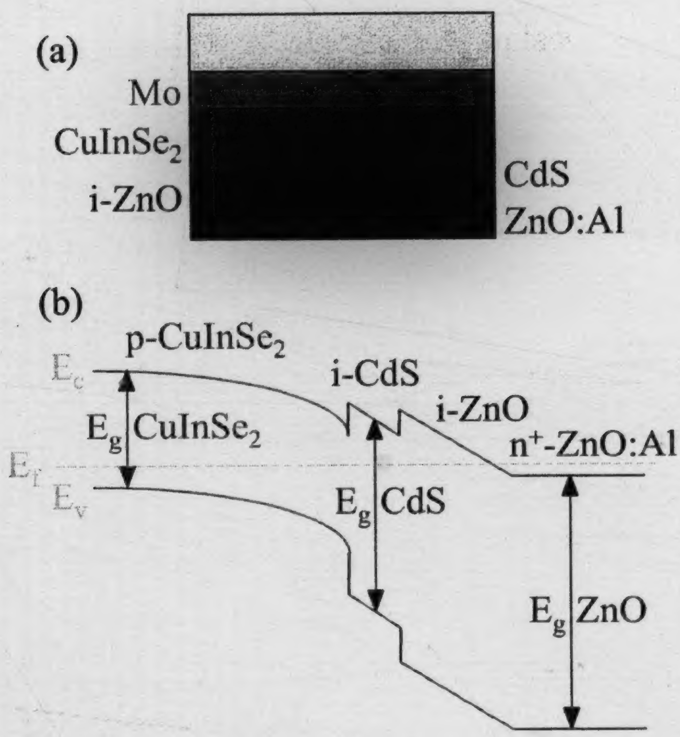

Figure 2.2. Schematic of the multiple layers in a CIGS thin film device (a), and a band diagram of the device (b).

barriers to the use of combinatorial strategies in materials science have been removed, and the approach has been applied successfully in many areas, including: superconducting materials,[68] dielectric and ferroelectric materials,[66,68,69] magnetic materials,[66,68,70] luminescent materials,[66,68,71] and battery materials.[72] Combinatorial methods have also been employed for the study, optimization, and development of PV materials and devices. These efforts have included the optimization of $CdTe_{(1-x)}S_x$ absorber layers and devices,[73] study of the amorphous to microcrystalline silicon transition,[74] and the development and optimization of transparent conducting oxides.[75,76]

Two methods of producing combinatorial libraries that been employed successfully with thin film systems are the quaternary mask approach, and the composition spread approach.[77] Within the Haber research group at the University of Alberta is a multi-chamber UHV thin film combinatorial deposition system that has been designed for fabrication of thin film libraries employing either one or both of these strategies. A photo of the deposition system is presented in Figure 2.3. The system is built around a six port central distribution chamber. Attached to this chamber is a sample and mask loading and storage chamber, an annealing chamber for processing samples under vacuum, inert, or reactive atmospheres at temperatures up to 1000 °C, and a deposition chamber with three 3" magnetron sputter sources, 2 DC and 1 RF, a four-pocket e-beam evaporation source, and an effusion cell. The deposition chamber can accommodate multiple sputter gases, and is equipped with a quartz lamp array for substrate heating up to 400 °C. The substrate holders are designed to accommodate 5 cm x 5 cm square samples.

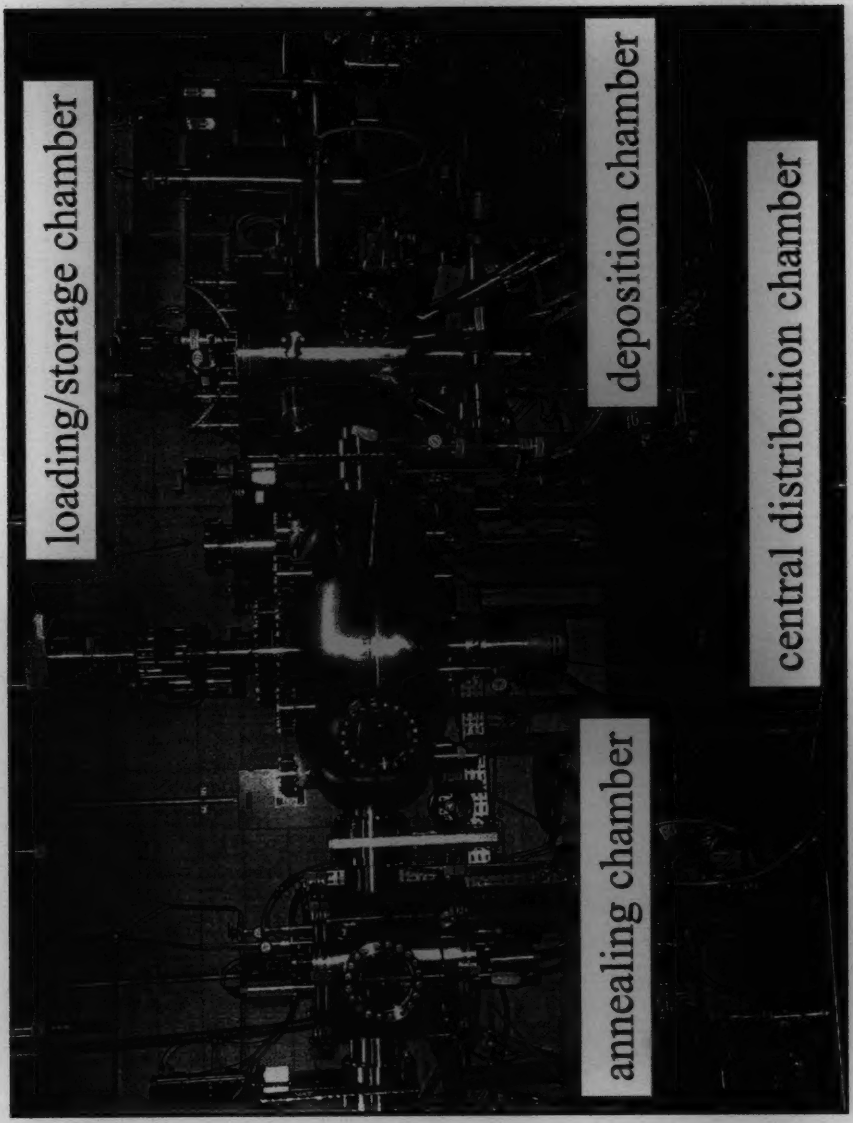

Figure 2.3. Photo of the Haber group multi-chamber UHV thin film combinatorial deposition system.

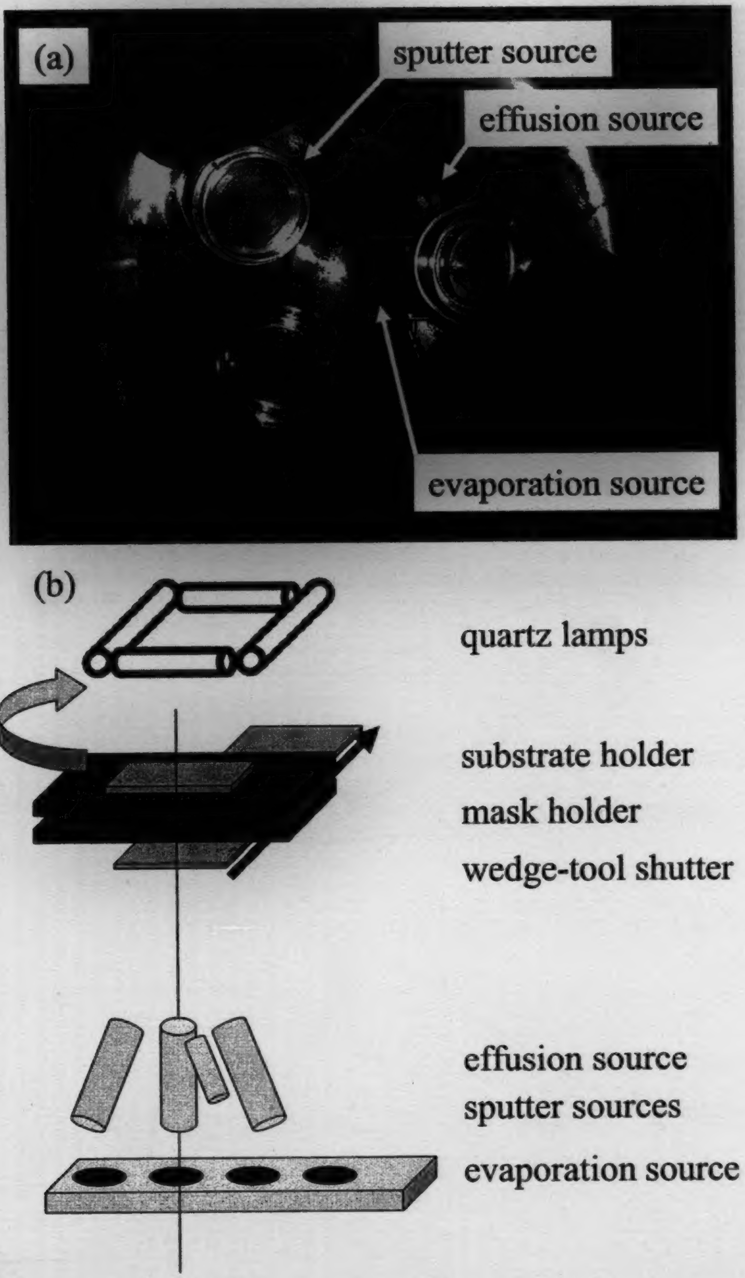

Figure 2.4. Photograph of deposition sources inside the UHV deposition chamber (a), and a schematic of the primary components showing the position of the substrate holder, mask holder, wedge tool, and quartz lamps relative to the deposition sources (b).

Using this system, combinatorial experiments can be executed in three ways: (1) using shadow masks that may be positioned between the substrate and sources, and rotated relative to the substrate in 90° increments, (2) using a wedge tool that may be positioned between the substrate and sources, and translated continuously or step-wise relative to the substrate, or (3) using the orientation of the sputter sources relative to the substrate. In Figure 2.4 is a photo of the interior of the deposition chamber showing the positioning of the deposition sources, and a schematic of the primary components in the deposition chamber. The wedge-tool and mask holder are located between the sources and substrate holder. The quartz lamp array is located above the substrate holder. The system is designed to execute combinatorial experiments; however, it may also be used for deposition of single films of uniform composition. Without the use of the wedge tool, or shadow masks, and with the substrate in continuous rotation, the system was used for the fabrication of the Cu_3BiS_3 thin films presented in Chapters 3 and 4, and the $Cu_{12}Sb_4S_{13}$ films presented in Appendices A and B.

The quaternary mask approach utilizes self-similar shadow masks, each of which exposes ¼ of the substrate in a varying distribution. By rotating each mask through 360° in 90° increments, and depositing a material through the mask at each step, four different materials are deposited, each one segregated from the others. The number of distinct combinations that result is given by 4^n, where n is the number of quaternary masks employed. A strategy for deposition of a library with 64 distinct PV devices, using 3 quaternary masks and a single absorber material, is presented in Figure 2.5. If the number of fractal masks was increased from three to four, for example by using four different absorber materials in step three of Figure 2.5, the number of discrete

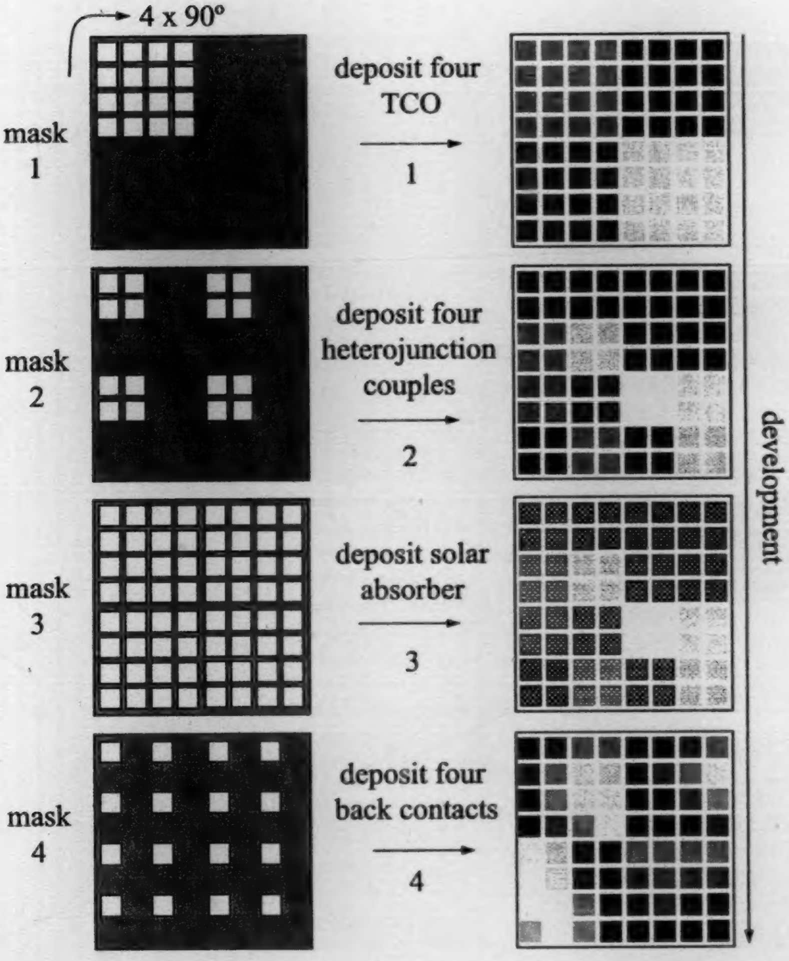

Figure 2.5. A generic combinatorial strategy employing quaternary masks for production of 64 distinct PV combinations on a 5 cm x 5 cm substrate with a single solar absorber layer.

combinations would increase to 256. A convenient screening criterion for PV libraries produced using quaternary masks is conversion efficiency, which can be rapidly measured for each of the library cells by collection of I-V curves. Development of device libraries using the quaternary masking approach, and library screening using conversion efficiency, is expected to rapidly provide either the identification of a device with a reasonable conversion efficiency (~5%), or lead to the conclusion that the novel absorber material under investigation is not suitable for PV applications.

A key step in implementation of the strategy outlined in Figure 2.5 is the identification of suitable materials for use as TCO, heterojunction couples, and metal back contacts. Identified in Table 2.3 are several TCO that may be suitable, a similar compilation is made in Table 2.4 for heterojunction couples. These tables are not meant to be exhaustive, but to illustrate a reasonable starting point. In both tables compounds are intentionally ordered from compounds widely used in thin film PV, to those that have been recently identified as promising alternatives. For TCO in particular, promising new compounds are being identified by targeting increasingly complex compositions, or by using combinatorial methods of discovery. For metal back contacts reasonable choices might include Mo, Ni, Al, or Sn.[78]

Table 2.3. Transparent conducting oxides for use in combinatorial PV device discovery strategies.

TCO	notes
In_2O_3:Sn	Has been used successfully with CIGS and CdTe devices.[24,79]
SnO_2:F	Commonly used with CdTe devices, often with intrinsic SnO_2 layer.[24,79]
ZnO:Al	Commonly used with CIGS devices, often with intrinsic ZnO layer.[24,79]
Cd_2SnO_4	Used in record efficiency CdTe cells in conjunction with Zn_2SnO_4.[80]
$Zn_{1-x}Mg_xO$:(Al,In)	Alloying ZnO with Mg increases band gap, double doping improves electrical properties.[81,82]
$Cd_{1+x}In_{2-2x}Sn_xO_4$	Study of compounds on Cd_2SnO_4 and $CdIn_2O_4$ tie line identified high quality TCO for $0.45<x<0.70$.[83]
$ZnSnO_3$	Little studied compound, shows promise for use as TCO, identified using composition gradient combinatorial methods .[76]

Table 2.4. Heterojunction couples for use in combinatorial PV device discovery strategies.

heterojunction couple	notes
CdS	Chemical bath deposited CdS has been used in top performing CdTe and CIGS cells.[24,79]
ZnS	Used in CIGS devices, efficiencies over 18% have been achieved with CBD.[84,85]
In_2S_3	Used in CIGS devices, efficiencies over 16% have been achieved with ALCVD,[85,86] slightly lower efficiencies have been obtained with evaporation[87] and sputter deposition.[85]
ZnSe	Used in CIGS devices, efficiencies of 13% and 11% have been achieved with MOVPE[88] and MOCVD[89] respectively. Optimum ZnSe layers are generally very thin (5-10 nm) regardless of deposition method.[85]
$ZnIn_xSe_y$	Used in CIGS devices, efficiencies of 15% have been obtained by co-evaporation.[90]
SnS_2	Recently employed as the heterojunction couple in a SnS_2/SnS solar cell.[91]

Composition gradient libraries employ a continuous or step-wise gradient across the substrate in one or more materials, and the screening criterion is evaluated as a function of this composition gradient. In the Haber combinatorial deposition system described above, composition gradients can be generated by taking advantage of the position of the sputter sources, which are located off-axis to the substrate normal, or by utilizing the wedge-tool which may be translated between the source and substrate in acontrolled fashion. PV libraries composed of a fixed set of layers, but with a thickness gradient of a buffer layer, or concentration gradient of an additive, could be rapidly screened by OBIC, with areas of maximum induced current correlating to the optimal layer thickness or additive concentration. Composition gradients produced using the wedge-tool and the system geometry are depicted in Figure 2.6 and 2.7, respectively. The application of these combinatorial strategies would be well suited to the second phase of device development, device optimization. It is expected that once promising configurations are identified using the quaternary masking approach outlined above, the judicious application of composition gradient strategies would facilitate rapid device optimization.

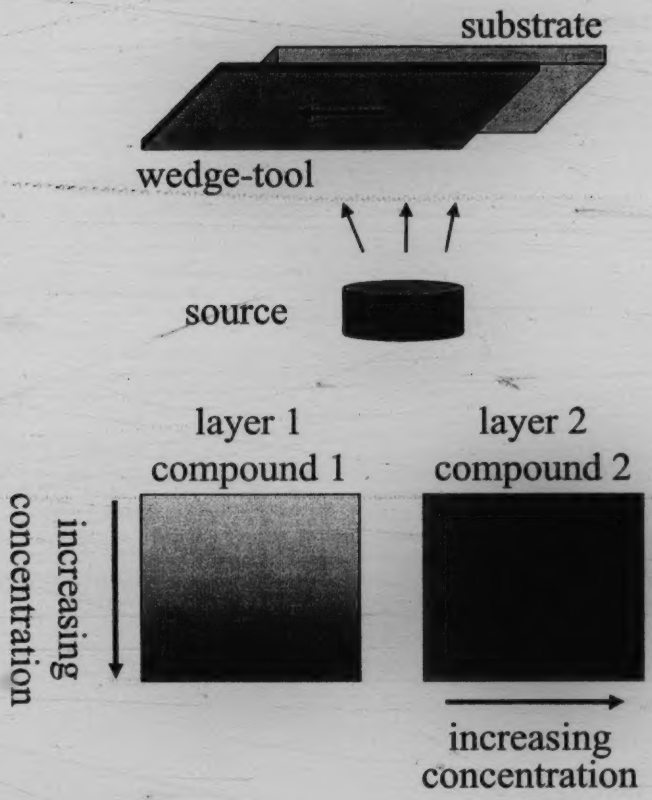

Figure 2.6. Continuous composition gradient of two compounds in orthogonal directions produced by translating a wedge-tool in front of the substrate during deposition, and rotating substrate by 90° between depositions.

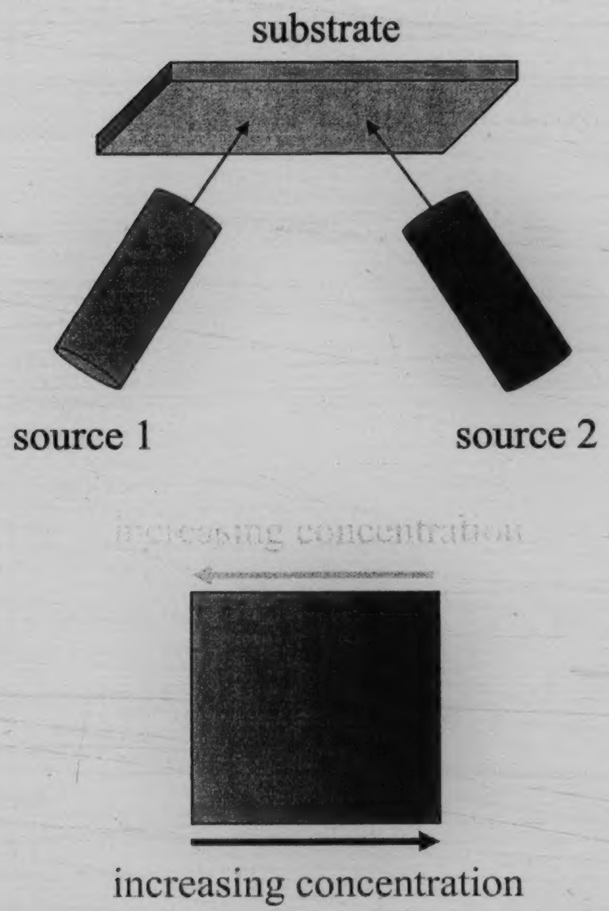

Figure 2.7. Continuous composition gradient of two compounds in opposite directions. Distribution is a result of deposition from sputter sources positioned off-axis from the substrate normal, with the substrate in a stationary position.

References

(1) Hoffert, M. I.; Caldeira, K.; Jain, A. K.; Haites, E. F.; Harvey, L. D. D.; Potter, S. D.; Schlesinger, M. E.; Schneider, S. H.; Watts, R. G.; Wigley, T. M. L.; Wuebbles, D. J. *Science* **1998**, *395*, 881-884.

(2) Hoffert, M. I.; Caldeira, K.; Benford, G.; Criswell, D. R.; Green, C.; Herzog, H.; Jain, A. K.; Kheshgi, H. S.; Lackner, K. S.; Lewis, J. S.; Lightfoot, H. D.; Manheimer, W.; Mankins, J. C.; Mauel, M. E.; Perkins, L. J.; Schlesinger, M. E.; Volk, T.; Wigley, T. M. L. *Science* **2002**, *298*, 981-987.

(3) Wigley, T. M. L.; Raper, S. C. B. *Science* **2001**, *293*, 451-454.

(4) Lewis, N. S.; Nocera, D. G. *Proc. Natl. Acad. Sci. U.S.A.* **2006**, *103*, 15729-15735.

(5) Eisenberg, R.; Nocera, D. G. *Inorg. Chem.* **2005**, *44*, 6799-6801.

(6) Kazmerski, L. L. *J. Electron. Spectrosc. Relat. Phenom.* **2006**, *150*, 105-135.

(7) Shockley, W.; Queisser, H. *J. Appl. Phys.* **1961**, *32*, 510-519.

(8) Miles, R. W.; Hynes, K. M.; Forbes, I. *Prog. Cryst. Growth Charact. Mater.* **2005**, *51*, 1-42.

(9) Taguchi, M.; Terakawa, A.; Maruyama, E.; Tanaka, M. *Prog. Photovolt.: Res. Appl.* **2005**, *13*, 481-488.

(10) Goetzberger, A.; Hebling, C.; Schock, H.-W. *Mater. Sci. Eng. R* **2003**, *40*, 1-46.

(11) Surek, T. *J. Cryst. Growth* **2005**, *275*, 292-304.

(12) Shaheen, S. E.; Ginley, D. S.; Jabbour, G. E. *MRS Bulletin* **2005**, *30*, 10-15.

(13) Weber, K. J.; Blakers, A. W.; Stocks, M. J.; Babaei, J. H.; Everett, V. A.; Neuendorf, A. J.; Verlinden, P. J. *IEEE Electron Device Lett.* **2004**, *25*, 37-39.

(14) Basore, P. A. In *Proceedings of the 31st IEEE Photovoltaic Specialists Conference*: Orlando, 2005, pp 967-970.

(15) Green, M. A. *Physica E* **2002**, *14*, 65-70.

(16) Carlson, D. E.; Wronski, C. R. *Appl. Phys. Lett.* **1976**, *28*, 671-673.

(17) Guha, S.; Yang, J. *J. Non-Cryst. Solids* **2006**, *352*, 1917-1921.

(18) Staebler, D. L.; Wronski, C. R. *Appl. Phys. Lett.* **1977**, *31*, 292-294.

(19) Visoly-Fisher, I.; Cohen, S. R.; Ruzin, A.; Cahen, D. *Adv. Mater.* **2004**, *16*, 879-883.

(20) Persson, C.; Zunger, A. *Phys. Rev. Lett.* **2003**, *91*, 266401-266404.

(21) Beck, M. E.; Wiederman, S.; Hungtington, R.; VanAlsburg, J.; Kanto, E.; Butcher, R.; Britt, J. S. In *Proceedings of the 31st IEEE Photovoltaics Specialists Conference*: Orlando, 2005, pp 211-214.

(22) Geyer, V.; Schuurmans, F.; Linden, H.; Kirchner, G.; Wienke, J.; Goris, M. In *Proceedings of the IEEE 4th World Conference on Photovoltaic Energy Conversion*: Waikoloa, HI, 2006, pp 333-337.

(23) Bonnet, D.; Meyers, P. *J. Mater. Res.* **1998**, *13*, 2740-2753.

(24) Dhere, N.; Dhere, R. *J. Vac. Sci. Technol. A* **2005**, *23*, 1208-1214.

(25) Andersson, B. A. *Prog. Photovolt.: Res. Appl.* **2000**, *8*, 61-76.

(26) Dittrich, H.; Vaughan, D. J.; Pattrick, R. A. D.; Graeser, S.; Lux-Steiner, M.; Kunst, R.; Lincot, D. In *Proceedings of the 13th European Photovoltaic Solar Energy Conference*, 1995, pp 1299-1302.

(27) George, M. W.; Carlin, J. F. J.; Edelstein, D. L. *Mineral Commodity Summaries*; U.S. Geological Survey, U.S. Government Printing Office: Washington, DC, 2006.

(28) Estrella, V.; Nair, M. T. S.; Nair, P. K. *Semicond. Sci. Technol.* **2003**, *18*, 190-194.

(29) Gerein, N. J.; Haber, J. A. *Chem. Mater.* **2006**, *18*, 6297-6302.

(30) Jeanloz, R.; Johnson, M. L. *Phys. Chem. Miner.* **1984**, *11*, 52-54.

(31) Bullett, D. W.; Dawson, W. G. *J. Phys. C: Solid State Phys.* **1986**, *19*, 5837-5847.

(32) Makovicky, E.; Skinner, B. *Can. Mineral.* **1979**, *17*, 619-634.

(33) Lide, D. R., Ed. *CRC Handbook of Chemistry and Physics*; Internet Version, 87th ed.; Taylor and Francis: Boca Raton, FL, 2007.

(34) Sonawane, P. S.; Wani, P. A.; Patil, L. A.; Seth, T. *Mater. Chem. Phys.* **2004**, *84*, 221-227.

(35) Rodriguez-Lazcano, Y.; Nair, M. T. S.; Nair, P. K. *J. Cryst. Growth* **2001**, *223*, 399-406.

(36) Rodriguez-Lazcano, Y.; Nair, M. T. S.; Nair, P. K. *J. Electrochem. Soc.* **2005**, *152*, G635-G638.

(37) Kocman, V.; Nuffield, E. W. *Acta. Cryst. B* **1973**, *29*, 2528-2535.

(38) Wang, N. *Mineral. Mag.* **1994**, *58*, 201-204.

(39) Makovicky, E.; Balic-Zunic, T. *Can. Mineral.* **1995**, *33*, 655-663.

(40) Makovicky, E. *J. Solid State Chem.* **1983**, *49*, 85-92.

(41) Hu, H.; Gomez-Daza, O.; Nair, P. K. *J. Mater. Res.* **1998**, *13*, 2453-2456.

(42) Nair, P. K.; Huang, L.; Nair, M. T. S.; Hu, H.; Meyers, E. A.; Zingaro, R. A. *J. Mater. Res.* **1997**, *12*, 651-656.

(43) Gerein, N. J.; Haber, J. A. *Chem. Mater.* **2006**, *18*, 6289-6296.

(44) Whitfield, H. J. *Solid State Comm.* **1980**, *33*, 747-748.

(45) Skinner, B.; Luce, F.; Makovicky, E. *Econ. Geol.* **1972**, *67*, 924-938.

(46) Allen, L. H.; Buhks, E. *J. Appl. Phys.* **1984**, *56*, 327-335.

(47) Allen, L. H.; Buhks, E. *J. Appl. Phys.* **1986**, *59*, 1360-1365.

(48) Buhks, E. *Sol. Energy Mater.* **1986**, *13*, 213-220.

(49) Buerger, M. J.; Wuensch, B. J. *Science* **1963**, *141*, 276-277.

(50) Makovicky, E.; Møller, S. K. *N. Jb. Miner. Abh.* **1994**, *167*, 89-123.

(51) Di Benedetto, F.; Bernardini, G. P.; Cipriani, C.; Emiliani, C.; Gatteschi, D.; Romanelli, M. *Phys. Chem. Miner.* **2005**, *32*, 155-164.

(52) Pfitzner, A.; Evain, M.; Petricek, V. *Acta. Cryst. B* **1997**, *53*, 337-345.

(53) Pattrick, R. A. D.; van der Laan, G.; Vaughan, D. J.; Henderson, C. M. B. *Phys. Chem. Miner.* **1993**, *20*, 395-401.

(54) Lind, I.; Makovicky, E. *N. Jb. Miner. Abh.* **1982**, *145*, 134-156.

(55) Delgado, J. M. In *Inst. Phys. Conf. Ser. No. 152: Section B: Thin Film Growth and Characterization*, 1998, pp 45-50.

(56) Deb, S. K. In *Inst. Phys. Conf. Ser. No. 152: Section B: Thin Film Growth and Characterization*, 1998, pp 923-929.

(57) Elhaddad, M. A.; Moh, G. H. *Mineral. Petrol.* **1992**, *46*, 185-193.

(58) Blöß, S.; Jansen, M. *Z. Naturforsch. B* **2003**, *58*, 1075-1078.

(59) Mishra, B.; Pruseth, K. L. *Contrib. Mineral. Petrol.* **1994**, *118*, 92-98.

(60) Nair, M. T. S.; Peña, Y.; Campos, J.; Garcia, V. M.; Nair, P. K. *J. Electrochem. Soc.* **1998**, *145*, 2113-2120.

(61) Kyono, A.; Kimata, M. *Am. Mineral.* **2005**, *90*, 162-165.

(62) Razmara, M. F.; Henderson, C. M. B.; Pattrick, R. A. D.; Bell, A. M. T.; Charnock, J. M. *Mineral. Mag.* **1997**, *61*, 79-88.

(63) Deshpande, A. P.; Sapre, V. B.; Mande, C. *J. Phys. C: Solid State Phys.* **1984**, *17*, 955-960.

(64) Wang, N. *N. Jb. Miner. Mh.* **1989**, *11*, 521-523.

(65) Soliman, L. I.; Abo El Soad, A. M.; Zayed, H. A.; El Ghfar, S. A. *Fizika A* **2002**, *4*, 139-152.

(66) Koinuma, H.; Takeuchi, I. *Nature Mater.* **2004**, *3*, 429-438.

(67) Hanak, J. J. In *Combinatorial Materials Synthesis*; Xiang, X.-D., Takeuchi, I., Eds.; Marcel Dekker, Inc.: New York, 2003, pp 7-34.

(68) Jandeleit, B.; Schaefer, D. J.; Powers, T. S.; Turner, H. W.; Weinberg, W. H. *Angew. Chem. Int. Ed.* **1999**, *38*, 2494-2532.

(69) van Dover, R. B.; Scheenmeyer, L. F.; Flemming, R. M. *Nature* **1998**, *392*, 162-164.

(70) Takeuchi, I.; Famodu, O. O.; Read, J. C.; Aronova, M. A.; Chang, K.-S.; Craciunescu, C.; Lofland, S. E.; Wuttig, M.; Wellstood, F. C.; Knauss, L.; Orozco, A. *Nature Mater.* **2003**, *2*, 180-184.

(71) Wang, J.; Yoo, Y.; Gao, C.; Takeuchi, I.; Sun, X.; Chang, H.; Xiang, X.-D.; Shultz, P. G. *Science* **1998**, *279*, 1712-1714.

(72) Todd, A. D. W.; Mar, R. E.; Dahn, J. R. *J. Electrochem. Soc.* **2006**, *153*, A1998-A2005.

(73) Hanak, J. J.; Bykov, E.; Elgamel, H.; Grecu, D.; Putz, J.; Reiter, N.; Shvydka, D.; Powell, R. C. In *26th IEEE Photovoltaic Specialists Conference*, 2000, pp 495-498.

(74) Wang, Q.; Yue, G.; Li, J.; Han, D. *Solid State Comm.* **2000**, *113*, 175-178.

(75) Taylor, M. P.; Readey, D. W.; Teplin, C. W.; van Hest, M. F. A. M.; Alleman, J. L.; Dabney, M. S.; Gedvilas, L. M.; Keyes, B. M.; To, B.; Perkins, J. D.; Ginley, D. S. *Meas. Sci. Technol.* **2005**, *16*, 90-94.

(76) Perkins, J. D.; del Cueto, J. A.; Alleman, J. L.; Warmsingh, C.; Keyes, B. M.; Gedvilas, L. M.; Parilla, P. A.; To, B.; Readey, D. W.; Ginley, D. S. *Thin Solid Films* **2002**, *411*, 152-160.

(77) Cawse, J. N. *Acc. Chem. Res.* **2001**, *34*, 213-221.

(78) Matson, R. J.; Jamjoum, O.; Buonaquisti, A. D.; Russell, P. E.; Kazmerski, L. L.; Sheldon, P.; Ahrenkiel, R. K. *Sol. Cells* **1984**, *11*, 301-305.

(79) Romeo, A.; Terheggen, M.; Abou-Ras, D.; Bätzner, D. L.; Haug, F.-J.; Kälin, M.; Rudmann, D.; Tiwari, A. N. *Prog. Photovolt.: Res. Appl.* **2004**, *12*, 93-111.

(80) Wu, X.; Asher, S.; Levi, D. H.; King, D. E.; Yan, Y.; Gessert, T. A.; Sheldon, P. *J. Appl. Phys.* **2001**, *89*, 4564-4569.

(81) Minemoto, T.; Negami, T.; Nishiwaki, S.; Takakura, H.; Hamakawa, Y. *Thin Solid Films* **2000**, *372*, 173-176.

(82) Cohen, D. J.; Ruthe, K. C.; Barnett, S. A. *J. Appl. Phys.* **2004**, *96*, 459-467.

(83) Kammler, D. R.; Mason, T. O.; Young, D. L.; Coutts, T. J. *J. Appl. Phys.* **2001**, *90*, 3263-3268.

(84) Nakada, T.; Mizutani, M. *Jpn J. Appl. Phys., Part 2* **2002**, *41*, L165-L167.

(85) Hariskos, D.; Spiering, S.; Powalla, M. *Thin Solid Films* **2005**, *480-481*, 99-109.

(86) Naghavi, N.; Spiering, S.; Powalla, M.; Cavana, B.; Lincot, D. *Prog. Photovolt.: Res. Appl.* **2003**, *11*, 437-443.

(87) Strohm, A.; Eisenmann, L.; Gebhardt, R. K.; Harding, A.; Schlötzer, T.; Abou-Ras, D.; Schock, H. W. *Thin Solid Films* **2005**, *480-481*, 162-167.

(88) Munzel, M.; Deibel, C.; Dyakonov, V.; Parisi, J.; Riedl, W.; Karg, F. *Thin Solid Films* **2001**, *387*, 231-234.

(89) Siebentritt, S.; Kampschulte, T.; Bauknecht, A.; Blieske, U.; Harneit, W.; Fiedeler, U.; Lux-Steiner, M. *Sol. Energy Mater. Sol. Cells* **2002**, *70*, 447-457.

(90) Ohtake, Y.; Okamoto, T.; Yamada, A.; Konagai, M.; Saito, K. *Sol. Energy Mater. Sol. Cells* **1997**, *49*, 269-275.

(91) Sánchez-Juárez, A.; Tiburcio-Silver, A.; Ortiz, A. *Thin Solid Films* **2005**, *480-481*, 452-456.

Chapter 3. Synthesis of Cu_3BiS_3 Thin Films by Heating Metal and Metal Sulfide Precursor Films under Hydrogen Sulfide

Introduction

In Chapter 2 the mineral phase Wittichenite, Cu_3BiS_3, was identified as a candidate material for use as the solar absorber layer in novel thin film PV devices. A critical first step in integrating Cu_3BiS_3 into a thin film PV device is the development of a deposition method that produces films of uniform composition and morphology across the entire substrate. Two-step processes are often employed to synthesize chalcogenide thin films, involving the deposition of a precursor film that is subsequently heated under a reactive gas to form the target compound. The utility of this approach for PV devices has been demonstrated by the synthesis of device quality films of $CuInS_2$, $CuInSe_2$, and $CuIn(S,Se)_2$ by heating precursors in H_2S,[1-6] H_2Se,[6-8] or H_2S/H_2Se[9] respectively. Heating of $Cu(In,Ga)Se_2$ in an H_2S/H_2Se atmosphere has also been used to produce graded absorber layers of $Cu(In,Ga)(S,Se)_2$.[10] In addition to the successful application of this two-step process to CIS and CIGS, the synthesis of numerous other sulfide thin films, including Ag_3SbS_3,[11] SnS,[12,13] In_2S_3,[14] and FeS_2,[15] has also been achieved.

The applicability of this method to the synthesis of Cu_3BiS_3 thin films has been evaluated by heating Cu-Bi metal precursor films and Cu-S-Bi metal sulfide precursor films, sputter deposited on soda-lime glass and fused silica substrates, in an H_2S atmosphere. Since Cu_3BiS_3 is being presented as a novel PV material, it was necessary to limit substrate choices to those that are transparent and non-conductive and would enable measurement of the optical and electrical properties of the deposited films. Evaluation included the systematic study of precursor composition and preparation, heating temperature, heating profile, and gas composition and pressure. Phase-pure Cu_3BiS_3 films were formed; however, it was found that precursor composition determines the reaction pathway, and that the reaction pathway is the dominant factor in controlling the morphology of the Cu_3BiS_3 thin film. Processing conditions were optimized, but the overriding influence of the precursor/pathway/morphology relationship results in Cu_3BiS_3 thin films that are discontinuous or contain hollow pockets between the film and substrate. Based on these results a one-step reactive deposition has been developed that overcomes the limitations of the two-step process for the deposition of Cu_3BiS_3, and produces films with morphology suitable for integration into PV devices. Details of this reactive deposition are reported in Chapter 4. In this chapter, details are reported on the synthesis and characterization of Cu_3BiS_3 thin films produced by heating metal and metal sulfide precursors in the presence of H_2S, including the relationship between precursor composition, reaction pathway, and film morphology.

Experimental Details

Cu-Bi metal precursor films were sputtered onto soda-lime glass and fused silica substrates (50 mm x 50 mm). Substrates were cleaned by immersing in 2-propanol in an ultrasonic bath for 30 minutes, followed by drying with a stream of N_2. To ensure residual contamination was not the cause of poor morphology, some substrates were cleaned in 2-propanol as above, immersed for 30 minutes in a 1:3 mixture of H_2O_2:H_2SO_4, rinsed with distilled H_2O, rinsed with 2-propanol, and dried with a stream of N_2.

Precursor films were deposited, employing either co-deposition or multi-layer deposition. Cu and Bi were DC sputtered from 3" diameter targets at 84 W and 20 W, respectively, at an Ar pressure of 5 mtorr. During deposition the platen was continuously rotated at 6 rpm. Under these conditions a Cu to Bi ratio of 3:1 is obtained with equal sputtering times. Sputter rates were calibrated by measuring the deposited mass/area, and determining the stoichiometery of co-sputtered films by WDX. Net binary film thicknesses ranged from approximately 250–2000 nm. Multilayer thin films were built up of elemental layers approximately 125 nm thick, starting with Cu and ending with Bi. The alternate stacking sequence was tested, with no significant impact on Cu_3BiS_3 film quality. Studies on the selenization of Cu-In metal precursors under H_2Se have also found that the stacking sequence of multi-layer precursors does not have a significant effect.[16] Cu and Bi elemental precursor films were deposited at the same powers employed for binary films and were approximately 500 nm thick.

Cu-S-Bi metal sulfide precursors were deposited only on fused silica substrates, cleaned in the same manner as outlined above. The CuS target was sputtered continuously at 80 W RF. The Bi target was sputtered at 10 W DC, and cycled on and off to achieve the required stoichiometry. Targets were 3" in diameter, the platen was rotated at 6 rpm, and the sputtering gas was Ar at a pressure of 5 mtorr. The stoichiometry of homogeneous thin films (Cu-S or Cu-Bi-S) was determined by WDX analysis. The correct elemental ratio of Cu:Bi (following heating under H_2S) was achieved by co-sputtering for 9 minutes, followed by 41 minutes of sputtering the CuS target only. Each 50 minute cycle produced approximately 130 nm of deposition, and was repeated six times to produce films with a final thickness of approximately 800 nm.

All precursor films were processed by heating in an H_2S atmosphere. The 40 l evacuated reaction chamber (~1×10^{-6} torr base pressure) was backfilled with 50 torr H_2S, 5 torr H_2S/45 torr Ar, 5 torr H_2S/5 torr Ar, or 1 torr H_2S/9 torr Ar yielding total chamber pressures of 50 or 10 torr. Heating was controlled by a programmable resistance heater. Precursor films were processed for 2-30 hours at temperatures ranging from 175-400 °C; heating rates were varied from 2 °C/minute to 20 °C/minute, with the cooling rate fixed at 2 °C/minute. Following heating under H_2S some films were also heated under vacuum (~10^{-7} torr) at 600 °C.

Product thin films were characterized using SEM/EDX (JEOL 6031F FESEM, Hitachi S-4800 FESEM, Hitachi S3000N VPSEM), WDX (JEOL 8900 microprobe), and XRD (Bruker D8 diffractometer with area detector). Sheet and electrical resistivities of the product films were measured using the Van der Pauw method[17] (square 2.5 cm x 2.5 cm sample, test leads attached with 1 mm silver print contacts on each edge, Keithley 2400 source/measure unit). The Van der Pauw method was employed because the use of larger silver print contacts, relative to a 4-point probe, enables reliable and reproducible contacts to be made to films with voids. 4-point probe measurements were also carried out, but the non-reproducible contacts that resulted were reflected in the data.

Results

Heating of both metal and metal sulfide precursor films in the presence of H_2S resulted in the synthesis of phase-pure Cu_3BiS_3; however, the morphology of the product films was highly dependent on precursor composition, processing conditions, and choice of substrate. The ternary phase diagram for Cu-Bi-S has been previously studied by solid-state methods at 200 °C and 300 °C, and Cu_3BiS_3 identified as a stable compound on the Cu_2S-Bi_2S_3 tie line at these temperatures.[18] The Cu_2S-Bi_2S_3 pseudo-binary phase diagram has been previously investigated from 270-1200 °C, also by solid-state methods, with Cu_3BiS_3 identified as a stable phase up to 517 °C.[19] Above 300 °C Cu_3BiS_3 forms a solid solution over a small range, containing ~1 mole % excess Cu_2S and Bi_2S_3.[19,20] The ternary phase diagram (modified from reference 18), and the pseudo binary phase diagram (reproduced from reference 19), are presented in Figure 3.1 and Figure 3.2, respectively.

Co-sputtered Cu-Bi metal precursors were smooth, continuous, and mirror-like in appearance, with insufficient surface topography to produce meaningful contrast in SEM images. Multi-layer Cu-Bi metal precursors exhibited increased roughness as a consequence of the Bi top layer (Bi films exhibit faceted island growth), but were still continuous and relatively smooth with feature sizes on the order of 200 nm. XRD powder patterns collected from multi-layer and co-sputtered Cu-Bi precursor films are presented in Figure 3.3, along with the standard powder patterns for Bi (PDF 85-1329) and Cu (PDF 89-2838). The XRD powder pattern collected from the multi-layer precursor indicates that the film is composed of crystalline Bi and Cu. The XRD powder pattern collected from the co-sputtered precursor indicates that the film is largely amorphous. This is consistent with the Cu-Bi binary phase diagram, presented in Figure 3.4 (reproduced from reference 21), which contains no stable intermetallic phases.[21] Broad peaks in the powder pattern from the co-sputtered precursor suggest that some crystalline Cu and Bi may be present, in addition to the amorphous material. There is also a relatively sharp peak at 12° 2-theta that has not been identified.

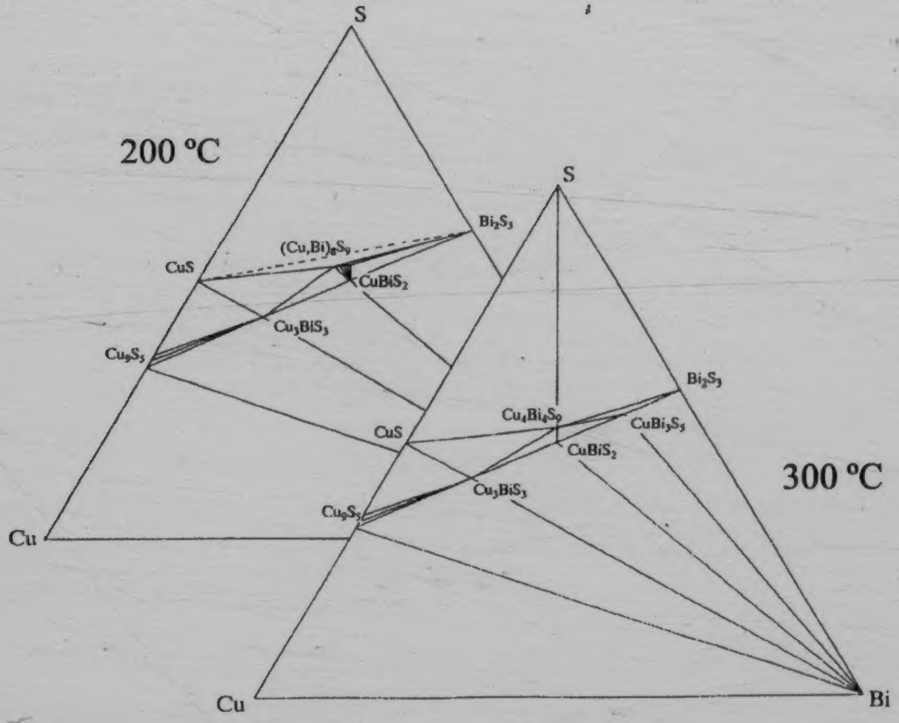

Figure 3.1. Cu-Bi-S phase diagram at 200 °C and 300 °C. Cu_3BiS_3 is identified as a stable phase on the Cu_2S-Bi_2S_3 tie line. Modified from reference 18.

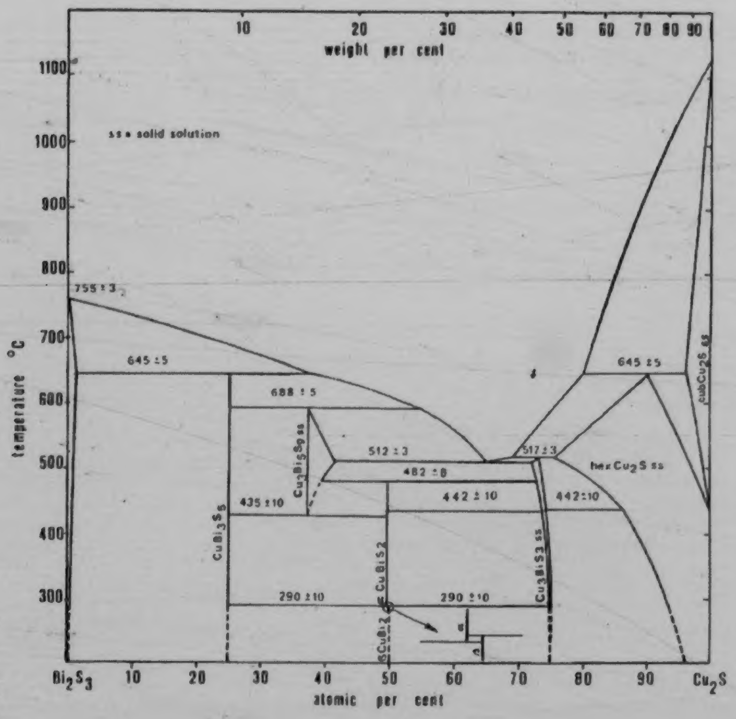

Figure 3.2. Bi_2S_3-Cu_2S pseudo binary phase diagram from 270-1200 °C. Cu_3BiS_3 is identified as a stable compound up to 517 °C, forming a solid solution above 300 °C. Reproduced from reference 19 with the permission of E. Schweizerbart, http://www.schweizerbart.de.

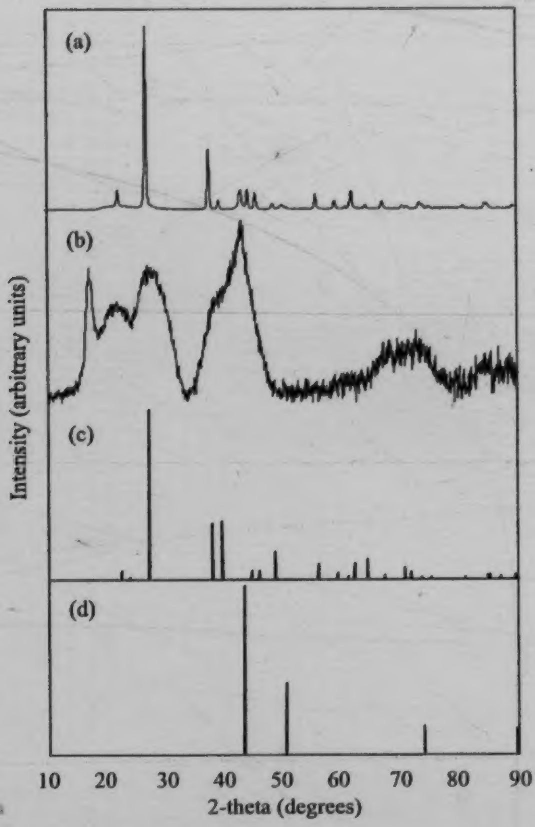

Figure 3.3. XRD powder patterns collected from multi-layer (a) and co-sputtered (b) Cu-Bi metal precursor films, and standard powder patterns for Bi (c) and Cu (d).

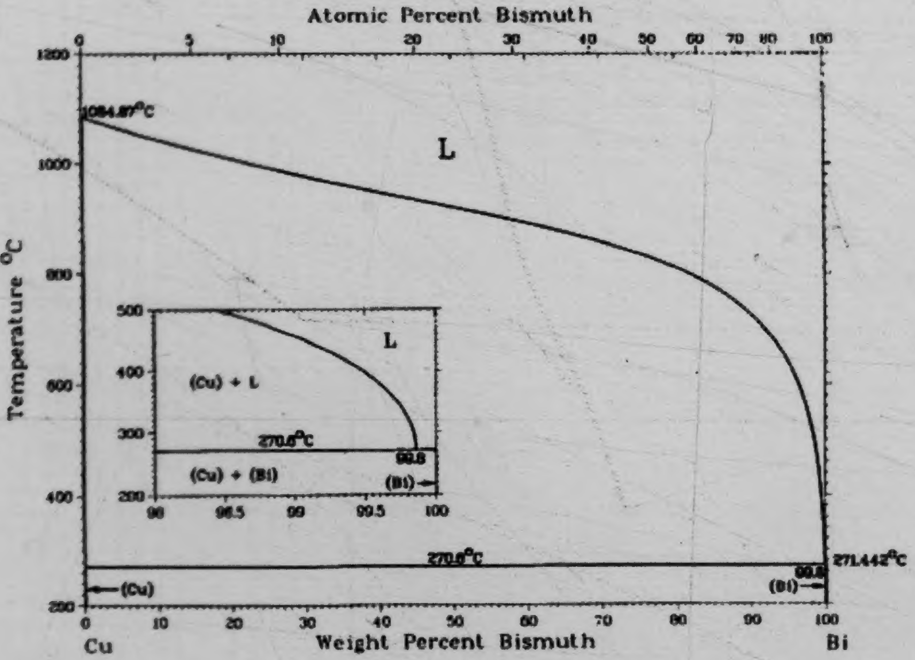

Figure 3.4. Cu-Bi binary phase diagram from 200–1200 °C. Reproduced from reference 21 with permission of ASM International®, all rights reserved, www.asminternational.org.

Thin films of Cu_3BiS_3 were synthesized from metal precursor films deposited on both fused silica and soda-lime glass substrates. When soda-lime glass substrates were employed the adhesion of the film, and the morphology of the film, were considerably worse than that observed with fused silica substrates. SEM images of a Cu_3BiS_3 thin film synthesized by heating a 2 μm thick co-sputtered metal precursor film on a soda-lime glass substrate at 270 °C for 16 hours under 5 torr H_2S/45 torr Ar are presented in Figure 3.5. Based on these results subsequent experiments with metal and metal sulfide precursors employed only fused silica substrates.

When synthesizing Cu_3BiS_3 films from metal precursors on fused silica substrates it was found that reaction conditions and precursor preparation significantly impacted the morphology of the resultant film. The best results were achieved with co-sputtered precursors processed at low H_2S partial pressures (5 torr), with faster heating rates (10-20 °C/minute), and long heating times (>16 hours) at 270 °C. SEM images of a representative sample (1 μm thick co-sputtered precursor, processed at 270 °C for 16 hours with a heating rate of 10 °C/minute, and 5 torr H_2S/5 torr Ar atmosphere) are presented in Figure 3.6 (a) and (b). The corresponding XRD powder pattern is shown in Figure 3.6 (c), along with the Cu_3BiS_3 standard powder pattern (PDF 43-1479) in Figure 3.6 (d). The powder pattern confirms that the target phase Cu_3BiS_3 has been synthesized, and shows no extraneous peaks. These films are characterized in general by relatively smooth surfaces, large crystallites (~3-10 μm diameter), and numerous void spaces in the film.

When the optimized conditions identified above are altered, the resultant films are invariably of poorer quality. Specifically, if multi-layer precursors, slower heating rates

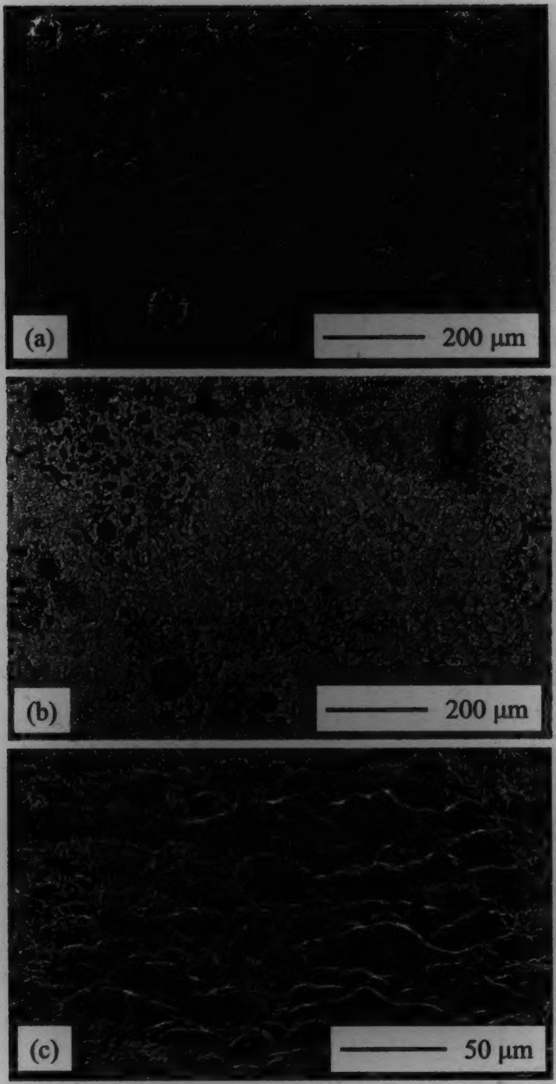

Figure 3.5. SEM images of a Cu_3BiS_3 film synthesized by heating a 2 μm thick co-sputtered metal precursor film on a soda-lime glass substrate at 270 °C for 16 hr under 5 torr H_2S/45 torr Ar. Images are secondary electron surface image (a), backscattered electron surface image where black areas are bare substrate (b), and secondary electron oblique image showing poor adhesion and roughness of film (c).

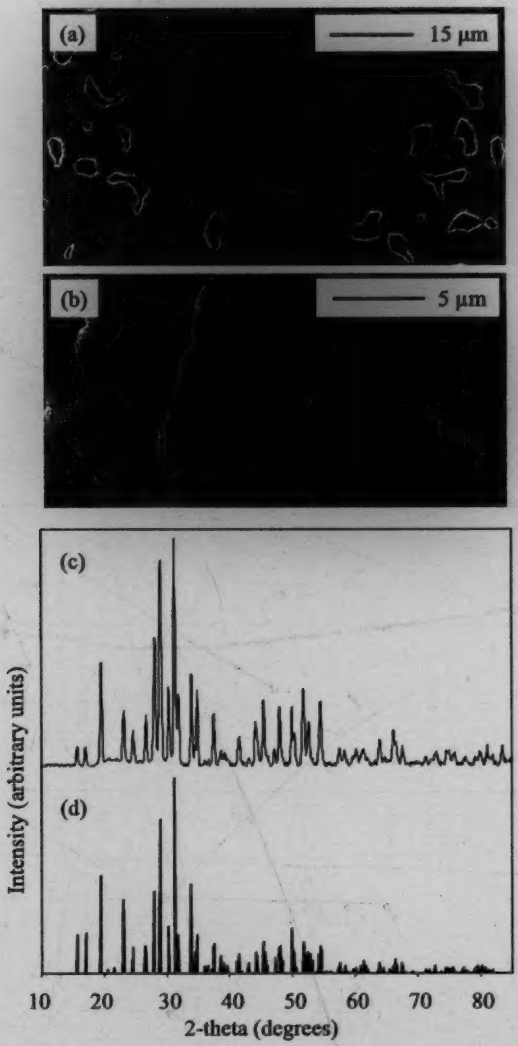

Figure 3.6. SEM images of a Cu_3BiS_3 film (a) and (b) synthesized by heating a co-sputtered metal precursor film at 270 °C for 16 hr under 5 torr H_2S/5 torr Ar, XRD powder pattern (c), and standard powder pattern for Cu_3BiS_3 (d).

or higher partial pressures of H_2S are employed, the resultant films are rougher and contain an increased number of voids. This is accompanied by occasional large outgrowths randomly distributed across the surface of the film, and isolated islands containing a secondary phase ($Cu_{1.8}S$ or Bi) identified by SEM/EDX. The exact nature of the resultant film morphology is, as expected, dependent on the specifics of precursor deposition and processing with a range of sub-optimum morphologies resulting. For example, presented in Figure 3.7 is a film formed by heating a 250 nm thick multi-layer precursor at 270 °C for 30 hours with a heating rate of 10 °C/minute, and 50 torr H_2S atmosphere. When compared to the optimized morphology (Figure 3.6) the film is significantly rougher, the crystallites are smaller, and the film contains an increased number of voids per unit area. Differences in morphology between the films in Figures 3.6 and 3.7 are not attributed to the difference in precursor thickness. A systematic study of the effect of precursor thickness was not performed; however, when precursors of varying thickness in the range of 250-1000 nm were prepared and processed under identical conditions, significant variations in morphology as a function of thickness were not observed.

When processing temperatures greater than 300 °C were employed, the resultant films were Bi depleted, and were of mixed composition containing both Cu_3BiS_3 and Cu_2S. SEM images of a film formed by heating a 1 μm thick multi-layer precursor at 400 °C for 2 hours under 50 torr H_2S are presented in Figure 3.8 (a) and (b). The corresponding XRD powder pattern and the standard powder pattern for Cu_3BiS_3 are presented in Figure 3.8 (c) and (d) respectively. In the backscattered electron image (Figure 3.8 (b)) two phases are evident, with EDX identifying the bright phase as

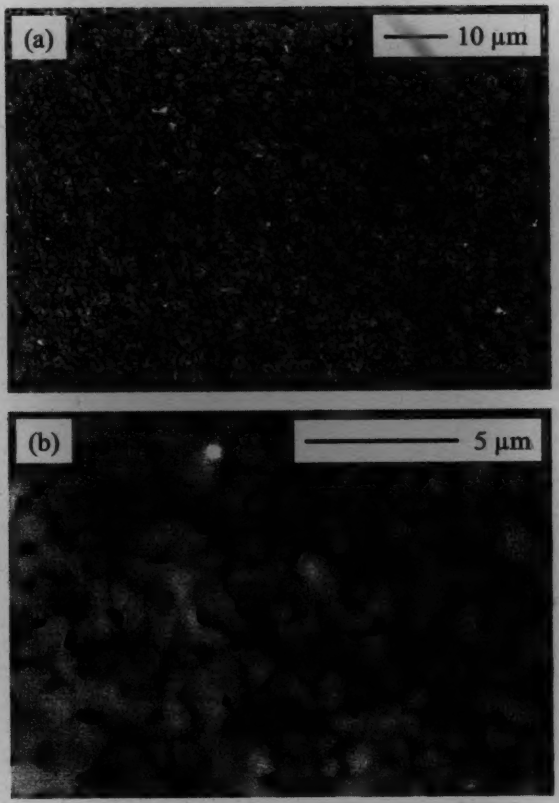

Figure 3.7. SEM images of a Cu_3BiS_3 film (a) and (b), formed by heating a multi-layer metal precursor film at 270 °C for 30 hr under 50 torr H_2S.

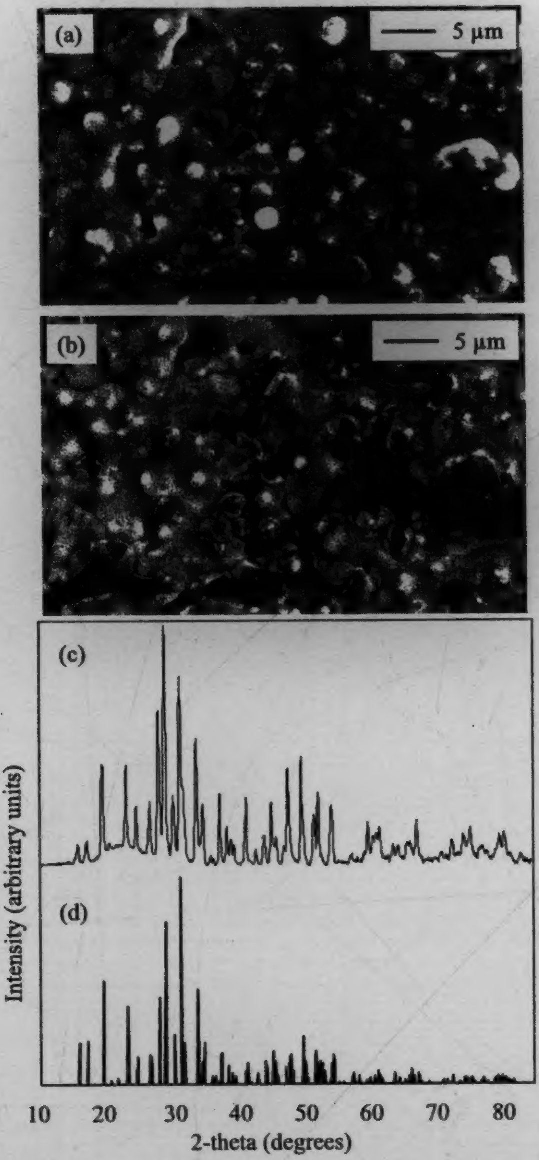

Figure 3.8. SEM images of a Cu_3BiS_3 film, synthesized by heating a multi-layer metal precursor film at 400 °C for 2 hr under 50 torr H_2S. Images are secondary electron (a) and backscattered electron (b). The light and dark areas are identified by EDX as Cu_3BiS_3 and Cu_2S respectively. The XRD powder pattern (c), and standard powder pattern for Cu_3BiS_3 (d) are also shown.

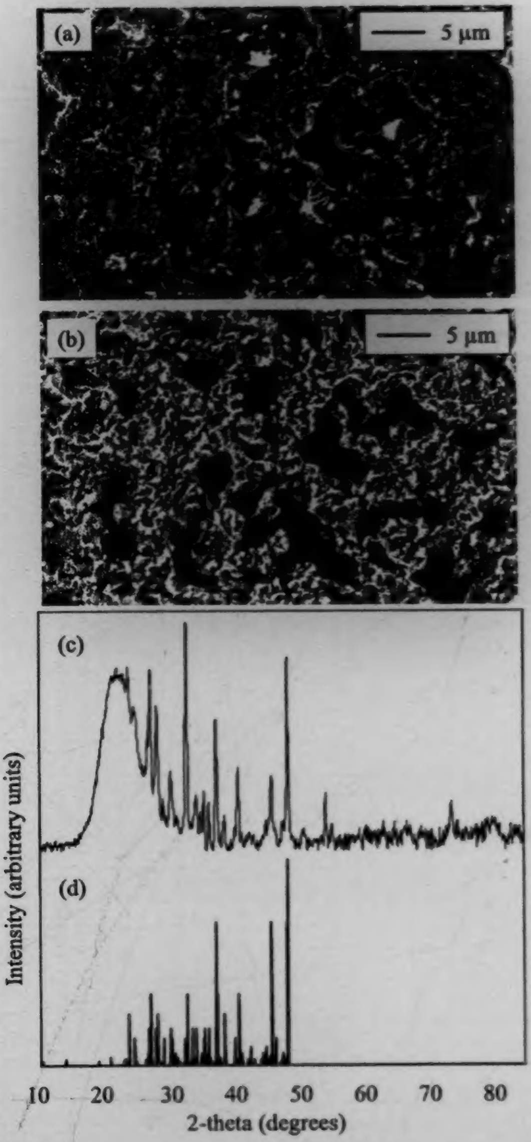

Figure 3.9. SEM images of a film synthesized by heating a Cu_3BiS_3 film (Figure 3.4) for 4 hr at 600 °C under vacuum. Images are secondary electron (a) and backscattered electron (b). The XRD powder pattern (c) and standard powder pattern for Cu_2S (d) are also shown.

Cu_3BiS_3 and the dark phase as Cu_2S. The Cu_2S is present as a minor phase, and due to the significant overlap between Cu_2S peaks and Cu_3BiS_3 peaks it is not identified in the corresponding powder pattern. When the same sample was subsequently heated at 600 °C under vacuum, complete loss of Bi and conversion to Cu_2S was observed. SEM images of a film formed by heating a 1 μm thick multi-layer precursor at 400 °C for 2 hours under 50 torr H_2S, followed by heating for 4 hours at 600 °C under vacuum ($\sim 10^{-7}$ torr) are presented in Figure 3.9 (a) and (b). The backscattered electron image (Figure 3.9 (b)) shows only a single phase, and the corresponding XRD powder pattern (Figure 3.9 (c)) matches the standard powder pattern for Cu_2S (PDF 33-490) shown in Figure 3.9 (d).

The vapor pressure of Bi and S as a function of temperature are presented in Figure 3.10.[22] In the upper frame is a linear plot of the log of vapor pressure against the inverse of temperature. In the lower frame is a plot of vapor pressure against temperature. On the linear plot lines of best fit have been calculated, and used to extrapolate Bi vapor pressures of 5×10^{-12} torr and 1×10^{-6} torr at 400 °C and 600 °C, respectively. In Figure 3.11 and Figure 3.12 the Bi-S and Cu-S phase diagrams are presented, reproduced from reference 21. Consistent with the phase diagrams and vapor pressure data it would appear that at 400 °C small amounts of Bi-S decomposition products are form and volatilized, subsequently subliming on the cooled walls of the chamber. At 600 °C Cu_3BiS_3 is no longer stable; Bi-S decomposition products are volatilized and sublimed onto the chamber walls leaving behind stable Cu_2S.

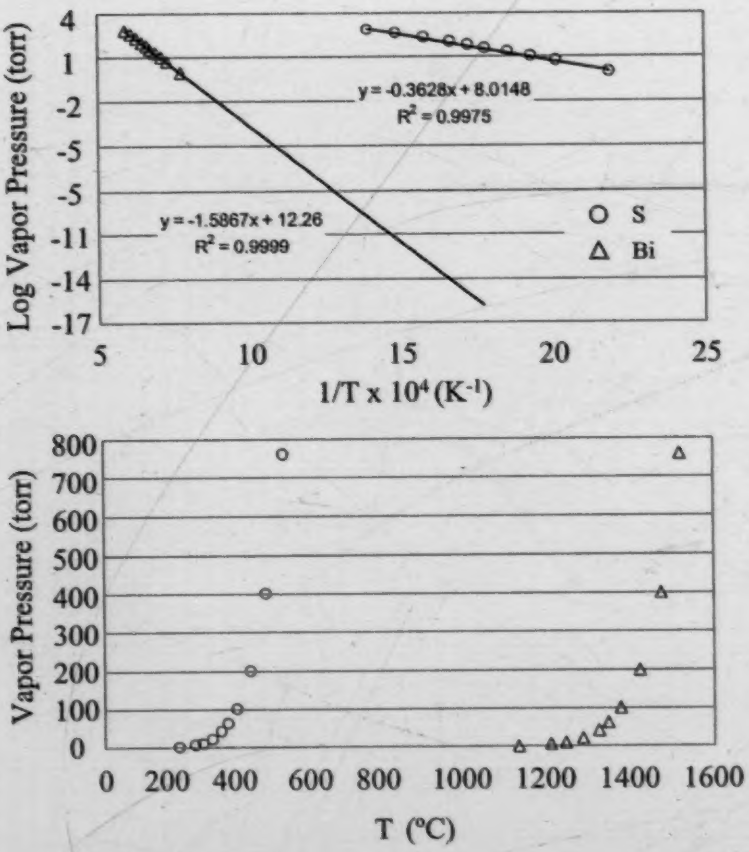

Figure 3.10. Plots of Bi (triangles) and S (circles) vapor pressure as a function of temperature. Log vapor pressure against the inverse of temperature with lines of best fit (upper plot) and vapor pressure against temperature (lower plot).

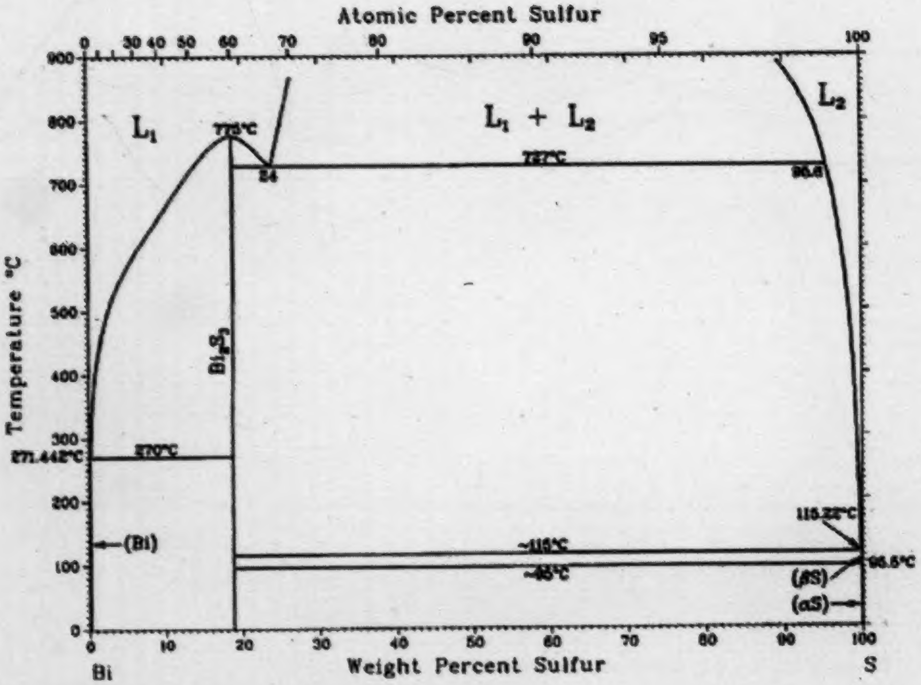

Figure 3.11. Bi-S binary phase diagram from 0–900 °C. Reproduced from reference 21 with permission of ASM International®, all rights reserved, www.asminternational.org.

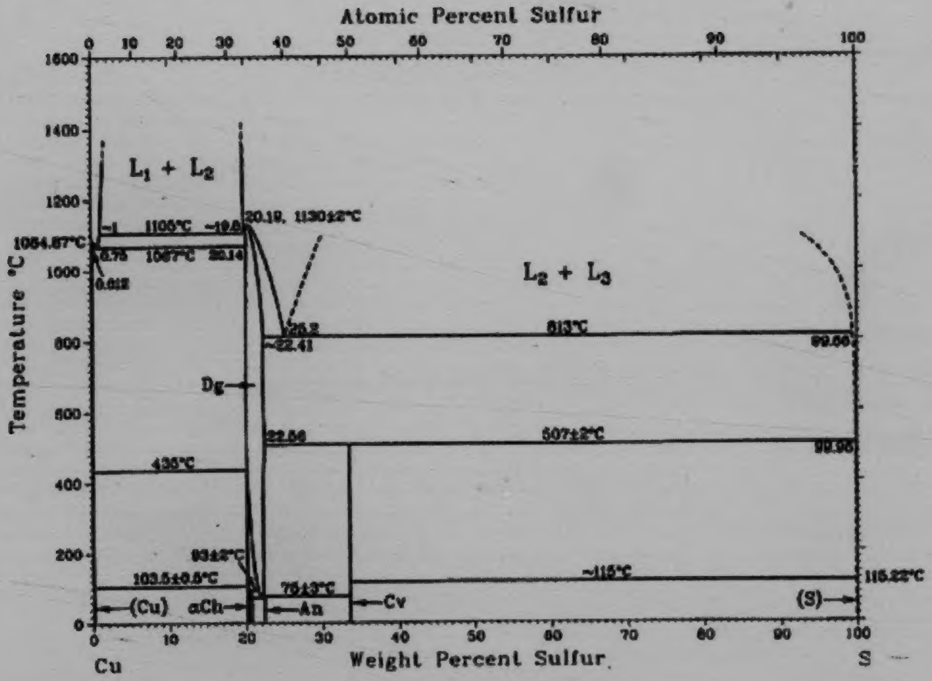

Figure 3.12. Cu-S binary phase diagram from 0–1600 °C. Reproduced from reference 21 with permission of ASM International®, all rights reserved, www.asminternational.org.

When heating times of less than 16 hours at 250–300 °C were employed, complete conversion of the precursor did not occur and the films were found to contain $Cu_{1.8}S$, Bi, and Cu_3BiS_3. A backscattered electron SEM image of a partially reacted film (1 μm thick co-sputtered precursor film processed at 300 °C for 2 hours with a heating rate of 1 °C/minute, and 50 torr H_2S atmosphere) is shown in Figure 3.13 (a), along with an XRD powder pattern collected from the film and standard powder patterns for Bi (PDF 65-1215) and $Cu_{1.8}S$ (PDF 88-2158). It should be noted that the $Cu_{1.8}S$ standard pattern is for a rhombohedral phase (space group R-3m), which has been identified as both a stable[23] and metastable[21,24] phase. Due to the weak diffraction signal from this phase, the assignment could not be made with certainty. However, the assignment is supported by the formation of the same $Cu_{1.8}S$ phase when copper precursor films are heated under similar conditions (see below). Reports on the formation of bulk Cu_xS phases has identified the formation of rhombohedral $Cu_{1.8}S$ above 132±6 °C, and persisting until 262±12 °C, at which point it is converted to $Cu_{1.96}S$.[24] These results are consistent with the observation of $Cu_{1.8}S$ in this work. No diffraction from Cu_3BiS_3 was evident in the powder pattern. EDX analysis was used to confirm the identity of elemental Bi and $Cu_{1.8}S$ phases, as well as to identify the third phase as having a composition of 3:1:3 Cu:Bi:S. The ternary phase, identified as Cu_3BiS_3, is present in much smaller amounts than the other two phases, explaining the lack of diffraction. When longer heating times are employed the elemental Bi reacts with the intermediate $Cu_{1.8}S$ and excess H_2S, yielding complete conversion to Cu_3BiS_3 (Figures 3.6 and 3.7).

When metal sulfide precursors produced by sputter deposition of Cu-S and Bi are employed for the synthesis of Cu_3BiS_3 the composition of the precursor film is more

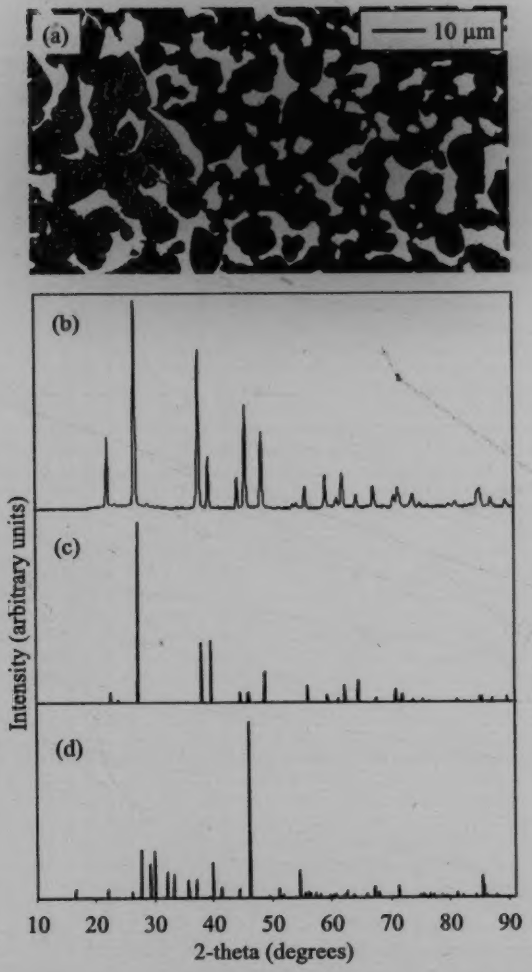

Figure 3.13. Backscattered SEM image of a film formed by heating a co-sputtered metal precursor at 300 °C for 2 hr under 50 torr H_2S (a) with phases identified by XRD/EDX as Bi (bright areas), $Cu_{1.8}S$ (dark areas), and by EDX as Cu_3BiS_3 (intermediate areas). XRD powder pattern (b) and standard powder pattern for Bi (c) and $Cu_{1.8}S$ (d) are also shown.

complex. As in the case of co-sputtered metal precursor films, the metal sulfide precursor is smooth, continuous, and mirror-like in appearance, with no topographic contrast visible in SEM images. SEM analysis of cross-sections of precursor films shows that a multilayer structure is retained during the deposition process (Figure 3.14 (a)). XRD analysis of these films suggests that a significant fraction of the film is amorphous; however, the presence of crystalline CuS, Bi_2S_3, and elemental S is also evident. The XRD powder pattern is presented in Figure 3.14 (b), along with the standard powder patterns for Bi_2S_3 (PDF 65-2435), CuS (PDF 6-0464), and S (PDF 71-0569). Diffraction from multiple phases makes phase identification difficult; however, key peaks for both Bi_2S_3 and CuS are identifiable. There is no evidence for the presence of crystalline Cu or Bi. These results suggest that when the CuS and Bi targets are sputtered simultaneously, Bi_2S_3 is formed. This is thought to occur by reaction of energetic Cu-S and Bi species incident on the deposition substrate.

Films of homogeneous composition, Cu-S and Cu-S-Bi, identical to the individual layers in the multi-layer metal sulfide precursor, were also prepared. WDX analysis of Cu-S films show that they are sulfur deficient, with a composition of 2.8:1.0 Cu:S. WDX analysis of Cu-S-Bi co-sputtered films determined a composition of 1.0:3.2:1.9 Cu:S:Bi. When the metal sulfide precursor is deposited, the relative thickness of these individual layers is modulated to provide a Cu:Bi ratio of 3:1. Based on the WDX analysis of single composition films, the sulfur balance in the multi-layer precursor film is calculated to be 2.6 (or 3:2.6:1 Cu:S:Bi), suggesting that the as-deposited sulfide precursor film has a net sulfur deficiency, necessitating sulfurization in an H_2S atmosphere.

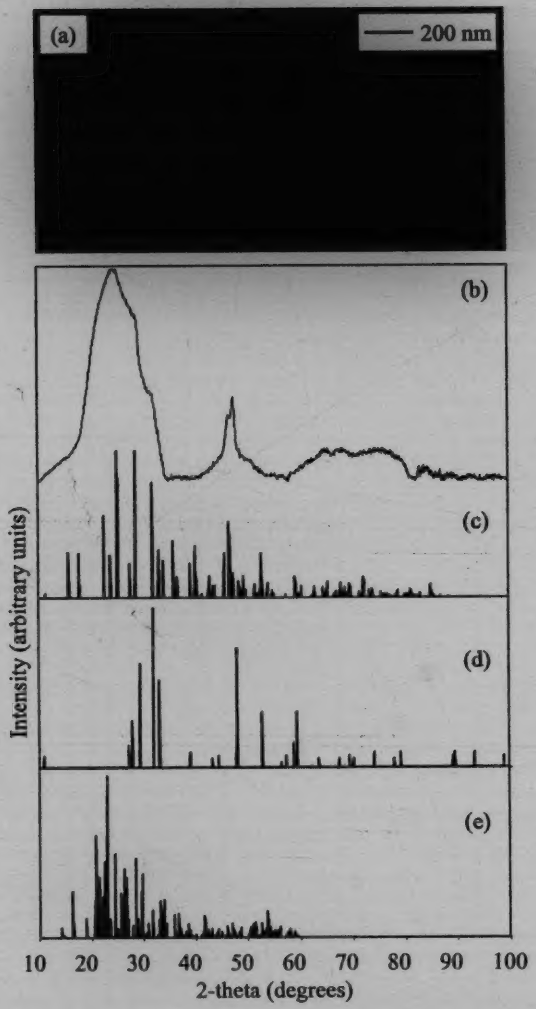

Figure 3.14. Backscattered SEM image of a metal sulfide precursor as-deposited (a), bright bands are composed of Cu-Bi-S, dark bands are Cu-S. XRD powder pattern (b) and standard powder pattern for Bi_2S_3 (c), CuS (d) and S (e) are also shown.

When metal sulfide precursors are heated in an H_2S environment the resultant Cu_3BiS_3 films are continuous, but they buckle, leaving 5-10 μm diameter round pockets between the film and the substrate. The individual crystallites are smaller than those observed in films synthesized from metal precursors. SEM images of a representative sample (metal sulfide precursor processed at 270 °C for 12 hours with a heating rate of 10 °C/minute, and 5 torr H_2S/45 torr Ar atmosphere) are presented in Figure 3.15 (a) and (b) along with the XRD powder pattern, and standard powder pattern for Cu_3BiS_3. The powder pattern indicates that phase-pure Cu_3BiS_3 has been synthesized. This morphology was obtained irrespective of H_2S partial pressure, heating rate, or processing temperature below 300 °C. Indistinguishable films could also be synthesized with heating times as short as 2 hours and with H_2S partial pressures as low as 1 torr. If temperatures greater that 300 °C were employed, it was again found that the product films were bismuth depleted.

$Cu_{1.8}S$ and Bi_2S_3 films were also synthesized via reactive annealing of Cu and Bi metal films under conditions similar to those employed for synthesis of ternary films. An SEM image of a $Cu_{1.8}S$ film (Cu precursor processed at 250 °C for 4 hours with a 10 °C/minute heating rate, and 5 torr H_2S/45 torr Ar atmosphere) along with an XRD powder pattern and $Cu_{1.8}S$ standard powder pattern (PDF 88-2158) is shown in Figure 3.16. The powder pattern collected from the film best matches the standard powder pattern for the rhombohedral $Cu_{1.8}S$ phase also identified in the powder pattern collected from the partially reacted ternary film (Figure 3.13 (b)). The morphological similarity between this film and the sub-optimum Cu_3BiS_3 film synthesized from a metal precursor (Figure 3.7) should also be noted. The size and distribution of the voids in each film are

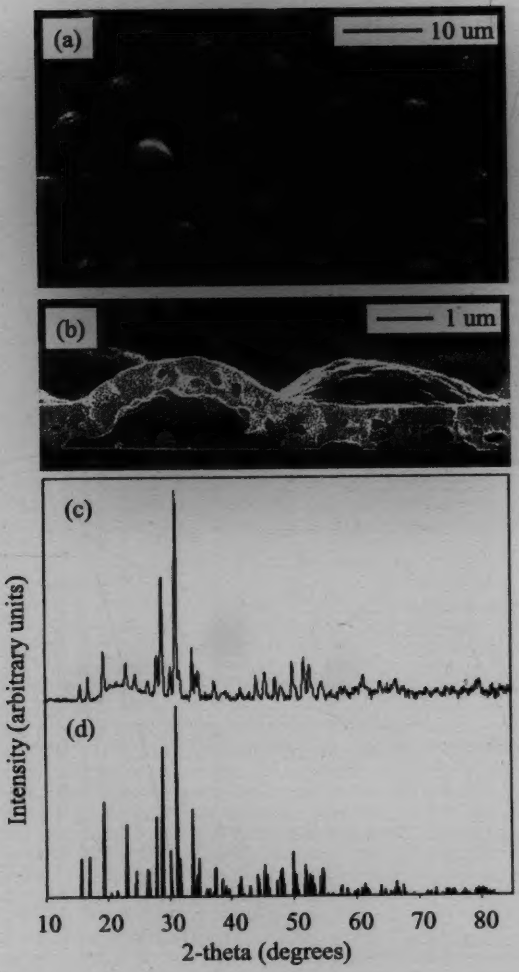

Figure 3.15. SEM images of a Cu_3BiS_3 film (a) and (b) synthesized by heating a metal sulfide precursor film at 270 °C for 12 hr under 5 torr H_2S/45 torr Ar, XRD powder pattern (c), and standard powder pattern for Cu_3BiS_3.

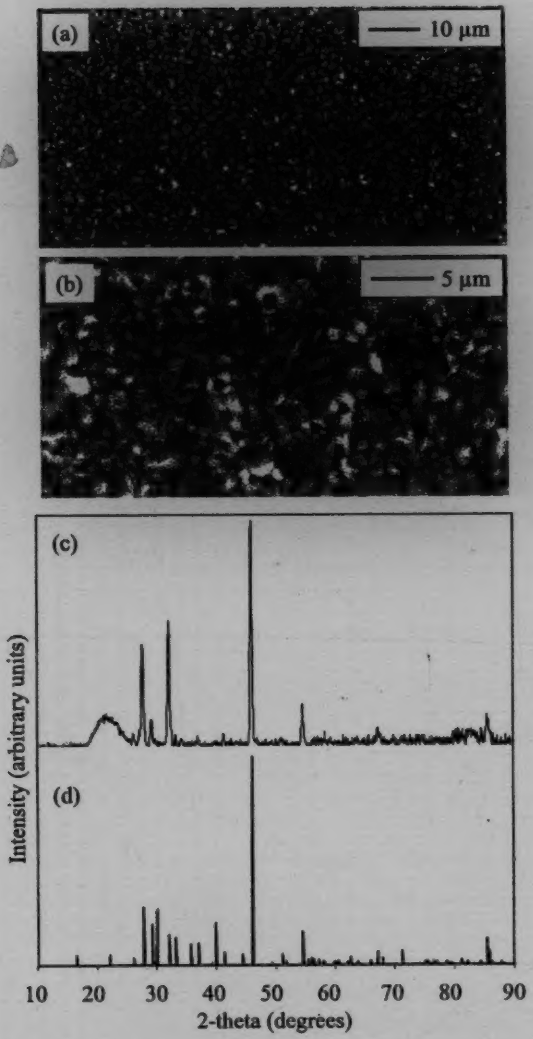

Figure 3.16. SEM image of a $Cu_{1.8}S$ film (a) and (b) synthesized by heating a Cu film at 250 °C for 4 hr under 5 torr H_2S/45 torr Ar, XRD powder pattern (c), and $Cu_{1.8}S$ standard powder pattern (d).

strikingly similar. The morphological similarity of the binary and ternary film, and the XRD data from the binary film and the partially reacted film, provide evidence for the assignment of $Cu_{1.8}S$ as the intermediate product in the synthesis of Cu_3BiS_3 from metal precursor films.

An SEM image of a Bi_2S_3 film (Bi film processed at 250 °C for 12 hours with a 10 °C/minute heating rate, and a 5 torr H_2S/45 torr Ar atmosphere) along with XRD powder pattern and Bi_2S_3 standard powder pattern (PDF 65-2435) is presented in Figure 3.17. The powder pattern confirms that Bi_2S_3 has been synthesized. In this case the morphological similarity to the Cu_3BiS_3 film synthesized from a metal sulfide precursor (Figure 3.15) should be noted. The size and distribution of the pockets under each film is comparable. This morphological similarity, in conjunction with XRD data from the metal sulfide precursor film (Figure 3.14) and WDX data from the Cu-S-Bi film (see above), provides evidence for the formation of Bi_2S_3 during the sputter deposition process, and subsequent reaction of this Bi_2S_3 intermediate with sputter-deposited Cu-S and H_2S to form Cu_3BiS_3 during annealing.

Sheet and electrical resistivity was measured on samples synthesized from both metal and metal sulfide precursors. On 1 μm thick Cu_3BiS_3 films synthesized from co-sputtered metal precursors, van der Pauw resistivity measurements gave a value of 3×10^4 Ω for the sheet resistivity or an electrical resistivity of 3 Ω·cm. On 800 nm thick films synthesized from metal sulfide precursors identical measurement methods gave a sheet resistivity of 2×10^6 Ω or an electrical resistivity of 2×10^2 Ω·cm. The discrepancy in these values is attributed to the variations in film structure, morphology, and synthesis method. Crystallite dimensions and differences in defect doping as a result of differing

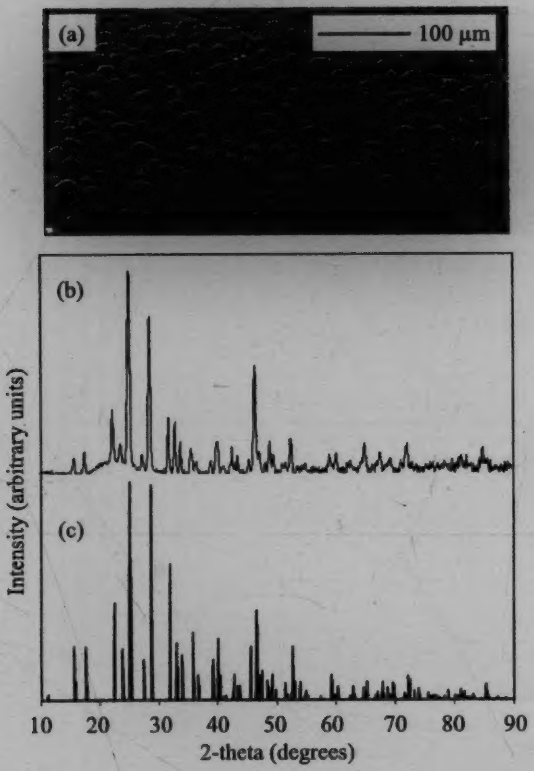

Figure 3.17. SEM image of a Bi_2S_3 film (a) formed by heating a Bi film at 250 °C for 12 hr under 5 torr H_2S/45 torr Ar, XRD powder pattern (b), and standard powder pattern for Bi_2S_3 (c).

syntheses are consistent with significant variations in electrical properties. It should be noted that, in this context, these values are in reasonable agreement with the previously reported value of $3\mathrm{x}10^1$ Ω·cm.[25]

Discussion

When Cu_3BiS_3 is synthesized from metal precursors, long reaction times are required, with SEM and XRD analysis of partially converted films showing the presence of $Cu_{1.8}S$, Bi, and Cu_3BiS_3 (Figure 3.13). Limited diffraction signal from the rhombohedral $Cu_{1.8}S$ phase makes this identification slightly ambiguous; however, this conclusion is supported by the fact that reaction of a Cu precursor film under similar conditions results in the synthesis of a phase that is identified as $Cu_{1.8}S$, and by the fact that the reaction temperatures employed are consistent with literature reports on the formation of this phase.[24] It is hypothesized that this $Cu_{1.8}S$ intermediate forms rapidly upon heating a Cu-Bi metal precursor in the presence of H_2S. The formation of binary sulfide intermediates has also been observed during the synthesis of $CuInS_2$ by heating Cu-In precursors in the presence of H_2S.[1] The formation of Cu_3BiS_3 results from the relatively slow diffusion and reaction of Bi with the $Cu_{1.8}S$ intermediate and H_2S, a pathway which is consistent with the observed growth of large crystallites. Due to sluggish reaction at temperatures low enough to minimize volatilization of bismuth ($T \leq$ 300 °C), complete reaction requires a long (16 hour) heating time.

The void space that is common to all Cu_3BiS_3 films synthesized by heating metal precursors in the presence of H_2S is a consequence of the rapid formation of the copper sulfide intermediate, which possesses a discontinuous morphology similar to that observed when $Cu_{1.8}S$ is synthesized from a copper precursor film. The formation of discontinuous copper sulfide films has also been observed during the synthesis of $CuInS_2$ thin films.[26] As Bi diffuses and reacts with the $Cu_{1.8}S$ intermediate, void spaces in the film are left behind. The influence of the copper sulfide intermediate on the morphology of the final film is supported by the similarity of Cu_3BiS_3 films and $Cu_{1.8}S$ films synthesized under similar conditions (Figures 3.7 and 3.16).

This reaction pathway is also consistent with the observed effects of precursor structure (multi-layer or co-sputtered), heating rates, and H_2S partial pressures. Lower H_2S partial pressures are expected to decrease the rate of formation of the $Cu_{1.8}S$ intermediate. Co-sputtered precursors and faster heating rates are expected to lead to increased nucleation of the ternary Cu_3BiS_3 phase. The rate of formation of the ternary phase can not be further increased by increasing reaction temperature, as a consequence of the volatility of bismuth. A decreased rate of formation of $Cu_{1.8}S$ (lower H_2S partial pressures), and rapid nucleation of the ternary phase (increased heating rates and co-sputtered precursors) should lead to smoother, more continuous films with decreased void space. This expectation is supported by the experimental results, with the best morphology obtained using co-sputtered precursors, faster heating rates, and lower H_2S partial pressures. Qualitatively it was found that increasing the heating rate above 10 °C/minute resulted in no appreciable improvement in film quality, while reducing H_2S partial pressures below 5 torr yielded incomplete conversion of the precursor.

Studies on the selenization of Cu-In multilayer precursors under H_2Se/Ar to form $CuInSe_2$ have also found that heating conditions have an impact on the product film morphology.[16] Alberts and Swanepoel found that when Cu-In samples were heated to

400 °C and then exposed to H_2Se at 400 °C (without a temperature ramp under H_2Se) the morphology of the final film was very rough and showed some segregation of $CuInSe_2$ and a secondary Cu_2Se phase. They attribute this to solid-liquid phase segregation resulting from the low melting point of indium (157 °C). When a ramp rate of 16 °C from an initial temperature of 150 °C under H_2Se was employed, they found that this phase segregation was avoided and film morphology improved significantly. They also report that precursor morphology directly influences product morphology.[16] This is consistent with the observation in this work that the smoother co-sputtered precursors produced product films with smoother morphology than those produced using the rougher multi-layer films; however, this is thought to play a minor role in the results of this work. Ultimately, the accessible range of processing conditions for the synthesis of Cu_3BiS_3 thin films from Cu-Bi precursors, limited by the volatility of Bi above 300 °C, is not sufficient to overcome the morphology-directing influence of the pathway described above. Consequently, smooth, continuous Cu_3BiS_3 films are not obtainable from metal precursor films, within the accessible parameter space of this study.

The synthesis of Cu_3BiS_3 from metal sulfide precursors proceeds via a different reaction pathway from that identified for synthesis from metal precursors. XRD analysis of metal sulfide precursor films identified the presence of some crystalline CuS and Bi_2S_3 in the multi-layer structure, in addition to elemental sulfur and significant amorphous content. The formation of these binary sulfides during the sputter deposition process, prior to heating, dictates the reaction intermediates and pathway. The complete conversion of the binary sulfide intermediates formed during deposition to Cu_3BiS_3 during heating occurs in a fraction of the time required for complete conversion of metal precursors. This is likely a result of the specific binary sulfide intermediates present (CuS and Bi_2S_3 vs. $Cu_{1.8}S$), but may also be due to the presence of S in the precursor film, which is expected to be more reactive than H_2S. (The Gibbs standard free energy for the reaction of Cu(s) and H_2S(g) to form CuS(s) and H_2(g) is -20.2 kJ/mol, while the value for the reaction of Cu(s) and $1/2S_2$(g) to form CuS(s) is -93.4 kJ/mol.) At 400 °C the Gibbs free energy for the decomposition reaction of H_2S(g) to H_2(g) and $1/2S_2$(g) is 56.9 kJ/mol; consequently, at the maximum reaction temperatures used in this work, 1 torr H_2S yields 7.12×10^{-4} torr S_2(g), demonstrating that a tiny amount of elemental sulfur is available during the processing of metal precursor films relative to metal sulfide precursor films. The short reaction time required (2 hours) is also similar to that reported previously for the reaction of chemical bath deposited Bi_2S_3 and CuS films to form Cu_3BiS_3.[27,28]

The morphological similarity of Cu_3BiS_3 films synthesized from metal sulfide precursors to Bi_2S_3 films (Figures 3.15 and 3.17), suggests that the Bi_2S_3 intermediate dictates the morphology of the Cu_3BiS_3 film. The fact that this morphology can not be controlled, or even influenced, by varying reaction conditions lends additional support to the hypothesis that the Bi_2S_3 forms during the deposition process, and to the conclusion that the final morphology of the Cu_3BiS_3 film is a function of the precursor, not the subsequent processing. It is concluded that the morphology of the Bi_2S_3 film is a consequence of the incorporation of sulfur into the metal precursor during the reaction with H_2S. This produces significant volume expansion of the film, which is relieved by buckling of the film, producing pockets between the film and substrate. This reasoning also applies to the morphology of Cu_3BiS_3 films synthesized via Bi_2S_3 and CuS intermediates. WDX results suggest that the as-deposited precursor is sulfur deficient. XRD shows that some crystalline Bi_2S_3 and CuS are present, but that the precursor film also has a significant amorphous component. Upon heating, the reaction of these intermediates, combined with uptake of additional sulfur, results in volume expansion of the film. In an analogous manner to the Bi_2S_3 thin film, this expansion produces buckling of the Cu_3BiS_3 thin film, and the formation of pockets between the film and substrate.

It has been demonstrated for the selenization of CuInGaSe precursors that increasing the Se content in the precursor from 5 to 30 atom percent reduces phase segregation and enhances grain growth in the resultant $Cu(In,Ga)Se_2$ films, yielding improved film morpholgy.[29] Kushiya et al. also identify reduced volume expansion during the selenization process when the Se content in the precursor is increased. Similar improvements in the morphology of $CuInS_2$ films heated under H_2S have been observed with increased sulfur content in the precursor film, with the improvement attributed to reduced phase segregation during processing.[30] When the results in this work for metal and metal sulfide precursors are compared, it appears that phase segregation during the synthesis of Cu_3BiS_3 is eliminated when sulfur is incorporated into the precursor film. This is attributed to the sluggish reactivity of elemental Bi, versus the much more facile reactivity of Bi_2S_3, with the copper sulfide intermediates.

While detailed electrical and optical characterization of these films could not be carried out as a consequence of the sub-optimum morphology obtained in all cases, it is worth noting that electrical resistivities agree reasonably well with previously reported values. In previous reports of the thin film synthesis of Cu_3BiS_3 by Nair and co-workers,[25,28] SEM images of the films are not presented and no specific discussion of film morphology is provided. Consequently the morphology of films in this work can not be compared with those reported previously. Based on optical data presented by Nair and co-workers, it may be inferred that smoother films were obtained when Cu_3BiS_3 was synthesized from the reaction of Bi and CuS,[25] rather than from the reaction of Bi_2S_3 and CuS.[28]

While synthesis of phase-pure Cu_3BiS_3 films by heating of metal and metal sulfide precursors in the presence of H_2S has been demonstrated, in both cases the morphology of the films was not suitable for use in thin film photovoltaics. Based upon the results of this study, it is clear that while processing conditions may have an impact, the dominant factor in determining film morphology in both cases is the reaction pathway, which is directly dependent on the precursor employed. As a consequence, under the scope of the current study, it is concluded that this two-step process is not applicable to the synthesis of smooth and continuous films of Cu_3BiS_3. However, if Cu_3BiS_3 is found to show potential as a solar absorber material in thin film PV devices, these results do not preclude the use of this method for the synthesis of smooth continuous Cu_3BiS_3 films employing alternate precursors, processing conditions, or conductive substrates such as metal foils or transparent conducting oxide coated glass. This method has also been applied to synthesis of $Cu_{12}Sb_4S_{13}$ thin films, with preliminary results presented in Appendix A.

Conclusions

A physical vapor deposition technique for the synthesis of Cu_3BiS_3 has been developed, employing the heating of metal or metal sulfide precursor films under $H_2S(g)$.

The morphology of the final film is controlled by the binary sulfide intermediates which are dependent on precursor composition. Synthesis from metal precursors proceeds via formation and reaction of a discontinuous $Cu_{1.8}S$ intermediate with elemental Bi and H_2S. These films are characterized by large crystallites and voids in the film. Synthesis from metal sulfide precursors proceeds via the reaction of Bi_2S_3 and CuS intermediates formed during film deposition. These films are continuous with smaller individual crystallites; however, reaction results in volume expansion and buckling that produces pockets between the film and substrate. While all films were phase-pure, they are not smooth and continuous—a requirement for application in thin film photovoltaic devices. Processing conditions have been thoroughly explored and it is not possible to overcome the controlling influence of the precursor composition and reaction pathway on film morphology. Consequently, while reactive annealing of Cu-In precursors under H_2S has been successfully employed for the synthesis of smooth, continuous thin films of $CuInS_2$, this work has shown that this method is not suitable for the production of Cu_3BiS_3 films of similar morphology on non-conductive transparent substrates. However, based on these results a one-step reactive deposition for Cu_3BiS_3 has been developed that produces device quality films, with details provided in Chapter 4.

References

(1) Dzionk, C.; Metzner, H.; Hessler, S.; Mahnke, H.-E. *Thin Solid Films* **1997**, *299*, 38-44.

(2) Gossla, M.; Mahnke, H.-E.; Metzner, H. *Thin Solid Films* **2000**, *361-362*, 56-60.

(3) Antony, A.; Asha, A. S.; Yoosuf, R.; Manoj, R.; Jayaraj, M. K. *Sol. Energy Mater. Sol. Cells* **2004**, *81*, 407-417.

(4) Binsma, J. J. M.; Van der Linden, H. A. *Thin Solid Films* **1982**, *97*, 237-243.

(5) Watanabe, T.; Nakazawa, H.; Matsui, M. *Jpn. J. Appl. Phys., Part 2* **1999**, *38*, L430-L432.

(6) Lokhande, C. D.; Hodes, G. *Sol. Cells* **1987**, *21*, 215-224.

(7) Yüksel, Ö. F.; Basol, B. M.; Safak, H.; Karabiyik, H. *Appl. Phys. A* **2001**, *73*, 387-389.

(8) Alberts, V. *Jpn. J. Appl. Phys., Part 1* **2002**, *41*, 518-523.

(9) Bekker, J.; Alberts, V.; Leitch, A. W. R.; Botha, J. R. *Thin Solid Films* **2003**, *431-432*, 116-121.

(10) Singh, U. P.; Shafarman, W. N.; Birkmire, R. W. *Sol. Energy Mater. Sol. Cells* **2006**, *90*, 623-630.

(11) Laubis, C.; Henrion, W.; Beier, J.; Dittrich, H.; Lux-Steiner, M. In *Inst. Phys. Conf. Ser. No. 152: Section B: Thin Film Growth and Characterization*, 1998, pp 289-292.

(12) Botero, M.; Cifuentes, C.; Romero, E.; Clavijo, J.; Gordillo, G. In *Proceedings of the IEEE 4th World Conference on Photovoltaic Energy Conversion*, 2006, pp 79-82.

(13) Reddy, K. T. R.; Reddy, P. P.; Dutta, P. K.; Miles, R. W. *Thin Solid Films* **2002**, *403-404*, 116-119.

(14) Yoosuf, R.; Jayaraj, M. K. *Sol. Energy Mater. Sol. Cells* **2005**, *89*, 85-94.

(15) Pimenta, G.; Kautek, W. *Thin Solid Films* **1994**, *238*, 213-217.

(16) Alberts, V.; Swanepoel, R. *J. Mater. Sci.: Mater. Electron.* **1996**, *7*, 91-99.

(17) Schroder, D. K. In *Semiconductor Material and Device Characterization*; 2nd ed.; John Wiley and Sons, Inc.: New York, 1998, pp 2-17.

(18) Wang, N. *Mineral. Mag.* **1994**, *58*, 201-204.

(19) Buhlmann, E. *N. Jb. Miner. Monat.* **1971**, 137-141.

(20) Chen, T. T.; Chang, L. L. Y. *Can. Mineral.* **1974**, *12*, 404-410.

(21) Baker, H., Ed. *ASM Handbooks Online, Vol. 3 Alloy Phase Diagrams*; ASM International, 2002.

(22) Green, D. W., Ed. *Perry's Chemical Engineers' Handbook*; 7th ed.; McGraw-Hill: New York, 1997.

(23) Gronvold, F.; Stolen, S.; Westrum., E. F.; Galeas, C. G. *J. Chem. Thermodynamics* **1987**, *19*, 1305-1324.

(24) Blachnik, R.; Müller, A. *Thermochim. Acta* **2000**, *361*, 31-52.

(25) Estrella, V.; Nair, M. T. S.; Nair, P. K. *Semicond. Sci. Technol.* **2003**, *18*, 190-194.

(26) Scheer, R.; Klenk, R.; Klaer, J.; Luck, I. *Sol. Energy* **2004**, *77*, 777-784.

(27) Hu, H.; Gomez-Daza, O.; Nair, P. K. *J. Mater. Res.* **1998**, *13*, 2453-2456.

(28) Nair, P. K.; Huang, L.; Nair, M. T. S.; Hu, H.; Meyers, E. A.; Zingaro, R. A. *J. Mater. Res.* **1997**, *12*, 651-656.

(29) Kushiya, K.; Shimizu, A.; Yamada, A.; Konagai, M. *Jpn. J. Appl. Phys., Part 1* **1995**, *34*, 54-60.

(30) Watanabe, T.; Matsui, M. *Jpn. J. Appl. Phys., Part 1* **1996**, *35*, 1681-1684.

Chapter 4. One-Step Synthesis and Optical and Electrical Properties of Thin Film Cu_3BiS_3 for Use as a Solar Absorber in Photovoltaic Devices

Introduction

In Chapter 3 a two-step method for the synthesis of Cu_3BiS_3 thin films was presented; however, even when optimized conditions were employed the morphology of the resultant films was not suitable for use in PV devices. Based on those results, a one-step reactive deposition process was developed, enabling the direct deposition of Cu_3BiS_3 thin films onto heated fused silica substrates. Deposition directly onto hot substrates under inert or reactive conditions has been utilized successfully for the synthesis of a wide variety of crystalline thin films including $CuInS_2$,[1] Cu_2S,[2] SnS,[3] In_2O_3,[4-6] CuO,[7] and $Zn_{1-x}Mg_xO$.[8]

The one-step reactive deposition developed for Cu_3BiS_3 yields thin films that are continuous, dense, and have a smooth, mirror-like surface—the morphology appropriate for photovoltaic device applications. These as-deposited films are also crystalline, phase-pure, and have the requisite optical and electrical properties for photovoltaic applications. Post-deposition annealing in an H_2S atmosphere increases crystallite size and decreases the resistivity of the film. In Chapter 5, results from the deposition of Cu_3BiS_3 thin films on TCO coated substrates by this one-step method, as well as an evaluation of the compatibility of this deposition method with the fabrication of the multi-layer structures required for device development, are reported. In this chapter details on the one-step synthesis, structure, morphology, and optical and electrical properties of Cu_3BiS_3 thin films on fused silica substrates, as well as the effect of post-deposition processing in an H_2S atmosphere are reported.

Experimental Details

Films were sputter deposited directly on fused silica substrates (50 mm x 50 mm). Substrates were cleaned in 2-propanol in an ultrasonic bath for 30 minutes, immersed for 30 minutes in a 1:3 mixture of H_2O_2:H_2SO_4, rinsed with distilled H_2O, rinsed with 2-propanol, and dried under N_2. During the deposition, substrates were maintained at temperatures of 250 to 300 °C. This temperature range was identified as optimal for synthesis of Cu_3BiS_3 thin films in Chapter 3. Substrates were heated by quartz lamps, and the temperature monitored by a thermocouple in contact with the substrate platen. During the deposition, the platen was continuously rotated at 6 rpm. Films were deposited by sputter deposition from a CuS target at 80 W RF and a Bi target at 10 W DC. Targets were 3" in diameter and the sputtering gas was Ar at a pressure of 5 mtorr. Stoichiometry of single composition, multi-element films deposited on unheated substrates was determined by WDX. Cu-S films were found to be sulfur deficient relative to the target, with a composition of 2.8:1.0 Cu:S. When the CuS target was co-sputtered with the Bi target, Cu-S-Bi films were sulfur rich relative to the target, with a composition of 1.0:3.2:1.9 Cu:S:Bi.

To deposit compound films on hot substrates with the desired 3:1:3 stoichiometry the CuS target was sputtered continuously and the Bi target cycled on and off. The correct elemental ratio was achieved by co-sputtering CuS and Bi targets for 5 minutes, followed by CuS target sputtering for 25-30 minutes, depending on substrate temperature.

Hotter substrates required shorter CuS-only sputter times to compensate for the increased sublimation of Bi. Each cycle produced approximately 75 nm of deposition, and was repeated 4 or 8 times resulting in films with final thicknesses of approximately 300 nm or 600 nm, respectively. Following deposition, the substrate temperature was maintained at the deposition temperature (250 to 300 °C) for 30 minutes, followed by cooling to 100 °C at 2 °C/minute. Some films were subsequently annealed at 250 to 300 °C for 2 hours under 1 torr H_2S/49 torr Ar, followed by cooling to 100 °C at 2 °C/minute. The volume of the annealing chamber is approximately 40 l, with heating provided by a programmable resistance heater.

Composition and morphology of the thin films was characterized using SEM/EDX (JEOL 6031F FESEM, Hitachi S-4800 FESEM, Hitachi S3000N VPSEM), WDX (JEOL 8900 microprobe), and XRD (Bruker D8 diffractometer with area detector). Additional characterization was carried out to measure the optical and electrical properties of the thin films. Transmission and reflection data (Bruker Vertex 70) was used to determine the optical band gap, band gap type, and optical absorption coefficient. For transmission measurements a clean fused silica substrate was used as the 100% transmission standard. Reflection measurements were made at 10° from normal, and an aluminum mirror deposited on a fused silica substrate was used as the 100% reflection standard. Prior to collection of reflection data the back side of each sample was roughened with a rotary grinder to eliminate backside reflection. Sheet and electrical resistivities were measured using a 4-point probe (Jandel 4-point probe with 0.5 mm probe spacing, Keithly 2400 Sourcemeter). Measurements were taken with a constant current set at 0.01-0.05 μA to produce a voltage drop in the range of 2-4 mV. These conditions minimized carrier injection and produced stable and consistent measurements. Doping type was determined using hot probe measurements with a hot probe temperature of 50-60 °C (in-house manufactured probe, Fluke DMM).

Results

Films of high quality were synthesized directly on fused silica substrates at temperatures of 250 to 300 °C; however, the morphology of the films varied over this temperature range, and changes in deposition parameters were required to compensate for the increased Bi vapor pressure at higher temperatures. In Chapter 3 the maximum temperature suitable for processing Cu_3BiS_3 films was identified as 300 °C, with film decomposition and Bi sublimation occurring at higher temperatures. In the present work, increasing the substrate temperature from 250 to 300 °C is accompanied by an increase in Bi sublimation. To compensate for this, it was necessary to decrease the CuS-only sputter time from 30 minutes to 25 minutes with a constant co-sputtered period of 5 minutes. Consistent with previous work, 300 °C is the maximum temperature at which this reactive deposition can be carried out successfully.

Changes in morphology as a function of substrate temperature were most evident when films were observed at a fracture. Films deposited at 300 °C were homogeneous throughout the depth of the film, while those deposited at 250 °C retained the layered structure of the deposition. SEM images of a film deposited at 300 °C are presented in Figure 4.1 (a) and (b). The film is smooth and continuous when viewed from the surface, and is dense and homogeneous when viewed edge-on at a fracture. SEM images in Figure 4.2 (a) and (b) for a Cu_3BiS_3 film deposited at 250 °C show the film is smooth and

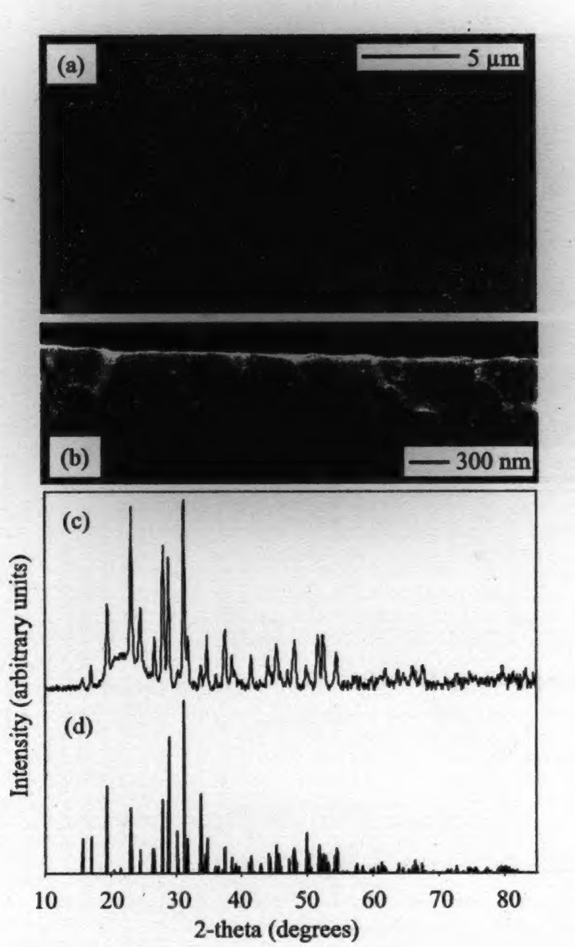

Figure 4.1. SEM images of a Cu_3BiS_3 film synthesized by reactive deposition with a substrate temperature of 300 °C (a) and (b), XRD powder pattern (c), and standard powder pattern for Cu_3BiS_3 (d).

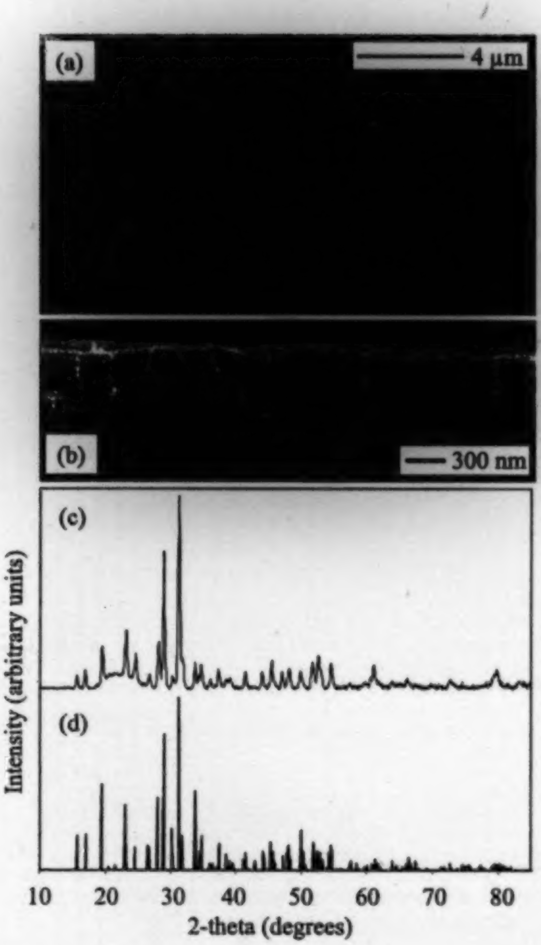

Figure 4.2. SEM images of a Cu_3BiS_3 film synthesized by reactive deposition with a substrate temperature of 250 °C (a) and (b), XRD powder pattern (c), and standard powder pattern for Cu_3BiS_3 (d).

continuous when viewed from the surface (Figure 4.2(a)). When viewed edge-on at a fracture, the film is observed to retain the layered structure of the deposition, with each of the 8 layers clearly visible (Figure 4.2(b)). For all films, backscattered SEM imaging was used to screen for secondary phases, with none detected, and the 3:1:3 Cu:Bi:S composition of the films was confirmed by EDX.

XRD powder patterns were used to identify the phase of all films. Films deposited at both 250 °C and 300 °C were identified as phase-pure and crystalline; however, differences in the intensity of the peaks were observed to correlate with deposition temperature. The powder pattern collected from a film deposited with a substrate temperature of 300 °C along with the standard powder pattern for Cu_3BiS_3 (PDF 43-1479) are shown in Figure 4.1 (c) and (d). The amorphous hump centered at 22° 2-theta is attributed to the fused silica substrate. Film texture is evident in the powder pattern, with enhanced intensity (relative to the standard powder pattern) of the (200) and (211) peaks at 2-theta 23.1° and 28.1°, respectively. The powder pattern collected from a film deposited with a substrate temperature of 250 °C and the standard powder pattern for Cu_3BiS_3 are presented in Figure 4.2 (c) and (d). As with the film deposited at higher temperature, the film is crystalline, with the amorphous hump at 22° 2-theta attributed to the fused silica substrate. However, at the lower deposition temperature of 250 °C the intensity profile of the experimental powder pattern is a good match with the standard powder pattern, indicating a random orientation of the crystallites.

Following reactive deposition, films were annealed under 1 torr H_2S/49 torr Ar for 2 hours at 250 to 300 °C to asses the effect on film properties. The most significant changes were observed when films deposited at 250 °C were annealed at 300 °C.

Annealing at lower temperatures resulted in similar changes, but the effects were less pronounced. SEM images and the XRD powder pattern of a film deposited at 250 °C (Figure 4.2) then annealed at 300 °C are presented in Figure 4.3. SEM images and the XRD powder pattern of a film deposited at 300 °C (Figure 4.1) then annealed at 300 °C are presented in Figure 4.4. It should be noted that while significant morphological differences were observed between the as-deposited films, the annealed films are very similar in appearance. Most noteworthy is the fact that the layered structure of the film deposited at 250 °C is eliminated. The only morphological difference between the two films following annealing is the residual presence of very small voids (indicating lower density) in the film deposited at 250 °C relative to the film deposited at 300 °C. In both cases post-deposition annealing increased the crystallite size, producing individual crystallites in the 0.5–1 μm range. These larger crystallites are columnar in shape and generally extend through the entire thickness of the film. Crystal growth was accompanied by a slight increase in the roughness of the film; however, annealed films retained the mirror-like surface of the as-deposited films. XRD powder pattern data collected from the annealed films show that the random orientation of films deposited at 250 °C is retained in the annealed film, with no indication of texture. Similarly, films deposited at 300 °C retained the preferred orientation along the [200]/[211] directions following annealing.

Transmission and reflection data collected from a 300 nm thick, as-deposited film is presented in Figure 4.5 (a). Similar data was collected from both as-deposited and annealed films with a thickness of 600 nm. No changes in optical properties were observed, demonstrating that there is no dependence of band gap on film thickness. This

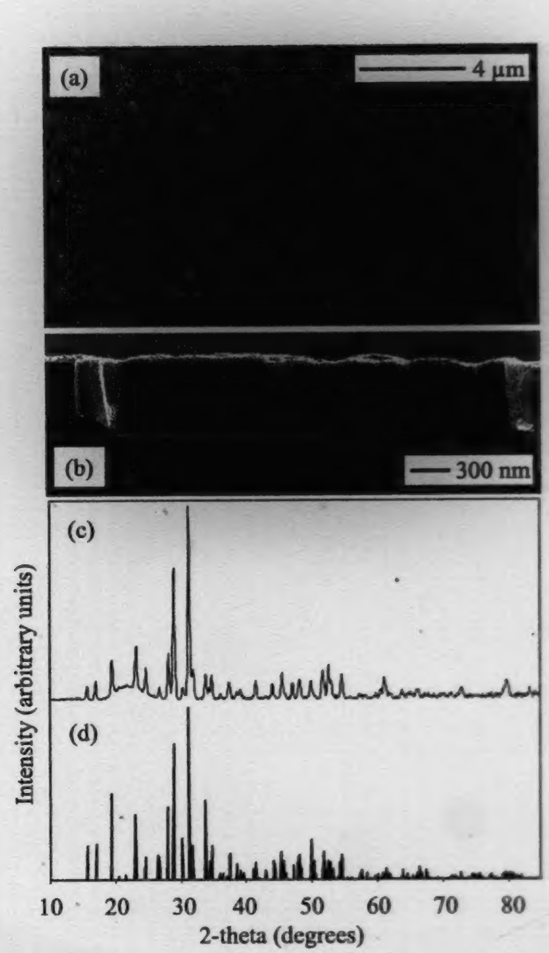

Figure 4.3. SEM images of a Cu_3BiS_3 film synthesized by reactive deposition with a substrate temperature of 250 °C (see Figure 4.2), followed by annealing at 300 °C under 1 torr H_2S/49 torr Ar for 2 hr (a) and (b), XRD powder pattern of the annealed film (c), and standard powder pattern for Cu_3BiS_3 (d).

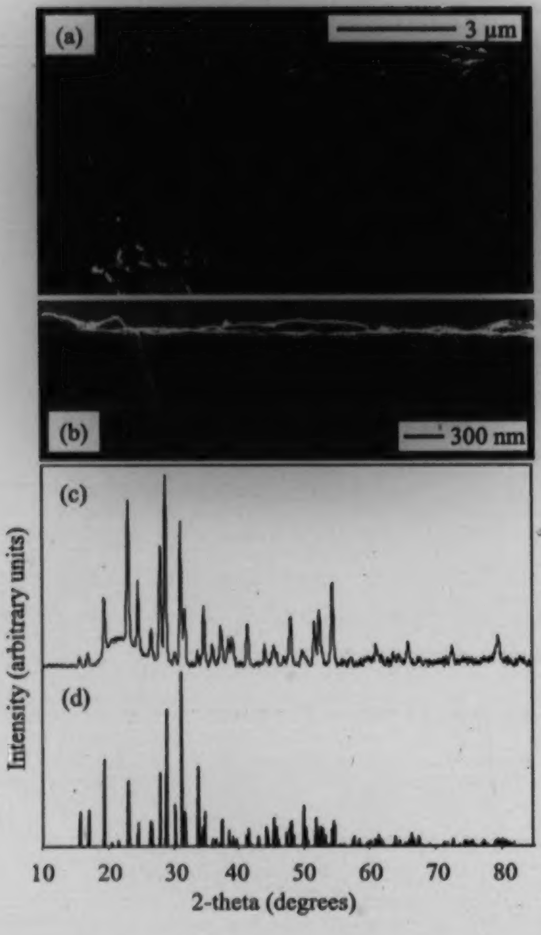

Figure 4.4. SEM images of a Cu_3BiS_3 film synthesized by reactive deposition with a substrate temperature of 300 °C (see Figure 4.1), followed by annealing at 300 °C under 1 torr H_2S/49 torr Ar for 2 hr (a) and (b), XRD powder pattern of the annealed film (c), and standard powder pattern for Cu_3BiS_3 (d).

data was used to determine the energy-dependent optical absorption coefficient, and the nature and magnitude of the optical band gap. The optical absorption coefficient can be calculated from

$$\alpha = 1/x \ln[(1-R)^2/T],$$

where x is the film thickness and R and T are reflection and transmission values respectively.[9] Plotted in Figure 4.5 (b) is α as a function of energy, with $\alpha = 1\text{x}10^5$ cm^{-1} at 1.9 eV. The nature and magnitude of the optical band gap may be determined from the fact that $\alpha h\upsilon$ is proportional to $(h\upsilon - E_g)^n$. As a consequence, plots of $(\alpha h\upsilon)^{1/n}$ against $h\upsilon$, with 1/n = 2, 2/3, 1/2, 1/3, are linear for direct, direct forbidden, indirect, and indirect forbidden, respectively, with the x-intercept yielding the value of the band gap.[9] Plots of $(\alpha h\upsilon)^{1/n}$ against energy for all four values of 1/n are shown in Figure 4.6. The best linearity is observed with 1/n = 2/3 (Figure 4.6 (b)), identifying the band gap as direct forbidden, with the intercept of the line of best fit yielding the magnitude of the band gap as 1.4 eV. The plot for 1/n = 1/2 (Figure 4.6 (c)) is only slightly less linear, and would yield an indirect band-gap of a similar value; however, this can be rejected based on the strong optical absorption coefficient, which is inconsistent with an indirect band-gap material.

The sheet and electrical resistivity of the films was measured using a 4-point probe[10] on both as-deposited and annealed films with a thickness of 600 nm. It was found that the sheet resistivity decreased by an order of magnitude from $1.4\text{x}10^6$ Ω to $1.6\text{x}10^5$ Ω when as-deposited films were annealed at 300 °C. The corresponding electrical resistivity values for these films are 84 Ω·cm and 9.6 Ω·cm, respectively. There was no significant variation in resistivity with deposition temperature. However, a slight

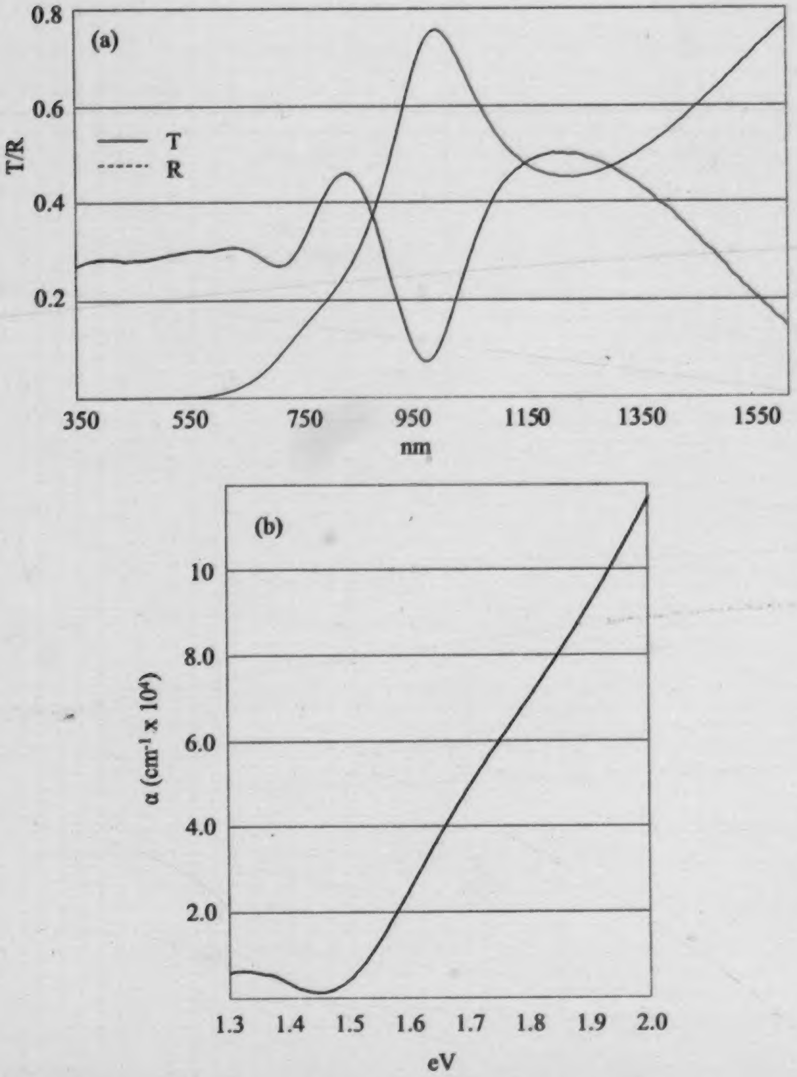

Figure 4.5. Transmission (solid line) and reflection (dashed line) data against wavelength collected from a 300 nm thick Cu_3BiS_3 film (a), and used to calculate α as a function of energy (b).

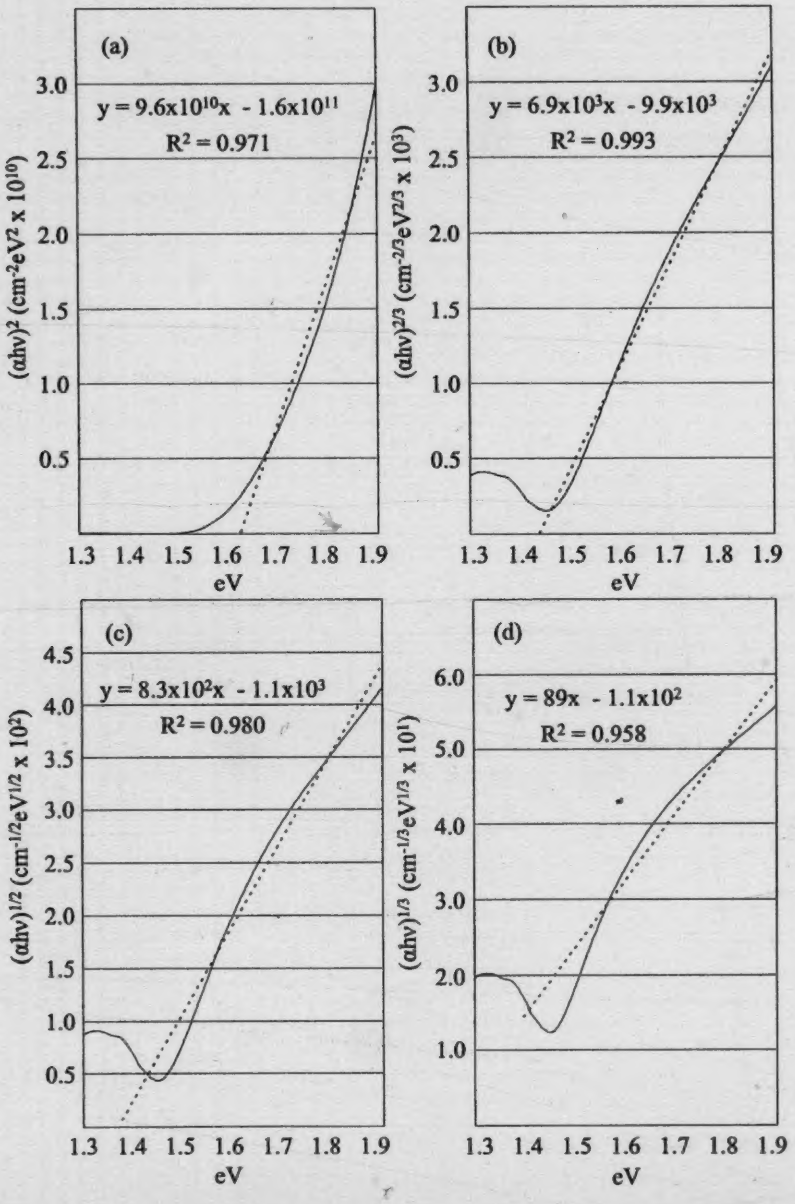

Figure 4.6. Plots of $(\alpha h\nu)^{1/n}$ against energy with $1/n = 2$, $2/3$, $1/2$, $1/3$ in (a), (b), (c), and (d), respectively, for a 300 nm thick Cu_3BiS_3 thin film deposited on fused silica. Best linearity is observed when $1/n = 2/3$, with dashed line of best fit showing an x-intecept of 1.4 eV (direct forbidden optical band gap) (b). Linear lines of best fit determined over 1.6-1.9 eV (a), and 1.5-1.9 eV (b), (c), (d).

increase in resistivity was observed in films aged in air for several weeks, presumably due to surface oxidation. Any oxidation that occurred was not detectable by XRD, and more detailed surface characterization capable of detecting low levels of oxidation was not carried out. Hot probe measurements were used to determine majority carrier type,[10] with all films clearly indicating p-type conductivity regardless of deposition temperature or post-deposition processing.

Discussion

For thin film photovoltaics to play a significant role in global energy production new materials will be required whose deployment is not limited by raw material availability. The development of successful devices incorporating new materials is likely to involve not only identifying new absorber materials, but other mutually compatible layers as well. This is a significant challenge, and a critical first step is the development of simple, efficient syntheses for individual components. This chapter reports a successful one-step deposition for high-quality Cu_3BiS_3 thin films, with measured optical and electrical properties that support its potential for application as an absorber layer in thin film PV devices.

In Chapter 3, a two-step synthesis of phase-pure Cu_3BiS_3 thin films by heating metal and metal sulfide precursor films in an H_2S atmosphere was identified; however, for both precursor types the reaction pathway was found to have a controlling influence on film morphology. In the case of metal precursor films, the formation of a discontinuous $Cu_{1.8}S$ intermediate followed by slow reaction with Bi translated into holes in the final film. In the case of metal sulfide precursors, volume expansion during the reaction of intermediate phases formed during sputter deposition resulted in buckling of the product film.

In the one-step synthesis, the reactive deposition is critical to avoiding the fundamental limitations of the two-step process for the synthesis of Cu_3BiS_3 thin films on fused silica substrates. The growth of Cu_3BiS_3 films by the one-step method is thought to proceed as follows. During the initial, co-sputtered period, Cu_3BiS_3 is deposited along with excess Bi. Previous results from depositions on unheated substrates (Chapter 3) show that the Bi reacts with Cu-S during co-sputtering, producing Bi_2S_3. Therefore, excess Bi is expected to be primarily present as Bi_2S_3. During the second phase of each deposition cycle only Cu-S is sputtered, which reacts with the excess Bi or Bi_2S_3 in the film, adding to the initially formed crystalline Cu_3BiS_3. This layered crystalline growth is supported by the observation of such a structure in the cross-section of films deposited at lower temperatures (Figure 4.2 (b)). The layer contrast in this image is a result of differences in crystallite sizes, with larger crystallites produced at the surface of each layer. These larger crystallites are consistent with a diffusive growth mechanism occurring within each layer. As the deposition cycle proceeds, Bi rich components diffuse to the increasingly Cu-S rich surface, where the two react, forming larger crystallites. At the end of the cycle, the layer is stoichiometric, the two crystallite sizes persist, and the process is repeated with the next layer. When higher deposition temperatures, or a subsequent annealing, are employed, thermally activated crystal growth throughout the film obscures the selective, diffusive crystal growth observed at lower temperatures.

The success of this one-step deposition is also consistent with previous results from the reactive annealing of metal sulfide precursor films. In both methods similar deposition techniques are employed; however, in the two-step process buckling occurs during conversion of the precursor film to the product film, which was attributed to the reaction of intermediate phases and additional sulfur uptake. The one-step reactive deposition method enables these pitfalls to be avoided by the direct layer-by-layer build-up of the Cu_3BiS_3 film without a sulfur deficiency.

This one-step deposition is attractive not only for its simplicity, but also for the control it provides over the final film structure. Films formed at lower deposition temperatures contain small crystallites with a random orientation. Films deposited at higher temperatures have larger crystallites that exhibit a preferred orientation in the [200]/[211] directions. In each case the crystallinity of the films may be improved by a post-deposition annealing that results in the formation of larger crystallites that span the thickness of the film, and are orientated perpendicular to the substrate. Significantly, the random or preferred orientation of the crystallites in the as-deposited films is preserved during this post-deposition processing step—a subtlety that could prove useful for optimizing device performance if Cu_3BiS_3 films are successfully incorporated into thin film PV devices. Similar control over film texture has been achieved with CIGS thin films, with films having random orientation or preferred orientation in [112] or [220]/[204] directions all being employed in PV devices.[11] The orientation of the crystallites perpendicular to the substrate is also ideal for use in PV devices, since this is the direction of charge transport, and this particular orientation would be expected to facilitate carrier movement through the bulk of the crystallites or along grain boundaries.

The electrical properties of the Cu_3BiS_3 thin films synthesized in this manner are also suitable for incorporation into conventional thin film devices, since both as-deposited and annealed films show p-type conductivity—a requirement for use with conventional n-type transparent conducting oxides and buffer layers. The electrical resistivity of as-deposited films is 84 Ω·cm, and following annealing this drops to 9.6 Ω·cm. This is comparable to the previously reported value of 30 Ω·cm.[12] The direct forbidden optical band gap of 1.4 eV is also close to the optimum for single junction PV applications, and while the direct forbidden band gap results in a slower rise of the optical absorption coefficient, it reaches a value of 1.0×10^5 cm^{-1} at 1.9 eV. These values are virtually identical with the previously reported direct forbidden optical band gap of 1.3 eV, and optical absorption coefficient of 10^5 cm^{-1} at 1.9 eV.[12] The similarity of these optical and electrical measurements to those previously reported by Nair and co-workers suggest that Cu_3BiS_3 is amenable to a variety of synthetic strategies. This synthetic flexibility could prove useful by enabling a variety of approaches to the integration of Cu_3BiS_3 into PV devices.

The high quality of the as-deposited films produced by this one-step deposition method, the improvements in film quality resulting from post-deposition annealing, and the measured optical and electrical properties all support the integration of Cu_3BiS_3 thin films into PV devices. To better asses the suitability of these films for use as a solar absorber layer more detailed characterization should be carried out to determine a wider range of material properties including carrier lifetime, concentration, and mobility, as well as the effect of processing parameters on these properties. A key first step in device development has been achieved by the successful application of this one-step reactive deposition method to the synthesis of Cu_3BiS_3 thin films on TCO coated substrates, as reported in Chapter 5. The one-step method reactive deposition method has also been applied to the synthesis of $Cu_{12}Sb_4S_{13}$ thin films, with preliminary results presented in Appendix B.

Conclusions

A one-step reactive deposition for the synthesis of Cu_3BiS_3 thin films has been developed. This process is appealing because of its simplicity, as well as its compatibility with PVD techniques that are widely employed in the production of thin film devices. As-deposited Cu_3BiS_3 films are crystalline, smooth, continuous, and phase-pure. The crystallite size of these films may be increased, and resistivity decreased by a subsequent annealing process, while maintaining the smooth, continuous aspects of the as-deposited films. The morphology of the films is ideal for incorporation into thin film photovoltaic devices. Optical and electrical properties of the films, including a direct forbidden band gap of 1.4 eV, an optical absorption coefficient of $1x10^5$ cm^{-1} at 1.9 eV, electrical resistivities in the range of 84 Ω·cm to 9.6 Ω·cm, and p-type conductivity, also support potential application as a solar absorber in photovoltaic devices.

References

(1) Ellmer, K.; Hinze, J.; Klaer, J. *Thin Solid Films* **2002**, *413*, 92-97.

(2) He, Y.; Kriegseis, W.; Bläsing, J.; Polity, A.; Krämer, T.; Hasselkamp, D.; Meyer, B.; Hardt, M.; Krost, A. *Jpn. J. Appl. Phys., Part 1* **2002**, *41*, 4630-4634.

(3) Reddy, N. K.; Ramesh, K.; Ganesan, R.; Reddy, K. T. R.; Gunasekhar, K. R.; Gopal, E. S. R. *Appl. Phys. A* **2006**, *83*, 133-138.

(4) Gopchandran, K. G.; Joseph, B.; Abraham, J. T.; Koshy, P.; Vaidyan, V. K. *Vac.* **1997**, *48*, 547-550.

(5) Casey, V.; Stephenson, M. I. *J. Phys. D: Appl. Phys.* **1990**, *23*, 1212-1215.

(6) Amaral, A.; Brogueira, P.; Nunes de Carvalho, C.; Lavareda, G. *Surf. Coat. Technol.* **2000**, *125*, 151-156.

(7) Ghosh, S.; Avasthi, D. K.; Shah, P.; Ganesan, V.; Gupta, A.; Sarangi, D.; Bhattacharya, R.; Assmann, W. *Vac.* **2000**, *57*, 377-385.

(8) Hwang, D.-K.; Jeong, M.-C.; Myoung, J.-M. *Appl. Surf. Sci.* **2004**, *225*, 217-222.

(9) Pankove, J. I. *Optical Processes in Semiconductors*; Prentice-Hall, Inc.: Englewood Cliffs, 1971.

(10) Schroder, D. K. In *Semiconductor Material and Device Characterization*; 2nd ed.; John Wiley and Sons, Inc.: New York, 1998, pp 2-17.

(11) Kemell, M.; Ritala, M.; Leskelä, M. *Crit. Rev. Solid State Mater. Sci.* **2005**, *30*, 1-31.

(12) Estrella, V.; Nair, M. T. S.; Nair, P. K. *Semicond. Sci. Technol.* **2003**, *18*, 190-194.

Chapter 5. One-Step Deposition of Cu_3BiS_3 on TCO and TCO/ZnSe Coated Substrates with Al, Ni, and Mo Back Contacts—Testing Method and Material Compatibilities

Introduction

In Chapter 4, details of a one-step reactive deposition for Cu_3BiS_3 thin films were presented. Films synthesized by this method had a morphology ideal for incorporation into thin film PV devices, and also had optical and electrical properties that met the basic requirements for use as a solar absorber layer. Current state-of-the-art thin film PV devices have benefited from basic science advances, and increased understanding of the behavior of complex polycrystalline materials systems is enabling rational device optimization. However, it is also the case that some aspects of these devices are not fully understood, and that many discoveries and advances, such as the beneficial effect of sodium, have been achieved by empirical and serendipitous routes. The functioning of any new polycrystalline thin film PV device, based on a novel light absorbing material, is likely to be equally complex; thus precluding development by predictive strategies. Consequently, integration of new materials into successful devices must be performed by empirical methods. If development of new thin film PV devices incorporating novel absorber materials proceeds by way of incremental improvements, mirroring the development of CIGS and CdTe devices, then it is likely that the pace of these improvements can be accelerated through the use of high-throughput combinatorial methods.

A brief introduction to combinatorial methods, and their application in thin film PV device development, was presented in Chapter 2. The production of the 64-spot libraries discussed in Chapter 2 is a significant challenge, with a single library employing Cu_3BiS_3 as the solar absorber requiring deposition of thirteen different thin films. Additional complexities arise from the need to have all sixty-four, 4.4 mm x 4.4 mm, individual devices on the library electrically isolated from one another. In previous work (Chapter 4), Cu_3BiS_3 thin films were deposited exclusively on fused silica substrates. Consequently, it was not known if the one-step reactive deposition would produce films of comparable morphology on TCO coated soda-lime and borosilicate glass substrates. It was also possible that additional complexities could arise when heterojunction couples and metal back contacts were incorporated into the multi-layer structures required for device fabrication.

Due to the complexity of library fabrication and uncertainty regarding the compatibility between deposition methods and materials required for fabrication of multi-layer devices, a series of experiments have been carried out as a preliminary step in the fabrication of 64-spot PV libraries. In brief, these experiments included the deposition of Cu_3BiS_3 thin films directly on ITO coated soda-lime glass and FTO coated borosilicate glass, and the deposition of Cu_3BiS_3 thin films on a ZnSe heterojunction couple deposited on ITO and FTO coated substrates. On each of these samples separate Al, Ni, and Mo metal back contacts were sputter deposited using a fractal mask. This series of experiments has allowed assessment of the compatibility of the one-step deposition method with TCO coated soda-lime and borosilicate glass substrates, the stability of ITO, FTO, and ZnSe during the reactive deposition process, and the stability and electrical isolation of sputter deposited metal back contacts.

Electrical contact to three-spot back contacts was achieved by two different methods, colloidal silver, and a pressure plate contact, enabling preliminary evaluation and comparison of these methods for contacting a 64-spot library. Multi-layer structures were also tested for PV performance. It was hoped that the fortuitous identification of a functional thin film PV device would result. While this did not prove to be the case, these preliminary experiments have paved the way for fabrication of more complex thin film PV libraries, employing Cu_3BiS_3 as the solar absorber layer. Results of these preliminary experiments are reported herein.

Experimental Details

Deposition of Cu_3BiS_3 Films. Cu_3BiS_3 thin films were deposited on 50 mm x 50 mm ITO coated soda-lime glass substrates (Precision Glass and Optics, 20 Ω/sq) or FTO coated borosilicate glass substrates (Solaronix, 10 Ω/sq). Substrates were cleaned in 2-propanol in an ultrasonic bath for 30 minutes, rinsed with 2-propanol, and dried with a stream of N_2. Cu_3BiS_3 films were deposited on the TCO coated substrates using the one-step reactive deposition method presented in Chapter 4. During deposition, substrates were maintained at a temperature of 250 °C, heated by quartz lamps, with the temperature monitored by a thermocouple in contact with the substrate platen. The platen was continuously rotated at 6 rpm. CuS was sputtered at 80 W RF, and Bi at 10 W DC. Targets were 3" in diameter, and were sputtered at an Ar pressure of 5 mtorr. The CuS target was sputtered continuously and the Bi target cycled on and off. The correct elemental ratio was achieved by co-sputtering CuS and Bi targets for 5 minutes, followed by sputtering only the CuS target for 27-29 minutes. Each cycle deposited ~75 nm of Cu_3BiS_3, and was repeated 16 times, resulting in films with final thicknesses of approximately 1.2 μm. At the completion of the deposition, the substrate temperature was maintained at 250 °C for 30 minutes, followed by cooling to 100 °C at 2 °C/minute.

Deposition of ZnSe Films and Buffer Layers. On some samples a 100 nm thick ZnSe buffer layer was deposited prior to deposition of the Cu_3BiS_3 absorber layer. ZnSe was RF sputtered from a 3" target at 80 W RF, with an Ar pressure of 5 mtorr. The substrate platen was rotated at 6 rpm. Deposition of a 100 nm thick film required 14 minutes of sputtering. No post-deposition treatments of the ZnSe films were carried out prior to deposition of Cu_3BiS_3. ZnSe films, 250 nm thick, were deposited under identical conditions (45 minute sputter time) on both ITO coated and uncoated soda-lime glass substrates. Following deposition, some of these 250 nm thick ZnSe films were heated to 250 °C for 45 min under the quartz lamps in the deposition chamber, at a pressure of 5 mtorr, with the substrate platen rotated at 6 rpm. These conditions were chosen to simulate the effect of substrate heating during the initial phase of Cu_3BiS_3 deposition.

Deposition of Metal Back Contacts. After deposition of Cu_3BiS_3 or ZnSe/Cu_3BiS_3 on a TCO coated substrate, metal back contacts were sputter deposited. Three different metals were employed, with each one deposited on ¼ of the active area (~15 mm x 15 mm). The deposition area was controlled by use of a quaternary shadow mask having a single opening, with the mask rotated by 90° relative to the substrate after each deposition. The three metals utilized were Al, Ni, and Mo. Al was sputtered at 150 W DC, Ni and Mo at 200 W DC. In all cases targets were 3" in diameter, the sputter gas was Ar at 5 mtorr, and the substrate platen rotation was 6 rpm. Deposition of layers with a thickness of ~500 nm required sputter times of 135 min, 45 min, and 70 min for Al, Ni, and Mo, respectively.

Characterization of Thin Films. The composition and morphology of deposited films were characterized using SEM/EDX (JEOL 6031F FESEM, Hitachi S3000N VPSEM) and XRD (Bruker D8 diffractometer with area detector). Scanning auger analysis of film cross-sections was performed on selected samples (JEOL JAMP 9500F). Optical properties of the TCO coated substrates and ZnSe films were measured on a UV/Vis spectrophotometer (Perkin Elmer Lambda 35). Transmission data was collected from TCO coated substrates to quantify absorption; transmission and reflection data were collected from ZnSe films on soda-lime glass substrates to verify the optical band gap, band gap type, and optical absorption coefficient. For transmission measurements on TCO coated substrates air was used as the background, while for ZnSe films a clean soda-lime glass substrate was employed. Reflection measurements were made at 15° from normal, and an aluminum mirror deposited on a fused silica substrate was used as the 100% reflection standard. Prior to collection of reflection data, the back side of each sample was roughened with a rotary grinder to eliminate backside reflection.

PV Performance of Multi-Layer Structures. On both three-layer and four-layer samples I-V data was collected using a Solartron SI 1287 electrochemical interface. I-V curves were collected over different voltage ranges: (1) from -100 to 600 mV on a small area commercial multi-crystalline Si cell (Radio Shack), (2) 0 to 600 mV on some multi-layer samples, (3) -2.5 to 22.5 mV on other multi-layer samples. Large reverse biases were avoided to prevent damage to the samples, and smaller voltage ranges were employed on later samples, since no power production was apparent. Samples were illuminated with a 1 KW Oriel solar simulator with a 1.5 AMG air mass filter and a 90% attenuation filter to approximate 1 sun irradiation. To make electrical contact to the TCO, a silver bus bar was applied to the exposed TCO along the edge of the substrate using a commercial silver colloid, and subsequently contacted with a copper alligator clip. Two different methods were tested for making electrical contact to the metal back contacts. First, wire test leads were attached directly to the metal back contacts using a commercial silver colloid. Second, a pressure contact system was fabricated. This system employed a square polycarbonate plate with holes drilled through it that coincided with the position of the metal back contacts. Flat braided wire leads were passed through the holes, so as to be positioned between the appropriate metal back contact and the polycarbonate plate. The contact apparatus was applied to the sample, and uniform pressure applied by attaching parallel clamps to two opposite edges.

Results

TCO Coated Substrates. Two different TCO coated substrates were employed for the fabrication of multi-layer samples. ITO coated soda lime glass substrates (20 Ω/sq) and FTO coated borosilicate substrates (10 Ω/sq) were purchased from outside suppliers (Precision Glass & Optics and Solaronix, respectively). ITO coated substrates were uniform in appearance, and highly transparent. FTO coated substrates had a non-uniform appearance with millimeter scale defects visible in the coating, lower apparent transparency, and a greenish-brown tint. SEM analysis and optical transmission measurements were employed to quantify the differences between the two TCO coatings.

Data collected from an ITO coated substrate is presented in Figure 5.1; data from an FTO coated substrate is presented in Figure 5.2. Consistent with visual assessment of the substrates, optical transmission in the visible region of the spectrum is much higher with ITO substrates at 85-90%, with FTO coated substrates having optical transmission of only 60-70% in the visible region. SEM images show that the ITO coating is also much thinner (~100 nm thick) and has a very smooth and uniform morphology. The FTO coating has a thickness of ~500 nm, and exhibits pronounced surface roughness with numerous outgrowths in the micrometer size regime.

ZnSe Thin Films. Two different thicknesses of ZnSe layers were deposited in this work. Thinner films (~100 nm) were employed as the heterojunction partner in some multi-layer samples, deposited between the ITO or FTO and the Cu_3BiS_3 layer. Thicker ZnSe films (~250 nm) were deposited on soda-lime glass or ITO coated soda-lime glass substrates to enable independent characterization of the morphology, crystallinity, and optical properties of these ZnSe films. Some 250 nm thick ZnSe films were subsequently annealed at 250 °C for 45 minutes to simulate the effect of substrate heating during the initial phase of the Cu_3BiS_3 reactive deposition.

An SEM image of an as-deposited ZnSe film, 250 nm thick, on a soda-lime glass substrate, along with the XRD powder pattern collected from the as-deposited film, the XRD powder pattern collected from an annealed film, and the standard powder pattern for ZnSe (PDF 80-21), are presented in Figure 5.3. The oblique SEM image confirms that the film is very smooth, uniform, and continuous. SEM images collected from annealed films were indistinguishable from those of as-deposited films. The XRD powder pattern collected from the as-deposited film has broad, poorly defined peaks.

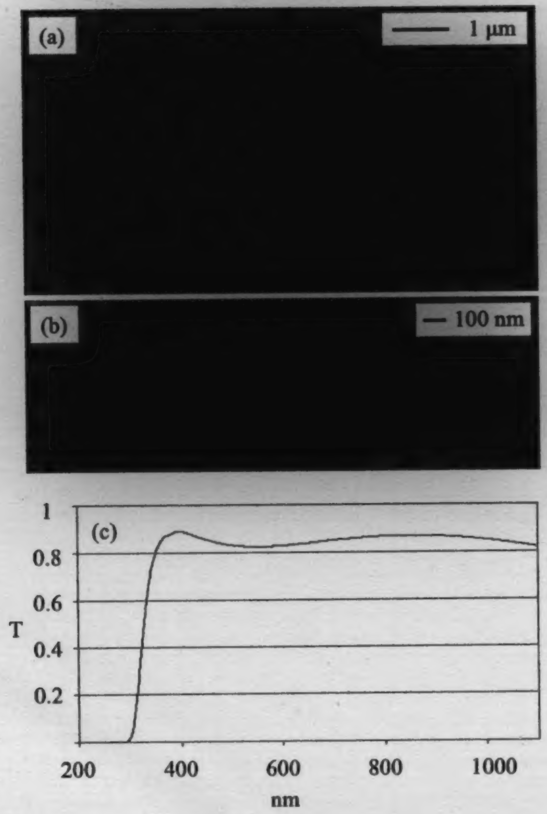

Figure 5.1. SEM images of an ITO film on soda-lime glass (a) and (b), manufactured by Precision Glass and Optics. Optical transmission data is shown in (c).

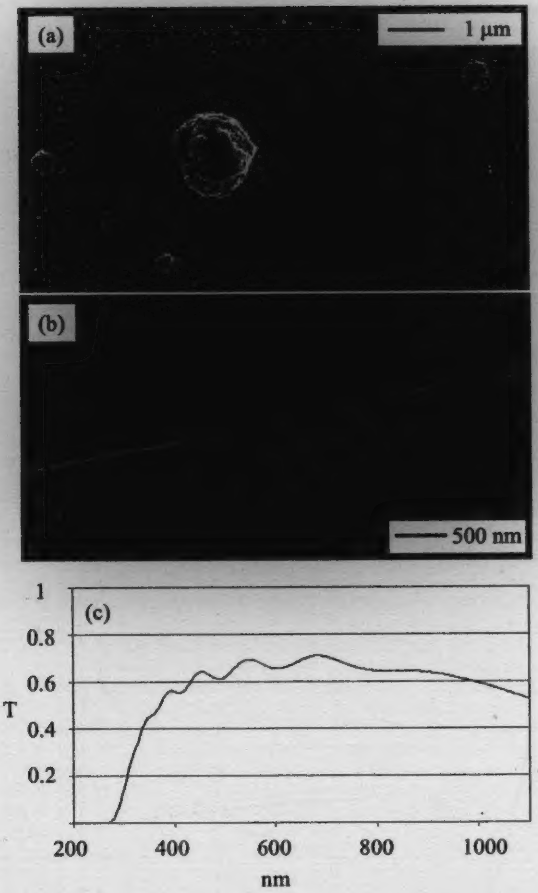

Figure 5.2. SEM images of an FTO film on borosilicate glass (a) and (b), manufactured by Solaronix. Optical transmission data is shown in (c).

The strongest peak in the experimental powder pattern matches the strongest peak in the standard powder pattern ((111) peak, 27.5° 2-theta); however, the major peak in the experimental pattern could also be considered consistent with, and attributed to, amorphous scattering from the ZnSe film or glass substrate. Relatively low counts per second were observed during data collection, necessitating longer collection times to improve the signal to noise ratio. This, along with the broad nature of the peak centered at 27.5° 2-theta, indicates that this is likely a result of amorphous scattering; suggesting that a significant fraction of the as-deposited ZnSe film is non-crystalline. Other peaks in the standard powder pattern could not be identified in the experimental data. Following annealing a negligible sharpening of the (111) peak is observed, relative to data collected from the as-deposited film. This indicates that substrate heating during reactive deposition (250 °C, 45 min) does not significantly impact the microstructure of the ZnSe film when it is deposited on an amorphous soda-lime glass substrate. For both as-deposited and annealed films EDX analysis showed that the films were slightly Zn poor, and contained small amounts of sulfur, with a composition of Zn, 48 atomic percent; Se, 50 atomic percent; S, 2 atomic percent.

An SEM image of a 250 nm thick ZnSe film, as-deposited on an ITO coated soda-lime glass substrate, is presented in Figure 5.4. Like the film deposited directly on soda-lime glass this film is smooth and continuous. Both the ITO layer and the ZnSe layer are clearly visible in the oblique image, with the ZnSe broken back from the edge of the ITO. Films subjected to annealing were indistinguishable by SEM from as-deposited films. The XRD powder patterns for as-deposited and annealed ZnSe films are presented in Figure 5.4 (b) and (c). Also shown is an XRD powder pattern collected from an ITO

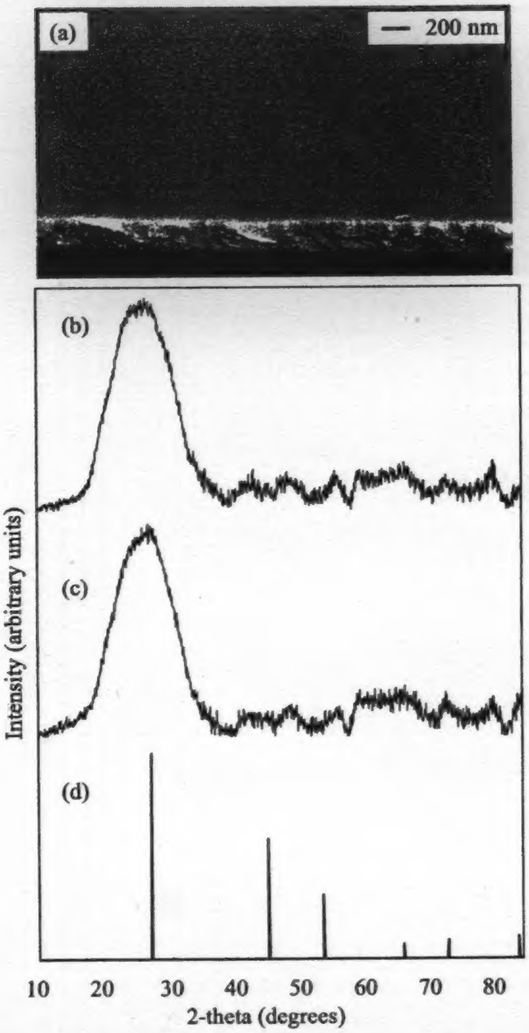

Figure 5.3. Oblique SEM image of an as-deposited ZnSe film on soda-lime glass (a), XRD powder pattern of as-deposited film (b), XRD powder pattern of film annealed at 250 °C for 45 min (c), and standard powder pattern for ZnSe (d).

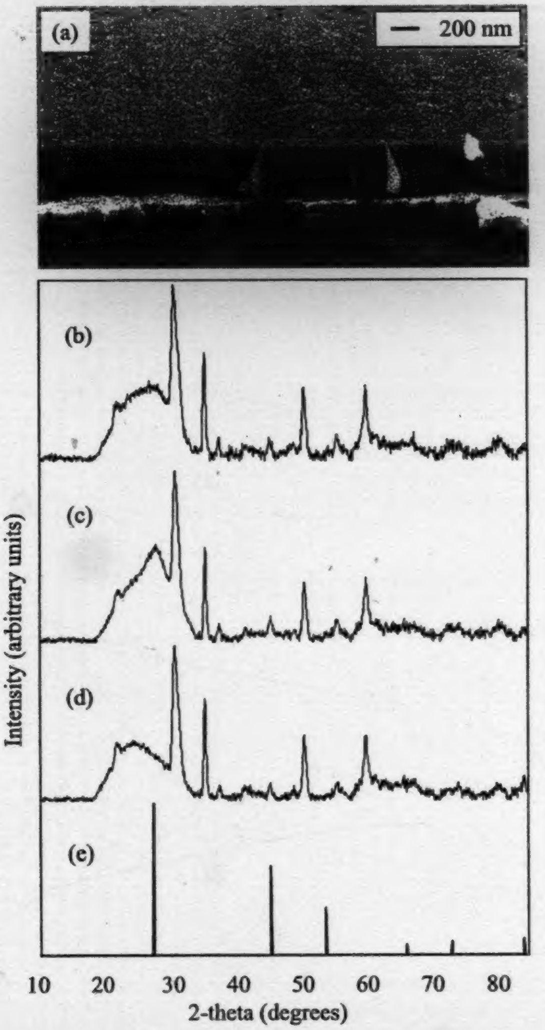

Figure 5.4. Oblique SEM image of an as-deposited ZnSe film on ITO coated soda-lime glass substrate (a), XRD powder pattern of as-deposited film (b), XRD powder pattern of film annealed at 250 °C for 45 min (c), XRD powder pattern of ITO coated substrate (d), and standard powder pattern for ZnSe (e).

coated soda lime glass substrate (Figure 5.4 (d)), and the standard powder pattern for ZnSe (Figure 5.4 (e)). The peak positions and intensities in the powder pattern collected from the ITO coated substrate match peaks in the powder patterns collected from the as-deposited and annealed ZnSe films. This suggests that the ITO coating has persisted through deposition, and annealing, of the ZnSe films. The powder patterns collected from the as-deposited ZnSe film on ITO coated soda-lime glass, and the as-deposited film on plain soda-lime glass, are similar. Again, the as-deposited film appears to be largely amorphous. When the ZnSe film deposited on ITO coated glass is annealed, a noticeable sharpening of the (111) peak is observed (Figure 5.4 (c)). This indicates that the crystallinity of the film has been enhanced, and that some grain growth has occurred, although overall the film can still be regarded as being poorly crystalline. Since no effect from annealing was observed on the plain soda-lime glass substrate, this indicates that the crystalline nature of the ITO coating acts to promote the effect of the modest annealing conditions (250 °C, 45 min) associated with the heating phase of the reactive deposition. The composition of films deposited on ITO coated substrates was identical to that of films deposited on soda-lime glass, with EDX results: Zn, 48 atomic percent; Se, 50 atomic percent; S, 2 atomic percent.

Transmission and reflection data were collected from 250 nm thick, as-deposited and annealed, ZnSe films on soda-lime glass substrates, with no differences between the data. Transmission and reflection data collected from an as-deposited sample is presented in Figure 5.5 (a). Using this data, the energy-dependent optical absorption coefficient was calculated, and the nature and magnitude of the optical band gap determined. The optical absorption coefficient was calculated from

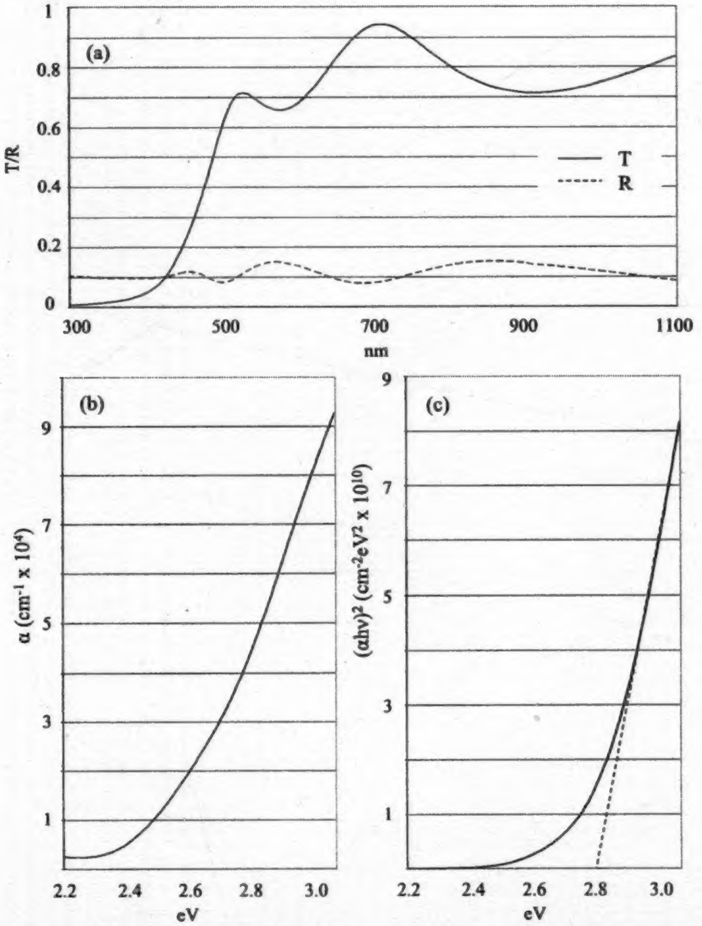

Figure 5.5. Transmission and reflection data for a 250 nm thick ZnSe film on soda-lime glass (a), plot of α against energy (b), and plot of $(\alpha h\nu)^2$ against energy with line of best fit showing a direct band-gap of 2.8 eV (c).

$$\alpha = 1/x \ln[(1-R)^2/T],$$

where x is the film thickness and R and T are the reflection and transmission.[1] Figure 5.5 (b) is a plot of α as a function of energy. The nature and magnitude of the optical band gap may be determined from the fact that $\alpha h\upsilon$ is proportional to $(h\upsilon - E_g)^n$. Plots of $(\alpha h\upsilon)^{1/n}$ against $h\upsilon$, with $1/n = 2, 2/3, 1/2, 1/3$, are linear for direct, direct forbidden, indirect, and indirect forbidden band gaps, respectively, with the x-intercept yielding the magnitude of the band gap.[1] The best linearity was observed with $1/n = 2$, indicating a direct band gap with a magnitude of the 2.8 eV (Figure 5.5 (c)), consistent with previously reported values for polycrystalline ZnSe films deposited by PVD methods.[2,3]

Deposition of Cu_3BiS_3 on TCO Coated Substrates. Three-layer samples (TCO/Cu_3BiS_3/metal back contact) were fabricated by depositing a 1.2 μm thick Cu_3BiS_3 film on either an ITO or FTO coated substrate, followed by deposition of Al, Ni, and Mo back contacts through a shadow mask. Only three metal back contacts were employed, leaving one quarter of the Cu_3BiS_3 film exposed. This enabled characterization of the as-deposited Cu_3BiS_3 thin film, allowing comparison of films deposited by the one-step method on fused silica substrates (Chapter 4) with those deposited on TCO coated substrates.

SEM images of a Cu_3BiS_3 film deposited on ITO coated glass are presented in Figure 5.6. Also presented in Figure 5.6 is the XRD powder pattern collected from the sample, and the standard powder pattern for Cu_3BiS_3 (PDF 43-1479). Films deposited on FTO coated glass were comparable, but the increased roughness of the FTO coating relative to the ITO coating, translated to increased surface roughness of the Cu_3BiS_3 film.

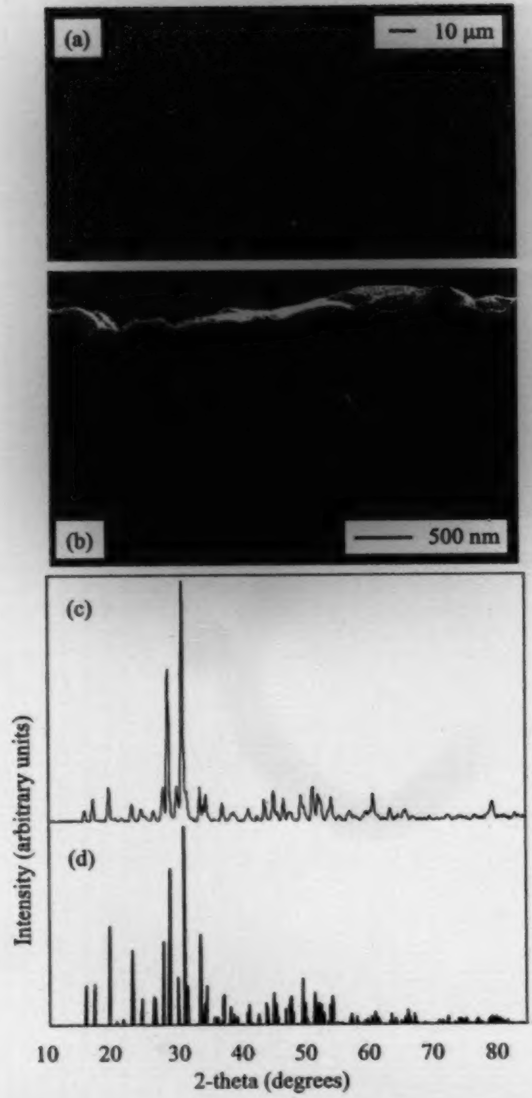

Figure 5.6. SEM images of a Cu_3BiS_3 thin film deposited by the one-step method on an ITO coated soda-lime glass substrate (a) and (b), XRD powder pattern collected from the film (c), and standard powder pattern for Cu_3BiS_3 (d).

Regardless of the substrate employed, films deposited on conductive substrates are of similar quality to those deposited previously on fused silica substrates. It should be noted that these Cu_3BiS_3 thin films (250 °C deposition temperature) are homogeneous throughout the depth of the film. It was found that films deposited on fused silica substrates at 250 °C retained the layered structure of the deposition, and that the films could be homogenized by a subsequent annealing step (Chapter 4). For Cu_3BiS_3 films deposited on an ITO or FTO coating this layered structure is not observed. The good match between both peak positions and intensities of the XRD powder pattern, and the standard powder pattern, confirms that Cu_3BiS_3 has been synthesized, and, like films deposited on fused silica substrates at 250 °C, that the crystallites have a random orientation. The composition of the film was confirmed by EDX analysis, with an elemental ratio of 3:1:3 Cu:Bi:S.

SEM images of three-layer structures deposited on ITO coated substrates with Al, Ni, and Mo back contacts are presented in Figure 5.7. In Figure 5.8 are SEM images of the analogous three-layer structures deposited on FTO coated substrates. In each set of images all three layers are clearly identifiable, and all three layers are in intimate contact. No peeling or separation of the films was observed, indicating good adhesion at all interfaces. To assess whether any interfacial reaction had occurred during the lengthy deposition at elevated temperature (~10 hours at 250 °C), auger line scan intensity data was collected. Line scans collected from cross-sections of ITO/Cu_3BiS_3/Al and FTO/Cu_3BiS_3/Al structures are presented in Figures 5.9 and 5.10, respectively, along with a corresponding SEM image. It should be noted that this data is not scaled to correspond directly to the SEM image, and that data from the glass substrate and the Al

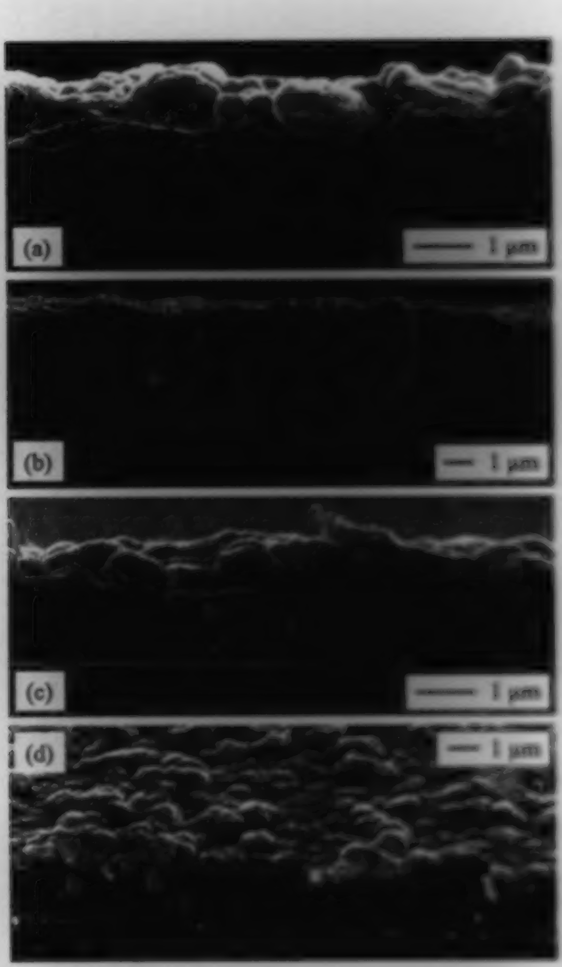

Figure 5.7. SEM images of 3-layer samples deposited on ITO coated glass with three different back contacts. Al on Cu_3BiS_3/ITO (a), Ni on Cu_3BiS_3/ITO (b), Mo on Cu_3BiS_3/ITO (c) and (d). The oblique image (d) clearly shows the three layers on top of the soda-lime glass substrate.

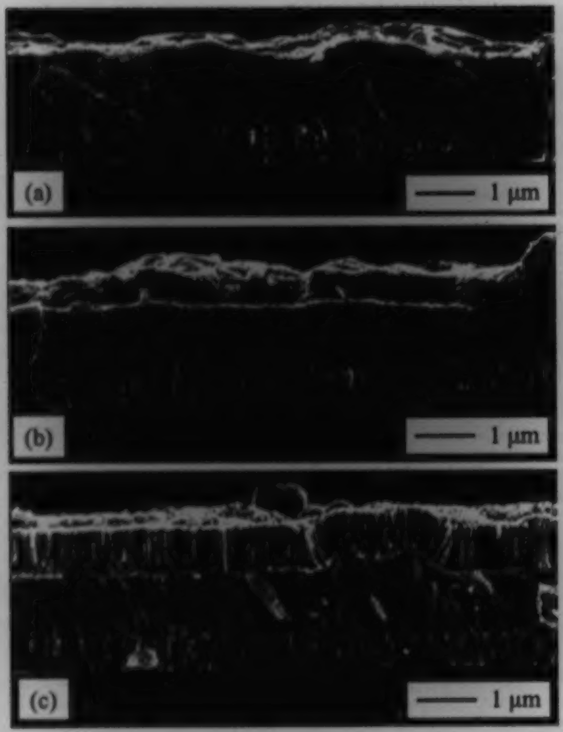

Figure 5.8. SEM images of 3-layer samples deposited on FTO coated glass with three different back contacts. Al on Cu_3BiS_3/FTO (a), Ni on Cu_3BiS_3/FTO (b), Mo on Cu_3BiS_3/FTO (c).

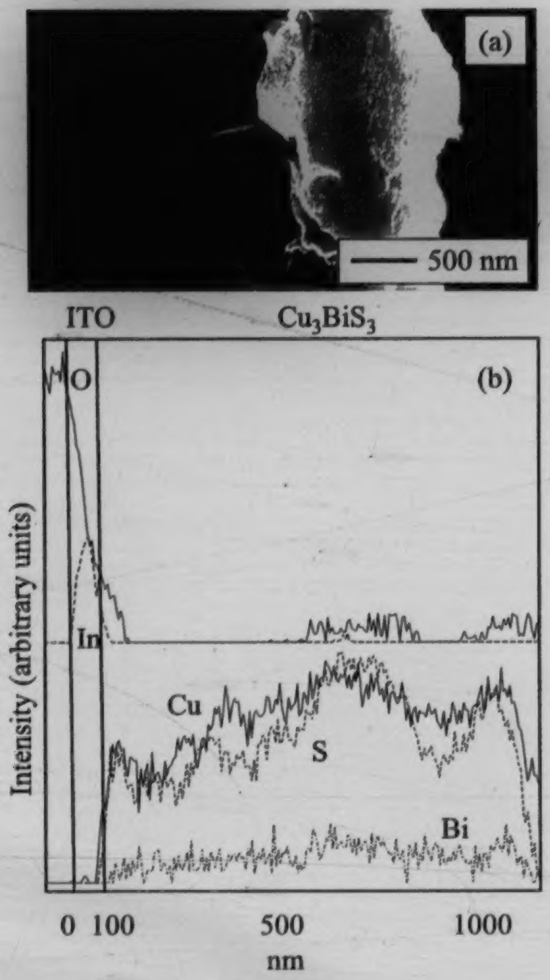

Figure 5.9. SEM image of Al/Cu_3BiS_3/ITO on soda-lime glass (a), and scanning auger intensity data (b). Data is offset for improved clarity, and does not include the aluminum contact (a thin layer of the glass substrate is included).

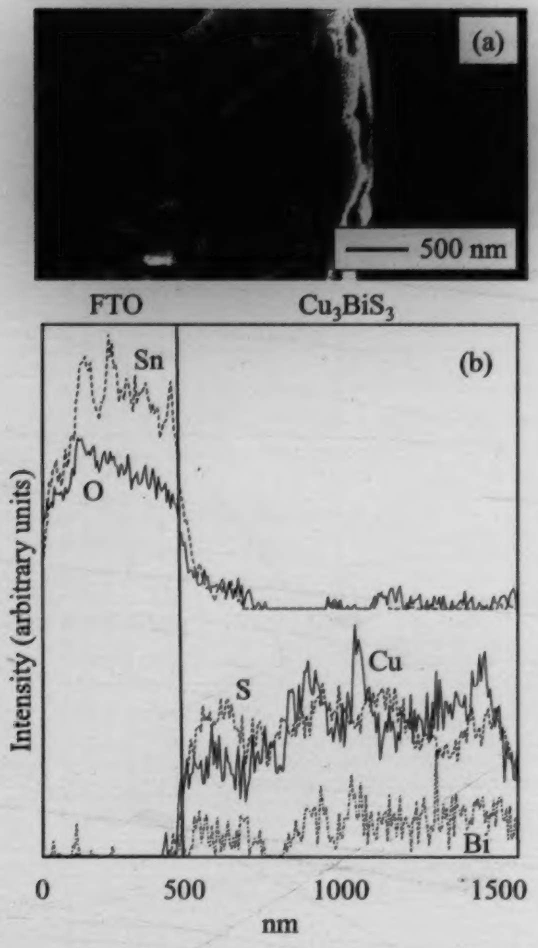

Figure 5.10. SEM image of Al/Cu_3BiS_3/FTO on borosilicate glass (a), and scanning auger intensity data (b). Data is offset for improved clarity, and does not include the glass substrate or aluminum contact.

contact have been omitted. For clarity, data corresponding to the elements in the ITO or FTO layer has been offset from data corresponding to the elements in the Cu_3BiS_3 layer. Samples were fractured immediately prior to loading, but were not sputtered prior to data collection.

The auger intensity data in Figure 5.9 indicates that the In is localized within the ITO layer. Similarly, the Cu, Bi, and S data indicates that these elements have not migrated appreciably into the ITO layer. However, the O signal extends ~100 nm into the Cu_3BiS_3 layer, indicating some oxidation of the Cu_3BiS_3 thin film adjacent to the ITO coated substrate. Since the ITO coating is relatively thin, the oxidation could result from reaction with the ITO and/or the underlying glass substrate. Auger intensity data collected from a structure deposited on an FTO coated substrate (Figure 5.10) shows that Cu, Bi, and S are primarily localized within the Cu_3BiS_3 layer. However, the auger signal from both Sn and O extends ~250 nm into the Cu_3BiS_3 layer, indicating that the degree of interfacial reaction is somewhat greater than that observed with ITO, and, in addition to oxidation, also includes interfacial reaction or diffusion of Sn. While auger data collected from both samples clearly indicates that some interfacial reaction occurred when Cu_3BiS_3 films were deposited on ITO or FTO substrates, data collected from film cross sections and surfaces also indicates that the identity of the individual films has been largely preserved during the deposition process.

Deposition of Cu_3BiS_3 on TCO/ZnSe Coated Substrates. Four-layer samples (TCO/ZnSe/Cu_3BiS_3/metal back contact) were fabricated in a similar manner to three-layer samples, with the exception of a ZnSe film, ~100 nm thick, being deposited on the ITO or FTO coating prior to Cu_3BiS_3 deposition. In Figure 5.11 are cross-sectional SEM images of a representative sample, fabricated on an FTO coated substrate with an Al back contact. Backscattered electron and secondary electron SEM images are presented in Figure 5.11 (a) and (b), respectively. In the backscattered image the bright band at the interface where the ZnSe layer was expected to be localized, indicates that this area contains a phase with a higher net atomic number. In the secondary electron image the FTO, Cu_3BiS_3, and Al layers are clearly identifiable; there is no evidence of the ZnSe layer.

Figure 5.11 (c) presents auger line scan intensity data collected from the sample cross-section. Data is not scaled to correspond directly to the SEM images, and data from the glass substrate and Al contact have been omitted. For clarity, data for the constituent elements of each of the deposited layers have been vertically offset. The sample was fractured immediately prior to loading, but was not sputtered prior to data collection. At the interface between the FTO and Cu_3BiS_3, where the ZnSe layer was expected, are well defined auger intensity peaks for Se and Bi, suggesting the possible formation of Bi_2Se_3. This would be consistent with the observation of a high net atomic number phase at this position in the backscattered SEM image. The formation of Bi_2Se_3 at the ZnSe/Cu_3BiS_3 interface is also consistent with EDX data collected from the surface of the Cu_3BiS_3 film, indicating a Bi deficiency. An auger peak for Zn, ~200 nm wide, is located in what could be regarded as the absorber layer adjacent to the interface. This zinc rich region is almost completely depleted in Bi, and intensity data for Cu and S also tails off towards the interface. In the outermost region, where the intensity data is representative of Cu_3BiS_3, it should also be noted that the film appears to be slightly S-rich, based on a comparison of Cu and S auger intensity data collected from Cu_3BiS_3

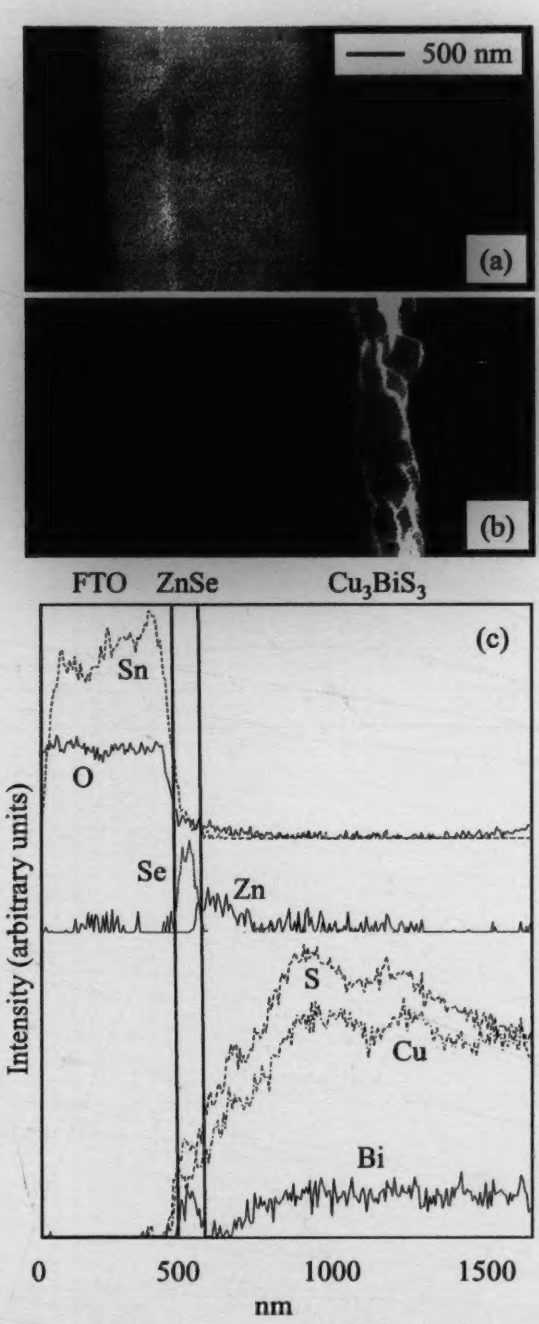

Figure 5.11. Backscattered and secondary SEM images of Al/Cu_3BiS_3/ZnSe (100nm)/FTO on borosilicate glass in (a) and (b), respectively, and scanning auger intensity data (c). Data is offset for improved clarity, and does not include glass or aluminum contact.

films deposited directly on ITO and FTO (Figures 5.9 and 5.10). While the identity of the phases formed as a result of interfacial reaction are not known, it is clear that the ZnSe has been completely consumed by reaction with the Cu_3BiS_3 layer during the deposition process, resulting in the formation of several compositionally distinct layers. Characterization of the surface of the Cu_3BiS_3 film by SEM/EDX and XRD does indicate that the outer layer is predominantly Cu_3BiS_3; however, as mentioned above, EDX indicates that the film is Bi poor, and XRD powder patterns indicate the presence of a minor sub-phase, although it could not be identified.

PV Performance of Multi-Layer Structures. All three-layer and four-layer samples were screened for PV performance by collecting I-V curves. In general, the behavior of the 4-layer samples was similar to that of the 3-layer samples, and only data collected from 3-layer samples is presented here. Representative data for a 3-layer sample with a Mo metal back contact deposited on an ITO coated substrate is presented in Figure 5.12 (a). Colloidal silver was used to attach the test leads to the metal back contacts, and the voltage range was 0 - 600 mV (reduced data range is shown in the main panel, with the full data range in the inset panel). Figure 5.12 (b) shows a representative I-V curve collected from a 3-layer sample with a Mo metal back contact deposited on an FTO coated substrate. For this sample the pressure contact was used to attach the test lead to the metal back contact (see experimental section for details), and the voltage range was -2.5 - 22.5 mV. An I-V curve was also collected from a small area commercial multi-crystalline silicon cell purchased from Radio Shack (Figure 5.12 (c)) with a voltage range of -100 – 600 mV. In all three frames light curves are depicted with solid lines, dark curves with dashed lines.

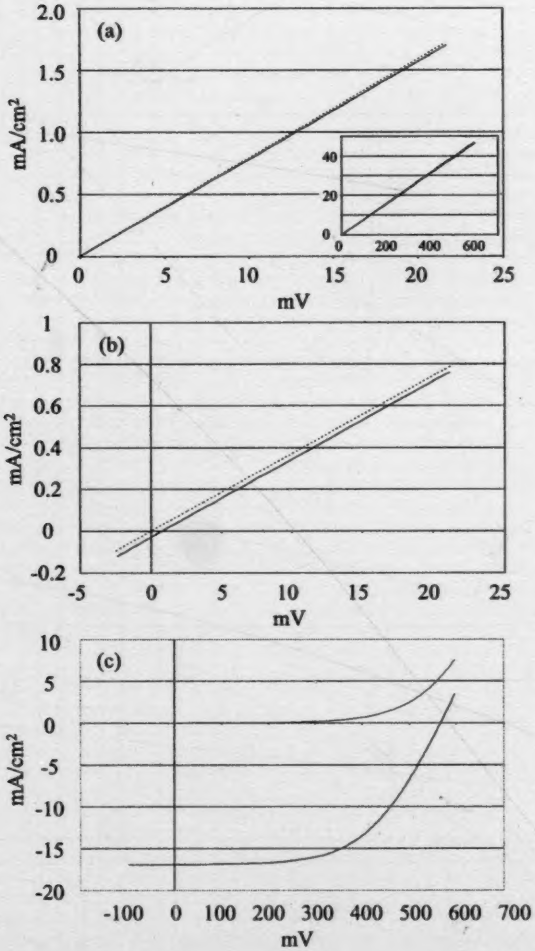

Figure 5.12. I-V data collected from a Mo/Cu_3BiS_3/ITO sample with colloidal silver contact (a), a Mo/Cu_3BiS_3/FTO sample with pressure contact (b), and commercial multi-crystalline Si solar cell (c). Inset plot in (a) shows complete data range, main plot reduced for comparison to (b). Light curves are depicted with a solid line, dark curves with a dashed line.

The behavior of all Cu_3BiS_3 based samples can be characterized as resistor-like, not diode-like as would be expected for a functional PV device, for example the polycrystalline Si cell tested in Figure 5.12 (c). The sample deposited on ITO exhibits a fixed resistance over the test range of ~12 Ω, while the device deposited on FTO shows a fixed resistance over the test range of ~30 Ω. For the sample deposited on ITO, and contacted with colloidal silver, there was only a slight discernable difference between the light and dark curves; however, for the sample deposited on FTO, and contacted with the pressure contact, the light curve is clearly offset from the dark curve, indicating that a small photo-voltage was produced under exposure to light. The production of even this small photo-voltage is encouraging for future device development.

No significant difference was observed between I-V data collected using any one of the three different metal back contacts. Visual assessment of the back contacts indicated that lateral spreading during sputter deposition resulted in metal deposition behind the shadow mask. In the current mask/substrate configuration there is a small gap between the mask and the substrate, and since the sputter source is located off-axis from the substrate normal, such an outcome is not surprising. Resistance measurements also supported this conclusion. The resistances measured between metal back contacts and the TCO front contact were consistent with each other, and also with the resistance value determined from the slope of the I-V data. The resistances measured between different metal back contacts were several times lower, and also consistent with each other. These observations indicate that the three metal back contacts were not electrically isolated from each other, and were likely behaving as a single contact.

During SEM analysis of multi-layer samples it was noted that the colloidal silver used for attaching test leads to the metal back contacts appeared to react with other components of the sample. Shown in Figure 5.13 is a cross-sectional SEM image through a three-layer sample; including the colloidal silver contact. This image was collected several days after testing and fracture. There is a sub-phase present on the sample cross-section, as well as on the fractured glass surface. Since this fracture was made after fabrication, application of the colloidal silver, and testing, it must be the case that this material has migrated onto the glass under ambient conditions. EDX identified this area as being Cu-S rich, relative to "clean" areas of the fracture. Similar spots were found on all samples where colloidal silver had been applied to the metal back contact.

It is speculated that once the Ag comes in contact with the Cu_3BiS_3 layer it reacts, forming an Ag-Bi-S phase and displacing excess Cu-S. Many Ag-Bi-S phases are known,[4,5] some of which would be consistent with the segregation of excess Cu-S following the reaction of Cu_3BiS_3 and Ag. Presented in Figure 5.14 are the Ag_2S-Bi_2S_3, Bi_2S_3-Cu_2S and Cu_2S-Ag_2S pseudo binary phase diagrams (reproduced from reference 4). Evident in these phase diagrams is the low temperature stability of Ag-Bi-S ternary compounds including $AgBiS_2$ and $AgBi_3S_5$. What is not clear is if the silver has flowed and reacted exclusively at the fracture site after testing, or if it has also been drawn through pores in the metal back contact, and reacted, prior to testing for PV performance.

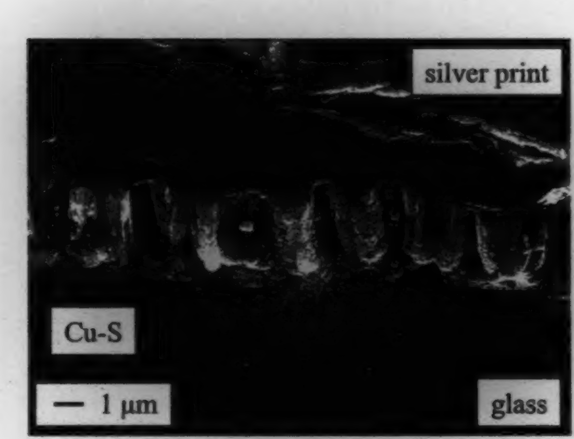

Figure 5.13. SEM image of cross section through a Ni/Cu_3BiS_3/ITO sample and silver print contact. Note presence of an unidentified material on the cross-section of sample and glass substrate. EDX indicates this area is Cu-S rich.

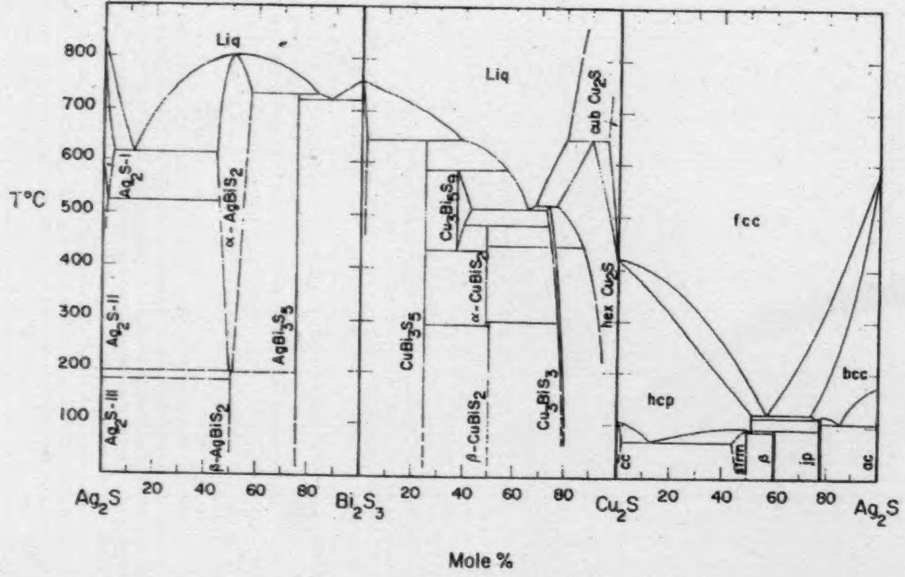

Figure 5.14. Ag_2S-Bi_2S_3, Bi_2S_3-Cu_2S and Cu_2S-Ag_2S pseudo binary phase diagrams from 0-900 °C. $AgBiS_2$ and $AgBi_3S_5$ are identified as stable Ag-Bi-S compounds. Reproduced from reference 4 with the permission of The Canadian Mineralogist.

Discussion

Deposition of Cu_3BiS_3 on TCO Coated Substrates. In Chapter 4 the synthesis of high quality Cu_3BiS_3 thin films on fused silica substrates was reported. In this chapter the applicability of the one-step deposition method has been successfully extended to the synthesis of Cu_3BiS_3 thin films on TCO coated soda-lime and borosilicate glass substrates. For films deposited on conductive substrates, a deposition temperature of 250 °C was used exclusively, and no post deposition annealings under H_2S were carried out.

In general, the quality of the films deposited on conductive substrates was comparable to that of films deposited on fused silica substrates. One significant difference between the two was that films deposited on amorphous fused silica substrates retained the layered structure of the deposition (Chapter 4), while those deposited on crystalline TCO coated substrates were uniform throughout the depth of the film. This is attributed to two possible effects. One, deposition on a crystalline layer (ITO or FTO) might promote enhanced grain growth and homogenization of the Cu_3BiS_3 film. (A similar substrate effect was observed for ZnSe films (see above), with films deposited on an amorphous substrate not affected by a modest annealing, while the same annealing conditions resulted in improved crystallinity and grain growth when the ZnSe was deposited on an ITO coated substrate.) Two, the longer deposition time associated with the deposition of thicker films on TCO coated substrates (12 cycles instead of 8 at ~35 minutes/cycle) may have an effect similar to the annealing step performed on thinner films deposited on fused silica substrates, which also resulted in film homogenization (Chapter 4).

Like films deposited at 250 °C on fused silica substrates, films deposited on TCO coated substrates exhibit a random orientation of the crystallites. In Chapter 4 it was found that films deposited at 300 °C had a preferred orientation in the [200]/[211] direction, and that random or preferred orientations were preserved during subsequent annealing. No experiments involving deposition at a substrate temperature of 300 °C have been carried out on TCO coated substrates, so it is not yet known what effect, if any, a crystalline substrate will have on the texture of films deposited at higher temperatures. Since the microstructure and texture of the absorber layer has been found to play a role in the performance of CIGS and CdTe devices,[6,7] it may prove useful to determine whether the control of Cu_3BiS_3 film texture achieved with fused silica substrates can also be obtained when TCO coated glass substrates (or other substrates such as metal foils) are employed.

When the Cu_3BiS_3 films were deposited on ITO and FTO coated substrates, auger intensity data collected from film cross-sections (Figures 5.9 and 5.10), indicates that some interfacial reaction has occurred. On ITO, interfacial reaction was limited to the oxidation of a thin layer of the Cu_3BiS_3 film adjacent to the ITO layer. In the case of deposition on FTO, auger intensity data indicated that some Sn and O had migrated into the adjacent absorber layer, and that the extent of reaction, as judged by the width of the affected area, was greater. However, SEM analysis of film cross-sections indicates that distinct ITO or FTO and Cu_3BiS_3 layers are present (Figures 5.6, 5.7, and 5.8), and SEM/EDX and XRD surface analysis of the Cu_3BiS_3 film is consistent with data collected previously from films deposited on fused silica substrates (Chapter 4). With the deposition taking ~10 hours at 250 °C, some interfacial reaction is expected; the fact that the extent of the reaction is minimal, and TCO and Cu_3BiS_3 films are for the most part intact following the deposition process, is a promising result for future device development based on the one-step deposition method for Cu_3BiS_3 films identified in Chapter 4.

Deposition of Cu_3BiS_3 on TCO/ZnSe Coated Substrates. When ZnSe was incorporated in the multi-layer stack, the results were less promising. SEM and auger data collected from a four-layer sample (Figure 5.11) indicate that significant interfacial reaction has occurred. When the ZnSe heterojunction couple was incorporated into the multi-layer structure, the Cu_3BiS_3 layer was isolated from the TCO coated substrate, and the TCO remained intact with a well defined boundary in the scanning auger data. On the other side of this interface, the ZnSe layer was completely consumed during the reactive deposition, and the auger intensity data indicates that several compositionally distinct layers were formed. The identity of the resultant phases is not known, but it is speculated that Bi_2Se_3 as well as unidentified Zn-Cu-S phases may have formed at the proximity of the interface. The outer most layer of the sample is identified as Bi poor Cu_3BiS_3, possibly containing a Cu-S impurity phase.

The choice of ZnSe as the buffer layer was based on two considerations. First, for straightforward processing consistent with deposition of the Cu_3BiS_3 layer, it was desirable to utilize a compound that could be easily deposited by sputter deposition. ZnSe was available as a stock sputter target, and the deposition of high quality films by RF sputter deposition had been reported in the literature.[8-10] Second, ZnSe has also been successfully employed as a buffer layer in CIGS devices, resulting in reasonable conversion efficinecies.[11,12] ZnSe films sputter deposited in this work were of reasonable quality, although a thorough evaluation was not made, since electrical properties of the films were not measured. CBD is the most commonly used method for buffer layer deposition, and PVD has in general been used with considerably less success.[11,12] However, since the objective of this work was to evaluate material compatibilities with the reactive deposition process, the method of deposition was not regarded as a critical parameter. Due to the incompatibility of ZnSe with the one-step deposition of Cu_3BiS_3, it will be necessary to utilize other buffer layers (several possibilities are identified in Chapter 2) in future device development strategies, or other fabrication strategies that limit thermal processing of the heterojunction (discussed in Chapter 8).

PV Performance of Multi-Layer Structures. The objective of this chapter was not to identify a functional PV device; however, there was a possibility that such a result might occur. With four-layer samples this would have been most likely by formation of a ZnSe-Cu_3BiS_3 p-n junction. For three-layer devices the scenario most likely to produce a device would have been the formation of a suitable heterojunction couple, for example In_2S_3 or SnS_2,[11,12] by interfacial reaction, and simultaneous formation of a p-n junction with Cu_3BiS_3. All samples were tested for PV performance by collecting I-V data, both in the dark and under exposure to simulated solar radiation. Unfortunately, none of the samples tested exhibited PV device characteristics. All samples produced could be characterized as having resistor-like behavior, and not the diode-like behavior expected for a p-n junction device. In most samples it was also the case that no photo-response was observed under exposure to light. One exception was the three-layer sample deposited on FTO coated glass with a Mo back contact (Figure 5.12 (b)) and electrical contact made using a pressure contact, where a small (~1 mV) photo-voltage was observed. For the comparable three-layer sample deposited on ITO coated glass, and contacted with colloidal silver, the light and dark curves were almost identical (Figure 5.12 (a)).

The formation of an ohmic contact has been previously reported for CIGS/ITO and CIGS/FTO junctions using a three-layer sample structure (Au/CIGS/TCO) that is similar to the ones employed in this work.[13,14] Since a limited voltage range, and no significant reverse bias, was employed during the collection of I-V curves in this work, the junctions can not be definitively characterized as ohmic. The formation of an ohmic contact at the TCO/Cu_3BiS_3 junction would be consistent with the resistor-like behavior observed in these samples. However, with the formation of an ohmic contact, a decrease in resistivity (increase in slope of the linear I-V curve) would be expected upon exposure to light, due to the photoconductivity of the Cu_3BiS_3 layer. While the photoconductivity of Cu_3BiS_3 was not measured as part of this work, Nair and co-workers have reported an order of magnitude increase in Cu_3BiS_3 conductivity under exposure to simulated solar radiation.[15] The fact that no change in conductivity was observed under illumination may indicate that the resistor-like behavior is due instead to electrical shorts between the front and back contacts. Also, the photo-voltage observed in the three-layer sample deposited on FTO is not necessarily consistent with the formation of a FTO/Cu_3BiS_3 ohmic contact, since formation of a photo-voltage implies the build-up of positive and negative carriers on opposite sides of one of the junctions in the sample. Due to the ambiguity of this data, and the uncertainty regarding the compositional make-up, and optical and electrical properties of the interfacial regions, a definitive explanation for the observed behavior of these multi-layer samples can not be made at this time. However, it is likely that a more detailed understanding of these interfacial properties and phenomena will be critical to producing a functional device, and that this will require more detailed knowledge of the optical and electrical properties of Cu_3BiS_3 as well.

Collection of I-V data also served the more immediate objective of identifying promising methods for contacting more complex library cells that may be produced in the future. Of the two contacting methods tested, it appears that the pressure contact is most suitable for further development, for two reasons. One, it is easier to apply consistently and quickly, making it more compatible with a high-throughput experimental method. Two, the results indicate that colloidal silver reacts with Cu_3BiS_3, and, as such, it would be prudent to avoid the use of silver in any aspect of device fabrication. Silver has also been found to be incompatible with $CuInSe_2$ devices when utilized as a metal back contact, where, over time, the Ag diffuses into the absorber layer and changes the doping from p-type to n-type.[16] In this case, results indicate that Ag reacts with Cu_3BiS_3 under ambient conditions. Many ternary and quaternary phases are known in the Cu_2S-Bi_2S_3-Ag_2S system,[4,5] and it is speculated that this reaction results in the formation of Ag-Bi-S and Cu-S phases. Formation of known Ag-Bi-S phases such as $AgBiS_2$ or $AgBi_3S_5$ would be consistent with segregation of excess Cu-S.[4,5,17]

Conclusions

In this Chapter an investigation of material and method compatibilities was carried out as a preliminary step in the development of thin film PV devices utilizing Cu_3BiS_3 as the solar absorber layer. ITO and FTO were identified as being compatible with the one-step deposition of Cu_3BiS_3, and under the limited I-V testing range, there is some indication that TCO/Cu_3BiS_3 junctions behave as ohmic contacts. Compatibility of the deposition process with a ZnSe buffer layer was also evaluated, and it was found that the ZnSe was completely consumed by reaction with the Cu_3BiS_3 layer. Consequently, additional buffer layers, and possibly alternative fabrication strategies will need to be employed in future combinatorial device development experiments. Two different methods of contacting completed devices were also investigated, and a pressure plate contact was identified as superior to the use of colloidal silver, due to increased compatibility with the Cu_3BiS_3 layer, and also with the high-throughout combinatorial approach to device development. It is expected that these results will facilitate implementation of combinatorial methods for the development of thin film PV devices based on Cu_3BiS_3. However, it is also expected that a more detailed understanding of the interfacial properties and phenomena will be required to optimize and interpret the behavior of devices identified in any future experiments, and that this in turn will require further characterization and understanding of the semiconductor properties of Cu_3BiS_3.

References

(1) Pankove, J. I. *Optical Processes in Semiconductors*; Prentice-Hall, Inc.: Englewood Cliffs, 1971.

(2) Stirn, R. J.; Nouhi, A. *Appl. Phys. Lett.* **1986**, *48*, 1790-1792.

(3) Caicedo, L. M.; Cediel, G.; Dussan, A.; Sandino, J. W.; Calderón, C.; Gordillo, G. *Phys. Stat. Sol. B* **2000**, *220*, 249-253.

(4) Chen, T. T.; Chang, L. L. Y. *Can. Mineral.* **1974**, *12*, 404-410.

(5) Chang, L.; Wu, D.; Knowles, C. *Econ. Geol.* **1988**, *83*, 405-418.

(6) Romeo, A.; Terheggen, M.; Abou-Ras, D.; Bätzner, D. L.; Haug, F.-J.; Kälin, M.; Rudmann, D.; Tiwari, A. N. *Prog. Photovolt.: Res. Appl.* **2004**, *12*, 93-111.

(7) Kemell, M.; Ritala, M.; Leskelä, M. *Crit. Rev. Solid State Mater. Sci.* **2005**, *30*, 1-31.

(8) Wasa, K.; Hayakawa, S. *Jpn. J. Appl. Phys.* **1973**, *12*, 408-414.

(9) Rizzo, A.; Tagliente, M. A.; Caneve, L.; Scaglione, S. *Thin Solid Films* **2000**, *368*, 8-14.

(10) Caneve, L.; Scaglione, S.; Martelli, S.; Emiliani, G. *J. Vac. Sci. Technol. A* **1991**, *9*, 515-518.

(11) Siebentritt, S. *Solar Energy* **2004**, *77*, 767-775.

(12) Hariskos, D.; Spiering, S.; Powalla, M. *Thin Solid Films* **2005**, *480-481*, 99-109.

(13) Nakada, T.; Hirabayashi, Y.; Tokado, T. *Jpn. J. Appl. Phys., Part 2* **2002**, *41*, L1209-L1211.

(14) Nakada, T.; Hirabayashi, Y.; Tokado, T.; Ohmori, D.; Mise, T. *Solar Energy* **2004**, *77*, 739-747.

(15) Estrella, V.; Nair, M. T. S.; Nair, P. K. *Semicond. Sci. Technol.* **2003**, *18*, 190-194.

(16) Matson, R. J.; Jamjoum, O.; Buonaquisti, A. D.; Russell, P. E.; Kazmerski, L. L.; Sheldon, P.; Ahrenkiel, R. K. *Sol. Cells* **1984**, *11*, 301-305.

(17) Kim, J.-H.; Chung, D.-Y.; Bilc, D.; Loo, S.; Short, J.; Mahanti, S.; Hogan, T.; Kanatzidis, M. *Chem. Mater.* **2005**, *17*, 3606-3614.

Part 2--Template Directed Synthesis of Copper Nanowires

Chapter 6. Synthesis of Nanomaterials by Electrodeposition into Porous Aluminum Oxide Templates

Introduction

Template-directed synthesis utilizing porous aluminum oxide templates has become a popular pathway to diverse nano-structured materials. These materials can have the form of wires[1-5] or tubes,[6-9] be of single composition (metal, semiconductor, polymer),[1,3,6,8-10] or mixed composition (composite, core-shell, or layered configuration).[7,11-14] Deposition methods employed for pore-filling are equally diverse, and include electrochemical deposition,[9,15-18] electroless deposition,[9,15-17] sol-gel deposition,[15,17,18] chemical vapor deposition,[15,17,18] polymerization,[15-17] and melt wetting.[8] PAO templates are easily fabricated and offer the benefit of high pore densities in a hexagonal close packed array and the ability to tailor pore diameters and depths.[19-21] Template pores are also uniform throughout their length, ensuring precise control over the resultant structure. Following the pore-filling process, the PAO host may be removed by dissolution in either acid or base, permitting the preservation of most guest materials. A schematic of a porous aluminum oxide template is shown in Figure 6.1.

One alternative to PAO templates are track-etched polymer templates.[22-25] Polymer templates are most commonly produced from polycarbonate, but other polymers are amenable to the process.[26] Like PAO these templates may be produced with a wide range of pore diameters, but the pore diameters are generally larger than those of PAO,[26] they vary in diameter from wider in the middle to narrower at the ends,[27] and they lack the close packed ordering possessed by PAO templates. Track-etched polymer templates

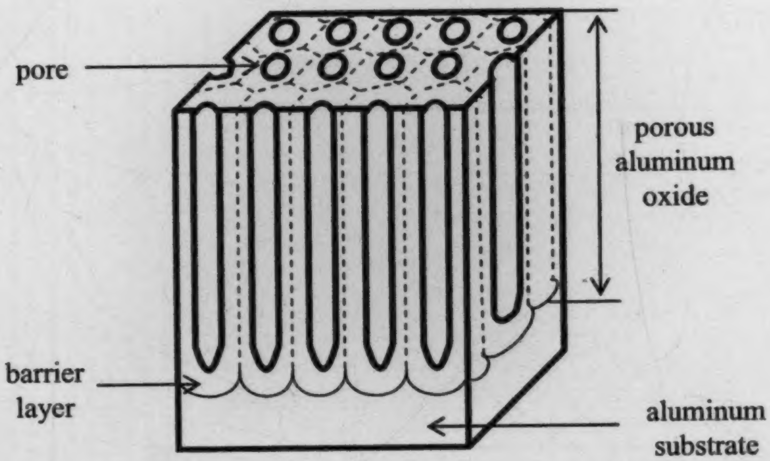

Figure 6.1. Schematic of a porous aluminum oxide template on the aluminum substrate.

are convenient, and may sometimes be necessitated if the guest material is to be liberated from the template, but is incompatible with acids and bases (polymer templates may be dissolved in organic solvents); however, PAO templates ultimately provide the user with increased control over the template, and consequently over the nanostructure of the template grown material. A second alternative to PAO template directed synthesis of nanowires is the use of solution based syntheses, an approach which does not require a hard template.[28-39]

Fabrication of Porous Aluminum Oxide Templates

The anodization of aluminum has been well documented in the literature, and has been used as an industrial process for protecting, strengthening, and coloring aluminum for several decades.[19-21] It has been found that the nature of the resultant oxide is dependent upon applied potential, temperature, and electrolyte. In general, in an electrolyte in which aluminum oxide has a very low solubility a solid barrier layer will be formed, in an electrolyte in which aluminum oxide is weakly dissolvable a thicker porous aluminum oxide layer will be formed, and in an electrolyte in which aluminum oxide is highly soluble electropolishing will occur.[21,40] The most commonly used electrolytes for the formation of PAO are sulfuric acid, oxalic acid, and phosphoric acid, depending upon the pore diameter and pore density required. Figure 6.2 contains SEM images of templates grown in 0.3 M sulfuric acid at 25 V, 0.3 M oxalic acid at 40 V, and 0.1 M phosphoric acid at 195 V. In all cases the bath temperature was 3 °C.

The formation of porous aluminum oxide results from the simultaneous occurrence of several processes: the oxidation of aluminum, the reduction of water, the

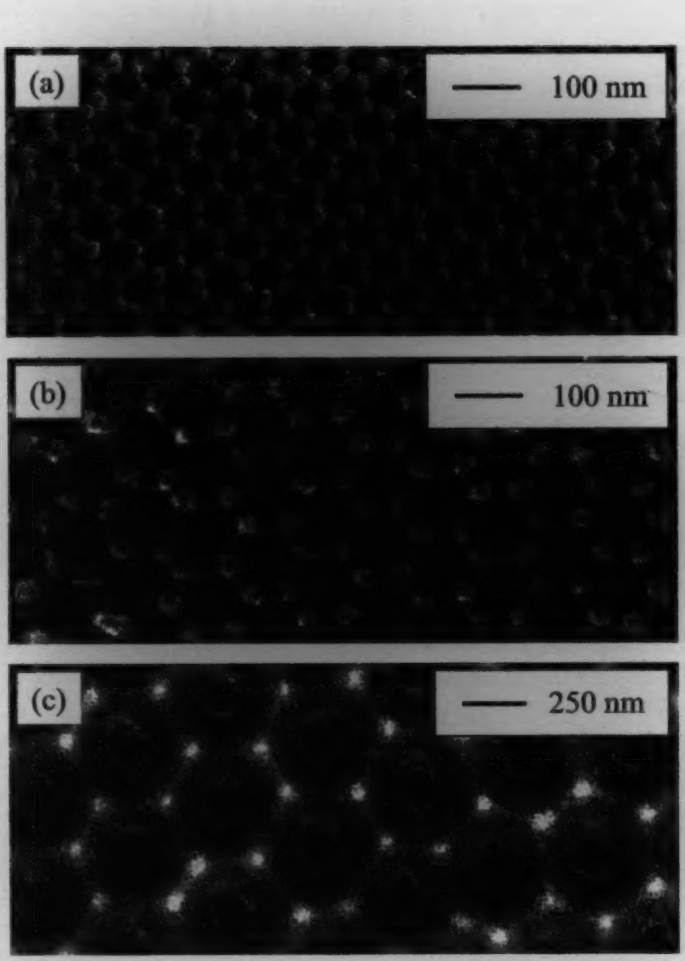

Figure 6.2. SEM images PAO templates anodized in sulfuric acid (a), oxalic acid (b), and phosphoric acid (c).

mass transport of ions through the electrolyte and the oxide layer, the growth of aluminum oxide at the metal/oxide interface, and the dissolution of aluminum oxide at the oxide/electrolyte interface.[40,41] Electric fields concentrated at pore tips can explain propagation of pores formed at surficial defects, but are insufficient to cause self-ordering of the pores.[42] Ordering of the pores requires a suitable mechanical strain at the interface of the Al and Al_2O_3 layers, which is achieved when an appropriate set of anodization conditions (temperature, electrolyte concentration, and voltage) are employed. The degree of strain at the interface is a function of the volume expansion (volume expansion is the ratio of the thickness of aluminum oxide formed to the thickness of aluminum consumed) resulting from the conversion of aluminum to aluminum oxide, followed by its partial dissolution.[42,43] With all other conditions constant, volume expansion may vary from 0.8 to 1.7 with increasing potential.[43]

For ordered growth to occur, volume expansion in the range of 1.2 to 1.4 is required, which corresponds to 60 to 70 % of the aluminum consumed being incorporated into the aluminum oxide.[40,43] When this occurs the mechanical strain in the material will be greatest in the solid areas of the oxide, and least in porous areas. The most stable porous aluminum oxide layer will occur when the pores are uniformly distributed, resulting in the pores ordering into a close-packed array.[42,43] If the mechanical strain is too low, this driving force is minimized and pore growth will not be ordered. If the mechanical strain is too great, the number of structural defects in the PAO will increase and pore growth will be irregular.[42] It is possible to vary the structure and short range order of the PAO layer by changing the anodization voltage, since the interpore spacing, and the equilibrium barrier layer thickness, are proportional to the voltage employed.[40]

However, as the voltage is varied, the electrolyte, electrolyte concentration, and temperature must also be changed to obtain a suitable volume expansion and mechanical strain, which is necessary for longer range ordering and formation of a close packed pore array.[40] The electrolyte composition and temperature also determines the diameter of the pores;[40] however, if larger pores are desired a post-growth etching may be employed.

When anodization is initiated, a thin barrier layer of thickness proportional to the anodization voltage is formed. The initial growth of this barrier layer is rapid, due to high current flow; however, as the thickness of the barrier increases, so too does electrical resistance--current drops off rapidly and growth slows.[41] The current flow is then concentrated through surface irregularities (thin spots, surface features) in the barrier layer, resulting in field and/or temperature enhanced dissolution at these points.[41,42] This results in the formation of pores that are located on the surface according to the positions of these irregularities. As a result, pore formation is random, with the regular array of pores developing over time as the aluminum oxide grows into the aluminum and repulsive forces between the pores increase.[41,42] This results in a discontinuity between the pore openings on the surface and the pore bottoms.

Formation of uniform, cylindrical, hexagonally ordered pores requires the use of a two-step anodization process[44,45] or pre-surface patterning.[46,47] When the two-step method is employed the first anodization is allowed to proceed until the pore bottoms grow into an ordered arrangement, producing a patterning on the aluminum substrate that mirrors the close-packed ordering of the pore bottoms.[44] This aluminum oxide layer is then chemically etched off, exposing the patterned aluminum surface. When anodized for a second time under identical conditions the patterning on the aluminum serves as initiation sites for pore formation, resulting in growth of ordered, close-packed hexagonal pores that are uniform and continuous from top to bottom.[40] The length of this second anodization determines the depth of the pores. SEM images of the rounded pore bottoms, underside of the PAO layer showing the ordered arrangement of the pore patterns, and the resultant patterning of the Al substrate required for producing ordered growth during the second anodization are shown in Figure 6.3.

Electrodeposition into Porous Aluminum Oxide Templates

Deposition into PAO templates using direct current electrodeposition has proven to be a particularly powerful technique, enabling substantial control over composition and crystallinity,[5] and easy access to compositional modulation along the wire lengths.[17] However, none of the DC techniques reported to date are amenable to industrial-scale processing, due to the laborious pre-processing that must be performed on the PAO template before deposition. In contrast, alternating current electrodeposition into PAO templates requires fewer processing steps and is more amenable to scale-up, but currently provides for less control over the structure of the material deposited. Schemes comparing and contrasting the two approaches to electrodeposition are presented in Figure 6.4.

Direct current electrodeposition into PAO templates is most commonly performed by removing the remaining aluminum substrate, opening the pore bottoms via etching in phosphoric acid, and finally depositing a conducting layer, such as gold, on one face of the template (Figure 6.4).[5,12,16-18,40] More recently, Gösele and coworkers have reported a method where the barrier layer was thinned to a thickness proportional to 1 V final anodization potential, at which point the barrier layer is thin enough to enable DC

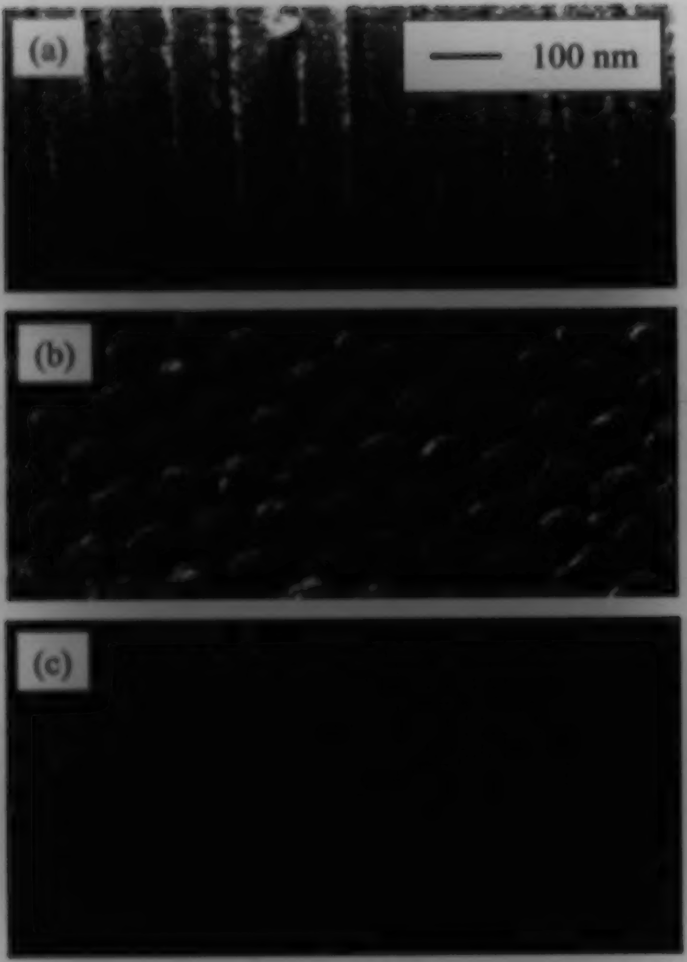

Figure 6.3. SEM images of pore-bottoms separated from aluminum substrate (a), underside of PAO showing close-packed arrangement of pore-bottoms (b), and patterned surface of the aluminum substrate where the PAO has peeled away (c).

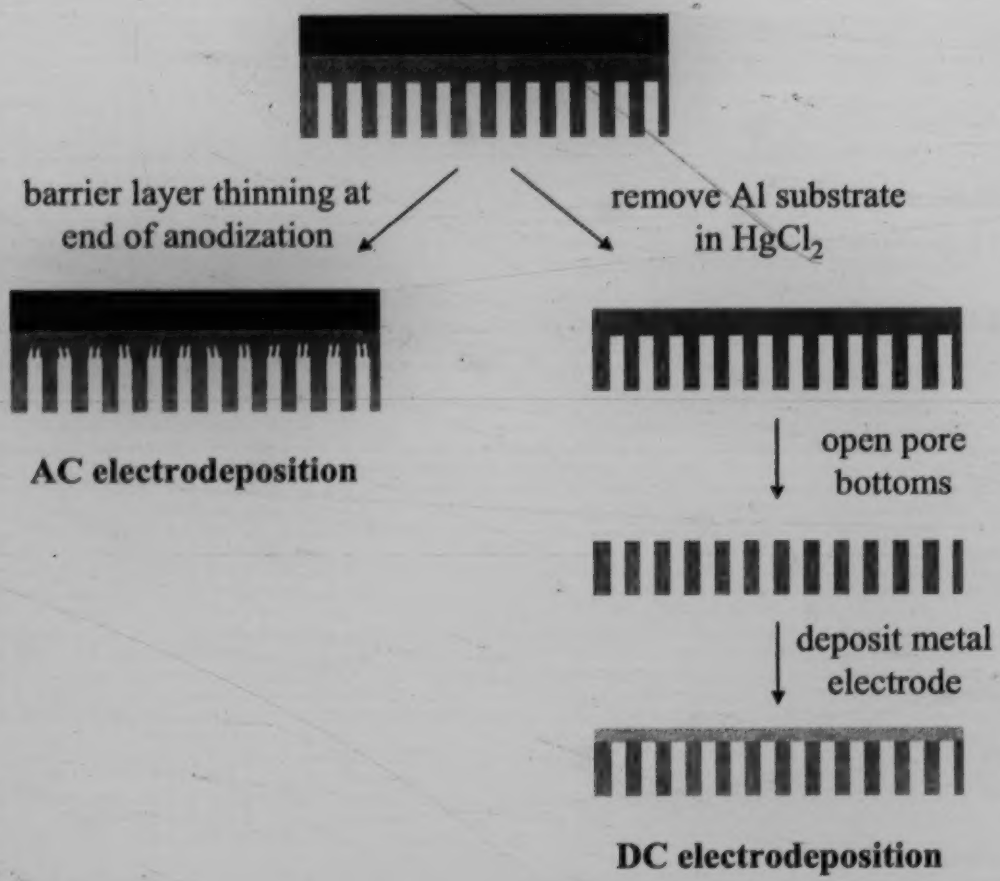

Figure 6.4. AC electrodeposition (left scheme) requires only a simple barrier layer thinning process at the end of the second anodization, and is easily scalable, but provides less control over the deposition. DC electrodeposition (right scheme) requires extensive and laborious post-anodization processing of the PAO template, and is not easily scalable, but provides increased control over the deposition.

electrodeposition without the prior removal of the aluminum substrate.[4] Using this method, electrodeposition of 30 μm long silver nanowires was achieved; however, this degree of barrier layer thinning is time consuming and must be precisely controlled to ensure that the resultant barrier layer is thinned uniformly.[4] Also recently, Stacey and coworkers have reported DC electrodeposition into PAO formed by depositing silver onto one side of a thin (<100 μm thick) Al foil, preparing an electrode, and anodizing the Al completely to the silver film.[3] However, this requires adhesion of a very thin foil to a substrate (such as glass), and it is difficult to uniformly anodize the entire foil completely to the silver film. For industrial scale processes, or applications where a rapid and simple method of template production is required, it is still preferable to develop an AC electrodeposition process that produces wires with length and uniformity comparable to that obtained with DC electrodeposition.

Without separation from the barrier layer or implementation of complex processing strategies such as those outlined above, electrodeposition into PAO templates is only possible under AC conditions, as a result of the aluminum oxide barrier layer at the base of the pores that is formed during the anodization process. This barrier layer blocks direct current with a high resistance of 10^{10} to 10^{12} $\Omega\cdot$cm.[49] However, under alternating current the anodic aluminum oxide is found to conduct preferentially in the cathodic direction and, as such, aluminum is known as a valve metal.[50,51] This inherent rectifying property of the barrier layer allows the reduction of ions in the pores during cathodic half-cycles, without allowing re-oxidation during the anodic half-cycles.[49,51-54] However, since the barrier layer is highly resistive, ease of electrodeposition is enhanced by slightly reducing the barrier layer thickness by chemical etching (which also increases the pore diameters), or by electrochemical barrier layer thinning, both of which are simple processes that generally require ~30-60 minutes at the end of the anodization.[2,51,52,55,56] The commonly employed electrochemical thinning is achieved by gradually reducing the anodization voltage to produce a thinner barrier layer, after the pores are grown to the desired depth. A secondary consequence of the reduced voltage is that conditions are no longer appropriate for achieving pore ordering in the electrolyte, and dendritic branching of the pore bottoms is typically observed (Figure 6.4).[52] For PAO templates formed at higher anodization potentials (and consequently having a thicker barrier layer), some degree of barrier layer thinning is essential to enable electrochemical deposition, even under AC conditions.

AC electrodeposition through the barrier layer is a complicated process, dependent on a variety of conditions, including: anodization electrolyte, barrier layer thickness, electrolyte concentration, composition, and temperature, deposition voltage, frequency, wave form (sine, square, and triangle), pulse polarity and sequence, and the metal deposited.[54,55,57,58] This complexity is due in large part to the complex and ill-defined chemical and structural nature of the barrier layer, particularly after barrier layer thinning. The structure of the barrier layer also changes over the course of the deposition, and dynamic changes occur in the barrier layer and the electrolyte in the pores during each deposition cycle.[58] As a result, optimizing template preparation and electrochemical deposition conditions is a formidable task.

In Chapter 7, the effect of multiple variables on the quality of pore-filling with copper using AC electrodeposition is reported. The variables studied include: final anodization potential (barrier layer thickness), AC deposition voltage, AC deposition frequency, pulsed or continuous deposition, electrolyte concentration, wave shape, and pulse polarity. The feasibility of copper electrodeposition into the pores of a PAO template under AC conditions has been reported by Moskovits and coworkers; however, experimental details were not reported and the resultant wires filled on average half the depth of the 5 μm deep pores.[59] Electrodeposition of other metals (including iron, nickel cobalt, cadmium, bismuth, gold, and silver) into PAO templates under AC conditions has also been reported.[51-54,57,60,61] Nearly all of the reported AC depositions through the barrier layer have been into <25 nm diameter, sulfuric acid grown pores. In most cases the quality of pore filling, in terms of length uniformity of the resultant wires and the height to which the pores were filled, is not reported. In cases in which complete pore filling has been reported, pore depth has ranged from 600 nm[53] to 2 μm.[60] With variation in pore diameter accessible by changing the electrolyte, and pore depths of well over 100 μm available, it is clear that AC techniques capable of uniformly filling much deeper pores of varying diameters would be of use. The results reported in Chapter 7 represent a significant improvement in the quality of pore-filling achieved with AC techniques for copper deposition into pores of varying diameter, and depth. It is expected that this advance can be leveraged to further improve the quality of pore-filling with copper, and other metals, into the pores of PAO templates by AC electrodeposition.

References

(1) Klein, J. D.; Herrick, R. D.; Palmer, D.; Sailor, M. J.; Brumlik, C. J.; Martin, C. R. *Chem. Mat.* **1993**, *5*, 902-904.

(2) Routkevitch, D.; Tager, A. A.; Haruyama, J.; Almawlawi, D.; Moskovits, M.; Xu, J. *IEEE Trans. Electr. Dev.* **1996**, *43*, 1646-1658.

(3) Sander, M. S.; Prieto, A. L.; Gronsky, R.; Sands, T.; Stacy, A. M. *Adv. Mater.* **2002**, *14*, 665-667.

(4) Choi, J.; Sauer, G.; Nielsch, K.; Wherspohn, R. B.; Gösele, U. *Chem. Mater.* **2003**, *15*, 776-779.

(5) Tian, M.; Wang, J. U.; Kurtz, J.; Mallouk, T. E.; Chan, M. H. W. *Nano Lett.* **2003**, *3*, 919-923.

(6) Han, C.-C.; Bai, M.-Y.; Lee, J.-T. *Chem. Mater.* **2001**, *13*, 4260-4268.

(7) Shelimov, K. B.; Moskovits, M. *Chem. Mater.* **2000**, *12*, 250-254.

(8) Steinhart, M.; Wendorff, J. H.; Greiner, A.; Wherspohn, R. B.; Nielsch, K.; Schilling, J.; Gösele, U. *Science* **2002**, *296*, 1997.

(9) Brumlik, C. J.; Menon, V. P.; Martin, C. R. *J. Mater. Res.* **1994**, *9*, 1174-1181.

(10) Kline, T. R.; Tian, M.; Wang, J.; Sen, A.; Chan, M. W. H.; Mallouk, T. E. *Inorg. Chem.* **2006**, *45*, 7555-7565.

(11) Cheng, B.; Murray, C. W.; Samulski, E. T. *Mat. Res. Soc. Symp. Proc.* **2003**, *737*, F3.23.21-25.

(12) Nicewarner-Pena, S. R.; Freeman, R. G.; Reiss, B. D.; He, L.; Pena, D. J.; Walton, I. D.; Cromer, R.; Keating, C. D.; Natan, M. J. *Science* **2001**, *294*, 137-141.

(13) Kovtyukhova, N. I.; Martin, B. R.; Mbindyo, J. K. N.; Mallouk, T. E.; Cabassi, M.; Mayer, T. S. *Mater. Sci. Eng. C* **2002**, *19*, 255-262.

(14) Zhang, Y.; Wang, C.; Rothberg, L.; Ng, M.-K. *J. Mater. Chem.* **2006**, *16*, 3721-3725.

(15) Huczko, A. *Appl. Phys. A* **2000**, *70*, 365-376.

(16) Martin, C. R. *Science* **1994**, *266*, 1961-1966.

(17) Hulteen, J. C.; Martin, C. R. *J. Mater. Chem.* **1997**, *7*, 1075-1087.

(18) Shingubara, S. *J. Nanopart. Res.* **2003**, *5*, 17-30.

(19) Thompson, G. E.; Wood, G. C. In *Treatise on Materials Science and Technology*; Scully, J. C., Ed.; Academic Press: New York, 1983; Vol. 23 Corrosion: Aqueous Processes and Passive Films, pp 205-329.

(20) Thompson, G. E. *Thin Solid Films* **1997**, *297*, 192-201.

(21) Diggle, J. W.; Downie, T. C.; Goulding, C. W. *Chem. Rev.* **1968**, *69*, 365-405.

(22) Schuchert, I. U.; Molares, M. E. T.; Dobrev, D.; Vetter, J.; Neumann, R.; Martin, M. *J. Electrochem. Soc.* **2003**, *150*, C189-C194.

(23) Chakarvarti, S. K.; Vetter, J. *J. Micromech. Microeng.* **1993**, *3*, 57-59.

(24) Martin, C. R. *Acc. Chem. Res.* **1995**, *28*, 61-68.

(25) Piraux, L.; Dubois, S.; Duvail, J. L.; Radulescu, A.; Demoustier-Champagne, S.; Ferain, E.; Legras, R. *J. Mater. Res.* **1999**, *14*, 3042-3050.

(26) Chakarvarti, S. K.; Vetter, J. *Nucl. Instrum. Methods Phys. Res. B* **1991**, *62*, 109-115.

(27) Schönenberger, C.; van der Zande, B. M. I.; Fokkink, L. G. J.; Henny, M.; Schmid, C.; Krüger, M.; Bachtold, A.; Huber, R.; Birk, H.; Staufer, U. *J. Phys. Chem. B* **1997**, *101*, 5497-5505.

(28) Gao, Y.; Jiang, P.; Liu, D. F.; Yaun, H. J.; Yan, X. Q.; Zhou, Z. P.; Wang, J. X.; Song, L.; Liu, L. F.; Zhou, W. Y.; Wang, G.; Wang, C. Y.; Xie, S. S. *Chem. Phys. Lett.* **2003**, *380*, 146-149.

(29) Gao, Y.; Jiang, P.; Liu, D. F.; Yaun, H. J.; Yan, X. Q.; Zhou, Z. P.; Wang, J. X.; Song, L.; Liu, L. F.; Zhou, W. Y.; Wang, G.; Wang, C. Y.; Xie, S. S.; Zhang, J. M.; Shen, A. Y. *J. Phys. Chem. B* **2004**, *108*, 12877-12881.

(30) Murphy, C. J.; San, T. K.; Gole, A. M.; Orendorff, C. J.; Gao, J. X.; Gou, L.; Hunyadi, S. E.; Li, T. *J. Phys. Chem. B* **2005**, *109*, 13857-13870.

(31) Sun, Y. G.; Gates, B.; Mayers, B.; Xia, Y. N. *Nano Lett.* **2002**, *2*, 165-168.

(32) Sun, Y. G.; Mayers, B.; Herricks, T.; Xia, Y. N. *Nano Lett.* **2003**, *3*, 955-960.

(33) Caswell, K. K.; Bender, C. M.; Murphy, C. J. *Nano Lett.* **2003**, *3*, 667-669.

(34) Hu, J. Q.; Chen, Q.; Xie, Z. X.; Han, G. B.; Wang, R. H.; Ren, B.; Zhang, Y.; Yang, Z. L.; Tan, Z. Q. *Adv. Funct. Mater.* **2004**, *14*, 183-189.

(35) Jana, N. R.; Gearheart, L.; Murphy, C. J. *Chem. Commun.* **2001**, 617-618.

(36) Zhang, S. H.; Jiang, Z. Y.; Xie, Z. X.; Xu, X.; Huang, R. B.; Zheng, L. S. *J. Phys. Chem. B* **2005**, *109*, 9416-9421.

(37) Wang, Z. H.; Liu, J. W.; Chen, X. Y.; Wan, J. X.; Qian, Y. T. *Chem.--Eur. J.* **2005**, *11*, 160-163.

(38) Liu, F. K.; Huang, P. W.; Chang, Y. C.; Ko, F. H.; Chu, T. C. *J. Mater. Res.* **2004**, *19*, 469-473.

(39) Murphy, C. J.; Gole, A. M.; Hunyadi, S. E.; Orendorff, C. J. *Inorg. Chem.* **2006**, *45*, 7544-7554.

(40) Wehrspohn, R. B.; Li, A. P.; Nielsch, K.; F. Muller; Erfurth, W.; Gösele, U. In *Proceedings of the 197th Meeting of the Electrochemical Society*; Herbert, K. R., Lillard, R. S., MacDougall, B. R., Eds.: Toronto, 2000, pp 271-282.

(41) Jessensky, O.; Muller, F.; Gösele, U. *J. Electrochem. Soc.* **1998**, *145*, 3735-3740.

(42) Jessensky, O.; Muller, F.; Gösele, U. *Appl. Phys. Lett.* **1998**, *72*, 1173-1175.

(43) Li, A. P.; Muller, F.; Birner, A.; Nielsch, K.; Gösele, U. *J. Appl. Phys.* **1998**, *84*, 6023-6026.

(44) Masuda, H.; Hasegwa, F.; Ono, S. *J. Electrochem. Soc.* **1997**, *144*, L127-L130.

(45) Masuda, H.; Yada, K.; Osaka, A. *Jpn. J. Appl. Phys.* **1998**, *37*, L1340-L1342.

(46) Asoh, H.; Nishio, K.; Nakao, M.; Tamamura, T.; Masuda, H. *J. Electrochem. Soc.* **2001**, *148*, B152-B156.

(47) Choi, J.; Luo, Y.; Wehrspohn, R. B.; Hillebrand, R.; Schilling, J.; Gösele, U. *J. Appl. Phys.* **2003**, *94*, 4757-4762.

(48) Zhang, X. Y.; Zhang, L. D.; Lei, Y.; Zhao, L. X.; Mao, Y. Q. *J. Mater. Chem.* **2001**, *11*, 1732-1734.

(49) Sellmyer, D. J.; Zheng, M.; Skomski, R. *J. Phys.: Condens. Matter* **2001**, *13*, R433-R460.

(50) Lohrengel, M. M. *Mater. Sci. Eng. R* **1993**, *11*, 243-294.

(51) AlMawlawi, D.; Coombs, N.; Moskovits, M. *J. Appl. Phys.* **1991**, *70*, 4421-4425.

(52) Nielsch, K.; Muller, F.; Li, A.-P.; Gösele, U. *Adv. Mater.* **2000**, *12*, 582-586.

(53) Sun, M.; Zangari, G.; Shamsuzzoha, M.; Metzger, R. M. *Appl. Phys. Lett.* **2001**, *78*, 2964-2966.

(54) Yin, A. J.; Li, J.; Jian, W.; Bennett, A. J.; Xu, J. M. *Appl. Phys. Lett.* **2001**, *79*, 1039-1041.

(55) Sun, M.; Zangari, G.; Metzger, R. M. *IEEE Trans. Magn.* **2000**, *36*, 3005-3008.

(56) Masuda, H.; Tanaka, H.; Baba, N. *Bull. Chem. Soc. Jpn.* **1993**, *66*, 305-311.

(57) Preston, C.; Moskovits, M. *J. Phys. Chem.* **1993**, *97*, 8495-8503.

(58) Gerein, N. J.; Haber, J. A. *J. Phys. Chem. B* **2005**, *109*, 17372-17385.

(59) Davydov, D. N.; Sattari, P. A.; AlMawlawi, D.; Osika, A.; Haslett, T. L.; Moskovits, M. *J. Appl. Phys.* **1999**, *86*, 3983-3987.

(60) Sauer, G.; Brehm, G.; Schneider, S.; Nielsch, K.; Wherspohn, R. B.; Choi, J.; Hofmeister, H.; Gösele, U. *J. Appl. Phys.* **2002**, *91*, 3243-3247.

(61) AlMawlawi, D.; Liu, C. Z.; Moskovits, M. *J. Mater. Res.* **1994**, *9*, 1014-1018.

Chapter 7. Effect of AC Electrodeposition Conditions on the Growth of High Aspect-Ratio Copper Nanowires in Porous Aluminum Oxide Templates

Introduction

In Chapter 6 porous aluminum oxide was shown to offer numerous benefits as a template material, including tunable pore diameter and depth, scalable production, and the ability to accommodate numerous methods of pore-filling, leading to diverse nano-structured materials. Of the pore-filling techniques available, AC electrodeposition through the resistive barrier layer was identified as a method compatible with the scalable nature of the PAO template, offering a low-cost, high-throughput route to metal nanowires.

In general, AC electrodeposition through the aluminum oxide barrier layer is a complicated process, with quality of pore-filling varying as a function of deposition conditions, including: electrolyte concentration, composition, and temperature;[1,2] and deposition voltage, frequency, wave form (sine, square, and triangle),[1-4] pulse polarity and sequence.[2] Moreover, the optimal deposition conditions appear to depend upon the metal or compound deposited.[1] This observed complexity is not surprising, since the chemical and structural nature of the barrier layer is complex and ill-defined, particularly after barrier layer thinning. It is also reasonable to expect that the structure of the barrier layer will be modified over the minutes to hours required for the electrodeposition. Add to this the dynamic changes occurring in the barrier layer and the electrolyte in the pores during a single deposition cycle, and optimizing the template preparation and electrochemical deposition conditions becomes a formidable task.

To identify a set of optimized conditions for AC electrodeposition of copper into PAO templates a systematic study of the effect of multiple variables has been carried out. Promising initial deposition conditions were identified using a fractional-factorial design of experiment, an experimental method that enables the simultaneous study of the effect of multiple variables on a response of interest.[5] In this approach, multiple variables are simultaneously changed in each carefully designed experiment, rather than changing only one variable while holding all others constant between experiments. The advantages of a FFDOE include determining the effect of several variables using fewer experiments, and insight into multiple-variable interactions. This method was used to examine the effect of final anodization potential (barrier layer thickness), AC deposition voltage, AC deposition frequency, pulsed or continuous deposition, and electrolyte concentration on the quality of pore-filling in oxalic acid-grown templates. This resulted in the identification of AC and pulsed AC conditions enabling the filling of 4 μm deep oxalic acid-anodized pores. It also identified damage occurring to the template under continuous deposition conditions, leading to the preferential use of pulsed AC electrodeposition conditions. By rational examination of these results and consideration of the effect of wave shape and pulse polarity, a further optimized set of pulsed AC conditions incorporating a square wave was developed enabling the filling of deeper oxalic and sulfuric acid-anodized pores. Quality of pore-filling was determined using SEM of pore cross-sections and of as-deposited and ion-milled surfaces. The structure and crystallinity of the resultant wires was studied using XRD of in-situ wires and TEM of liberated nanowires.

Experimental Details

Electrode Preparation. All electrodes were constructed from Aldrich or Alfa Aesar high purity aluminum foil (99.99+%), 1 mm thick, annealed in air at 500 °C for 24 hours in a tube furnace. Aluminum pieces, 1.7 cm x 1.0 cm in size, were etched in 1.3 M sodium hydroxide at 60 °C for 2 minutes to remove the native oxide layer and to clean and degrease the foil. After etching, the foil was rinsed in distilled water. Two methods of electrode construction were employed. For the FFDOE, an 18 gauge tin-plated copper wire was soldered to the back of the foil with Pb/Sn solder and the back and edges of the electrode and the wire were encapsulated in Dexter Hysol Epoxi-Patch structural adhesive, and the exposed wire sealed into a 20 cm long Pyrex tube. For wave shape and pulse polarity experiments the Al foil was anodized directly on both sides by attaching a copper clip to a portion of the foil not immersed in the electrolyte. A bead of structural adhesive was applied to separate the immersed electrode area from the electrical contact area to provide a well defined anodization surface and prevent runaway anodization at the electrolyte/air/aluminum interface. The encapsulation was eliminated on these electrodes to simplify electrode mounting for post deposition ion milling (see below).

Immediately prior to anodization the sodium hydroxide etching was repeated, and each electrode was electropolished at 3 ± 2 °C in a magnetically stirred 100 ml aliquot of a solution composed of 130 ml 70% perchloric acid, 600 ml ethanol, 90 ml 2-butoxyethanol, and 135 ml distilled water.[6] The aluminum electrode was set as the anode against a platinum gauze counter electrode and electropolished to a mirror-like finish at 500 mA/cm^2 using a KEPCO BOP 100-1M or Lambda EMS 300-3.5 power supply in three 10 second intervals with 15 second cooling periods between each interval. Following electropolishing each electrode was rinsed in distilled water.

Anodization of the aluminum electrode was carried out in a two-step process following the methods of Masuda: 0.30 M sulfuric acid at 25.0 V,[7] and 0.30 M oxalic acid at 40.0 V.[8] Anodizations were carried out at 3 ± 2 °C with magnetic stirring against a platinum gauze counter electrode. The potential was applied using one of a variety of commercially available or in-house fabricated DC power supplies. Following an initial anodization of two hours, electrodes were rinsed in distilled water and the oxide layer etched off in a 1:1 mixture of 0.2 M chromic acid and 0.6 M phosphoric acid at 60 °C for 30 minutes.[9] This was followed by a second anodization of two hours to ten hours depending on the electrolyte and the pore depth desired. Growth rates of the PAO layer were approximately 6.0 µm/hour in sulfuric acid, and 2.4 µm/hour in oxalic acid. Pore diameters were 20 nm and 35 nm in sulfuric and oxalic acid-anodized templates, respectively. Following the second anodization, the voltage was systematically reduced in order to promote thinning of the barrier layer. In oxalic acid the voltage was lowered by 2 V/minute until 30 V was reached, after which the voltage was lowered by 1 V/minute until a final anodization voltage of 15 V or 10 V was reached, depending on the barrier layer thickness required. The anodization was then continued for 10 minutes at this final voltage to allow for partial equilibration of the barrier layer. In sulfuric acid-anodized pores barrier layer thinning was achieved by reducing the voltage by 2

V/minute to 19 V, 1 V/minute to 10 V, and finally holding the voltage at 10 V for 8 minutes.

Electrodeposition. Prior to electrodeposition, the edges of the face of the encapsulated electrodes were re-sealed with epoxy to prevent current leakage through aluminum exposed along the edges of the Al_2O_3 where the Al/Al_2O_3 was no longer in contact with the epoxy as a result of electropolishing and removal of Al_2O_3 produced during the first anodization step. On the non-encapsulated electrodes, the back and edges of the electrodes were sealed with nail polish to produce an electrode with only one face exposed. In all cases the macroscopic active area of the electrode was approximately 1 cm^2. Each electrode was then immersed in an ultrasonic bath in distilled H_2O for 5-15 minutes (depending upon pore depth), soaked in water for an additional 5 minutes to ensure thorough pore wetting, and then equilibrated in the deposition bath a further 5 minutes prior to deposition. For electrodeposition the AC signal, applied across the PAO electrode and a platinum gauze counter electrode, was generated using a Tabor 8023 arbitrary function generator, and amplified with a KEPCO BOP 100-1M amplifier to the desired voltage.

Fractional Factorial Design of Experiment. A ¼ fraction, resolution III, FFDOE[9] was employed to examine the effect of five variables (final anodization voltage, deposition voltage, deposition frequency, pulsed or continuous deposition, cupric sulfate concentration), on three different responses: pore-filling as measured by the percentage of pores that were filled completely, wire length dispersity qualitatively categorized based on the difference between the maximum and minimum pore filling, and pitting of the electrode qualitatively categorized based on the degree of damage to the template. All runs were performed in duplicate, requiring 16 runs in total.

For the FFDOE specific conditions for each run were determined by the experimental design, with experimental design and analysis performed using Minitab statistical software (©1972-2004 Minitab Inc., www.minitab.com). Variables were each set at a low and high level, chosen to lie within the condition space expected to produce reasonable quality results based on extensive previous experiments employing a wide variety of sine wave voltages, frequencies, pulse frequencies, barrier layer thinning processes, and electrolyte compositions. All runs utilized oxalic acid-anodized templates with a pore depth of 4 μm, and final anodization voltages of 10 V or 15 V. The variable levels and deposition times employed in the FFDOE are summarized in Table 7.1.

Table 7.1. Summary of deposition variables employed for FFDOE.

variable level	deposition voltage (V_{rms})	deposition frequency (Hz)	trigger frequency (Hz)	electrolyte (M)	deposition time* (min)
low	12	50	20 (pulsed)	0.50 $CuSO_4$/ 0.57 H_3BO_3	15-25 (pulsed)
high	14	200	200 (continuous)	1.0 $CuSO_4$/ 0.57 H_3BO_3	1.5-2.5 (continuous)

* deposition time was scaled with deposition voltage over the ranges stated

Following collection of the responses for each set of conditions in the experiment, the data was analyzed using normal probability plots. Those main variables and interactions that produced an effect outside of a normal probability were flagged, with the magnitude of the effect indicated by the degree of deviation from normal probability.

The data corresponding to flagged variables and interactions were then removed from the data set, and the residual data analyzed to verify that all residuals were random and all effects within a normal distribution.

Wave Shape and Pulse Polarity. Wave shape and pulse polarity experiments were carried out using oxalic and sulfuric acid-anodized pores, with pore depths of 12.4 ± 0.6 μm (sine wave depositions only) and 24.3 ± 1.2 μm deep pores (sine wave and square wave depositions). In all cases the final anodization voltage was 10 V. The electrolyte was 0.50 M $CuSO_4$/0.57 M H_3BO_3 for all depositions, and the electrodeposition variables employed for wave shape and pulse polarity experiments were: 200 Hz (5 ms duration) wave-forms, single pulses triggered at 20 Hz (50 ms intervals), with a sine wave voltage of 13 V_{rms} (18.4 V_{peak}), and a square wave voltage of 17 V_{peak}. Current data was recorded using a Tektronix TDS 1002 digital capture oscilloscope equipped with a compact flash memory module reading a current sense (pin 10) on the KEPCO amplifier. A current trace corresponding to one 5 ms pulse cycle was recorded at specific times during each deposition. Deposition times for sulfuric acid-anodized pores were 17 minutes (current trace recorded at 5 and 15 minutes) and 35 minutes (current trace recorded at 5, 15, and 30 minutes) for 12 μm and 24 μm pore depths, respectively. Deposition times for oxalic acid-anodized pores were 35 minutes (current trace recorded at 5 and 30 minutes) and 75 minutes (current trace recorded at 5, 35, and 65 minutes) for 12 μm and 24 μm pore depths, respectively. Using this data, average net charge density (summed over entire pulse width), average component charge density (summed separately for oxidative and reductive components of the pulse), and average current density traces were determined for each set of deposition conditions and pore type.

Square waves used for wave shape and pulse polarity experiments were selected based upon preliminary experiments performed using square waves with voltages ranging from 13 V_{peak} to 22 V_{peak}. Pulse frequency and pulse width were also varied with 200 Hz square waves pulsed at 5 Hz, 100 Hz square waves pulsed at 10 Hz, and 80 Hz square wave with 60% duty on the reductive component (7.5 ms reductive component/5 ms oxidative component) pulsed at 6.5 Hz. In these preliminary experiments other variables, such as electrolyte composition and final anodization voltage, remained fixed at those levels which had been identified as optimum for sine wave depositions in the results of the FFDOE. It was found that higher square wave voltages produced inconsistent results, while variations in pulse trigger frequency and pulse width did not noticeably alter the quality of deposition. Qualitatively, the best results were achieved with square wave conditions chosen for pulse polarity and wave shape experiments outlined above. Sine wave conditions for pulse polarity and wave shape experiments were those identified as optimum in the FFDOE.

Characterization of Pore Filling. The quality of pore filling (percentage of pores filled and the height to which they were filled) was evaluated by SEM (JEOL 6031F FESEM) analysis of cross-sections and of as-deposited and ion milled surfaces of PAO/copper samples. Cross-sections were prepared by cutting the electrodes from the back until approximately 90% of the aluminum substrate was severed. This was judged by observing the cross section of the electrode visually, as well as by the appearance of cracks in the porous aluminum oxide surface. The electrode was then pulled apart in the plane of the electrode with force applied perpendicular to the cut. This resulted in a clean exposure of the pore cross-sections suitable for characterization of pore filling and PAO film thickness.

In order to quantitatively assess the effects of pulse polarity and wave shape on the degree of pore filling, the as-deposited samples were milled to uniformly expose the pore openings at the surface of the template, or at some specified depth below the initial surface. Milling of samples was carried out using an Oxford Ion Fab 300+ ion mill. These surfaces were characterized by SEM, and the percentage pore filling determined using Image J image analysis software (Wayne Rasband, Research Services Branch, National Institute of Mental Health, Bethesda, Maryland, USA, http://rsb.info.nih.gov/ij/). All samples were analyzed at three randomly selected points distributed across the surface of the sample, and a representative percentage pore filling calculated.

Wire Characterization. Wires were characterized in situ by XRD (Bruker D8 diffractometer with area detector). Powder patterns were collected on as-deposited samples, as well as on samples which had been ion milled to remove surface deposition. Liberated wires were characterized by TEM (JEOL 2010 TEM equipped with a CCD camera and EDX system). To prepare TEM samples, the PAO template was dissolved in 0.6 M phosphoric acid at 60 °C, or 0.1 M sodium hydroxide at 40 °C. The liberated wires were then rinsed multiple times in distilled water, and finally dispersed in methanol. At each stage wires were sonicated in an ultrasonic bath for 1-2 minutes, and solvent exchange was carried out by centrifuging, extracting the supernatant, and adding fresh solvent. To prepare the TEM sample, one drop of the final suspension in methanol was placed on a nickel/lacy carbon TEM grid and the methanol allowed to evaporate.

Results

Fractional Factorial Design of Experiment. In a full factorial design of experiment each variable of interest is set at different levels, and all possible combinations of variables and their levels are determined, with these combinations constituting the complete experiment. This is simplified when each variable is set at only two levels (high and low), in which case the number of experiments for a full factorial design is given by 2^k where k is the number of variables.[5] There are several advantages to this type of experiment. First of all, it can provide information simultaneously on multiple variables. Secondly, it provides information on multi-variable interactions. In a one-factor-at-a-time approach each variable is examined against a predetermined and fixed background of the other variables. As a consequence, information obtained from this type of experiment is only relevant if the effects of the variables are additive.

While full factorial experiments are useful for examining multiple variables simultaneously, it is likely that any such design will contain a certain amount of redundancy. This arises for two reasons. First of all, a full factorial design includes all multi-variable interactions and it is likely that higher order interactions will be insignificant. Secondly, when a large number of variables are being screened it is likely that some of them will have no effect on the response of interest. When these two concepts are combined it is realized that many runs might be eliminated without losing any useful information.[5] This is what is known as a fractional factorial design. The possible fractions for a two level design are of the type $1/2^n$, where n is any positive integer. Since a fraction of the full factorial has been eliminated, all multi-variable interactions are no longer resolved, and as a result lower order interactions are confounded with higher order interactions. As the fraction of the experiment is varied, the resolution of the experiment will vary as well, with the resolution of a design being a statement of the confounding pattern.[5] Since we assume that higher order interactions are negligible, a confounded effect will usually be attributed to the lower order interaction. However, this confounding may occasionally lead to ambiguity when interpreting results, in particular with lower resolution designs.[5]

To examine the effect of 5 variables on pore filling, a ¼ fraction, resolution III design was employed, comprised of 8 sets of experimental conditions, each of which was run in duplicate. In a resolution III design, the main effects are confounded with two-factor interactions. The experiment was designed and analyzed using Minitab statistical software. The five variables, each set at high and low levels, were as follows: final anodization voltage (10/15 V), deposition voltage (12/14 V_{rms}), deposition frequency (50/200 Hz), pulsed or continuous deposition (pulsed at 10% of waveform frequency/100% of waveform frequency), cupric sulfate concentration (0.5/1.0 M). The details of each of the 8 different sets of conditions employed in this experiment are summarized in Table 7.2.

The samples from the 16 runs were characterized via SEM of sample cross-sections in order to determine the percent uniform pore filling. This was qualitatively judged to be the pore depth to which 90% of the pores were filled and calculated as a percentage of the total pore depth. These percentages are listed in Table 7.2, along with the corresponding deposition conditions. Two other responses, the wire length dispersity, and pitting of the electrode, were assessed qualitatively on a scale of one to three. For dispersity, 1 was equated with monodisperse wire lengths, 3 with highly polydisperse

Table 7.2. Summary of runs and responses for ¼ fraction resolution III experimental design for identification of deposition conditions enabling filling of 4 μm deep oxalic acid-anodized pores.

sample	final V A	depos. V B	depos. Hz C	trigger (%) D	[$CuSO_4$] E	pore filling (%)	dispersity (1-3)	pitting (1-3)
1(a)	10	12	50	100	1	65	3	2
1(b)						55	3	2
2(a)	15	12	50	10	0.5	20	2	1
2(b)						25	2	1
3(a)	10	14	50	10	1	40	3	2
3(b)						35	3	2
4(a)	15	14	50	100	0.5	45	2	1
4(b)						30	1	1
5(a)	10	12	200	100	0.5	98	1	2
5(b)						98	1	3
6(a)	15	12	200	10	1	40	2	1
6(b)						50	3	1
7(a)	10	14	200	10	0.5	95	2	2
7(b)						95	2	2
8(a)	15	14	200	100	1	95	2	2
8(b)						95	2	3

wire lengths, with 2 representing intermediate length dispersity. Similarly, with pitting of the electrode, 1 was equated with no pitting, 3 with extreme pitting, and 2 with an intermediate degree. The results of these qualitative assessments are also tabulated in Table 7.2. The effect of the variables on each of the three responses was then analyzed using normal probability plots of the standardized effects. Those effects that lie outside of a normal distribution are labeled with a letter, or letters, corresponding to the variable, or interaction, that produced the effect. The normal plot for each response is provided in Figure 7.1. When interpreting normal plots it must first be considered whether the response of interest is to be maximized or minimized. Yield, or pore-filling, is a response which is to be maximized; therefore, a variable producing a high result should be set at its high level, and a variable producing a low result should be set at its low level. Conversely, wire length dispersity and pitting are responses to be minimized (1 is optimum). Therefore, the reverse is true and a variable producing a high result should be set at its low level, and a variable producing a low result should be set at its high level.

The normal probability plot for yield or pore-filling is provided in Figure 7.1 (a). Examination of the plot indicates that the frequency of the deposition signal (C) had the most significant effect on pore-filling, with the high setting for deposition frequency (200 Hz) producing increased pore-filling. Use of pulsed or continuous deposition (D) also impacted the results, with the positive deviation from normal distribution indicating that continuous wave depositions result in improved pore filling. While the magnitude of the effect was less, pore-filling was also increased with deposition voltage (B) set at the high level (14 V_{rms}). A positive impact on pore-filling was also observed for the frequency-voltage two-factor interaction (BC), consistent with the impact of the single variables. At the same time, a negative deviation from the normal plot indicates that final anodization voltage (A) (and consequently the barrier layer thickness) should be set at the low level (10 V) to maximize pore filling.

The normal probability plot for wire length dispersity is provided in Figure 7.1 (b). In general, variable levels for minimization of dispersity are in agreement with those for maximized pore-filling. The deposition frequency (C) should be set at the high level, continuous deposition employed (D), and cupric sulfate concentration (E) (which did not have a significant effect on pore filling) should be set at its low value (0.5 M).

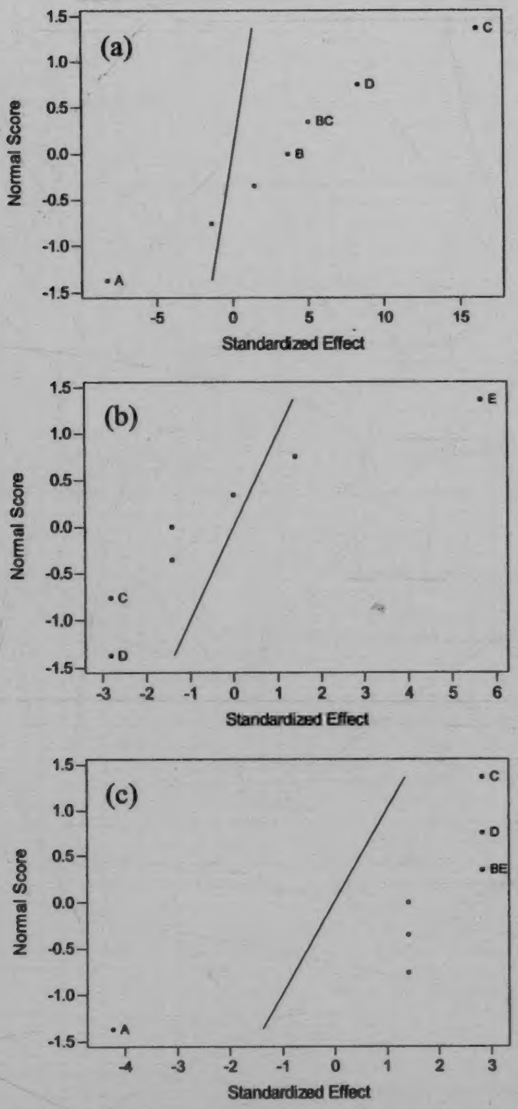

Figure 7.1. Normal probability plots for the standardized effect of variables and interactions on the following responses: yield (a), wire length dispersity (b), and electrode pitting (c). Correspondence between letter code and variable provided in Table 7.2.

The normal probability plot for template pitting is provided in Figure 7.1 (c). The variable levels for minimization of pitting are, in general, opposed to variable levels for maximized pore filling and minimized dispersion. For the minimization of pitting the final anodization voltage (A) (and consequently barrier layer thickness) should be set at the high level (15 V), while deposition frequency (C) should be set at the low level (50 Hz) and pulsed deposition (D) employed. There is also a two-factor interaction (BE) which produces a positive deviation from the normal distribution. The two-factor interaction BE is associated with the deposition voltage and concentration variables; however, in the alias structure BE is confounded with CD, the two factor interaction for deposition frequency and pulsed/continuous deposition. Since neither deposition voltage nor concentration produces a significant effect individually, while both deposition frequency and pulsed/continuous deposition do, this two-factor interaction is probably better assigned to CD, whose interpretation is consistent with the two main variable effects.

Based on the results for pore-filling and wire length dispersity, the following set of optimized conditions was identified: 10 V final anodization voltage, 13 V_{rms} deposition voltage, 200 Hz deposition frequency, continuous wave deposition, 0.5 M cupric sulfate. An intermediate voltage of 13 V_{rms} was chosen rather than the high level of 14 V_{rms} since the effect of deposition voltage in terms of yield was small, and higher deposition voltage was also linked with increased pitting. These conditions resulted in complete filling of 4 μm deep oxalic acid-anodized pores with monodisperse wires, but extreme pitting of the electrode also resulted. SEM micrographs are presented in Figures 7.2 (a) and (b).

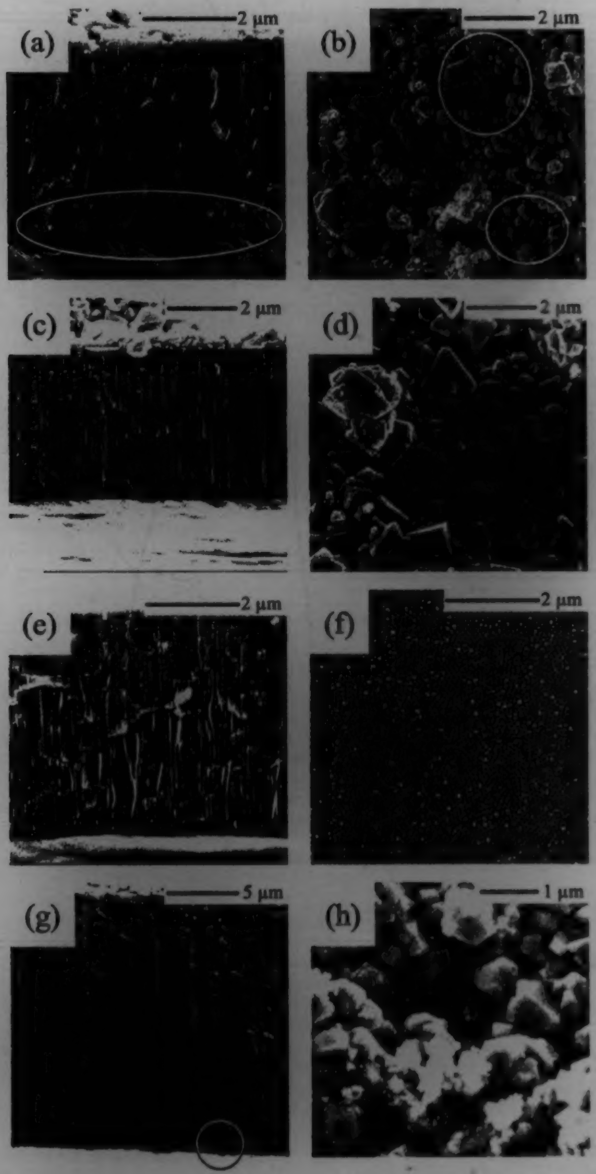

Figure 7.2. SEM images of oxalic acid-anodized templates filled using: continuous sine wave deposition with bulk growth (a) and (b), pulsed sine wave deposition with bulk growth (c) and (d), continuous sine wave deposition without bulk growth (e) and (f). SEM images of sulfuric acid-anodized templates filled using continuous sine wave deposition with bulk growth (g) and (h). In samples (a) – (f) pores are 4 µm deep, in (g) and (h) pores are 25 µm deep. Circles in (a), (b), and (g) identify areas of template damage. Images are of cross-sections (a), (c), (e), (g), and surfaces (b), (d), (f), (h).

In an effort to minimize the pitting of the electrode the optimized conditions were modified according to the results of the FFDOE for template pitting, while still trying to maintain conditions expected to maximize yield and minimize wire length dispersity. To achieve this, all conditions were maintained at the previously stated levels maximizing pore filling and dispersity, with the exception of pulse trigger frequency, which was reduced to its minimum value by employing a pulsed wave deposition with a 200 Hz sine wave triggered at 20 Hz. While this resulted in a slight increase in wire length dispersity, good uniformity of pore filling was maintained and the pitting of the electrode was eliminated. SEM micrographs are displayed in Figure 7.2 (c) and (d). It was found that pitting could also be prevented when continuous wave depositions were employed by ensuring bulk growth did not occur (Figure 7.2 (e) and (f)). When continuous wave depositions were employed in sulfuric acid-anodized pores pitting was found to occur to a lesser degree (Figure 7.2 (g) and (h)). Also, in almost all depositions, some overgrowth of the template occurred. This overgrowth results in less wire length dispersity being observed than would be noted if the deposition was immediately halted when wires first reached the surface of the template.

Effects of Pulse Polarity and Wave Shape. Based on the three responses evaluated in the FFDOE (pore-filling, wire length dispersity, and pitting), the best set of conditions identified incorporated the pulsed sine wave. In AC electrodeposition the deposition wave shape may be varied, and in pulsed AC electrodeposition the pulse may also be applied in two different polarities; oxidative/reductive or reductive/oxidative. To examine the effect of wave shape and pulse polarity, multiple experiments were executed using pulsed 13 V_{rms} (18.4 V_{peak}) sine waves or 17 V_{peak} square waves (200 Hz frequency pulsed at 20 Hz), utilizing each of the possible pulse polarities. Schematics of two of the four possible combinations are illustrated in Figure 7.3.

SEM images of 24 μm deep sulfuric and oxalic acid-anodized templates deposited using sine waves with the different pulse polarities and then milled to expose the surface of samples and a depth of 5 μm below the surface, are shown in Figure 7.4. Figure 7.5 shows images collected at the surface, and depths of 5 μm, 10 μm, and 15 μm below the surface, of 24 μm deep sulfuric and oxalic acid-anodized templates deposited using square waves with the different pulse polarities. A graphical summary of the percentage pore filling vs. depth below the initial sample surface for all four deposition conditions and both sulfuric and oxalic acid-anodized templates is presented in Figure 7.6. In general the percentage of pore filling increases nearly linearly with depth.

Current traces corresponding to a 5 ms pulse were collected at the start, mid-point, and end-point of depositions. A complete set of current trace data collected at the mid-point of depositions into 24 μm deep pores is presented in Appendix C, Figure C1. Also presented (Appendix C, Figure C2) is a set of charge density data, calculated from current traces collected at the start, mid-point, and end-point of each deposition.

These results identify the impact of both wave shape and pulse polarity on the quality of pore filling. In all cases superior pore filling (measured by the number of pores filled to the surface of the template) was obtained when square wave pulsed electrodepositions were employed. Pulse polarity also impacted the quality of pore filling; however, the polarity that produced the best filling was dependent on the wave shape employed. For sine wave pulsed depositions into pores grown in sulfuric acid (both 12 and 24 μm deep), pulse polarity had no significant effect on the percentage of

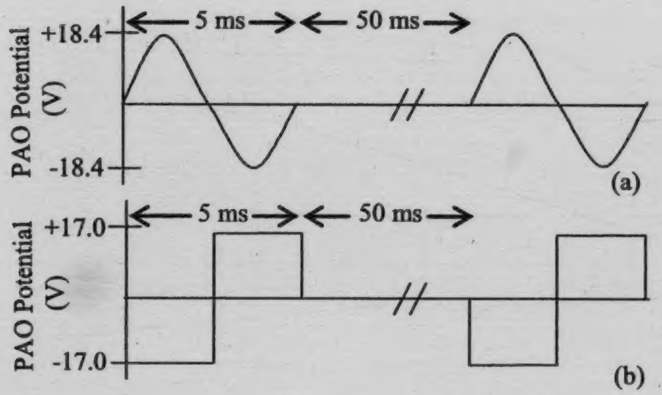

Figure 7.3. Schematics of two of the wave shapes employed in this work, pulsed sine wave with oxidative/reductive pulse polarity (a), and pulsed square wave with reductive/oxidative pulse polarity (b).

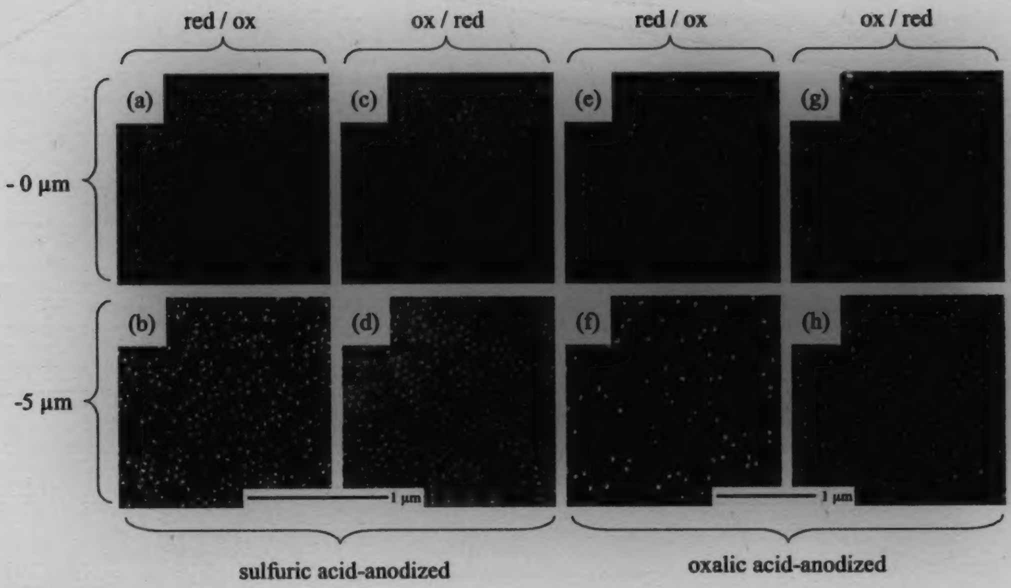

Figure 7.4. SEM images of 24 μm deep sulfuric acid-anodized ((a)-(d)) and oxalic acid-anodized ((e)-(h)) pores with copper deposited using sine waves with reductive/oxidative and oxidative/reductive pulse polarity. Samples have been ion milled to expose the surface, and 5 μm below the original surface, showing the progression of pore filling as a function of depth. Images (a),(b) and (e),(f) taken progressively from samples deposited using reductive/oxidative pulse polarity. Images (c),(d) and (g),(h) taken progressively from samples deposited using oxidative/reductive pulse polarity.

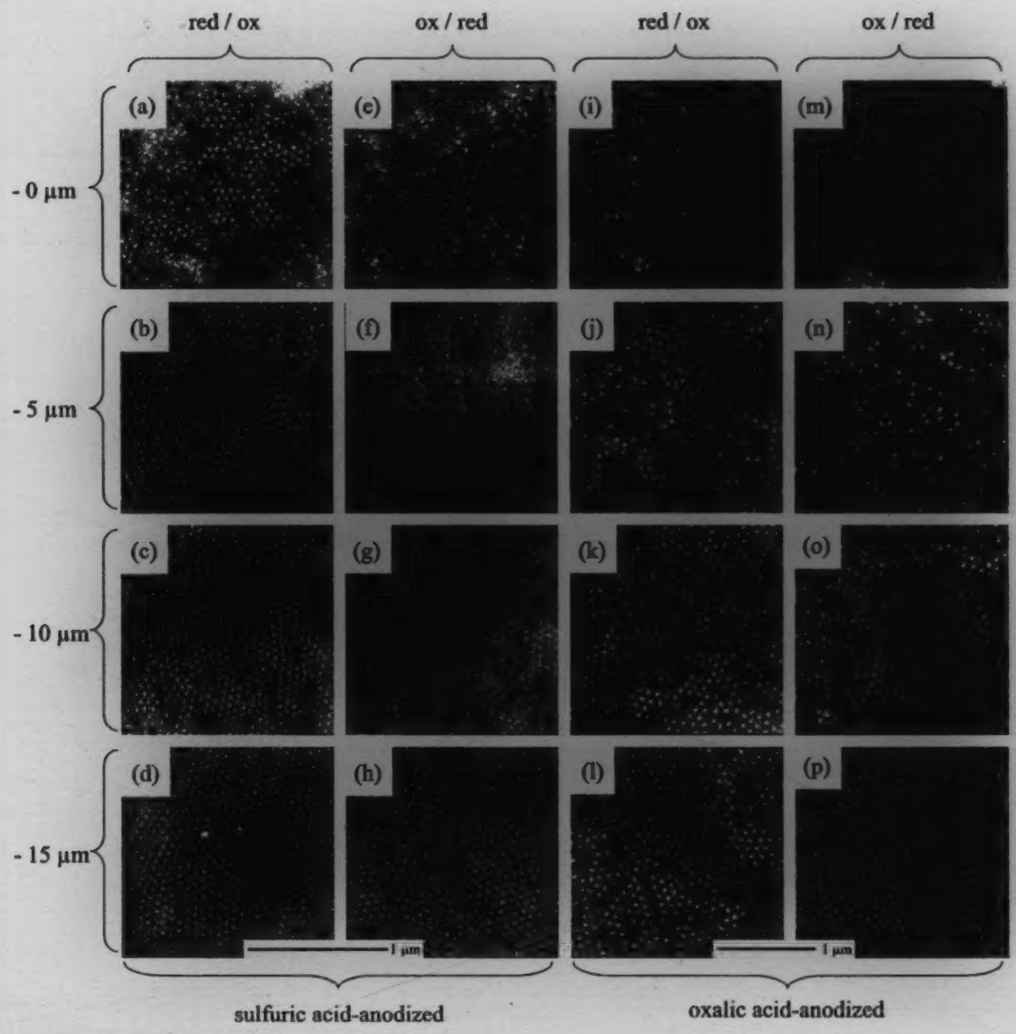

Figure 7.5. SEM images of 24 µm deep sulfuric acid-anodized ((a)-(h)) and oxalic acid-anodized ((i)-(p)) pores with copper deposited using square waves with reductive/oxidative and oxidative/reductive pulse polarity. Samples have been ion milled to expose the surface, and 5 µm, 10 µm and 15 µm below the original surface, showing the progression of pore filling as a function of depth. Images (a)-(d) and (i)-(l) taken progressively from samples deposited using reductive/oxidative pulse polarity. Images (e)-(h) and (m)-(p) taken progressively from samples deposited using oxidative/reductive pulse polarity.

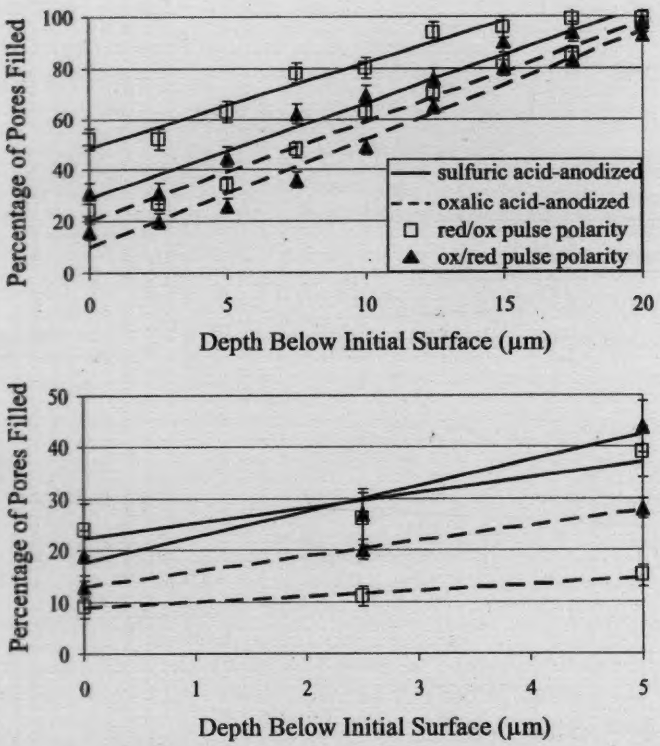

Figure 7.6. Percentage pore filling as a function of depth below original surface of the template for 24 µm deep pores. 17 V_{peak} square wave pulsed depositions (upper plot) and 13 V_{rms} sine wave pulsed depositions (lower plot). Data points are average values, error bars are standard deviations, and lines are linear best fits.

pores filled to the top of the film (Table 7.3). In contrast, pulse polarity had a major impact upon the quality of pore-filling for sine wave depositions into pores grown in oxalic acid. In particular, the percentage of 12 μm deep pores completely filled increased two-fold when the oxidative/reductive polarity was used rather than the reductive/oxidative pulse polarity. In the 24 μm deep oxalic acid-grown templates the improvement was significant, but not as dramatic. The overall greater pore-filling of 12 μm deep pores relative to the 24 μm deep pores is attributed to the decrease in pore depth.

When square wave depositions were employed the relationship between pulse polarity and filling was reversed, with reductive/oxidative pulse polarity resulting in improved pore filling (Table 7.3). Square wave depositions into 24 μm deep sulfuric acid-anodized pores produced pore filling of 52% and 31% using reductive/oxidative and oxidative/reductive pulse polarity respectively. The use of reductive/oxidative pulse polarity also resulted in improved deposition for square wave pulsed depositions into 24 μm deep oxalic acid-anodized pores; however, the effect was less pronounced. On the basis of these results, the two best sets of conditions are 13 V_{rms}, 200 Hz sine wave pulsed at 20 Hz with oxidative/reductive pulse polarity, and 17 V_{peak}, 200 Hz square wave pulsed at 20 Hz with reductive/oxidative pulse polarity, with the square wave pulsed electrodeposition conditions resulting in superior pore filling. The best pore filling overall was achieved in sulfuric acid-anodized pores using the pulsed square wave with reductive/oxidative pulse polarity resulting in complete filling of greater than 50% of 24 μm deep pores.

Table 7.3. Summary of percentage of pores completely filled using pulsed electrodeposition.

waveform	pore depth	anodization electrolyte	pulse polarity	percentage filled
sine (13 V_{rms})	12 µm	H_2SO_4	reductive/oxidative	30 ± 3
			oxidative/reductive	32 ± 2
		$(COOH)_2$	reductive/oxidative	10 ± 2
			oxidative/reductive	20 ± 4
	24 µm	H_2SO_4	reductive/oxidative	24 ± 5
			oxidative/reductive	19 ± 2
		$(COOH)_2$	reductive/oxidative	9 ± 2
			oxidative/reductive	13 ± 1
square (17 V_{peak})	24 µm	H_2SO_4	reductive/oxidative	52 ± 4
			oxidative/reductive	31 ± 3
		$(COOH)_2$	reductive/oxidative	24 ± 6
			oxidative/reductive	16 ± 2

Variations in pore-filling were found to correlate with variations in the current density trace, and charge density data, collected during the course of the depositions. Figure 7.7 shows current density traces corresponding to single 5 ms active pulses collected at the midpoint of sine wave pulsed electrodepositions into 24 µm deep oxalic acid-anodized templates using both reductive/oxidative and oxidative/reductive pulse polarity. Also shown in Figure 7.7 is component charge density per pulse obtained via separate integration of the reductive component and oxidative component of each current trace. Examination of the current traces indicates that the peak reductive current density during oxidative/reductive pulse polarity depositions is approximately 44% (40 mA/cm^2) greater than during reductive/oxidative pulse polarity depositions. When the oxidative and reductive components of the traces were integrated to yield the corresponding component charge density, it was found that the reductive charge per pulse when

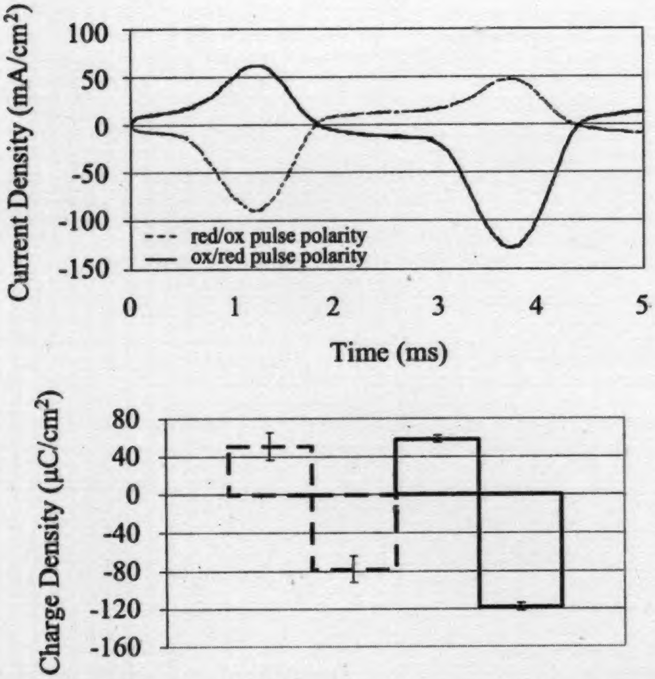

Figure 7.7. Current density traces (top figure), and component charge density per pulse obtained from integration of current traces (bottom figure), collected during sine wave pulsed electrodepositions into 24 µm deep oxalic acid-anodized pores. Data collected at deposition mid-point (35 min) using reductive/oxidative pulse polarity, and oxidative/reductive pulse polarity.

oxidative/reductive pulse polarity is employed is approximately 50% (40 μC/cm^2) greater than when using reductive/oxidative pulse polarity, while the oxidative charge per pulse is approximately equal in both cases (Figure 7.7). This suggests that increased pore filling observed with oxidative/reductive pulse polarity sine wave depositions into oxalic acid-anodized pores results from increased reductive charge, corresponding to increased reduction of copper. When cross-sectional images are examined it is clear that wires have grown to a greater height, but there is no indication that significant improvement in the uniformity of deposition and pore filling accompanies the increased deposition.

When the comparable current density and charge density data is examined for pulsed sine wave depositions into 24 μm deep sulfuric acid-anodized templates (Figure 7.8) a slight increase in peak reductive current (~4%) and net reductive charge (~10%) is observed with oxidative/reductive pulse polarity relative to reductive/oxidative pulse polarity. However, due to the small magnitude of the difference, no change in the magnitude or quality of the deposition is observed.

Conversely, when the current trace density and charge density data for square wave depositions is examined, the most significant variation as a consequence of pulse polarity occurs in the oxidative component of the active pulse. This is illustrated in Figure 7.9, showing current density traces collected at the midpoint and endpoint of a square wave reductive/oxidative pulse polarity deposition into 24 μm deep sulfuric acid-anodized pores. While the reductive current density of each pulse is almost identical, the oxidative current density increases significantly over the course of the deposition, with a five-fold increase in current density at the tail of the current traces. In the corresponding oxidative charge density an approximately 200% increase (142 μC/cm^2) between the

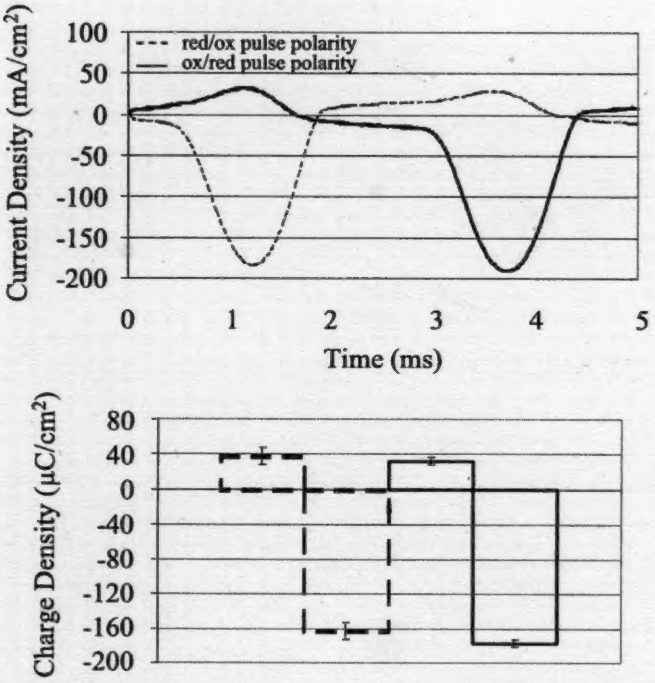

Figure 7.8. Current density traces (top figure), and component charge density per pulse obtained from integration of current traces (bottom figure), collected during sine wave pulsed electrodepositions into 24 µm deep sulfuric acid-anodized pores. Data collected at deposition mid-point (15 min) using reductive/oxidative pulse polarity, and oxidative/reductive pulse polarity.

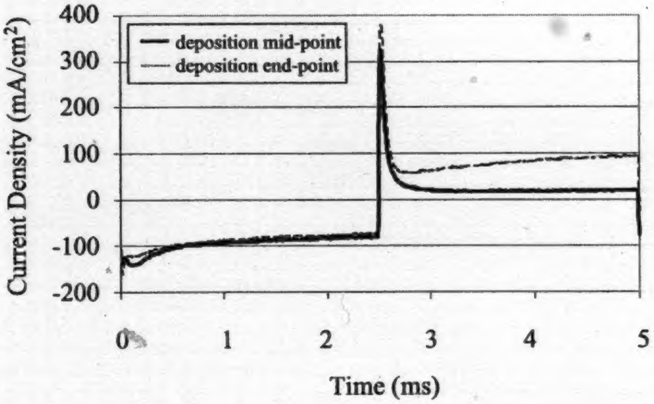

Figure 7.9. Current density traces collected during square wave pulsed electrodepositions into 24 μm deep sulfuric acid-anodized pores collected at deposition mid-point (15 min) and deposition end-point (30 min) shown as solid trace and dotted trace respectively.

midpoint and endpoint of the deposition is observed. This increase in oxidative charge density is accompanied by net reductive charge density being reduced to almost zero by the end of the deposition (Appendix C, Figure C2).

With reductive/oxidative pulse polarity, square wave depositions into 24 μm deep oxalic acid-anodized pores yield a much smaller increase in the oxidative current density (approximately two-fold at the tail of the current trace) over the course of the deposition (Figure 7.10). A corresponding increase in oxidative charge density of approximately 31% (36 $\mu C/cm^2$) between the midpoint and endpoint of the deposition is also observed. This is accompanied by a downward trend in net reductive charge density over the course of the deposition, similar to that observed for sulfuric acid-anodized templates, but less pronounced (Appendix C, Figure C2).

When the oxidative/reductive pulse polarity square waves are employed, this degree of variation in the oxidative current density over the course of the deposition is no longer observed, and the magnitude of the change in oxidative charge density is significantly reduced. Specifically, in sulfuric acid-anodized templates the change in oxidative charge density per pulse is reduced to approximately 160% (60 $\mu C/cm^2$), while in oxalic acid-anodized pores the oxidative charge density per pulse remains constant over the course of the deposition. Additionally, in both sulfuric and oxalic acid-anodized templates a much smaller decrease in net reductive charge density is observed, and only at the end of the deposition (Appendix C, Figure C2).

The summary observation is that while pulsed square wave depositions result in improved pore-filling regardless of pulse polarity, the degree of pore-filling increases significantly when reductive/oxidative pulse polarity is employed, with the magnitude of

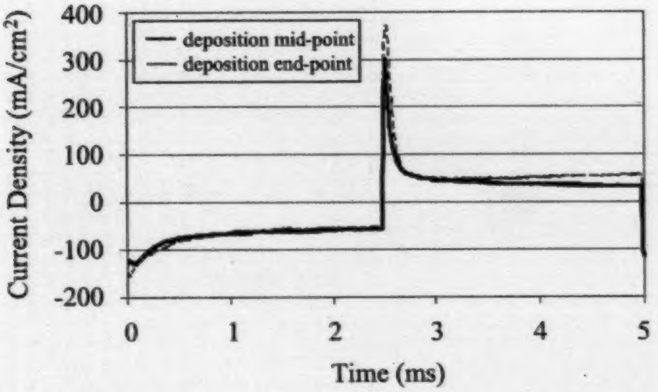

Figure 7.10. Current density traces collected during square wave pulsed electrodepositions into 24 μm deep oxalic acid-anodized pores collected at deposition mid-point (35 min) and deposition end-point (65 min) shown as solid trace and dashed trace respectively.

the improvement in pore-filling correlating with the magnitude of the increase in oxidative current density/charge density over the course of the deposition. In pulsed sine wave depositions, variations in pore-filling are found to correlate with variations in the reductive current density/charge density, with oxidative/reductive pulse polarity leading to increased copper deposition.

Wire Characterization. Wires deposited using the best pulse sequences were shown to be crystalline copper by TEM (Figure 7.11) and XRD (Figure 7.12). TEM results indicate that the wires are either single crystalline or composed of several large crystallites that span the diameter of the wire and are on the order of micrometers in length along the wire axis, and that the as-deposited wires contain numerous crystal defects. EDX results obtained during TEM analysis of liberated wires show the presence of aluminum, likely due to residual Al_2O_3 not removed during the liberation process. The oxide sheath visible in Figure 7.11 (c) may also be partially composed of copper oxide resulting from oxidation during or after liberation.

XRD patterns of the as-deposited, un-milled films after 3 days of air exposure (Figure 7.13) show large peaks well matched with those of Cu_2O (PDF 65-3288), with a preferred orientation along the [200] direction. These patterns may be compared to those collected following ion milling to remove bulk growth (Figure 7.12). The post ion-milling powder pattern of wires deposited in sulfuric acid-anodized pores (Figure 7.12 (a), collected 6 days after ion milling, stored in air) contains no significant copper oxide peaks, and the copper peaks show only a slight preferred orientation along the [220] direction when compared to the standard powder pattern for Cu (PDF 89-2838). In contrast, the post ion-milling powder pattern of wires deposited in oxalic acid-anodized

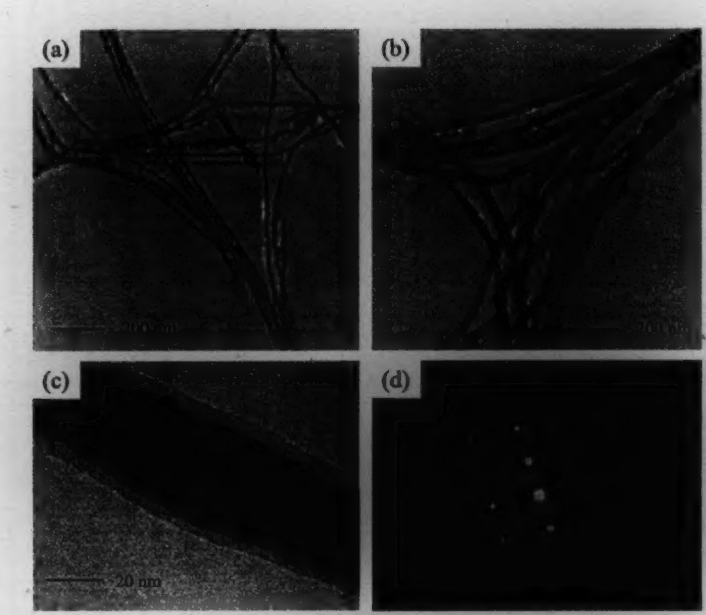

Figure 7.11. TEM images of wires liberated from sulfuric acid-anodized pores (a), wires liberated from oxalic acid-anodized pores (b) and (c), and SAED pattern from (c) in (d).

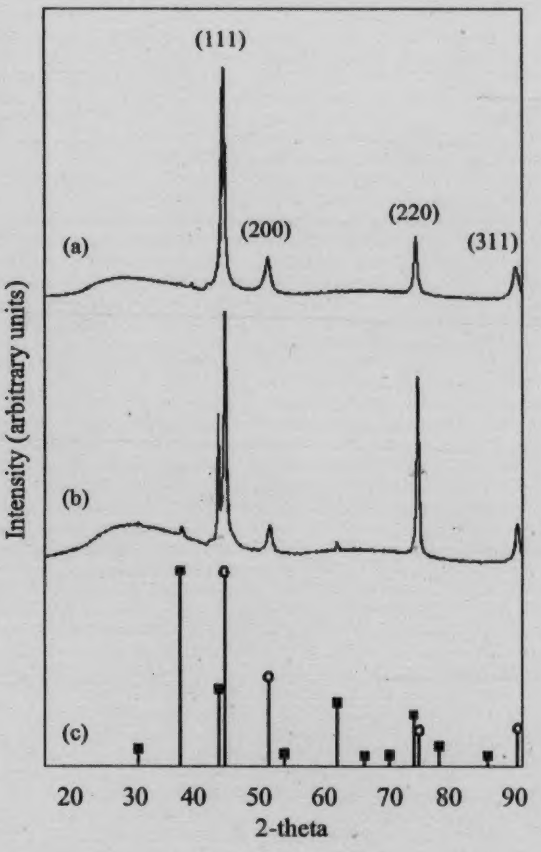

Figure 7.12. In-situ XRD powder patterns from wires deposited in sulfuric acid-anodized pores with ion milled surface and copper peaks indexed (a), wires deposited in oxalic acid-anodized pores with ion milled surface (b), and standard powder patterns for Cu (round heads) and Cu_2O (square heads) (c).

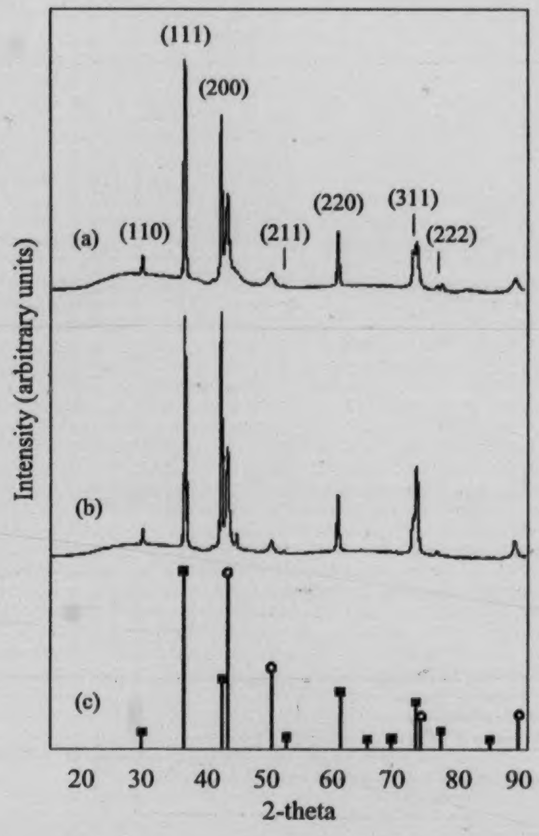

Figure 7.13. In-situ XRD powder patterns from wires as-deposited in sulfuric acid-anodized pores with Cu_2O peaks indexed (a), wires as-deposited in oxalic acid-anodized pores (b), and standard powder patterns for Cu (round heads) and Cu_2O (square heads) (c).

pores (Figure 7.12 (b), collected 2 days after milling, stored in air) indicates a much stronger preferred orientation of the copper nanowires along the [220] direction. In addition, Cu_2O peaks are still present and show a retention of the preferred orientation along the [200] direction. On these samples non-uniform Debye rings were observed for the copper (220) peaks, and the copper oxide (200) peaks, providing further evidence for wire texture.

On the whole, the data suggests that the PAO matrix protects the bulk of the nanowires from oxidation, confining oxidation to the exposed wire tips. The absence of copper oxide in the milled sulfuric acid-anodized samples is attributed to the nearly complete filling of the pores; resulting in efficient removal of the oxidized tips during ion-milling. In contrast, the pores of the oxalic acid-grown PAO are not as uniformly filled, such that after ion-milling the oxidized tips of the shorter nanowires remain, with the preferred orientation and texture of the copper oxide related to the preferred orientation of the parent copper nanowires.

Discussion

The difference in pore-filling achieved in sulfuric and oxalic acid-anodized templates is explained by the different chemistry, structure, and properties of the barrier layers resulting from the growth and barrier layer thinning process in these two acids. The superior pore-filling of the oxidative/reductive pulse polarity over that of the reductive/oxidative pulse polarity upon application of pulsed sine-waveforms results from polarization effects in the electrolyte during the rest period between pulses. Square-waveforms produce better pore-filling with the opposite reductive/oxidative polarity because migration of cationic defects in the Al_2O_3 barrier during the deposition pulses increases resonant tunneling through the barrier layer. The effect of this increased tunneling over the course of the deposition is reduced rectification of the barrier layer. This results in increased oxidative current flow and a reduction in net copper deposition into the pores with the thinnest barrier layers, enabling the pores with initially more resistive barrier layers to "catch-up."

Structure of Pore Bottoms and Barrier Layer in PAO. The structure of porous aluminum oxide has been, and continues to be, the subject of intensive investigation.[10-14] The schematic honey-comb structure of PAO presented in Chapter 6 is widely used and accurately reflects the physical structure of as-grown, well-ordered PAO; however, it does not accurately reflect the chemical complexity of the as-grown PAO. A more accurate representation of the physical and chemical structure of as-grown PAO is shown in Figure 7.14 (a). Porous aluminum oxide is, in fact, not pure Al_2O_3, but incorporates significant amounts of the acid anion into the walls and barrier layer.[10] Moreover, these acid anions are not uniformly distributed throughout the barrier layer or pore walls, but are concentrated on the electrolyte side of the layer, while the middle of the walls and Al side of the barrier layer is pure Al_2O_3. Furthermore, the total amount of acid anion incorporation, and fraction of the barrier layer incorporating the acid anion, depends primarily upon the acid type and secondarily upon the anodization conditions (voltage, temperature, and possibly concentration).[10,13,14] The chemical, mechanical, and electrical properties of the anion incorporating layers are quite different from those of pure Al_2O_3. Typical concentrations of acid anion incorporation are 12-14 weight % sulfate and 2-4 weight % oxalate. Correlated with these amounts of anion incorporation, the relative

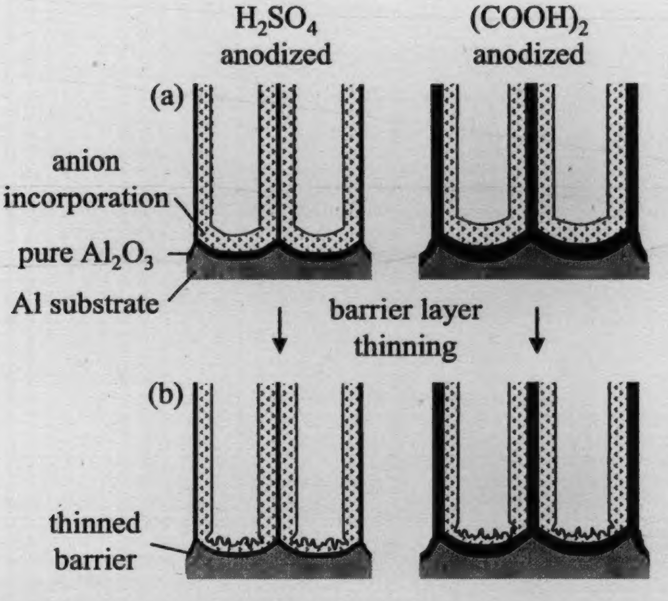

Figure 7.14. Schematic of PAO pore bottoms showing (a) compositional variation as a function of anodizing electrolyte, and (b) structural change that results from thinning of the barrier layer to facilitate AC electrodeposition.

thickness of the pure Al_2O_3 portion of the barrier layer is less for pores grown in sulfuric acid (~5%) than in oxalic acid (~10%).[10,13,14] Because the pure Al_2O_3 layer is proportionately thinner in sulfuric acid-grown pores than in oxalic acid-grown pores, the anodization current and growth rate is much greater in sulfuric acid than in oxalic acid. It is also known that the acid ion incorporating layer has a much higher rate of chemical etching than the relatively pure aluminum oxide layer.

The gradual reduction of the anodization voltage to thin the barrier layer not only reduces the thickness of the barrier layer, but also alters the pore size and distribution at the pore bottoms. This produces a thin, branched (possibly dendritic) structure at the bottom of the uniform pores, rather than the test-tube bottoms that are produced if the anodization is simply stopped.[15] A schematic representation of the barrier-thinned pores is shown in Figure 7.14 (b). SEM images collected from pore cross-sections and bottoms that have been subjected to the electrochemical thinning process are presented in Figure 7.15, showing the physical structure that is depicted schematically in Figure 7.14 (b).

The impact of the thinning process on the structure of the pores in this thin, non-uniform layer, and upon the relative thickness of the pure and impure sections of the barrier layer, has not been investigated. Clearly, the exact nature of these structures will depend upon the rate of voltage decrease. At a sufficiently slow rate the steady state structure (and interpore spacing) will be maintained throughout the process, producing a branched pore structure with the expected barrier layer thickness and relative thicknesses of the pure and impure layers. At a sufficiently rapid rate of voltage decrease, the rate of electrochemical barrier layer thinning will not keep up with the rate of voltage decrease, and the current will fall to zero. At this point, the much slower chemical etching will

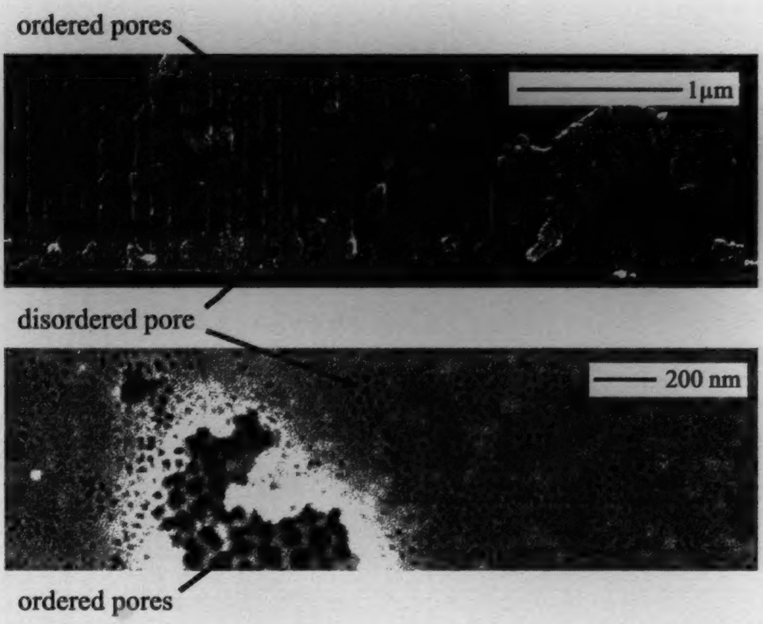

Figure 7.15. SEM images showing disordered layer that forms during barrier layer thinning. Top image shows cross section with ordered pores transition to disordered barrier layer. Lower image shows bottom view with aluminum substrate removed and pores partially opened via dissolution in phosphoric acid. Large openings are ordered pores, small openings are smaller dendritic pores formed at reduced voltage during the barrier thinning process.

predominate over the electric field assisted anodization process, and the impure portion of the barrier layer will be preferentially removed, leaving a proportionately larger fraction of the pure Al_2O_3 portion of the barrier layer.

In practice, the barrier layer thinning process was selected to be as rapid as possible to minimize both the pore branching and the thickness of the dendritic layer relative to the ordered layer, while still retaining a measurable anodization current. Because similar barrier-layer thinning protocols were used both in sulfuric and oxalic acid, and because the rate of anodization is much slower in oxalic acid, it is expected that the structure of the barrier layer will deviate from the steady-state ratio in oxalic acid more than in sulfuric acid. Specifically, it is expected the fraction of pure aluminum oxide in the barrier layer will be enhanced in the oxalic acid-anodized material more than in the sulfuric acid-anodized material. This difference in composition is thought to contribute to the different results for sulfuric and oxalic acid-grown pores for the different electrodeposition processes.

Uniform Electrodeposition into PAO. In order to fill all pores uniformly and completely, it is necessary to achieve a consistent growth rate in all pores. As individual wires reach the surface of the electrode ahead of the growth front in other pores, they will inhibit the growth of wires in unfilled pores in two ways. First, wires in contact with the bulk electrolyte provide an electrical pathway of lowered resistance. In those pores where wires have yet to reach the surface of the template, mass transfer limitations within the pore result in increased resistance relative to the bulk electrolyte. As a result, reductive current will be preferentially shunted through the wire or wires in contact with the bulk electrolyte, limiting growth of wires in the partially filled pores. This is experimentally supported by the observation of shoulder peaks on current density traces at a lower potential position on the sine wave that develop as the deposition proceeds, and bulk growth becomes evident. An example of this shoulder peak is shown in Figure 7.16 for deposition into sulfuric acid-anodized pores. Second, bulk growth on the surface of the electrode with pulsed depositions is in the form of crystalline polyhedra, which block access to the 10-100s of pores surrounding them, limiting further growth in those pores. As a result, it is critical to obtain consistent growth rates of all wires in order to achieve complete pore filling.

One approach to controlling the growth rate of the wires is to maintain a uniform and controlled potential at the wire growth front. If this potential is maintained at the minimum potential required for the reduction of metal ions, slow and uniform wire growth would occur in all pores. This approach is commonly used for controlled DC metal deposition into PAO templates.[16] In AC deposition through the barrier layer this is not feasible for two reasons. First, the barrier layer is known to exhibit small, random fluctuations in thickness[17] that will correspond to random fluctuations in resistance. Second, since the barrier layer thinning process results in disordered growth of branched or dendritic pores that decrease in spacing and diameter, the structure of the porous layer at the bases of the pores will be variable (Figures 7.14 (b) and 7.15). This will produce variations in the area of the pore bottoms, and consequently the current density in the pore, further complicating the matter.

A second general approach to producing uniform growth is via control of reactant availability. In this case, reactant availability is controlled by diffusion of metal ions from the bulk electrolyte to the wire growth front. Continuous AC depositions maintain a

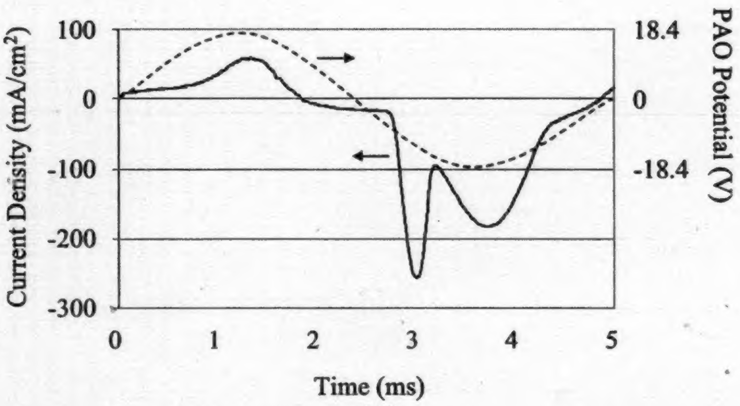

Figure 7.16. Current density trace collected at the end of a deposition into sulfuric acid-anodized pores showing the presence of a lower potential shoulder peak resulting from bulk deposition.

state of ion depletion in the pores at all times; consequently, the growth rate is limited by diffusion of ions along the length of the pore. Since constant bulk electrolyte concentration is maintained at the electrode surface via stirring, and the pore diameters are produced with a narrow size distribution, the rate of diffusion and the subsequent wire growth rate are expected to be consistent among the pores, resulting in uniform wire growth and complete pore-filling. In pulsed AC deposition, maintaining diffusion controlled growth is more challenging.

Gösele and coworkers have reported that increased uniformity of growth may be achieved via application of relatively high constant current density pulses.[17] A high current density results in high nucleation rates, which is followed by wire growth. In pores that have a thinner barrier layer, metal ions are rapidly depleted, resulting in increased resistance in the pore electrolyte. This will result in increased current flow in pores with a thicker barrier layer and higher metal ion concentration allowing them to "catch-up." In between pulses, a rest period is used during which no current is applied to allow re-equilibration of the electrolyte concentration in the pores.[17] A schematic of the deposition sequence used by Gösele and coworkers is presented in Figure 7.17 (a). Using this deposition sequence they have reported uniform filling of 1 μm deep pores with Ni,[15] and 2 μm deep pores with Ag.[17] However, if a current control method is to be implemented consistently, it is critical to have well defined electrode areas. As previously mentioned, the dendritic pore structure produced during the barrier layer thinning process is irregular and ill-defined; therefore, reproducibly producing large-area electrodes with identical active deposition areas may be precluded. For a simple and

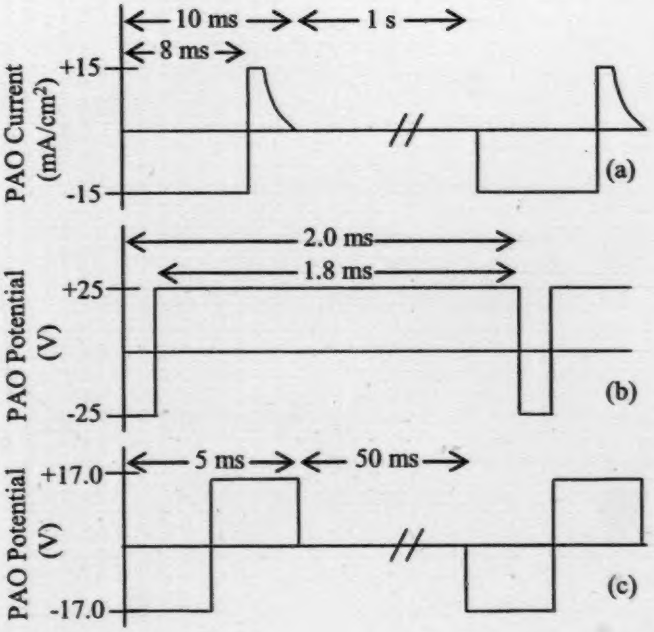

Figure 7.17. Deposition sequences used by Gösele and coworkers (a), Metzger and coworkers (b), and in this work (c).

convenient method of deposition it is preferable to use voltage-controlled waveforms that are insensitive to electrode area.

Metzger and coworkers have reported uniform growth of wires in 600 nm deep pores was achieved using a continuous square wave, where a short reductive pulse was followed by an extended oxidative pulse.[18] A schematic of the voltage controlled deposition sequence used by Metzger and coworkers is presented in Figure 7.17 (b). The deposition sequences employed by Gösele and coworkers, and Metzger and coworkers, may be contrasted with the best voltage controlled sequence used in this work, presented in Figure 7.17 (c).

Continuous vs. Pulsed Electrodeposition. Diffusion limited growth was achieved using continuous wave depositions, which as a result yielded superior pore-filling in the results of the FFDOE. Qualitative evidence that diffusion-limited growth was occurring under the continuous wave regime is the observation that less active deposition time was required to yield a comparable amount of metal deposition using pulsed electrodeposition than continuous electrodeposition. Unfortunately, continuous wave conditions were also accompanied by template damage. Metzger and coworkers have also reported observing template damage when employing the deposition sequence illustrated in Figure 7.17 (b), and have speculated that it is due to aluminum oxide hydroxide dissolution producing hydrogen gas.[18] It is believed to be the case that the damage observed in this work results from ohmic heating, an explanation that is consistent with the fact that damage is only observed when deposition proceeds to bulk growth—an event that is accompanied by increased current density corresponding to rapid deposition of metal from the bulk electrolyte, and consequently, increased ohmic heating.

Other possible implications of continuous wave depositions include reduced crystallite dimensions of the as-deposited wires. Schmid and coworkers have performed detailed X-ray characterization of copper nanowires deposited using continuous wave AC conditions similar to those used in this work, and reported an average crystallite size of 12 nm.[19] In contrast, the copper nanowires produced in this work using pulsed electrodeposition are composed of several much larger crystallites. This distinction is also made evident by the observation that overgrowth from continuous wave AC conditions are spherical and of nanometer dimensions, while overgrowth from pulsed deposition conditions consists predominantly of large, faceted crystallites (Fig 7.2 (b) and (d)).

The FFDOE results showed that electrode damage could be eliminated by using pulsed wave deposition conditions with only a modest decrease in quality of pore filling in 4 μm deep oxalic acid-anodized pores. The elimination of template damage and the ability to grow highly crystalline wires makes the use of pulsed electrodeposition appealing. It is also expected that pulsed deposition conditions should be less affected by increasing pore depths than continuous deposition conditions, where diffusion limitation and ion depletion are expected to impact wire growth. The challenge with pulsed electrodeposition is that uniform growth in all pores is more difficult to achieve, since metal ion concentration at the growth front is no longer diffusion rate limited. Ion depletion occurs during the reductive pulse, with the concentration at the wire tip then returning to bulk concentration during the period of zero applied potential. In pores which are significantly deeper than those used in the FFDOE, the impact of this is expected to be magnified, with wire length dispersion increasing with pore depth.

Effect of Wave-form. A rationalization for the improved results obtained with square wave depositions relative to that achieved with sine wave depositions follows intuitively from the discussion of slower growing pores being able to "catch-up" during the duration of the pulse. In a sine wave deposition, peak potential is realized for only a small fraction of the 2.5 ms pulse width, and the effective pulse width where the potential is above the minimum required for current flow is relatively short. In a square wave deposition the step nature of the potential change makes the effective and actual pulse widths identical at 2.5 ms. The fact that substantially improved deposition and pore-filling was observed in this work when the square wave was employed lends support the "catch-up" theory proposed by Gösele and coworkers.[17]

Effect of Pulse-polarity. In addition to wave shape the effect of pulse polarity was also examined, something that had not been previously reported in the literature. Based on the concept that the oxidative component of the pulse removes the capacitive charge buildup across the barrier layer that occurs during the reductive component, all pulsed depositions reported to date have employed reductive/oxidative pulse polarity. In this work, increased deposition over an identical time period was observed when the oxidative/reductive pulse polarity was employed, rather than the reductive/oxidative pulse polarity, in conjunction with sine wave depositions. However, when square wave depositions were employed, the conventional reductive/oxidative pulse polarity produced the most uniform pore-filling.

These two phenomena are a consequence of different processes occurring during the course of the deposition; however, both are a direct consequence of the structure and composition of the aluminum oxide barrier layer and the dynamic changes that occur therein during the course of the deposition. Once metal deposition into the pores has begun, the metal/insulator/electrolyte structure is replaced by the metal/insulator/metal structure. In contrast to DC electrodeposition, which may be regarded as standard electrodeposition through a nanostructured deposition mask, AC deposition inherently requires electron transport through this device. The quality of the metal deposition will critically depend upon how the MIM capacitor responds to the deposition sequence, a response that this work has shown to vary with deposition conditions. This indicates that the PAO should not be regarded as a simple template for AC electrodeposition, but rather should be treated as a dynamic variable affecting the outcome of the deposition process.

The effect of pulse polarity on pore-filling for the sine wave pulses is explained by the nature of the electrical double layer resulting from charge stored on the barrier layer during the zero potential periods between active pulses. When oxidative/reductive pulse polarity is employed, negative charge will be stored on the barrier layer, and the resultant electrical double layer will incorporate copper cations to balance charging at the wire tip. It is well known that adsorption of species at an electrode surface can impact the kinetics of electron transfer,[20] and it is thought that adsorption and/or increased concentration of copper ions resulting from the formation of the electrical double layer results in the observed increase in deposition rates. This relies on the adsorption and/or increased concentration persisting during the oxidative pulse, which is thought to be the case. A rough estimate of the diffusion distance of copper cations during the oxidative pulse is obtained by calculating the root-mean-square displacement based on the diffusion coefficient and elapsed time ($D = 7.14 \times 10^{-6}$ cm^2/s, t = 2.5 ms) where $\Delta = \sqrt{(2Dt)}$.[20] This yields a diffusion distance of less than 2 μm, and does not take into account any specific adsorption, ensuring that the increased concentration and/or adsorption will largely persist during the oxidative pulse. Since the effective width of the sine wave reductive pulse is very short (< 2.5 ms) a significant fraction of the ions reduced during the pulse are those that had been incorporated into the electrical double layer. Consequently, increased electron transfer and/or deposition rates are observed when using oxidative/reductive pulse polarity relative to reductive/oxidative pulse polarity with sine wave pulsed electrodeposition.

The difference in the magnitude of the effect between oxalic and sulfuric acid-anodized templates is a consequence of the difference in the structure and composition of the barrier layer. In sulfuric acid-anodized pores the barrier layer is inherently thinner due to the fact that barrier layer thickness is proportional to anodization voltage, and the large difference in initial barrier layer thickness between sulfuric and oxalic acid-anodized pores is maintained to some degree during the thinning process. As previously discussed, the composition and thickness of the barrier layer is also modified during the thinning process, with the relative thickness of pure aluminum oxide remaining relatively constant in sulfuric acid-anodized pores, while the relative thickness of the pure aluminum oxide layer in oxalic acid-anodized pores increases. This is born out experimentally by the significantly larger current densities and shorter deposition times observed during electrodeposition into sulfuric acid-anodized pores relative to oxalic acid-anodized pores. As a consequence of this variation in barrier layer thickness and composition, less charge is stored on the barrier layer during the zero potential periods between active pulses during depositions into sulfuric acid-anodized templates, and fewer metal cations are incorporated into the electrical double layer and/or adsorbed at the tip of the growing wire.

The magnitude of the difference in capacitive charging may be approximately quantified by comparing the average oxidative charge density per pulse, which is 50 μC/cm^2 for oxalic acid-anodized templates compared to 40 μC/cm^2 for sulfuric acid-anodized templates. This difference may be attributed directly to the charge stored on the barrier layer, and if it is recognized that these figures are convoluted with any oxidative current that is passed, it is likely that the difference in stored charge is underestimated since leakage current density varies as an inverse exponential with thickness of the insulating oxide layer.

When square wave pulsed electrodepositions are employed, effects of the electrical double layer are still observed as a variation in the magnitude of net reductive charge passed with differing pulse polarities. However, since the effective pulse width is equivalent to the actual pulse width at 2.5 ms, the ions incorporated into the electrical double layer are a smaller fraction of the total number reduced during a single pulse and, consequently, the effect is not observed in SEM analysis of pore filling. Nonetheless, pulse polarity does impact the quality of deposition when square waves are employed; however, the quality of pore filling is observed to correlate with increasing oxidative current over the course of deposition when reductive/oxidative pulse polarity is used. It is speculated that this increase in oxidative current occurs due to resonant tunneling which is enhanced over the course of the deposition by migration of higher oxidation state aluminum defects.

When an aluminum/aluminum oxide/metal junction is formed with a metal that has a work function greater than that of aluminum, it is known that the junction will act to rectify current; specifically, due to the asymmetric nature of the potential barrier, current will be passed preferentially when the aluminum is biased as the cathode. This behavior is depicted schematically in Figure 7.18. Conductance through, and dielectric breakdown of, anodic oxides on Al and other valve metals has been extensively studied experimentally and theoretically for several decades. Although complete consensus regarding the processes has not yet been achieved, the presence of ionic impurities is known to have a large impact on the potential barrier in a metal/insulator/metal junction.

In 1965 Schmidlin modeled the trapezoidal potential barrier that results when a potential is applied across a dielectric layer between two metals, the impact of ionic impurities on the shape of this barrier, and the implications this has for electron tunneling through the MIM junction.[21] His calculations show that a cationic impurity located in the dielectric film near the metal polarized as the cathode has the effect of substantially reducing the barrier height, and of producing what is akin to two potential barriers separated by a potential well. It was qualitatively recognized that because of the reduction in barrier height adjacent to the metal cathode, thermally excited carriers could more easily surmount the barrier with the junction polarized in this direction. He further calculated that a single positive ion per unit area equal to the square of the film thickness (corresponding to one cationic impurity per 100 nm^2 for the ~10 nm thick barrier layers in this work) can increase the tunnel current by an order of magnitude.[21]

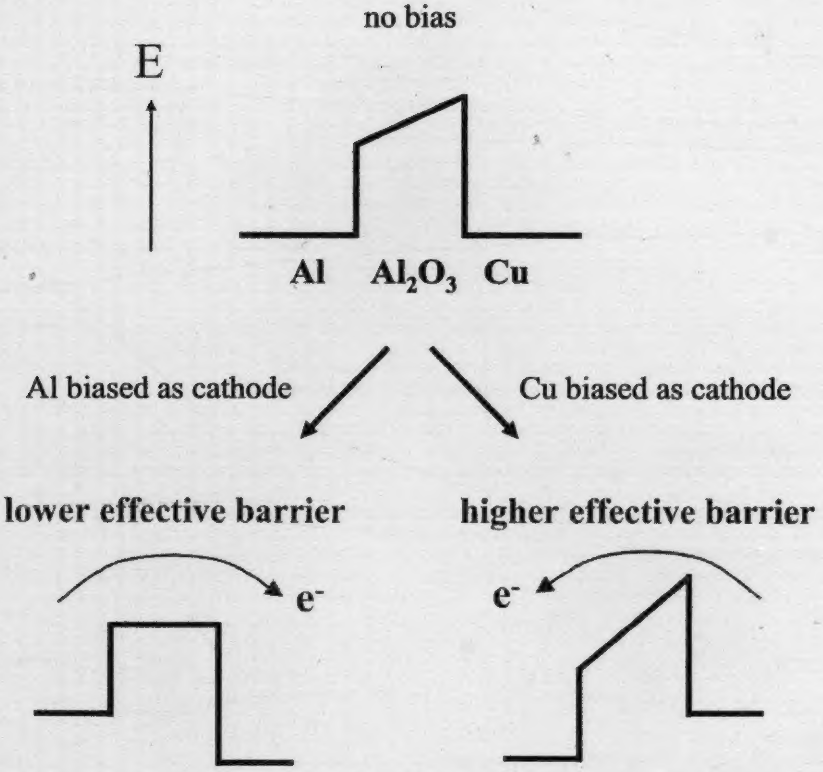

Figure 7.18. Schematic representation of the trapezoidal potential barrier at an Al/Al_2O_3/Cu junction, and the difference in effective barrier height when biased in anodic and cathodic directions, which results in current rectification.

Subsequent researchers have tended to emphasize the increase in tunneling current enabled by cationic defects over the enhancement of thermal emission over the barrier.[22] Mujica and Ratner have calculated the rate of tunneling through single rectangular potential barrier relative to a barrier with a discrete structure of wells and barriers for metal/molecule/metal (MMM) junctions.[23] Their calculations also show that the inclusion of potential wells in a potential barrier greatly enhances tunneling rates relative to a continuous potential barrier.[23] Ratner and others have also considered the increased current that defects in a molecular layer may enable through a thermally activated hopping mechanism.[24,25]

Based on these theoretical treatments it is expected that cationic defects in the aluminum oxide layer of PAO templates will have a similar impact on tunneling barriers, and anodic conductivity through the barrier layer. In particular, if these defects are located adjacent to the copper-filled pore or distributed throughout the barrier layer, they can lead to increased electron transport when the electrode is biased in the anodic direction (copper biased as the cathode), reducing or eliminating the inherent rectification of the aluminum/aluminum oxide/metal junction. These two explanations for the onset of anodic electrical breakdown are presented schematically in Figure 7.19.

It is also known that these aluminum ion defects may become mobilized under direction of a potential applied across the MIM junction. Such an effect has been reported in aluminum/anodic aluminum oxide/silver junctions[22] with aluminum oxide layers that are of comparable thickness to those encountered in PAO templates in this work. Hassel and Diesing report that as-grown anodic aluminum oxide contains a fixed density of higher oxidation state centers that are stable up to the formation voltage (the

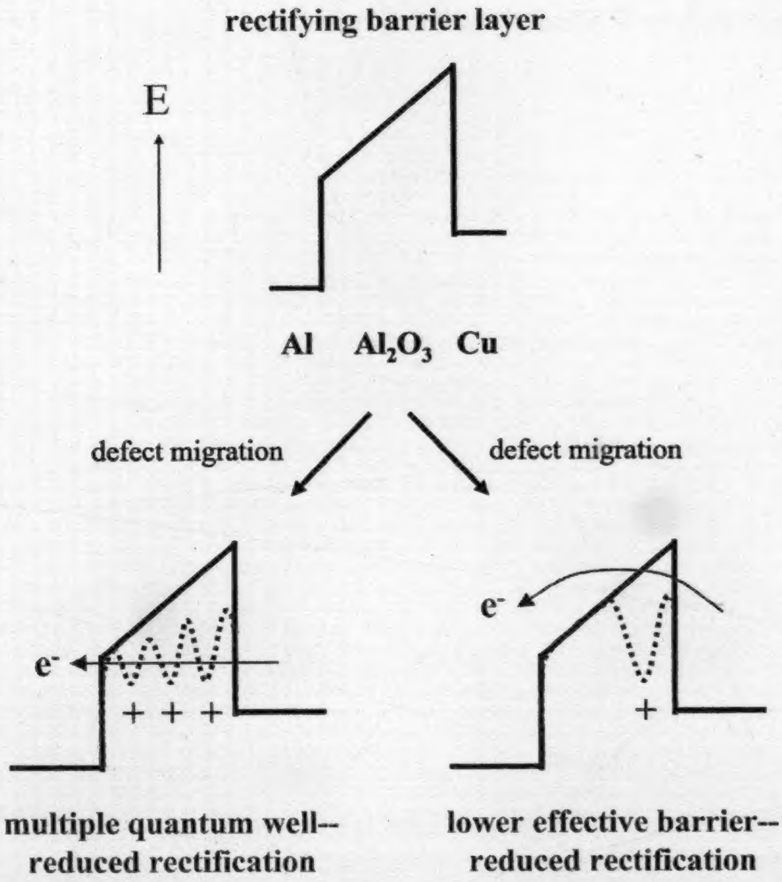
rectifying barrier layer
E
Al
Al$_2$O$_3$
Cu
defect migration
defect migration
e$^-$
+ + +
e$^-$
+
multiple quantum well-- reduced rectification
lower effective barrier-- reduced rectification

Figure 7.19. Schematic representation of the two possible defect migration scenarios that would result in reduction or elimination of current rectification in an Al/Al$_2$O$_3$/Cu junction. Formation of a multiple quantum well structure (left) results in increased anodic tunneling, location of a positive defect adjacent to the copper filled pore (right) results in a reduced effective barrier height and increased thermal activation of electrons over the barrier in the anodic direction.

voltage applied during growth of the anodic oxide). Upon application of potentials greater than the formation voltage, defect migration occurs, with increasing voltage increasing the rate of migration. Migration rates are also enhanced by increased temperature. Activation of defect migration is not observed on time-scales of < 1 ms. As defects align themselves across the barrier layer, resonant tunneling rates may approach those observed with direct tunneling through much thinner barriers.[22] In this work it is thought that a similar phenomenon is occurring during pulsed square wave electrodepositions, with defect migration leading to increased rates of resonant tunneling, thereby decreasing the rectifying effect of the barrier layer.

In sulfuric acid-anodized templates, ionic defects are less stable due to a lower formation voltage and will tend to migrate more readily than those defects formed via anodization in oxalic acid. The migration rate is further enhanced when reductive/oxidative pulse polarity is employed, since ohmic heating during the reductive pulse results in greater defect mobility during the oxidative pulse. Furthermore, it is expected that these effects would be most pronounced in those pores with thinner barrier layers. These pores require the migration of fewer defects to achieve high rates of resonant tunneling, and due to higher current density increased ohmic heating leads to increased rates of defect migration. During deposition these pores initially fill faster, but defect migration leads to resonant tunneling and increased oxidative current, until rectification is ineffective in that pore. As a result, copper metal is re-oxidized and the rate of growth slows, or stops, in these pores. This allows other pores, with thicker barrier layers that continue to rectify current, to catch-up. In oxalic acid-anodized pores the effect is less pronounced since the higher anodization potential increases the stability of ionic impurities formed during anodization, which reduces defect migration during the subsequent electrodeposition.

This gradual onset of oxidative breakdown in sulfuric acid-anodized templates when reductive/oxidative pulse polarity is employed with square wave deposition sequences is further supported by the observation of significant gas evolution in the final minutes of the deposition. This was not observed with any other deposition sequences, and when the as-deposited electrodes were examined, it was found that a nearly solid copper electrode had formed on the surface, as shown in Figure 7.20. It is expected that the gas evolution observed was the result of water oxidation at the surface of the electrode--a consequence of the barrier layer modification that had occurred in a large number of pores by this stage of the deposition. This gas evolution is not attributed to reduction of water or protons since a similarly solid copper electrode was formed when oxidative/reductive pulse polarity was employed (Figure 7.20) but no gas evolution was observed. It is thought that this process does not occur to any appreciable degree with pulsed sine wave depositions since the root-mean-square voltage is too low to significantly activate defects, and the effective pulse width is below the time required for appreciable defect migration to occur.

Ionic defect migration has been argued to lead to enhanced deposition of copper into sulfuric acid-anodized templates when reductive/oxidative pulse polarity square waves are employed. It is not yet known if this result is general for other metals. It has been reported that the field-emitting properties of the second metal in the junction is likely to influence breakdown voltage, with increasing work function of the metal leading to increased breakdown strength.[26] It is expected, however, that these results on copper

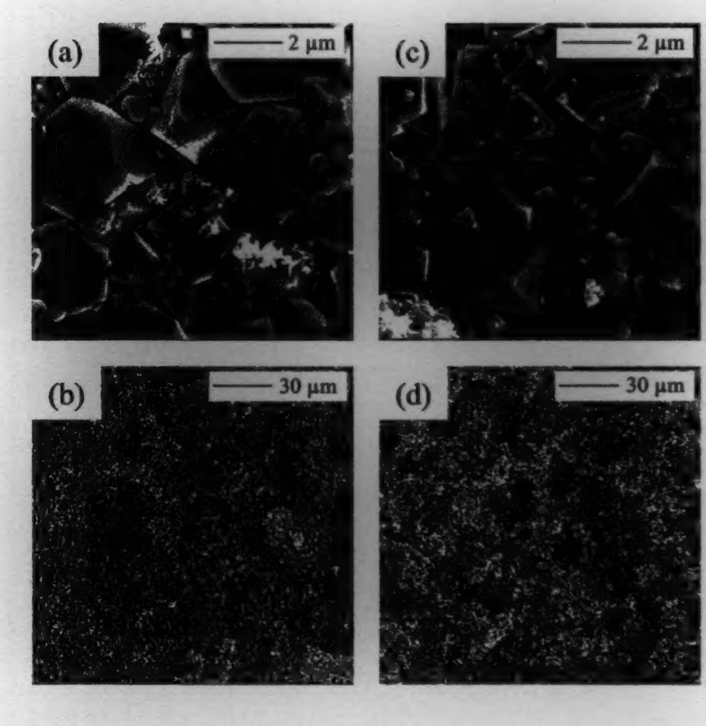

Figure 7.20. SEM images of as deposited sulfuric acid-anodized templates. Images from a sample deposited using a square wave with reductive/oxidative pulse polarity (a) and (b). Images from a sample deposited using a square wave with oxidative/reductive pulse polarity (c) and (d). Images show a nearly solid copper electrode forms regardless of pulse polarity.

pore filling as function of deposition conditions, including wave shape and pulse polarity, should be useful for optimizing the electrodeposition of other metals into PAO templates.

Conclusions

A systematic investigation of the effect of the deposition wave-form on the uniformity and completeness of copper deposition through the barrier layer into PAO templates grown in sulfuric or oxalic acid led to the following conclusions:

1. Continuous deposition produces the best pore-filling, but damages the PAO template and copper nanowires when deposition is continued until bulk copper is deposited on the surface of the PAO film. This damage is much more pronounced for the 35 nm diameter pores grown in oxalic acid than in the 20 nm diameter pores grown in sulfuric acid. This damage is likely caused by ohmic heating during bulk electrodeposition.
2. Pulsed electrodeposition conditions will produce good uniformity of deposition into relatively deep pores, without damage to the PAO template or nanowires when deposition is continued to bulk deposition onto the surface of the PAO film.
3. Square wave-forms yield better pore filling than comparable sine wave-forms.
4. Pulse polarity significantly impacts the rate and uniformity of pore-filling, but the specific effect is dependent upon both the wave-form and the structure and chemistry of the barrier layer.
5. Highly uniform deposition into oxalic acid grown pores by AC deposition is significantly more challenging than deposition into sulfuric acid grown pores, due to the different chemistry and structures of the barrier layers.

6. Under the influence of some electrodeposition sequences, changes in the rectification of the barrier layer will occur over the course of the deposition. These changes may be leveraged to improve the quality of pore-filling achieved.

References

(1) Yin, A. J.; Li, J.; Jian, W.; Bennett, A. J.; Xu, J. M. *Appl. Phys. Lett.* **2001**, *79*, 1039-1041.

(2) Gerein, N. J.; Haber, J. A. *J. Phys. Chem. B* **2005**, *109*, 17372-17385.

(3) Sun, M.; Zangari, G.; Metzger, R. M. *IEEE Trans. Magn.* **2000**, *36*, 3005-3008.

(4) Preston, C.; Moskovits, M. *J. Phys. Chem.* **1993**, *97*, 8495-8503.

(5) Box, G. E. P.; Hunter, W. G.; Hunter, J. S. *Statistics For Experimenters*; John Wiley & Sons: New York, 1978.

(6) Li, F.; Zhang, L.; Metzger, R. M. *Chem. Mater.* **1998**, *10*, 2470-2480.

(7) Masuda, H.; Hasegwa, F.; Ono, S. *J. Electrochem. Soc.* **1997**, *144*, L127-L130.

(8) Masuda, H.; Fukuda, K. *Science* **1995**, *268*, 1466-1468.

(9) Li, A. P.; Muller, F.; Birner, A.; Nielsch, K.; Gösele, U. *J. Vac. Sci. Technol. A* **1999**, *17*, 1428-1431.

(10) Thompson, G. E.; Wood, G. C. In *Treatise on Materials Science and Technology*; Scully, J. C., Ed.; Academic Press: New York, 1983; Vol. 23 Corrosion: Aqueous Processes and Passive Films, pp 205-329.

(11) Thompson, G. E. *Thin Solid Films* **1997**, *297*, 192-201.

(12) Diggle, J. W.; Downie, T. C.; Goulding, C. W. *Chem. Rev.* **1968**, *69*, 365-405.

(13) Vrublevsky, I.; Parkoun, V.; Sokol, V.; Schreckenbach, J. *Appl. Surf. Sci.* **2004**, *236*, 270-277.

(14) Vrublevsky, I.; Parkoun, V.; Sokol, V.; Schreckenbach, J.; Marx, G. *Appl. Surf. Sci.* **2004**, *222*, 215-225.

(15) Nielsch, K.; Muller, F.; Li, A.-P.; Gösele, U. *Adv. Mater.* **2000**, *12*, 582-586.

(16) Gao, T.; Meng, G.; Wang, Y.; Sun, S.; Zhang, L. *J. Phys.: Condens. Matter* **2002**, *14*, 355-363.

(17) Sauer, G.; Brehm, G.; Schneider, S.; Nielsch, K.; Wherspohn, R. B.; Choi, J.; Hofmeister, H.; Gösele, U. *J. Appl. Phys.* **2002**, *91*, 3243-3247.

(18) Sun, M.; Zangari, G.; Shamsuzzoha, M.; Metzger, R. M. *Appl. Phys. Lett.* **2001**, *78*, 2964-2966.

(19) Benfield, R. E.; Grandjean, D.; Dore, J. C.; Wu, Z.; Kroll, M.; Sawitowski, T.; Schmid, G. *Eur. Phys. J. D* **2001**, *16*, 399-402.

(20) Bard, A. J.; Faulkner, L. R. *Electrochemical Methods*; 2nd ed.; John Wiley and Sons: New York, 2001.

(21) Schmidlin, F. W. *J. Appl. Phys.* **1966**, *37*, 2823-2832.

(22) Hassel, A. W.; Diesing, D. *Thin Solid Films* **2002**, *414*, 296-303.

(23) Mujica, V.; Ratner, M. A. *Chem. Phys.* **2001**, *264*, 365-370.

(24) Joachim, C.; Ratner, M. A. *Nanotechnology* **2004**, *15*, 1065-1075.

(25) Joachim, C.; Ratner, M. A. *Proc. Natl. Acad. Sci. U.S.A.* **2005**, *102*, 8801-8808.

(26) Shousha, A. H. M. *J. Non-Cryst. Solids* **1975**, *17*, 100-108.

Conclusions and Future Work

Chapter 8. General Conclusions and Future Work

Novel Thin Film Semiconductors for Photovoltaic Applications

Global energy demand is rapidly increasing, as are CO_2 emissions from conventional energy sources and concerns about climate change. In Chapter 2, thin film photovoltaic devices were identified as one of several PV technologies with the potential to evolve into a primary source of clean power. However, if thin film PV devices are to realize this potential, new materials will be required whose use will not be curtailed by the limited abundance of constituent elements. Several Cu−Bi−S and Cu−Sb−S mineral phases have the potential to replace CIGS and CdTe as the solar absorber in thin film PV devices, significantly raising the energy production ceiling.

In Chapter 3 the synthesis of Cu_3BiS_3 thin films on fused silica substrates, by heating metal and metal sulfide precursors under H_2S, was investigated. It was found that the morphology of the product films was controlled by the formation of binary sulfide intermediates. For metal and metal sulfide precursors the specific intermediates and morphologies were different; however, in each case the morphology rendered the Cu_3BiS_3 thin films unsuitable for use in PV devices. In Chapter 4, based on the results of the precursor-processing synthetic strategies of Chapter 3, a one-step reactive deposition was developed that produced films of superior quality. By synthesizing Cu_3BiS_3 directly on a hot substrate the morphology-directing intermediates were avoided, producing smooth, mirror-like films ideal for thin film PV devices. Basic semiconductor properties suitable for device applications were measured, including: a direct forbidden band-gap of 1.4 eV, an optical absorption coefficient of $1x10^5$ at 1.9 eV, and a resistivity of 84 $\Omega \cdot cm$.

By subsequently annealing films deposited by the one-step method, the grain sizes of the films could be increased, and the resistivty decreased to 9.6 Ω·cm.

High-throughput combinatorial experimental methods are considered to be a promising approach for integration of Cu_3BiS_3, or other novel semiconductors, into thin film PV devices. In Chapter 5, as a preliminary step in the application of combinatorial strategies to Cu_3BiS_3 device development, material and method compatibilities, as well as techniques for making electrical contact to library cells, were investigated. It was found that Cu_3BiS_3 thin films deposited on TCO coated soda-lime and borosilicate glass substrates were of similar quality to those synthesized on fused silica substrates in Chapter 4. Scanning auger data indicated that some interfacial reaction occurred between the ITO or FTO coating and the deposited Cu_3BiS_3 film; however, the integrity of individual films was largely maintained, and XRD and SEM data collected from the surface of the Cu_3BiS_3 thin film was consistent with data collected from films deposited on uncoated fused silica substrates. In some samples a ZnSe buffer layer was deposited on the TCO prior to Cu_3BiS_3 deposition, this ZnSe layer was found to be incompatible with the one-step deposition process, being consumed by reaction with Cu_3BiS_3. Aluminum, nickel, and molybdenum metal back contacts were sputter deposited following deposition of the absorber layer, all of which exhibited conformal coating and good adhesion.

The multi-layer samples were fabricated to test material and method compatibilities, but I-V data was collected to test for serendipitous PV performance. Two different methods of making electrical connection to the metal back contacts were evaluated. The use of colloidal silver to attach test leads was deemed unsuitable, due to evidence of reaction with the Cu_3BiS_3 film. A pressure contact was also fabricated, which eliminated the possibility of reaction, and was judged to be superior for eventual use with 64 spot combinatorial libraries. I-V curves collected from these samples were linear, with behavior best described as resistor-like. When exposed to light, a small photo-voltage was observed in a minority of samples, and for all samples the slope of the I-V curve was unchanged from the I-V data collected in the dark. Resistor-like behavior is consistent with the formation of ohmic contacts at the TCO/Cu_3BiS_3 and Cu_3BiS_3/metal junctions. Junctions of this type have been previously documented for ITO/CIGS/Au and FTO/CIGS/Au three-layer samples.[1,2] However, since no photoconductivity (or decreased resistivity) was observed during the collection of I-V curves under illumination, it is possible that the resistor-like behavior of samples in this work may be due to electrical shorts between the front and back contacts.

The synthesis of high quality Cu_3BiS_3 thin films, and the compatibility of this synthetic method with a variety of substrates, is a promising first step in the identification of novel device configurations based on Cu–Bi–S and Cu–Sb–S solar absorber materials. However, integration of Cu_3BiS_3, or other novel absorber materials, into a device exhibiting reasonable conversion efficiency will require additional effort. Key components of this future work can be expected to include the exploration of alternative configurations for device fabrication, a fuller implementation of the combinatorial strategy, additional characterization of Cu_3BiS_3 semiconductor properties, and extension of the one-step deposition method to other compounds in the Cu–Bi–S and Cu–Sb–S phase systems.

When fabricating a thin film PV device, one of two configurations is commonly employed: superstrate and substrate. These two configuration types are depicted in Figure 8.1, and are named on the basis of whether light is incident upon the device on the deposition substrate (superstrate configuration) or opposite the deposition substrate (substrate configuration).[3,4] The configuration choice is based in part on the thermal stability of the various junctions in the device. The substrate configuration minimizes thermal processing of the heterojunction, and is conventionally employed for the production of CIGS devices.[3,5,6] The superstrate configuration has been tested for CIGS devices, but the elevated temperatures required for absorber deposition result in the unwanted interdiffusion of Cd into the CIGS layer, and poor device performance.[5] Conversely, when the CIGS layer is deposited on the Mo back contact, a beneficial reaction results in the formation of a semiconducting $MoSe_2$ layer at the Mo/CIGS interface.[7] $MoSe_2$ is a p-type semiconductor with a band-gap of 1.3 eV, slightly larger than that of the CIGS absorber layer. The CIGS/$MoSe_2$ valence band offset reflects electrons, and the $MoSe_2$/Mo junction provides a low-resistance contact for holes, enhancing the overall performance of the device.[7]

For CdTe devices the superstrate configuration is conventionally employed.[3,5,6] The CdS/CdTe junction is relatively robust, and able to withstand high growth and annealing temperatures with minimal adverse effects on device performance.[6] Forming a high-quality ohmic back contact to CdTe is more difficult. A metal ohmic contact to a p-type semiconductor requires the metal to have a work function greater than that of the semiconductor. The work function of CdTe is sufficiently large (5.8 eV) that any metal contacts would form a Scottky barrier.[5,6] As a result, it is necessary to form low-

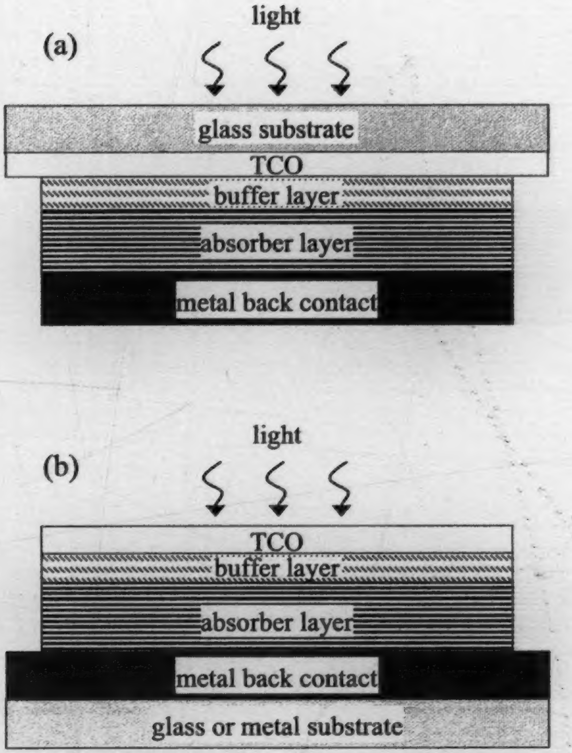

Figure 8.1. Superstrate (a) and substrate (b) configurations for thin film PV devices.

resistance contacts by modifying the surface of the CdTe layer to produce a heavily p-doped region and/or utilizing semiconductor contacts.[5,8] Contacts produced in this manner are sensitive to thermal processing, and superior device performance is realized when they are applied last, and shielded from thermal processing.[5,6]

In Chapter 5, the superstrate configuration was employed for sample preparation for two reasons: (1) it permits the purchase and use of high-quality TCO coated substrates, reducing the complexity of sample fabrication, and (2), a single transparent contact is required for the collection of sequential I-V curves for screening combinatorial device libraries. Increased complexity associated with the deposition of TCO layers can be accommodated; however, the requirement of a single transparent contact is necessary for library screening, and must be incorporated into PV libraries. A pseudopotentiostat system previously developed for analysis of battery materials,[9] has been reproduced in our lab by Dr. T.D. Hatchard, one of the authors of the original paper. A schematic of the system is presented in Figure 8.2. The system is designed to use a common transparent front (or back) contact and 64 distinct back (or front) contacts. Although it has not yet been tested, it is expected that this system will be suitable for rapid sequential collection of I-V curves, and mapping of library cell conversion efficiencies. If the substrate configuration is to be applied to library development, it would be necessary to utilize a transparent back contact, since the electrical contact plate would be applied to the TCO front contacts, preventing illumination from that side.

It has been previously mentioned that ITO and FTO have been identified as forming an ohmic contact with CIGS.[1,2] In Chapter 5, one possible explanation for the resistor-like behavior of the 3-layer samples is the formation of a similar TCO/Cu_3BiS_3

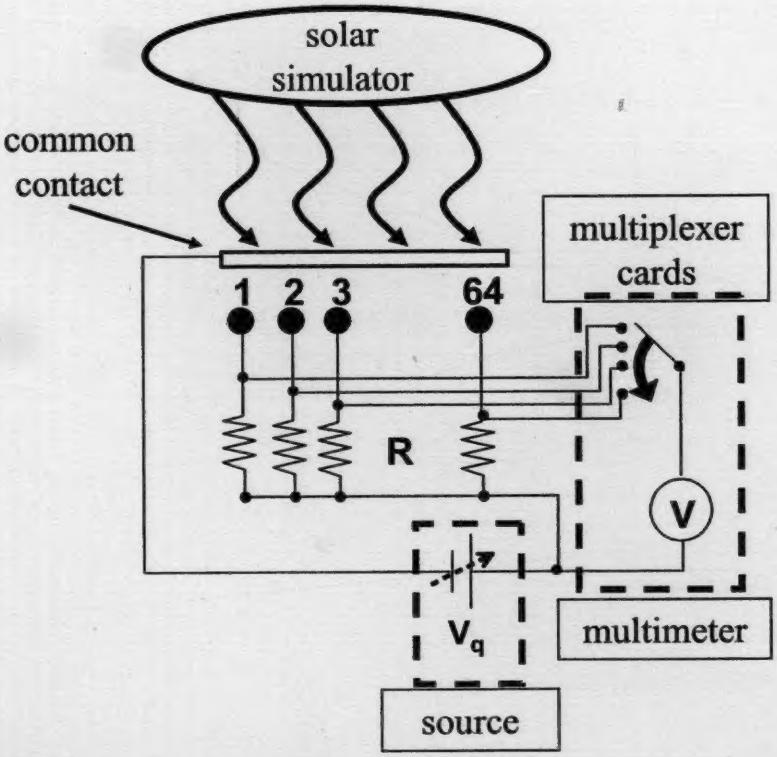

Figure 8.2. Schematic of a pseudopotentiostat for collection of sequential IV curves from a library chip containing 64 distinct PV devices, with 64 discrete contacts and one common contact.

ohmic contact. If these contacts are confirmed to be ohmic, it would provide an ideal route to implementation of the substrate configuration, with a single transparent back contact. This would also be consistent with the use of TCO back contacts for the fabrication of bifacial thin film PV devices, of the type reported in the literature.[2,10] If it is found that the contact is not ideal, it may still be possible to utilize this approach, since the degradation in performance at the back contact would be consistent across the library, and a relative comparison of device configurations could still be made. This would be similar to some bifacial devices reported in the literature, where an ideal transparent ohmic contact was not realized, and functional devices with lower conversion efficiencies were produced.[10]

In Figure 8.3 and 8.4 are proposed combinatorial strategies, employing the superstrate and substrate configurations, respectively. Combinatorial methods are particularly applicable in areas where limited understanding dictates that success is most likely to be achieved by empirical methods.[11] This makes them ideally suited to the discovery of novel thin film PV devices, including the identification of a heterojunction couple able to persist through the reactive deposition process. In Chapter 5, ZnSe was identified as being incompatible with the one-step deposition of Cu_3BiS_3; however, it is possible that implementation of the combinatorial strategy in Figure 8.3 (superstrate configuration), will result in the identification of a buffer layer that is able to withstand the reactive deposition process (4 buffer layers per library, multiple libraries). A partial list of materials suitable for use as the buffer layer was provided in Chapter 2. Any promising configurations identified using the superstrate configuration of Figure 8.3, could be compared and contrasted with devices identified from the substrate

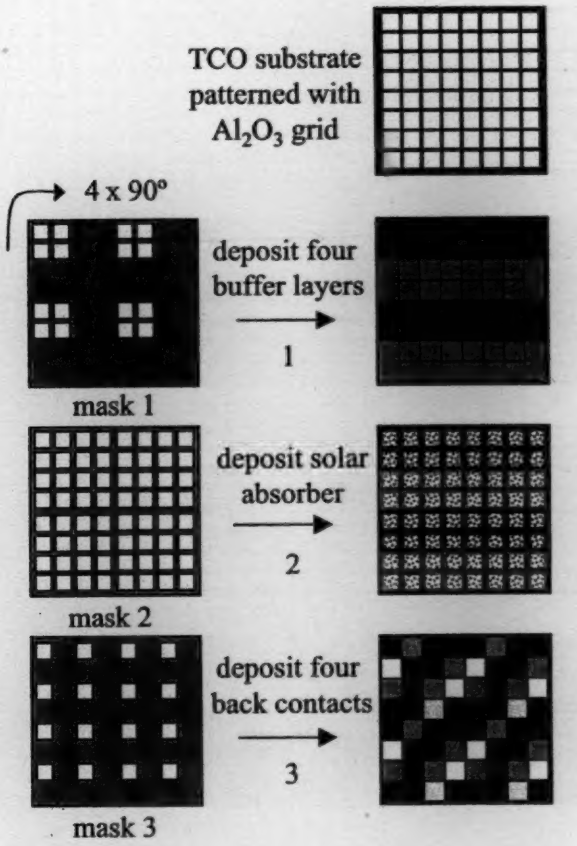
TCO substrate patterned with Al_2O_3 grid
4 x 90°
deposit four buffer layers
1
mask 1
deposit solar absorber
2
mask 2
deposit four back contacts
3
mask 3

Figure 8.3. Superstrate configuration combinatorial strategy using a TCO substrate patterned with an alumina grid. Complete library contains 64 discrete cells, but only 16 distinct combinations. Each quadrant is identical.

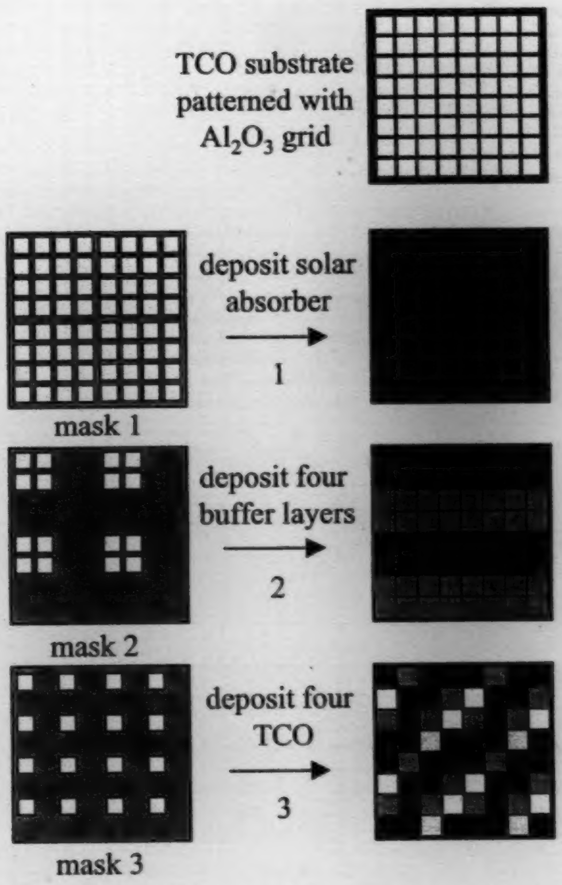
TCO substrate patterned with Al_2O_3 grid
mask 1
deposit solar absorber
1
mask 2
deposit four buffer layers
2
mask 3
deposit four TCO
3

Figure 8.4. Substrate configuration combinatorial strategy using a TCO substrate patterned with an alumina grid. Complete library contains 64 discrete cells, but only 16 distinct combinations. Each quadrant is identical.

configuration of Figure 8.4, where the buffer layer and front contact had been subjected to minimal thermal processing. By utilizing both approaches in parallel, additional information could be obtained on the thermal stability of different materials, and also on the effect of processing conditions on device performance.

There are two additional features that the strategies of Figure 8.3 and Figure 8.4 have in common. One is the fact that each strategy produces 64 discrete cells, but only 16 distinct configurations. For each configuration there are 4 duplicate cells distributed across the substrate (each of the four quadrants are identical). This would enable identification of any differences in device performance due to variations in deposition and processing across the substrate, and also minimize the possibility of false negatives for a particular configuration, which would be much more likely if assessments were based on a single cell. The second feature is that library fabrication is carried out on a TCO substrate patterned with an alumina grid. A photolithographic process has been developed, whereby a patterned photo-resist is applied to the substrate, an alumina film sputter deposited, and the resist removed, leaving behind the alumina grid. The details of this process are not reported, but the alumina grid can be varied in thickness, and coincides with the shadowed bars of the fractal masks in Figures 8.2 and 8.3. The advantages of this substrate patterning are two-fold. One, it provides a well defined area for each cell of the library. Two, following library deposition the cells could be scribed, ensuring electrical isolation between the cells, while maintaining the common TCO contact required for library screening.

In addition to developing combinatorial strategies based on the one-step deposition of Cu_3BiS_3, it would also be advantageous to extend this deposition method to other novel semiconducting phases in the Cu–Bi–S and Cu–Sb–S phase systems. Having identified combinatorial strategies for Cu_3BiS_3 using this deposition method, it should be relatively straightforward to substitute additional absorber materials that are deposited in a similar manner. The one-step deposition method has been successfully applied to the synthesis of $Cu_{12}Sb_4S_{13}$ (Appendix B). Although this phase is an unlikely candidate for application in PV devices, it is expected that the one-step method could be adapted for the synthesis of other more promising compounds in the Cu–Bi–S and Cu–Sb–S phase systems (Chapter 2). More detailed characterization of the semiconductor properties of Cu_3BiS_3, and any additional compounds synthesized, is also required. This would enable better assessment of the suitability of these materials for use as a solar absorber, and would also be useful in interpreting the performance of any devices identified. Properties of immediate interest include the carrier concentration, mobility, and lifetime, which could be determined by a combination of Hall-effect[12,13] (carrier concentration and mobility) and photoconductivity decay[14] (carrier lifetime) measurements.

Template Directed Synthesis of Copper Nanowires

In Chapter 6 porous aluminum oxide was introduced as a versatile template material for the fabrication of nanostructures in general, and for the electrodeposition of metal nanowires in particular. DC electrodeposition has been successfully employed for metal deposition into PAO template pores, and provides a high degree of control over the metal nanostructure and uniformity of growth, but requires laborious separation of the PAO template from the aluminum substrate. AC electrodeposition has also been used for metal deposition into PAO templates, and since removal from the aluminum substrate is not required, it is more generally suited to the scalable nature of the template; however, it provides considerably less control over the uniformity of pore filling.

In Chapter 7, the effect of AC eletrodeposition conditions on the growth of copper nanowires in PAO templates was investigated. Using a FFDOE, an improved set of conditions was identified. Based on examination of the effect of pulse polarity and wave shape, a further optimized set of conditions was developed, enabling more uniform filling of deep pores (24 μm). The conditions producing superior deposition utilized a square waveform, and the improved pore-filling achieved with these deposition conditions was attributed to the migration of defects in the Al_2O_3 barrier layer, and the loss of rectification in certain pores. Defect migration is dependent on voltage and temperature, and in pores where the barrier layer is thinner, loss of rectification occurs more quickly. Initially, filling in pores with thinner barrier layers is faster. Once these pores no longer rectify current, filling slows, and wire growth in pores with thicker barrier layers can catch-up.

It is expected that the best set of deposition conditions identified in Chapter 7 can be further optimized for the deposition of copper, and also extended to other metals. Defect migration is dependent on anodization voltage, deposition voltage, and temperature. By varying these parameters, it should be possible to control the fraction of pores in which loss of rectification occurs, and the stage of the deposition at which it occurs. This has not yet been investigated. Since it is desirable to have complete filling of all pores, the ideal conditions may be different for different pore depths, with growth in the fastest filling pores being shut down only once they are almost completely filled.

For shallower pores, increasing the deposition voltage or temperature should produce more rapid loss of rectification in a greater number of pores, while for deeper pores, lower deposition voltage and temperature should have the opposite effect. Further control and fine tuning is expected to be accessible by varying the thickness of the barrier layer in the final stage of template anodization.

With this approach, control over wire growth is achieved through modification of the potential barrier by selectively changing the defect distribution in the Al_2O_3 pore bottoms during the course of the deposition. Since the shape of this barrier is dependent on the work function of Al, and the second metal in the MIM junction, optimized deposition conditions are expected to vary with the metal being deposited. The work functions of Al and Cu are 4.28 eV and 4.65 eV, respectively.[15] If Ni, with a work function of 5.15 eV[15] is deposited in the pores, the barrier height in the anodic direction will be increased significantly, possibly requiring modified deposition conditions for uniform wire growth. On the other hand, if Fe, with a work function of 4.5 eV[15], is deposited in the pores, the potential barrier will be similar to that with deposited copper, and the deposition conditions optimized for copper may translate well. Preliminary results for the deposition of iron indicate this to be the case.[16] Optimizing AC electrodeposition conditions for each metal of interest would be a time consuming process, and in some cases optimization may be less successful. To avoid this complication it may be possible to define the nature of the MIM interface by initially depositing a small amount of copper. The PAO electrode with copper-filled pore bottoms could then be transferred to a second deposition bath, for pore-filling with the desired metal. Utilizing this approach, it is likely that the conditions identified for copper deposition could be directly translated to any metal of interest.

Another area of future work requires the identification of novel applications for copper nanowires produced using this low-cost, high throughout approach. This has been an active area of research in the Haber group, and significant advances have been made in both the scale-up of copper nanowire synthesis to the multi-gram scale,[17] and blending the nanowires into polystyrene to produce electrically conductive nanocomposites.[18,19] A comprehensive review of these advances is provided in the doctoral thesis of Haber group alumnus Genaro A. Gelves.[20]

References

(1) Nakada, T.; Hirabayashi, Y.; Tokado, T. *Jpn. J. Appl. Phys., Part 2* **2002**, *41*, L1209-L1211.

(2) Nakada, T.; Hirabayashi, Y.; Tokado, T.; Ohmori, D.; Mise, T. *Solar Energy* **2004**, *77*, 739-747.

(3) Miles, R. W.; Hynes, K. M.; Forbes, I. *Prog. Cryst. Growth Charact. Mater.* **2005**, *51*, 1-42.

(4) Hegedus, S. S.; Shafarman, W. N. *Prog. Photovolt.: Res. Appl.* **2004**, *12*, 155-176.

(5) Romeo, A.; Terheggen, M.; Abou-Ras, D.; Bätzner, D. L.; Haug, F.-J.; Kälin, M.; Rudmann, D.; Tiwari, A. N. *Prog. Photovolt.: Res. Appl.* **2004**, *12*, 93-111.

(6) Dhere, N.; Dhere, R. *J. Vac. Sci. Technol. A* **2005**, *23*, 1208-1214.

(7) Rau, U.; Schock, H. W. In *Clean Electricity From Photovoltaics*; Archer, M. D., Hill, R., Eds.; Imperial College Press: London, 2001, pp 277-345.

(8) Bonnet, D.; Meyers, P. *J. Mater. Res.* **1998**, *13*, 2740-2753.

(9) Cumyn, V. K.; Fleischauer, M. D.; Hatchard, T. D.; Dahn, J. D. *Electrochem. Solid-State Lett.* **2003**, *6*, E15-E18.

(10) Young, D. L.; Abushama, J.; Noufi, R.; Li, X.; Keane, J.; Gessert, T. A.; Ward, J. S.; Contreras, M.; Symko-Davies, M.; Coutts, T. J. In *Proceedings of the 29th IEEE Photovoltaic Specialists Conference*: New Orleans, 2002, pp 608-611.

(11) Cawse, J. N. *Acc. Chem. Res.* **2001**, *34*, 213-221.

(12) He, Y. B.; Polity, A.; Österreicher, I.; Pfisterer, D.; Gregor, R.; Meyer, B. K.; Hardt, M. *Physica B* **2001**, *308-310*, 1069-1073.

(13) Hamberg, I.; Granqvist, C. G. *J. Appl. Phys.* **1986**, *60*, R123-R159.

(14) McGuire, G. E., Ed. *Characterization of Semiconductor Materials*; Noyes Publications: Park Ridge, New Jersey, 1989.

(15) Michaelson, H. B. *J. Appl. Phys.* **1977**, *48*, 4729-4733.

(16) Gerein, N. J.; Mithani, S. S.; Haber, J. A. In *Materials Research Society Symposium Proceedings*; Peng, X., Feng, X., Liu, J., Ren, Z., Voigt, J. A., Eds.: San Francisco, CA, 2005; Vol. 879E, pp Z11.19.11-16.

(17) Gelves, G. A.; Murakami, Z. T. M.; Krantz, M. J.; Haber, J. A. *J. Mater. Chem.* **2006**, *16*, 3075-3083.

(18) Gelves, G. A.; Sundararaj, U.; Haber, J. A. *Macromol. Rapid Commun.* **2005**, *26*.

(19) Gelves, G. A.; Lin, B.; Sundararaj, U.; Haber, J. A. *Adv. Funct. Mater.* **2006**, *16*, 2423-2430.

(20) Gelves, G. A. *Synthesis of Copper and Silver Nanowires in Porous Alumina Templates and Preparation of Polymer Nanocomposites*, Chemistry; University of Alberta: Edmonton, AB, 2007.

Appendices

Appendix A. Synthesis of $Cu_{12}Sb_4S_{13}$ Thin Films by Heating Metal Precursor Films under Hydrogen Sulfide

Introduction

In Chapter 3 a two-step method for the synthesis of Cu_3BiS_3 thin films was presented, involving the heating of precursor films under H_2S. This method has been extended to the synthesis of copper-poor tetrahedrite. The mineral phase tetrahedrite is known to exist over a wide composition range from copper-poor $Cu_{12}Sb_4S_{13}$ to copper-rich $Cu_{14}Sb_4S_{13}$.[1,2] The stoichiometry of copper-poor tetrahedrite is similar to that of famatinite (Cu_3SbS_4) and skinnerite (Cu_3SbS_3), and it has been reported previously that synthetic skinnerite often contains small amounts of tetrehedrite.[3] Reported syntheses of $Cu_{12}Sb_4S_{13}$ have been by solid-state[2,4] and hydrothermal[5,6] methods. Details of this synthesis are presented below.

Experimental Details

Cu-Sb multilayer precursors were deposited on fused silica substrates in a similar manner to that described in Chapter 3 for Cu-Bi precursors. Substrates were cleaned by immersion in 2-propanol in an ultrasonic bath for 30 minutes, after which they were dried with a stream of N_2. Multilayer Cu-Sb metal precursor films, 500 nm thick, were deposited by sputtering Cu at 72 W, and Sb at 18 W, with an Ar pressure of 5 mtorr. Each repeat layer was 250 nm thick. The substrate platen was rotated at 6 rpm during deposition. Precursor films were subsequently heated under 50 torr H_2S at 10°C/minute to 250 °C, with the temperature maintained at 250 °C for 25 hours. After heating, the sample was cooled to 100 °C at 2 °C/minute. Product thin films were characterized using SEM/EDX (JEOL 6031F FESEM), WDX (JEOL 8900 microprobe), and XRD (Bruker D8 diffractometer with area detector).

Results and Discussion

SEM images collected from the product film are presented in Figure A1. The morphology of the film is characterized by a regular repeating pattern produced by the film lifting off the substrate (Figure A1 (a)). Where pockets have formed between the film and the substrate significant cracking and breakage is evident, resulting in holes in the film. This particular morphology is thought to be a consequence of sulfur uptake, producing expansion and strain in the film. This is similar to what was observed for Cu-Bi-S and Bi precursors heated under H_2S as described in Chapter 3. Higher magnification SEM images (Figure A1 (b) and (c)) reveal the micron sizes of the individual crystallites in the product film, as well as the presence of what appears to be a secondary phase with a different morphology that has segregated to the surface of the film.

The XRD powder pattern collected from this film, along with the standard powder pattern for $Cu_{12}Sb_4S_{13}$ (PDF 24-1318), is presented in Figure A2. The standard powder pattern is a good match in terms of both peak position and intensity, suggesting the $Cu_{12}Sb_4S_{13}$ film is composed of randomly orientated crystallites. There is also evidence of a secondary phase, with the most obvious peak observed at 49.5° 2-theta. The observation of a second phase in the XRD powder pattern is consistent with the apparent presence of a sub-phase in the SEM images. This secondary-phase could not be

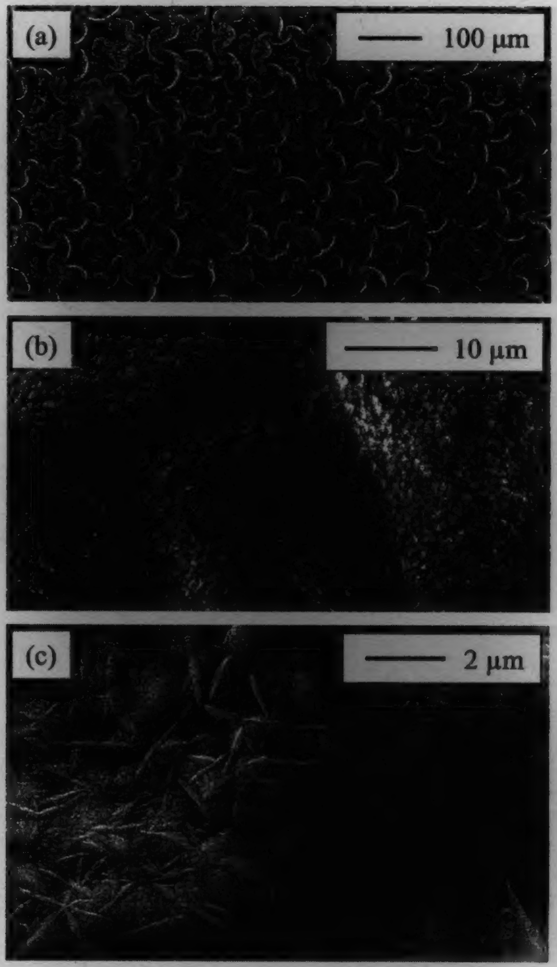

Figure A1. SEM images collected from a $Cu_{12}Sb_4S_{13}$ thin film synthesized by heating a metal precursor film under 50 torr H_2S for 25 hr at 250 °C. Note the presence of what appears to be a secondary phase in (c).

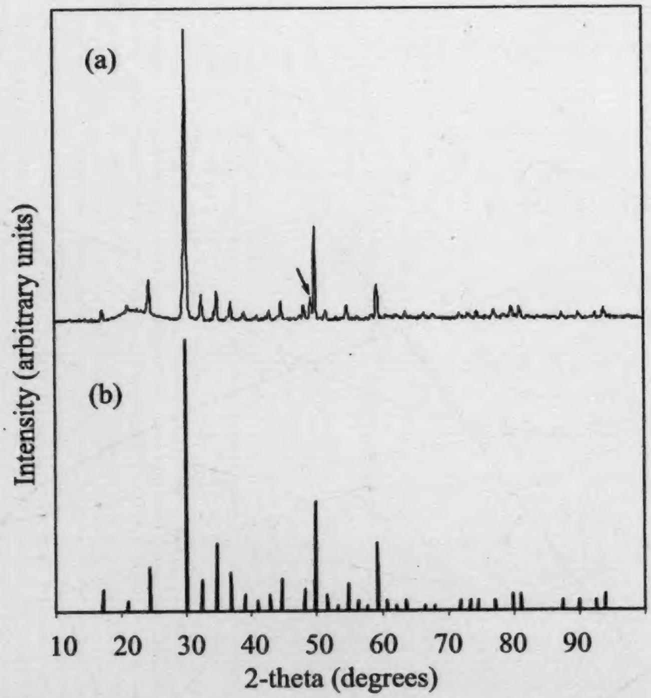

Figure A2. XRD powder pattern collected from a $Cu_{12}Sb_4S_{13}$ thin film synthesized by heating a metal precursor film under 50 torr H_2S for 25 hr at 250 °C (a), and standard powder pattern for $Cu_{12}Sb_4S_{13}$ (b). In panel (a) the peak extraneous peak at 49.5° 2-theta is marked with an arrow.

identified by XRD, but numerous Cu-Sb-S phases are known, some with stoichiometry close to that of copper-poor tetrahedrite, including copper rich tetrahedrite ($Cu_{14}Sb_4S_{13}$), famatinite (Cu_3SbS_4), and skinnerite (Cu_3SbS_3).[2,3] WDX analysis of the product film yielded a stoichiometry of Cu:Sb:S of 12:4:13. This is the expected stoichiometry for copper poor-tetrahedrite, and would support the conclusion that the secondary phase is present in small quantities, and that it is likely to have a stoichiometry close to that of copper-poor tetrahedrite.

No efforts have been made to optimize the synthesis to produce films with smoother morphology, or phases expected to be better suited to PV applications such as Cu_3SbS_3 or Cu_3SbS_4. It is possible that varying precursor preparation (multi-layer or sulfide precursor) or processing conditions (temperature, gas composition) could be effective at controlling the morphology and/or product obtained. This could be incorporated into future investigations.

Conclusions

Copper-poor tetrahedrite, $Cu_{12}Sb_4S_{13}$, has been synthesized by heating metal precursor films under H_2S. Product thin films contained an unidentified secondary phase, present in small quantities on the surface of the film. These films also suffered from poor morphology, thought to result from uptake of sulfur during the heating process. No effort was made to optimize the synthesis, so it is not known at this time if this method could produce films with improved morphology.

References

(1) Bullett, D. W.; Dawson, W. G. *J. Phys. C: Solid State Phys.* **1986**, *19*, 5837-5847.

(2) Skinner, B.; Luce, F.; Makovicky, E. *Econ. Geol.* **1972**, *67*, 924-938.

(3) Makovicky, E.; Balic-Zunic, T. *Can. Mineral.* **1995**, *33*, 655-663.

(4) Pfitzner, A.; Evain, M.; Petricek, V. *Acta. Cryst. B* **1997**, *53*, 337-345.

(5) Lind, I.; Makovicky, E. *N. Jb. Miner. Abh.* **1982**, *145*, 134-156.

(6) An, C.; Jin, Y.; Tang, K.; Qian, Y. *J. Mater. Chem.* **2003**, *13*, 301-303.

Appendix B. One-Step Synthesis of $Cu_{12}Sb_4S_{13}$ Thin Films

Introduction

In Chapter 4 a one-step reactive deposition was reported for the synthesis of smooth and continuous Cu_3BiS_3 thin films. This method has been extended to the synthesis of copper-poor tetrahedrite, $Cu_{12}Sb_4S_{13}$. The stoichiometry of copper-poor tetrahedrite is similar to famatinite (Cu_3SbS_4) and skinnerite (Cu_3SbS_3), and it has been reported that synthetic Cu_3SbS_3 often contains small amounts of tetrahedrite.[1] Tetrahedrite has been synthesized previously by solid-state[2,3] and hydrothermal[4,5] methods. Results of this synthesis are reported below.

Experimental Details

$Cu_{12}Sb_4S_{13}$ thin films were deposited on fused silica substrates in a one-step process similar to that employed for the deposition of Cu_3BiS_3 thin films as described in Chapter 4. Substrates were cleaned in 2-propanol in an ultrasonic bath for 30 minutes, immersed for 30 minutes in a 1:3 mixture of H_2O_2:H_2SO_4, rinsed with distilled H_2O, rinsed with 2-propanol, and dried under N_2. CuS was sputtered at 80 W RF, Sb at 15 W DC, with an Ar pressure of 5 mtorr. During deposition the substrate temperature was maintained at 250 °C, and the substrate platen rotated at 6 rpm. At the end of the deposition the temperature was maintained at 250 °C for 30 minutes, and then cooled to 100 °C at 2°C/minute. To obtain the correct stoichiometry CuS and Sb were co-sputtered for 5 minutes, followed by CuS only sputtering for 24 minutes. Each cycle deposited ~75 nm, and the cycle was repeated 8 times for a film thickness of ~600 nm. Following deposition, some films were subsequently annealed under 1 torr H_2S/49 torr Ar at 250 °C for 2 hours, followed by cooling to 100 °C at 2 °C/minute. Product films were characterized using SEM (JEOL 6031F FESEM), and XRD (Bruker D8 diffractometer with area detector).

Results and Discussion

SEM images of a film deposited at 250 °C are presented in Figure B1. The surface of the film is very smooth, with a mirror-like appearance. When viewed at a cross-section (Figure B1 (b)) the layered structure of the film deposition is observed. It should be noted that this layered structure was also observed when Cu_3BiS_3 thin films were deposited in a similar manner with a substrate temperature of 250 °C. Also presented in Figure B1 is the powder pattern collected from this film along with the standard powder pattern for $Cu_{12}Sb_4S_{13}$ (PDF 24-1318). The powder pattern is a good match with the standard powder pattern in terms of both peak position and intensity, suggesting that the film is phase pure with a random orientation of crystallites.

Presented in Figure B2 are SEM images of a film deposited at 250 °C, followed by annealing at 250 °C under H_2S for 2 hr. When compared to SEM images of the as-deposited film, two morphological differences are apparent. One, a roughening of the surface of the film is observed following annealing, although the film is still smooth and mirror-like in appearance. Two, the layered structure of the film is no longer evident when the film is observed at a cross-section (Figure B2 (b)). The homogenizing effect of annealing was also observed when Cu_3BiS_3 thin films deposited at 250 °C were annealed (Chapter 4). Also presented in Figure B2 is the powder pattern collected from this film

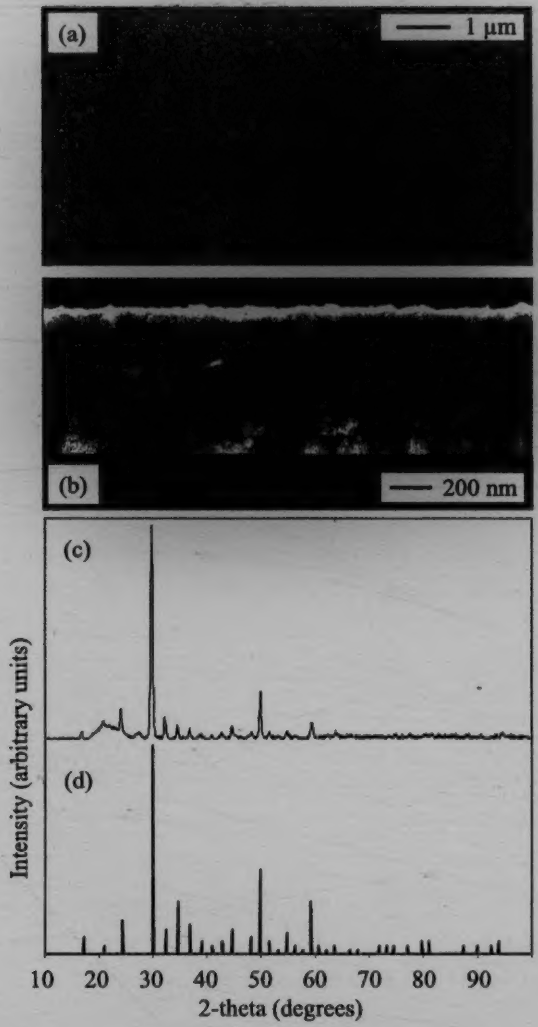

Figure B1. SEM images collected from a $Cu_{12}Sb_4S_{13}$ film deposited with a substrate temperature of 250 °C (a) and (b), powder pattern collected from the film (c), and standard powder pattern for $Cu_{12}Sb_4S_{13}$ (d).

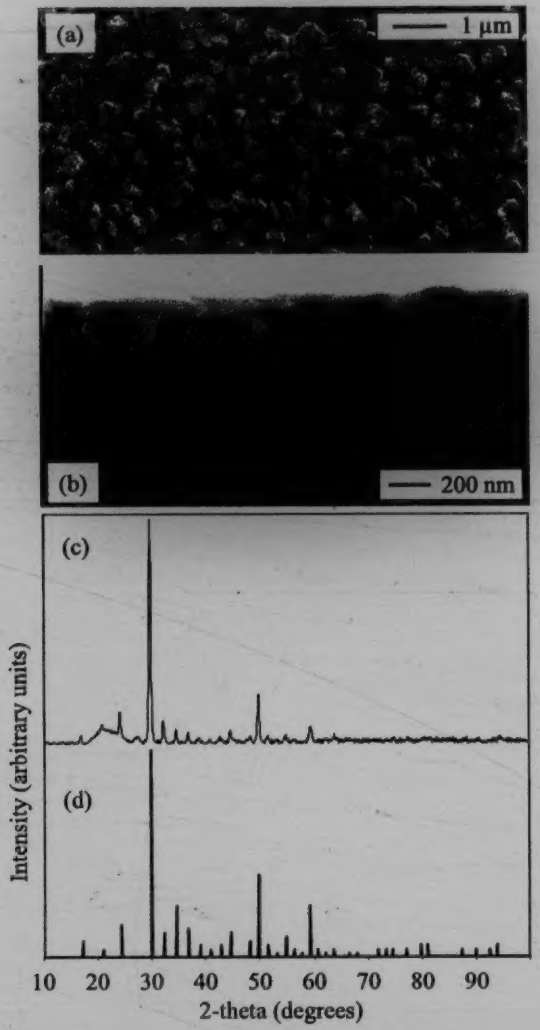

Figure B2. SEM images collected from a $Cu_{12}Sb_4S_{13}$ film deposited with a substrate temperature of 250 °C and then annealed for 2 hr at 250 °C under 1 torr H_2S/49 torr Ar (a) and (b), powder pattern collected from the film (c), and standard powder pattern for $Cu_{12}Sb_4S_{13}$ (d).

along with standard powder pattern for $Cu_{12}Sb_4S_{13}$. The sample powder pattern is a good match with the standard powder pattern, with no significant changes from the powder pattern collected from the as-deposited sample.

The morphology of the $Cu_{12}Sb_4S_{13}$ films synthesized by the one-step method was significantly improved relative to the morphology of the films produced by the two-step method in Appendix A. When exposed to atmosphere, these $Cu_{12}Sb_4S_{13}$ films took on a whitish hue. This change took place rapidly (hours to days) and is expected to be a result of oxidation. Consequently no further characterization of these films was carried out, and no assessment of the optical and electrical properties of these films was made. The band gap for copper-poor tetrahedrite has been calculated to be 1.2 eV, which is within the acceptable range for use in a single junction cell; however, the valence band is not filled and the compound exhibits metallic behavior.[6] It has also been reported that copper-poor tetrahedrite exhibits ionic conductivity at room temperature as a result of mobile copper ions.[7] (See Chapter 2 for further details) Consequently, copper-poor tetrahedrite is not expected to be suitable for incorporation into PV devices. It is possible that varying deposition conditions (temperature) or post-deposition annealing conditions (temperature, gas composition, time) could produce other phases such as Cu_3SbS_3 or Cu_3SbS_4, which are expected to be better candidates for PV applications. This has not been investigated and could be incorporated into future work.

Conclusions

Copper-poor tetrahedrite, $Cu_{12}Sb_4S_{13}$, has been synthesized by reactive deposition on heated substrates. These thin films are phase-pure and smooth. They also undergo rapid oxidation upon exposure to air. No optical or electrical characterization of these films has been performed; consequently, the suitability of these $Cu_{12}Sb_4S_{13}$ thin films for PV applications was not assessed. However, it has been reported that copper-poor tetrahedrite exhibits metallic behavior and is a room temperature ionic conductor, which would make it unsuitable for application in PV devices. The possibility of varying deposition or annealing conditions to produce Cu_3SbS_3 or Cu_3SbS_4 has not been investigated.

References

(1) Makovicky, E.; Balic-Zunic, T. *Can. Mineral.* **1995**, *33*, 655-663.

(2) Pfitzner, A.; Evain, M.; Petricek, V. *Acta. Cryst. B* **1997**, *53*, 337-345.

(3) Skinner, B.; Luce, F.; Makovicky, E. *Econ. Geol.* **1972**, *67*, 924-938.

(4) Lind, I.; Makovicky, E. *N. Jb. Miner. Abh.* **1982**, *145*, 134-156.

(5) An, C.; Jin, Y.; Tang, K.; Qian, Y. *J. Mater. Chem.* **2003**, *13*, 301-303.

(6) Bullett, D. W.; Dawson, W. G. *J. Phys. C: Solid State Phys.* **1986**, *19*, 5837-5847.

(7) Makovicky, E.; Skinner, B. *Can. Mineral.* **1979**, *17*, 619-634.

Appendix C. Current Density and Charge Density Data for Electrodeposition of Copper into Porous Aluminum Oxide Templates

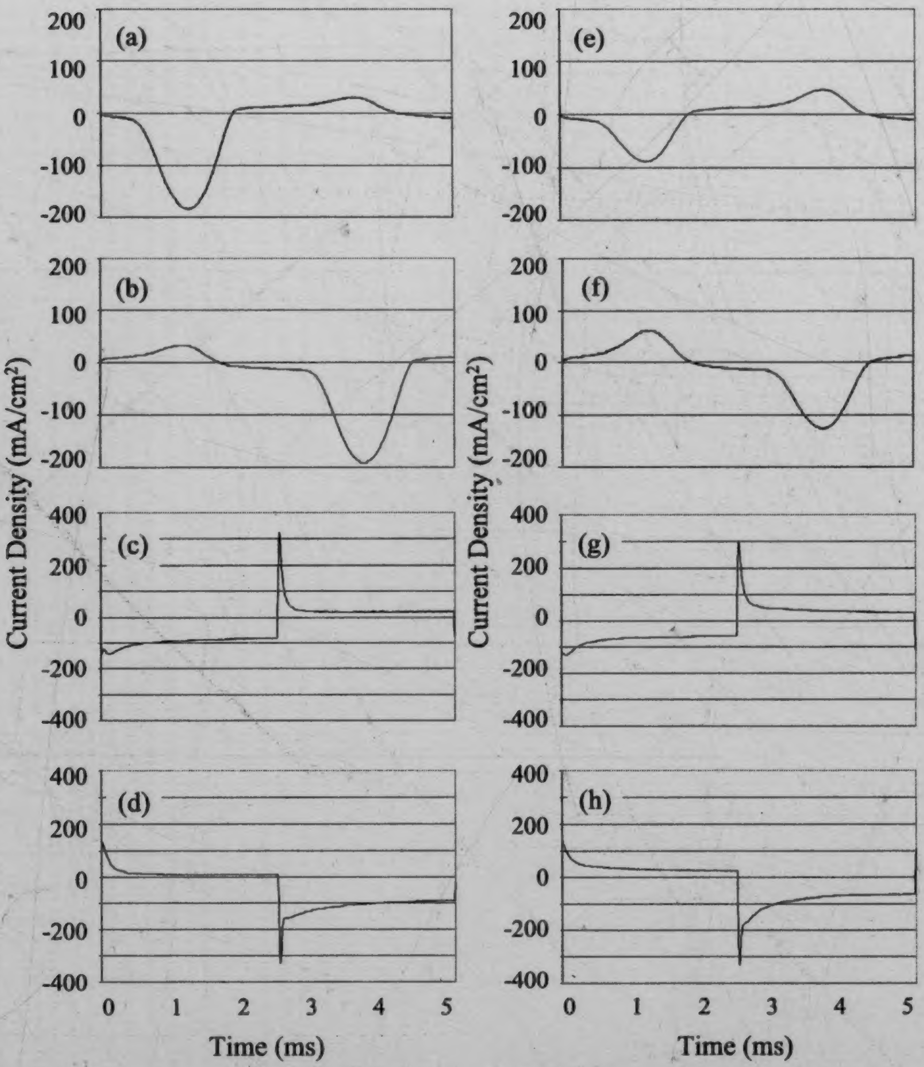

Figure C1. Current density traces for deposition into 24 μm deep pores recorded at the midpoint of the deposition. Plots (a)-(d) sulfuric acid-anodized pores, plots (e)-(h) oxalic acid-anodized pores. Sine wave with reductive/oxidative polarity (a) and (e), and oxidative/reductive polarity (b) and (f). Square wave with reductive/oxidative polarity (c) and (g), and oxidative/reductive polarity (d) and (h).

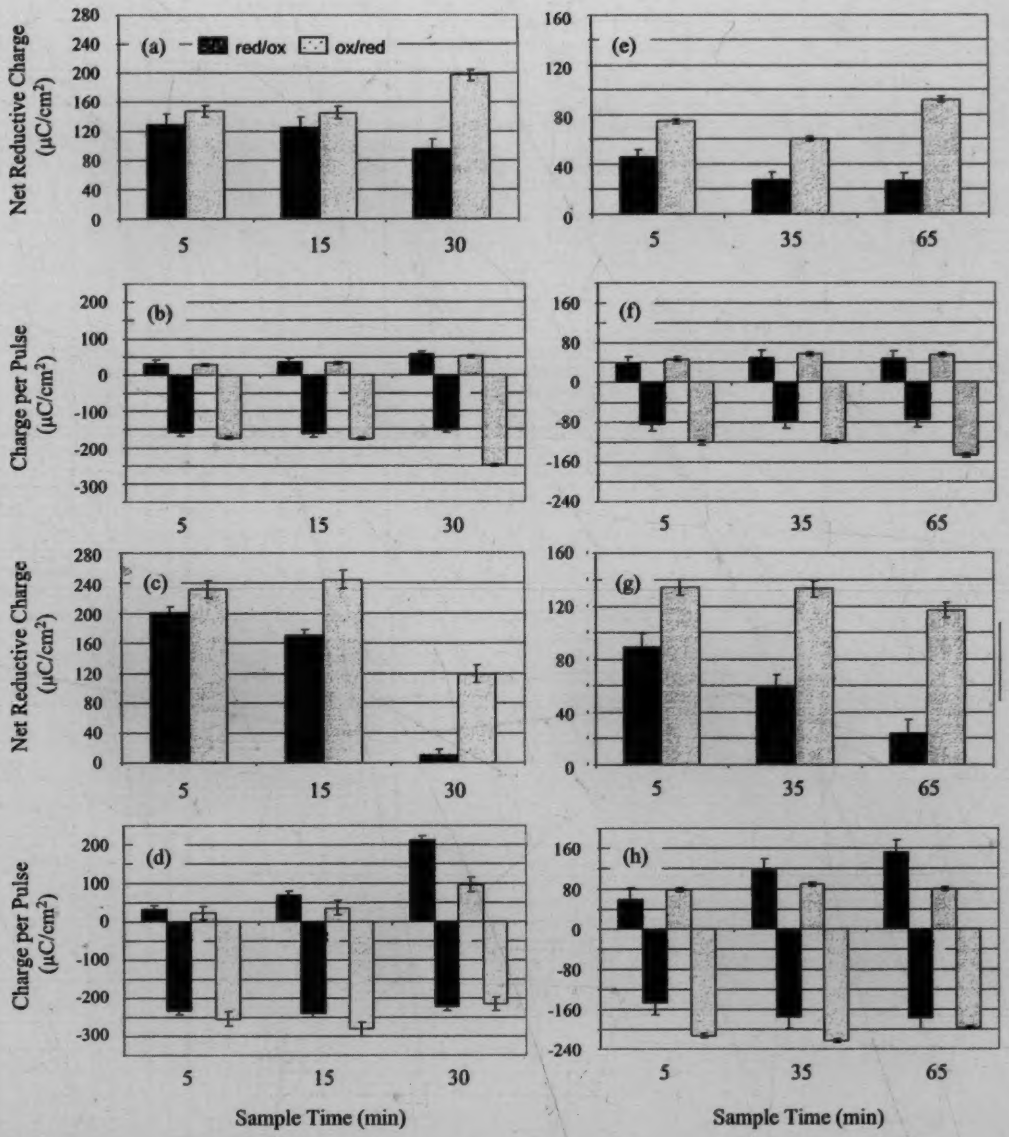

Figure C2. Charge density data for depositions into 24 μm deep sulfuric acid-anodized templates (a)-(d), and oxalic acid-anodized templates (e)-(h). Data in (a), (b), (e) and (f) collected during sine wave depositions, data in (c), (d), (g) and (h) collected during square wave depositions. Plots (a), (c), (e) and (g) show net reductive charge, plots (b), (d), (f) and (h) show charge separated into oxidative (positive) and reductive (negative) components. Reductive/oxidative pulse polarity dark bars, oxidative/reductive pulse polarity light bars.